

Copyright  
by  
Tianbo Liang  
2016

**The Dissertation Committee for Tianbo Liang certifies that this is the approved  
version of the following dissertation:**

**Water Block from Hydraulic Fracturing in Low Permeability Rocks:  
Experimental Studies on Causes and Potential Mitigation Methods**

**Committee:**

---

David A. DiCarlo, Supervisor

---

Quoc P. Nguyen, Co-Supervisor

---

Hugh C. Daigle

---

Kishore K. Mohanty

---

Michael A. Reynolds

**Water Block from Hydraulic Fracturing in Low Permeability Rocks:  
Experimental Studies on Causes and Potential Mitigation Methods**

**by**

**Tianbo Liang, B.S.E.; M.E.**

**Dissertation**

Presented to the Faculty of the Graduate School of

The University of Texas at Austin

in Partial Fulfillment

of the Requirements

for the Degree of

**Doctor of Philosophy**

**The University of Texas at Austin**

**December 2016**

## **Dedication**

To my parents, Bei Zhang and Dianyin Liang,  
for their endless love, encouragement and support.

&

To my grandparents in heaven, Huibi Li, Zhongming Zhang and Shuxiang Liang,  
whose memory I cherish always.



## **Acknowledgements**

This dissertation could not have been accomplished without the guidance, encouragement and support of my research advisors, Dr. David DiCarlo and Dr. Quoc Nguyen. No words can express my heartfelt gratitude for their mentoring in both research and life throughout my entire PhD. I would like to extend my gratitude to other members of my dissertation committee, Dr. Hugh Daigle, Dr. Kishore Mohanty and Dr. Michael Reynolds. Their valuable advice and insightful comments further enriched this dissertation.

I am extremely grateful to Royal Dutch Shell and CMG for their financial support to this research through Shell-UT Unconventional Research (SUTUR) program and Foundation CMG. I am also very thankful to Glen Baum, Gary Miscoe, Daryl Nygaard, Mark Smith, John Cassibry, Leilani Swafford, Gregory Siebers, Barbara Messmore, Frankie Hart and Amy Stewart for their technical and administrative support.

I would like to acknowledge my wonderful and helpful officemates and colleagues at the University of Texas at Austin, Xiongyu Chen, Xiao Luo, Oualid M'barki, Hasan Khan, Uyen Huynh, Jun Lu, Ke Xu, Yu Liang, Amir Kianinejad, Siddharth Senthilnathan, Yanzun Li, Xing Zhang, Lauren Churchwell, Sujeewa Palayangoda, Rafael Longoria, Mohammad Lotfollahi, Amir Taghavy, Behdad Aminzadeh and Mohammad Mirzaei. A special acknowledgement is given to my undergraduate interns and assistants, Tianlong Wang, Subbu Kumarappan and Sofiane Achour. These talented individuals gave me tremendous inspiration and great passion on this work. I would also like to thank all my friends in Austin for making my graduate school years so memorable.

Finally, I would love to thank my parents and all family members for their endless love, understanding, encouragement and support throughout these years.

# **Water Block from Hydraulic Fracturing in Low Permeability Rocks: Experimental Studies on Causes and Potential Mitigation Methods**

Tianbo Liang, Ph.D.

The University of Texas at Austin, 2016

Supervisor: David A. DiCarlo

Co-Supervisor: Quoc P. Nguyen

In the U.S., over half of the oil and gas production comes from hydraulically fractured wells in 2015; and the current trend is to inject more fracturing fluids (typically water) and proppants to create more complex fracture network and maximize the contact area with the formation. Hydrocarbon is mainly produced from the reservoir rock adjacent to the open fractures; therefore, any water left behind therein can block the flow of hydrocarbon and thus reduce the overall well productivity.

In this study, it is proposed that matrix-fracture interaction is crucial to understanding the water block. Water can be retained in the matrix through this interaction, which is analogous to capillary end effect in laboratory measurements. This can be typically ignored in conventional reservoirs with long length scales and large pressure drawdown relative to capillary pressure. However, this should not be ignored in the fractured low permeability reservoirs where hydrocarbon production comes from short distances from the fractures and pressure drawdown is not significantly higher than capillary pressure. Additionally, water block in different wetting conditions needs to be studied so that mitigation methods can be wisely chosen to solve the right problem and enhance hydrocarbon production effectively and efficiently.

This is experimentally achieved by using a three-step coreflood platform. This platform simulates the fracturing fluid invasion as well as the flowback occurring within the rock matrix adjacent to the fracture face. Under various mimicked reservoir/production conditions, regaining of rock permeability to hydrocarbon is obtained from measuring pressure drop versus time; this is further compared with the change of phase saturations in real-time either through flowback/effluent measurement or CT scans for the entire period of the coreflood. Based on the coreflood results, a more comprehensive understanding is achieved regarding the water block from fracturing in low permeability rocks.

To mitigate water block, three major methods have been suggested based on field and/or laboratory studies. They are drawdown management, shut-in/soaking treatment, and surfactant or volatile additive treatment. Our experimental methods also provide a new avenue to compare the efficiency and effectiveness of various mitigation methods in different mimicked reservoir conditions, so that their governing mechanisms can be elucidated from the viewpoint of multiphase flow.

For water-wet portion of the rock, matrix-fracture interaction dominates the early-time water block; the smaller the rock permeability, the longer its time-span. Once this interaction disappears, water block becomes the general form of capillary trapping. Shut-in/soaking is only effective on cleaning up the first form of water block and increasing the early-time production; however, it is unlikely to accelerate the spontaneous imbibition that mitigates such damage naturally, and shut-in does not increase the ultimate hydrocarbon production rate. Surfactant is very promising on cleaning up both forms of water block; among all tested formulations, the one generating Winsor type-I microemulsions with the mimicked reservoir oil shows the best performance.

For oil-wet portion of the rock, water block is mainly in the general form of capillary trapping. Trapped water within pore bodies creates a more serious reduction on

rock permeability to hydrocarbon comparing to the water-wet condition. To mitigate such water block, two typical surfactant treatments are mainly focused and compared, which are altering the rock wettability and achieving ultralow IFT with the reservoir oil. Synthesizing all the results, it is proposed that achieving ultralow IFT seems to be a better option for mitigating water block in oil-wet low permeability rocks.

## Table of Contents

List of Tables .....	xvi
List of Figures .....	xvii
Chapter 1: Introduction .....	1
Chapter 2: Background and Literature Review .....	6
2.1 Pore system of shale and its wettability .....	6
2.2 Hydraulic fracture and fracture network for fluid flow .....	8
2.2.1 Dimensions of hydraulic fractures .....	8
2.2.2 Natural fractures .....	11
2.2.3 Fracture network and area contributes to total hydrocarbon production .....	12
2.3 Mechanisms governing water block and permeability regaining from various enhancing methods .....	13
2.3.1 Mechanisms governing water block .....	13
2.3.2 Permeability regaining from various enhancing methods .....	15
2.3.2.1 Drawdown management .....	15
2.3.2.2 Shut-in/soaking treatment .....	15
2.3.2.3 Surfactant or volatile additive treatment .....	17
Chapter 3: Water Block within Fracturing Fluid Invaded Zone for Water-Wet Systems .....	19
3.1 Quick overview of this chapter .....	19
3.2 Introduction .....	20
3.3 Materials and methods .....	25
3.3.1 Field geometry and laboratory scaling .....	25
3.3.2 Core rock type and dimensions .....	26
3.3.3 Choice of hydrocarbon .....	27
3.3.4 Fracturing fluids and interfacial tension reducers .....	27
3.3.5 Interfacial tension measurements .....	29
3.3.6. Coreflood sequence and setup .....	29

3.4 Results.....	31
3.4.1 Capillary vs. viscous forces at core scale.....	35
3.4.2 Effect of reduction of capillary forces .....	35
3.4.3 Effect of shut-ins.....	40
3.5 Discussion .....	40
3.5.1 Implications for unconventional tight reservoirs .....	42
3.5.2 Implications for the use of surfactant-based EOR techniques in unconventional tight reservoirs.....	43
3.5.3 Role of reservoir rock wettability .....	45
3.6 Conclusions.....	45
3.7 Supplemental material (characteristic capillary pressure) .....	46
Chapter 4: Water Block within the Entire Rock Matrix Adjacent to the Propped Fractures for Water-Wet Systems.....	48
4.1 Quick overview of this chapter .....	48
4.2 Introduction.....	48
4.3 Materials and methods .....	52
4.3.1 Proxy fluids.....	54
4.3.2 Rock samples .....	54
4.3.3 Coreflood schemes.....	56
4.4 Results.....	57
4.4.1 Change during water invasion (Step-2) .....	57
4.4.2 Change during flowback and hydrocarbon production (Step-3).....	59
4.4.3 Understand the formation and mitigation of water block through calculation .....	62
4.4.4 Permeability reduction and regaining as a function of rock permeability .....	64
4.5 Discussion .....	66
4.5.1 Permeability reduction due to different types of water block.....	66
4.5.2 Influence of oil-wet part on mitigation of water block .....	67
4.6 Conclusions.....	68

Chapter 5: Evaluation of Shut-in/Soaking Treatment on Mitigating Water Block for Different Initial Reservoir Conditions .....	69
5.1 Quick overview of this chapter .....	69
5.2 Introduction.....	70
5.3 Materials and methods .....	72
5.3.1 Proxy fluids .....	73
5.3.2 Rock samples .....	73
5.3.3 Coreflood schemes .....	74
5.4 Results.....	77
5.4.1 Shut-ins for IRC-1.....	80
5.4.2 Shut-ins for IRC-2.....	82
5.4.2.1 Mitigation of water block after various lengths of shut-ins .....	82
5.4.2.2 Observing the mitigation of water block during shut-in treatment through CT scans .....	84
5.5 Discussion .....	87
5.6 Conclusions.....	92
Chapter 6: Evaluation of IFT Reduction on Mitigating Water Block for Water-Wet Systems .....	94
6.1 Quick overview of this chapter .....	94
6.2 Introduction.....	95
6.3 Materials and methods .....	98
6.3.1 Rock samples .....	98
6.3.2 Choice of hydrocarbon.....	98
6.3.3 Fracturing fluid additives.....	99
6.3.4 Coreflood schemes.....	102
6.4 Results.....	105
6.4.1 Simulation of fracturing fluid invasion (Step-2).....	105
6.4.1.1 Water invasion without additives.....	105
6.4.1.2 Water invasion with methanol as a moderate IFT modifier .....	106

6.4.1.3 Water invasion with surfactant as a strong IFT modifier ...	107
6.4.2 Simulation of fracturing fluid flowback (Step-3) .....	110
6.4.2.1 Flowback without additives .....	110
6.4.2.2 Flowback with methanol.....	113
6.4.2.3 Flowback with surfactant.....	115
6.5 Discussion.....	120
6.5.1 Fracturing fluid invasion.....	121
6.5.2 Flowback/hydrocarbon production .....	124
6.5.2.1 Permeability recovery without additives .....	124
6.5.2.2 Permeability recovery with additives that moderately reduce IFT.....	125
6.5.2.3 Permeability recovery with additives that provide ultralow IFT.....	125
6.5.3 Influence of oil-wet pores or small pores .....	127
6.6 Conclusions.....	128
Chapter 7: Evaluation of Microemulsion-Forming Surfactant Additives on Mitigating Water Block through a Glass Microfluidic Model .....	130
7.1 Introduction.....	130
7.2 Materials and methods .....	132
7.2.1 Microfluidic model .....	132
7.2.2 Choice of hydrocarbon.....	134
7.2.3 Surfactant-aided fracturing fluid.....	134
7.2.4 Flood schemes.....	136
7.3 Results and Discussion .....	138
7.3.1 Simulation of fracturing fluid invasion (Step-2).....	138
7.3.1.1 Water invasion without surfactant .....	138
7.3.1.2 Water invasion with surfactant at Winsor type-I condition .....	142
7.3.1.3 Water invasion with surfactant at Winsor type-III condition .....	146



7.3.1.4 Water invasion with surfactant at Winsor type-II condition .....	152
7.3.2 Simulation of fracturing fluid flowback (Step-3) .....	156
7.3.2.1 Flowback without surfactant.....	156
7.3.2.2 Flowback with surfactant at Winsor type-I condition...	160
7.3.2.3 Flowback with surfactant at Winsor type-III condition	167
7.3.2.4 Flowback with surfactant at Winsor type-II condition .	173
7.4 Conclusions.....	179
Chapter 8: Evaluation of Wettability Alteration and IFT Reduction on Mitigating Water Block for Oil-Wet Systems .....	180
8.1 Quick overview of this chapter .....	180
8.2 Introduction.....	181
8.3 Materials .....	185
8.3.1 Rock and hydrocarbon proxies .....	185
8.3.2 Wettability alteration agent.....	185
8.3.3 Surfactant formulation for IFT reduction .....	186
8.4 Methods.....	187
8.4.1 Wettability alteration tests .....	189
8.4.1.1 Imbibition cell test .....	189
8.4.1.2 Grinded sample test.....	189
8.4.2 Coreflood schemes.....	190
8.5 Results.....	192
8.5.1 Wettability alteration tests .....	192
8.5.1.1 Imbibition cell test .....	192
8.5.1.2 Grinded powder test.....	194
8.5.2 Water block vs. wettability and IFT at the same hydrocarbon flow rate.....	195
8.5.2.1 Water invasion (Step-2) at different wetting states and oil-water IFTs .....	196
8.5.2.2 Flowback and hydrocarbon production (Step-3) at different wetting states and oil-water IFTs.....	201

8.5.3 Water block vs. flow rates under different wettability .....	206
8.5.3.1 Flowback and hydrocarbon production (Step-3) under different drawdowns for water-wet rock (Coreflood #2 vs. Coreflood #1) .....	207
8.5.3.2 Flowback and hydrocarbon production (Step-3) under different drawdowns for oil-wet rock (Coreflood #4 vs. Coreflood #3) .....	209
8.6 Discussion .....	210
8.6.1 Permeability regaining as a function of wettability and IFT ....	210
8.6.1.1 Water block and permeability regaining in the water-wet state .....	210
8.6.1.2 Water block and permeability regaining in the oil-wet state .....	211
8.6.1.3 Using surfactants for oil-wet reservoirs: reducing IFT or altering wettability? .....	212
8.6.2 Permeability regaining as a function of drawdown in water-wet or oil-wet states .....	213
8.7 Conclusions.....	214
Chapter 9: Exploration of the Relationship between Flowback and Permeability Enhancement.....	216
9.1 Quick overview of this chapter .....	216
9.2 Introduction.....	217
9.3 Materials and methods .....	219
9.3.1 Rock type and core dimensions .....	219
9.3.2 Choice of hydrocarbon.....	219
9.3.3 Coreflood sequence and experimental setup.....	219
Step-1 – Establishing a hydrocarbon-rich reservoir.....	220
Step-2 – Simulating fracturing fluid invasion.....	220
Step-3 – Simulating fracturing fluid flowback and hydrocarbon production .....	220
9.4 Results and discussion .....	221
9.5 Conclusions.....	226

Chapter 10: Conclusions and Potential Future Work .....	228
10.1 Conclusions of the completed work.....	228
10.2 Recommendations for the potential future work .....	230
Nomenclature .....	232
Appendix A: Experimental Procedure of Three-Step Coreflood Sequence .....	233
A.1 General setup parameters .....	233
A.2 Experimental setup.....	233
A.3 Experimental procedure (without CT scans) .....	237
Step-0: Dry, mount and evacuate core sample.....	237
Step-1: Simulate hydrocarbon-rich reservoir.....	237
Step-2: Simulate fracturing fluid invasion.....	238
Step-3: Simulate fracturing fluid flowback during hydrocarbon production .....	239
Step-4: Remove core sample .....	239
Appendix B: CT Scan Parameters and Saturation Calculation from CT Scan Results .....	240
B.1 CT scan parameters .....	240
B.2 Saturation calculation for two-phase flow .....	240
Appendix C: Detailed Surfactant Formulations.....	243
C.1 Surfactant solution used in Chapter 3 .....	243
C.2 Surfactant solution used in Chapters 6&7 .....	243
Bibliography .....	244

## List of Tables

Table 3.1: Interfacial tensions between pentane and different proxy fracturing fluids used. ....	28
Table 4.1: Information of core samples and coreflood experiments (Corefloods #1-#2 are Corefloods #11-#12 in Chapter 5 (see Table 5.2), and results of Coreflood #2 will be shown in Chapter 5).....	55
Table 4.2: Parameters for history-matching the pressure drop curve during flowback of Coreflood #1. ....	63
Table 4.3: Petrophysical properties for scaling/extrapolating the duration of water block.....	66
Table 5.1: Information of core samples used in this study. ....	74
Table 5.2: List of corefloods conducted in this study (Corefloods #11-#12 are Corefloods #1-#2 in Chapter 4; more details refer to Table 4.1).....	75
Table 5.3: Changes of the total water saturation within the core under various flow rates for IRC-1 (Corefloods #1-#6).....	81
Table 6.1: Interfacial Tension (IFT) by Various Fracturing Fluid Additives. ....	100
Table 6.2: Schedule of Coreflood Experiments. ....	102
Table 7.1: Geometric dimensions of 2.5D glass microfluidic model (Ke Xu et al., Submitted).....	134
Table 8.1: Basic Information about Cyclohexanepentanoic Acid (by Sigma-Aldrich). ....	186
Table 8.2: Schedule of Coreflood Experiments in Sequence. ....	188

## List of Figures

Figure 1.1: U.S. primary energy consumption from various resources (EIA, 2016a)	1
Figure 1.2: Crude oil production from hydraulically fractured wells in the U.S. (EIA, 2016b)	2
Figure 1.3: Natural gas production from hydraulically fractured wells in the U.S. (EIA, 2016c)	2
Figure 2.1: Examples of interparticle pores within various mudrocks (intraparticle pores and organic-matter pores are also labelled): A: Pearsall; B: Austin Chalk; C: Haynesville; D: Atoka. (Loucks et al., 2012)	7
Figure 2.2: Example of intraparticle pores within Haynesville shale. (Milner et al., 2010)	7
Figure 2.3: Example of organic-matter pores within Barnett shale. (Milner et al., 2010)	8
Figure 2.4: Hydraulic fracture height growths in Barnett shale. (Fisher and Warpinski, 2012)	9
Figure 2.5: Microseismic mapping results for two adjacent wells in Marcellus shale. (Mayerhofer et al., 2011)	10
Figure 2.6: Comparison between relative contribution of hydrocarbon production (center), natural fracture frequency (bottom) and microseismic detected events (top) per stage of a well in an Upper Devonian shale gas reservoir. (Moos et al., 2011)	12

Figure 3.1: Schematic of field geometry and laboratory scaling. Fracturing fluid leaks off to the formation through the fracture face during hydraulic fracturing operations. This generates a water loading zone which can reduce the matrix permeability to the formation. This geometry is obtained in the lab by considering one of the faces of a core sample as the fracture face through which water penetrates the matrix and hydrocarbon flows out of it. ....	26
Figure 3.2: proRheo LS300 viscometer. ....	28
Figure 3.3: Schematic of experimental setup. A three-step coreflood sequence is used to simulate a hydrocarbon rich formation, fracturing fluid invasion and flowback, and hydrocarbon production. The pressure drop across the core and the effluent mass are recorded as a function of time. ....	31
Figure 3.4: The amount of fracturing fluid recovered as flowback depends on the injection flow rate. At the end of Step-3 of the coreflood sequence only hydrocarbon flows out of the core. The pressure drop at the end of this flooding step is used to calculate the final relative permeability to pentane. ....	33

Figure 3.5: The final relative permeability to hydrocarbon increases as viscous forces, relative to capillary forces, increase. A) Final relative permeability to pentane increases for low hydrocarbon injection flow rates during the fluid flowback and hydrocarbon production steps of our experiment but reaches a plateau for higher injection rates. Similarly, water recovered during flowback increases with increasing hydrocarbon flow rate until it reaches a plateau. B) A more physically meaningful scaling for the x-axis is the ratio of viscous to capillary forces.  $\Delta P$  is the pressure drop across the core at the end of the flowback phase and  $P_c$  is a characteristic capillary pressure obtained from the  $P_c$  vs.  $S_w$  curve for our rock sample.....34

Figure 3.6: Reduction of IFT between fracturing fluid and hydrocarbon increases the hydrocarbon relative permeability in the capillary dominated region. A) Supplementing the fracturing fluid with methanol reduces the IFT between pentane and brine by a factor of about 2. This is sufficient to significantly enhance the final relative permeability to pentane during the production phase of our experiment. B) Rescaling the data by the corresponding  $P_c$  in each case results in the overlap of both curves indicating that a competition between viscous and capillary forces is the controlling parameter for the observed permeability reduction.....37

Figure 3.7: Shut-ins after the flowback phase ended result on capillarity dependent permeability increases. The largest enhancements of permeability take place when capillary forces dominate over viscous forces (e.g. at low flow rates such as 0.1 ml/min for our system) but decrease or completely disappear as capillarity plays a smaller role (high flow rates or lower IFT between brine and hydrocarbon). No additional fluid flowback was observed upon resuming flow after the shut-in suggesting that enhancements are due to a capillarity-driven redistribution of the fluid inside the core. The capillarity-mediated matrix fracture interaction leads to an increased brine saturation near the fracture face which in turn reduces the final relative permeability to the hydrocarbon. This interaction is reduced during the shut-in period resulting on the observed increase in permeability. ....38

Figure 3.8: The capillary discontinuity between the matrix and the fracture at the fracture face is responsible for water block in unconventional reservoirs. Water block significantly affects production in formations where the pressure drawdown does not exceed a characteristic capillary pressure by at least 1 order of magnitude. Unconventional reservoirs fall in such a category. Interfacial tension reducers can help mitigate the impact of water block by reducing the capillary discontinuity between the matrix and the fracture rather than by capillary desaturation of the fracturing fluid lost to the formation. ....39



Figure 3.9: Mercury extrusion capillary pressure curve for Texas Cream Limestone scaled to the pentane/water system using Leverett J-function equation. The dashed lines show the possible water saturations. The green star indicates the characteristic capillary pressure for this case. The value of IFT between pentane and water and the contact angle used are 50mN/m and 18°, respectively. ....	47
Figure 4.1: Field geometry (A) comparing to the lab model (B). ....	53
Figure 4.2: Coreflood setup in the lab. ....	53
Figure 4.3: Change of water saturation profile (top) and side views of water distribution within the core sample at different time slices (bottom) during DI water invasion. ....	58
Figure 4.4: Change of water saturation profile within the core sample at different time slices during flowback and hydrocarbon production in Coreflood #1. ....	60
Figure 4.5: Changes of the overall water saturation inside the core sample (blue discrete data points) and the measured pressure drop across the core (black curve) during flowback and hydrocarbon production in Coreflood #1; red discrete data points shows the calculated pressure drops at different time slices through the fitted Corey-type relative permeability curves. ....	61
Figure 4.6: Comparison of changes of the pressure drop across the core during flowback and hydrocarbon production on three different core samples with different permeabilities (Coreflood #1, #3 and #4). ....	64
Figure 4.7: Duration of water block for rocks with different petrophysical properties. ....	65

Figure 5.1: Pressure drop across the core as a function of time (in PV) during water invasion and flowback for IRC-1 (A) or IRC-2 (B). Post-production shut-in is performed after Step-3 for all IRC-1 cases. ....	79
Figure 5.2: Regained relative permeabilities to hydrocarbon before (blue columns) and after (red columns) performing shut-ins at various flow rates. The volume of flowback water in each case is shown as the orange diamond dot; no detectable change was observed after performing the shut-in (Corefloods #1-#6).....	81
Figure 5.3: Pressure drop across the core during flowback and hydrocarbon production (Step-3) as a function of time (in PV) after different shut-in time spans after water invasion (Step-2). All the comparisons are conducted on the same core sample (Corefloods #7-#10). ....	83
Figure 5.4: Change of water saturation profile within the core sample at different time slices during the shut-in treatment (Coreflood #12). ....	84
Figure 5.5: Change of water saturation profile within the core sample at different time slices during flowback and hydrocarbon production after 15hr-shut-in treatment (Coreflood #12).....	85
Figure 5.6: Changes of the overall water saturation inside the core sample (blue discrete data points) and the measured pressure drop across the core (black curve) during flowback and hydrocarbon production after 15hr-shut-in treatment; red discrete data points shows the calculated pressure drops at different time slices through the fitted Corey-type relative permeability curves (Coreflood #12). ....	86

Figure 5.7: Pressure drop across the core during flowback and hydrocarbon production (Step-3) as a function of time (in PV) after different shut-in time spans after water invasion (Step-2). Pressure drops are shifted to compare the permeability enhancement at the same time since the end of invasion process. This figure is modified from Figure 5.3 shown above.	89
Figure 5.8: Comparison of the regained relative permeability to pentane during flowback and hydrocarbon production after 15hr-shut-in treatment was performed or not (Corefloods #11-#12).	91
Figure 5.9: Comparison of the change of water saturation within the core during flowback and hydrocarbon production after 15hr-shut-in treatment was performed or not (Corefloods #11-#12).	92
Figure 6.1: Phase behavior tests between pentane and various fracturing fluid additives. 2mL pentane and 2mL mimicked fracturing fluid were added in each pipette, gently shaken several times, and then allowed to equilibrate at 25°C. Black arrow points to the interfaces before mixing and red arrows points to the interfaces after mixing.	101
Figure 6.2: Field geometry (A) comparing to the lab model (B).	103
Figure 6.3: Changes of water saturation profile (A) and the pressure drop across the core (B) during fracturing fluid invasion in the baseline case (Coreflood #1).	106
Figure 6.4: Changes of water saturation profile (A) and the pressure drop across the core (with comparison to the baseline) (B) during fracturing fluid invasion in the methanol case (Coreflood #2).	107

Figure 6.5: Comparison of changes of water saturation profile during fracturing fluid invasion in various surfactant cases (Left column: baselines; right column (from top to bottom): conditions that form Winsor type-I, type-II and type-III microemulsions).....	109
Figure 6.6: Comparison of changes of pressure drop across the core during fracturing fluid invasion among various surfactant cases (Corefloods #1, #3, #5 and #7). .....	110
Figure 6.7: Change of water saturation profile during flowback and hydrocarbon production the baseline case (Coreflood #1). .....	112
Figure 6.8: Changes of the overall water saturation inside the core (blue discrete data points) and the pressure drop across the core (black curve) during flowback and hydrocarbon production the baseline case (Coreflood #1). .....	112
Figure 6.9: Change of water saturation profile during flowback and hydrocarbon production the methanol case (Coreflood #2).....	114
Figure 6.10: Comparison of changes of the overall water saturation inside the core between the methanol and baseline cases (Coreflood #2). .....	114
Figure 6.11: Comparison of changes of pressure drop across the core between the methanol and baseline cases (Coreflood #2). .....	115
Figure 6.12: Comparison of changes of water saturation profile during flowback and hydrocarbon production among various surfactant cases (Left column: baselines; right column (from top to bottom): conditions that form Winsor type-I, type-II or type-III microemulsions).....	116

Figure 6.13: Comparison of changes of the overall water saturation within the core (left column) and the pressure drop across the core (right column) during flowback among various surfactant cases (From top to bottom: conditions that form Winsor type-I, type-II or type-III microemulsions). .....	119
Figure 6.14: Comparison of water saturation profile at the end of fracturing fluid invasion among various surfactant cases (From left to right: conditions that form Winsor type-I, type-II or type-III microemulsions) .....	122
Figure 7.1: Sketch and microscopic characterization of 2.5D glass microfluidic model (Ke Xu et al., Submitted). .....	133
Figure 7.2: Sketch of cross-sectional view of 2.5D pore-throat structure (Ke Xu et al., Submitted). .....	133
Figure 7.3: Results of phase behavior tests between various surfactant solutions and n-pentane or n-hexane at room temperature. 2mL hydrocarbon and 2mL surfactant solution were added in each pipette, gently shaken several times, and then allowed to equilibrate at 25°C. Black arrow points to the interfaces before mixing and red arrows points to the interfaces after mixing. All surfactant solutions passed the aqueous stability tests without any precipitation at their assigned salinities. ....	135
Figure 7.4: Experimental platform for observing the phase change during surfactant- aided water invasion and flowback in a 2.5D glass microfluidic model. Two Fusion 400 syringe pumps are used to inject oil and water separately into this model; the microscope is equipped with a digital camera that all images and videos are directly recorded by a computer. .....	136

Figure 7.5: Changes of local phase saturations during water invasion (left column) or pump shut-in (right column) within 20 seconds. Closed transparent circles are solid grains of the microfluidic model, and the rest space is the porous media; dyed DI water is blue while n-hexane is white. 140

Figure 7.6: Local water saturation at the invasion front (top), within the middle range of the invasion body (center), or at the invasion tail near the inlet of the porous media (bottom) after DI water invaded the microfluidic model from the right-hand side. ....141

Figure 7.7: Changes of local phase saturations during type-I surfactant solution invasion within 20 seconds. Closed transparent circles are solid grains of the microfluidic model, and the rest space is the porous media; dyed DI water is blue while n-hexane is white. ....143

Figure 7.8: Local water saturation at the invasion front (top), within the middle range of the invasion body (center), or the invasion tail near the inlet of the porous media (bottom) after type-I surfactant solution invaded the microfluidic model from the right-hand side. ....144

Figure 7.9: Close-up view of the near-invasion-front region after type-I surfactant solution invaded the microfluidic model. Red arrows point the fuzzy clusters that are likely the microemulsions. ....145

Figure 7.10: Changes of local phase saturations during type-III surfactant solution invasion within 20 seconds. Closed transparent circles are solid grains of the microfluidic model, and the rest space is the porous media; dyed DI water is blue while n-hexane is white. ....148

Figure 7.11: Local water saturation at the invasion front (top), within the middle range of the invasion body (center), or the invasion tail near the inlet of the porous media (bottom) after type-III surfactant solution invaded the microfluidic model from the right-hand side. ....	149
Figure 7.12: Close-up view of the near-invasion-tail region after type-III surfactant solution invaded the microfluidic model. Red arrows point the fuzzy clusters that are likely the microemulsions. ....	150
Figure 7.13: Close-up view of the formation of type-III microemulsions. Red arrows point the residual oil droplets that were gradually sheared to form the microemulsions and carried away by the surfactant solution. ....	151
Figure 7.14: Changes of local phase saturations during type-II surfactant solution invasion within 20 seconds. Closed transparent circles are solid grains of the microfluidic model, and the rest space is the porous media; dyed DI water is blue while n-pentane is white. ....	153
Figure 7.15: Close-up view of the formation of type-II microemulsions during the initial mixing at the invasion front. Dyed DI water is blue while n-pentane is white; the light blue fluid formed during the mixing is very likely the type-II microemulsion. ....	154
Figure 7.16: Local water saturation at the invasion front (top), within the middle range of the invasion body (center), or the invasion tail near the inlet of the porous media (bottom) after type-II surfactant solution invaded the microfluidic model from the right-hand side. ....	155

Figure 7.17: Changes of local phase saturations during flowback and hydrocarbon production from the DI water invaded microfluidic model for 180s (0.05PV). Closed transparent circles are solid grains of the microfluidic model, and the rest space is the porous media; dyed DI water is blue while n-hexane is white. ....158

Figure 7.18: Changes of local water saturation at the invasion front (top), within the middle range of the invasion body (center), or at the invasion tail (bottom) after 0.5PV of hexane flood through the DI water invaded microfluidic model.....159

Figure 7.19: Changes of local phase saturations during flowback and hydrocarbon production from the type-I surfactant solution invaded microfluidic model for 360s (0.10PV). Closed transparent circles are solid grains of the microfluidic model, and the rest space is the porous media; dyed DI water is blue while n-hexane is white. ....163

Figure 7.20: Changes of local water saturation at the invasion front (top), within the middle range of the invasion body (center), or at the invasion tail (bottom) after 0.5PV of hexane flood through the type-I surfactant solution invaded microfluidic model. ....164

Figure 7.21: Changes of the trapped bubbles for 108s (0.03PV) after 0.5PV of hexane flood through the type-I surfactant solution invaded microfluidic model. Red arrows point the change within the same pore at different time slices.....165

Figure 7.22: Changes of local water saturation across the invaded region (from the original invasion front to the invasion tail) after 3.5PV of hexane flood through the type-I surfactant solution invaded microfluidic model.166



Figure 7.23: Changes of local phase saturations during flowback and hydrocarbon production from the type-III surfactant solution invaded microfluidic model for 360s (0.10PV). Closed transparent circles are solid grains of the microfluidic model, and the rest space is the porous media; dyed DI water is blue while n-hexane is white. ....	169
Figure 7.24: Changes of local water saturation at the invasion front (top), within the middle range of the invasion body (center), or at the invasion tail (bottom) after 0.5PV of hexane flood through the type-III surfactant solution invaded microfluidic model. ....	170
Figure 7.25: Changes of the trapped bubbles for 432s (0.12PV) after 0.5PV of hexane flood through the type-III surfactant solution invaded microfluidic model. Red arrows point the change within the same pore at different time slices.....	171
Figure 7.26: Changes of local water saturation across the invaded region (from the original invasion front to the invasion tail) after 2.5PV of hexane flood through the type-III surfactant solution invaded microfluidic model. ....	172
Figure 7.27: Changes of local phase saturations during flowback and hydrocarbon production from the type-II surfactant solution invaded microfluidic model for 360s (0.10PV). Closed transparent circles are solid grains of the microfluidic model, and the rest space is the porous media; dyed DI water is blue while n-pentane is white. ....	175
Figure 7.28: Changes of local water saturation at the invasion front (top), within the middle range of the invasion body (center), or at the invasion tail (bottom) after 0.5PV of pentane flood through the type-II surfactant solution invaded microfluidic model. ....	176

Figure 7.29: Changes of the trapped bubbles for 108s (0.03PV) after 0.5PV of pentane flood through the type-II surfactant solution invaded microfluidic model. Red arrows point the formation of two preferred flow paths with time.....	177
Figure 7.30: Changes of local water saturation at the invasion tail (i.e., the matrix outlet) across the matrix width after 2.5PV of pentane flood through the type-II surfactant solution invaded microfluidic model. Red arrows point the formed preferred flow paths.....	178
Figure 8.1: Phase behavior test between n-pentane and 1wt% surfactant solution at a salinity of 47500ppm. Red arrow points the original oil-water contact before mixing .....	187
Figure 8.2: Schematic of the coreflood setup (A) and three-step coreflood sequence (B) (Modified from (Liang et al., 2015a, 2016)). .....	192
Figure 8.3: Results of imbibition cell tests after 30 days when the wettability alteration agent was applied (A) or not applied (B). In each figure, the black short line labeled on the imbibition cell shows the original oil-water contact; the black dotted-line arrow points the oil-water contact after 30 days, and the red solid-line arrow points the oil droplet(s) displaced out of the core sample within these 30 days. ....	193
Figure 8.4: Results of grinded powder tests after 15 days when the wettability alteration agent was applied (left) or not applied (right). ....	195
Figure 8.5: Change of water saturation profile during DI water invasion into the core sample at the water-wet state (Step-2, Coreflood #1).....	197

Figure 8.6: Comparison of changes of pressure drop across the core during fracturing fluid invasion under various conditions (Step-2, Corefloods #1, #3 and #5). .....	198
Figure 8.7: Change of water saturation profile during DI water invasion into the core sample at the oil-wet state (Step-2, Coreflood #3). .....	199
Figure 8.8: Change of water saturation profile during surfactant solution invasion into the core sample at the oil-wet state (Step-2, Coreflood #5).....	200
Figure 8.9: Change of water saturation profile during flowback after DI-water invasion into the core sample at the water-wet state (Step-3, Coreflood #1). .....	202
Figure 8.10: Comparison of changes of the total water saturation within the core (A) or the pressure drop across the core (B) during flowback under various conditions (Step-3, Corefloods #1, #3 and #5). .....	203
Figure 8.11: Change of water saturation profile during flowback after DI-water invasion into the core sample at the oil-wet state (Step-3, Coreflood #3). .....	204
Figure 8.12: Change of water saturation profile during flowback after surfactant solution invasion into the core sample at the oil-wet state (Step-3, Coreflood #5). .....	206
Figure 8.13: Change of water saturation profile during flowback (flow rate=0.1cc/min) after DI-water invasion into the core sample at the water-wet state (Step-3, Coreflood #2). .....	208
Figure 8.14: Comparison of changes of the total water saturation within the core (A) or the pressure drop across the core (B) during flowback under various conditions (Step-3, Corefloods #1-#4).....	209

Figure 8.15: Comparison of changes of regained permeability to pentane under various conditions. ....	211
Figure 8.16: Comparison of changes of regained permeability to pentane with time (in pore volumes (A) or hours (B)) under various conditions. ....	213
Figure 9.1: Schematic of coreflood sequence and setup. A) A three-step coreflood sequence that simulates fracturing fluid loss, fluid flowback and production from a hydraulically-fractured reservoir was developed. B) Hydrocarbon and water are injected through opposite faces of the core. The core face from which water is injected represents the fracture face of a hydraulically-fractured reservoir. ....	221
Figure 9.2: Effective relative permeability to hydrocarbon as a function of average water saturation of the core sample. The final water saturation is the result of the initial water saturation plus a slug of water injection (0.2PV) minus the total recovered water during flowback for 1PV. ....	222
Figure 9.3: Flowback vs. initial water saturation ( $S_{wi}$ ). A 0.2PV water slug was injected into cores with different initial water saturations. The amount of fluid recovered as flowback increases with increasing initial water saturation of the core. The recovered flowback is reported as a percent of the injected water slug volume. ....	223
Figure 9.4: Effective hydrocarbon permeability vs. recovered flowback. A 0.2PV water slug was injected into cores with different initial water saturations. The hydrocarbon permeability was calculated after 1 PV of hydrocarbon flowed through the core and decreases with increasing fluid recovery during flowback. The recovered flowback is reported as a percentage of the original volume of water injected. ....	224

Figure 9.5: Pressure drop across core during flowback and production phase (Step-3) as a function of time (in pore volumes, PV) for different initial water saturations. A 0.2PV water slug was injected into cores with different initial water saturations. In all cases, the flowback phase began immediately after the slug-sized water injection. ....	226
Figure A.1: Schematic of experimental setup when CT scanner is not used. ....	233
Figure A.2: Pump used in the coreflood experiments (Jasco PU-2080 HPLC pump). .....	234
Figure A.3: Coreflood setup inside an oven when CT scanner is not used. ....	235
Figure A.4: Coreflood setup when CT scanner is used. ....	236
Figure B.1: PEEK container for measuring the fluid bulk CT number at the required pressure. ....	241

## Chapter 1: Introduction

According to the Annual Energy Outlook 2016 provided by the U.S. Energy Information Administration (EIA), more than 65% of U.S. primary energy consumption relies on oil and natural gas in 2015, and this trend is likely to continue up to 2040 (Figure 1.1). Most of these resources are stored in low permeability rocks where hydraulic fracturing has to be applied to obtain an economical production rate; also according to EIA, 51% of crude oil production and 67% of natural gas production in the U.S. came from hydraulically fractured wells in 2015 (Figure 1.2 and Figure 1.3).

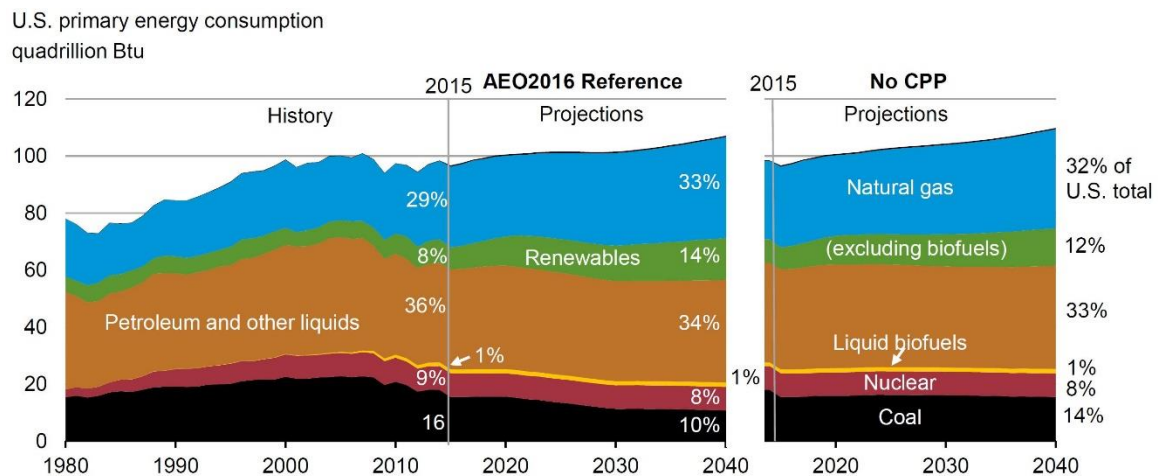


Figure 1.1: U.S. primary energy consumption from various resources (EIA, 2016a)

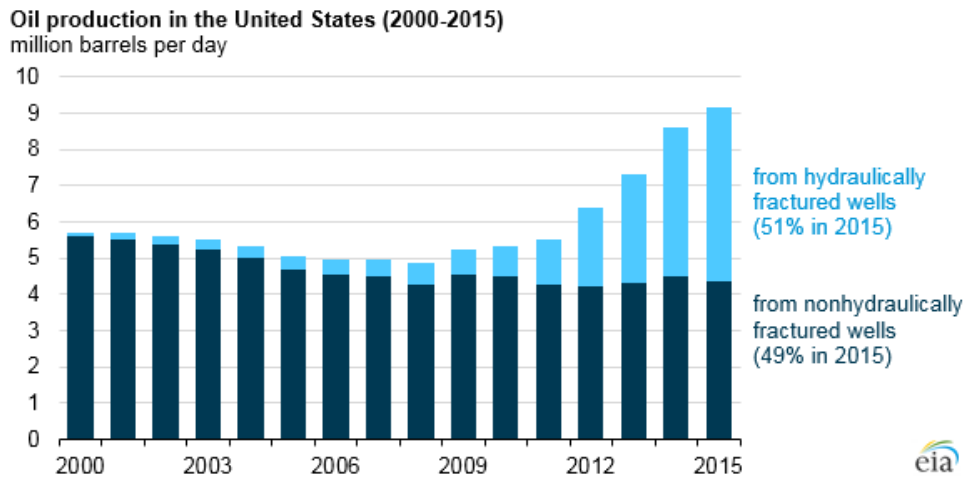


Figure 1.2: Crude oil production from hydraulically fractured wells in the U.S. (EIA, 2016b)

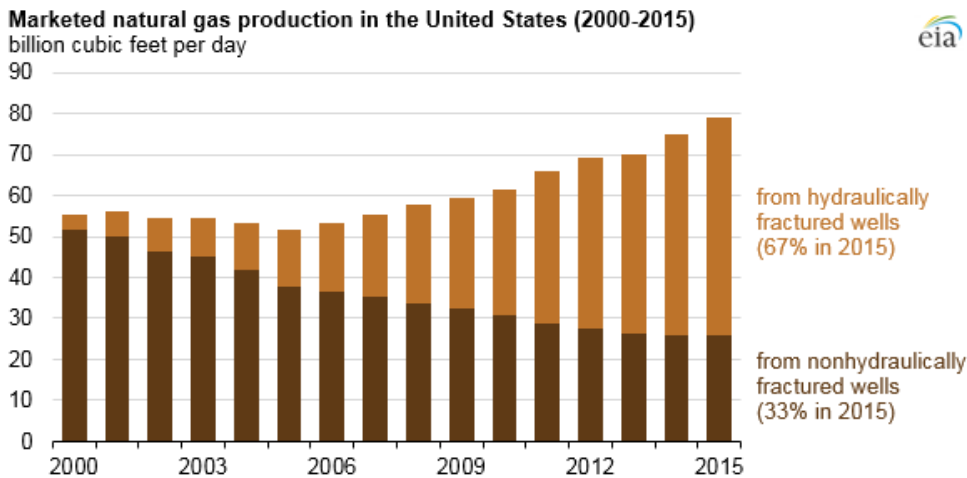


Figure 1.3: Natural gas production from hydraulically fractured wells in the U.S. (EIA, 2016c)

During hydraulic fracturing, several million gallons of water is typically injected through each well into the formation to create a fracture network (Kondash and Vengosh, 2015); this network maximizes the contact area with the formation and also provides pathways for hydrocarbons to flow. However, it has been reported that only 5% to 50% of

the injected water can be recovered as “flowback” after the fracturing (Penny and Pursley, 2007; Zelenev and Ellena, 2009; King, 2012; Wasylishen and Fulton, 2012). Water loss into the formation can have detrimental effects on the hydrocarbon flow from chemical and mechanical damage, for example, clay swelling or rock softening (Abrams and Vinegar, 1985; Alramahi and Sundberg, 2012; Das et al., 2014; Zhang et al., 2015), and/or relative permeability reduction due to multiphase flow. The last effect of permeability reduction is the focus of this PhD research, and it is referred as the “water block” in this dissertation. Although it is widely accepted that this type of water block is attributed to the capillary trapping of the water phase, the detailed mechanisms regarding its form, severity, time span and clean-up under different reservoir/production conditions have not been clearly elucidated yet.

To mitigate water block so as to enhance the hydrocarbon production after hydraulic fracturing, various methods have been proposed. Three major ones are (1) drawdown management (Holditch, 1979; Abrams and Vinegar, 1985; Parekh and Sharma, 2004; Sharma and Agrawal, 2013), (2) shut-in/soaking treatment (Cheng, 2012; Almulhim et al., 2014; Bertonecello et al., 2014; Dutta et al., 2014; Yaich et al., 2015) and (3) surfactant or volatile additive treatment (Parekh and Sharma, 2004; Paktinat et al., 2005; Penny and Pursley, 2007; Zelenev and Ellena, 2009; Agee et al., 2010; Howard et al., 2010; Ahmadi et al., 2011; Wang et al., 2012; Xu and Fu, 2012; Crafton and Noe, 2013; Pagels et al., 2013; Rostami and Nasr-El-Din, 2014; Alvarez and Schechter, 2015; He et al., 2015; Morsy and Sheng, 2015; Sun et al., 2015; Bui et al., 2016; Kim et al., 2016; Neog and Schechter, 2016; Shuler et al., 2016). Enhancements of hydrocarbon production from these managements/treatments have been reported either from the lab or from the field; however, unconventional tight reservoirs can differ significantly from one another, which could make the use of these techniques effective in some cases while not in others. Screening



criteria are very necessary for optimizing fracturing fluid additives and/or managing flowback operations to enhance hydrocarbon production from different types of unconventional tight reservoirs.

In this study, a coreflood platform is developed that simulates the fracturing fluid invasion as well as the flowback during hydrocarbon production occurring in the reservoir rock near the fracture face. Regaining of rock permeability to hydrocarbon is obtained from measuring pressure drop versus time; this is further compared with the changes of phase saturations in real-time either through flowback/effluent measurement or CT scans for the entire period of the experiment. Based on results from this platform, a new blocking mechanism is proposed that can dominate the permeability reduction due to multiphase flow especially during the early time of hydrocarbon production. Permeability regaining from all three managements/treatments are further evaluated in the lab that their mechanisms of enhancement can be compared under different reservoir conditions (e.g., rock permeability and wettability).

To elaborate this study, the dissertation is organized as follows:

Chapter 2 provides a brief literature review on the pore structure of shale as well as its connection with the hydraulic fractures; this section serves as the theoretical foundation of the experimental design for the entire study. Chapter 2 also reviews the mechanisms people have proposed to explain the water block in tight rocks as well as the impacts of three managements/treatments on enhancing the rock permeability to hydrocarbon.

Chapter 3 focuses on water block within the water invaded zone for water-wet systems. A new blocking mechanism is proposed that may give rise to the major permeability reduction in the low permeability water-wet rocks after hydraulic fracturing.

Chapter 4 extends the focus to the entire body of rock adjacent to the fractures that can contribute to the hydrocarbon production. The impact of the water invaded zone on the

effective rock permeability to hydrocarbon is studied as a function of time and absolute rock permeability.

Chapter 5 provides the evaluation of shut-in/soaking treatment for different reservoir conditions with different initial water saturation.

Chapter 6 provides the evaluation of surfactant treatment for a range of interfacial tension (IFT) reductions. For surfactants generate the ultralow IFT reductions, a range of salinities is tested to compare the effects of various Winsor-type microemulsions on the efficiency of water flowback as well as the improvement of rock permeability to hydrocarbon.

Chapter 7 shows an in-depth study on the effect of surfactants, which generate ultralow oil-water IFT, on mitigating water block through a 2.5D (i.e., pseudo-three-dimensional) glass microfluidic model. The phase changes of oil-water system during fracturing fluid invasion and flowback can be directly visualized and then compared with the coreflood results shown in Chapter 6.

Chapter 8 extends the study of water block to the oil-wet systems. Surfactant treatment is explored for this system as well; permeability enhancement through either wettability alteration or IFT reduction are compared on the same porous media.

Chapter 9 compares the percentage of flowback water and the regaining of rock permeability to hydrocarbon under various reservoir/production conditions. From the viewpoint of multiphase flow in porous media, it suggests that the amount of flowback cannot be used for judging the quality of overall well stimulation.

Chapter 10 summarizes this study and gives some pertinent recommendations for the future work.

## **Chapter 2: Background and Literature Review**

This chapter first provides a brief literature review on the pore structure of shale as well as its connection with the hydraulic fractures; this serves as the theoretical foundation of the experimental design for the entire study. Second, it reviews the mechanisms people have proposed to explain water block in tight rocks as well as the impacts of three managements/treatments on enhancing the rock permeability to hydrocarbon.

More detailed and relevant literature reviews are given at the beginning of each chapter, depending on their topics.

### **2.1 PORE SYSTEM OF SHALE AND ITS WETTABILITY**

According to the definition provided by the U.S. Department of Energy, shale is originated from mud deposition in low-energy environment and it primarily consists of consolidated clay-sized particles (DOE, 2009). After lithified and transferred into thin layered shale (i.e., mudrock), formation has very limited horizontal permeability and extremely limited vertical permeability. Although shale composition varies with different basins or even within the same basin, it is generally composed of clay, quartz, carbonate, pyrite and kerogen (Curtis et al., 2012b). For the typical unfractured shale plays in North America, the matrix permeability could be of the order of microDarcies down to nanoDarcies (DOE, 2009; Nelson, 2009).

The pore system of shale is crucial to the storage and transport of hydrocarbons in the reservoir; it is normally classified into three types: interparticle pores and intraparticle pores associated with the inorganic matrix, as well as pores associated with the organic matter (Curtis et al., 2010; Milner et al., 2010; Loucks et al., 2010, 2012). Figure 2.1-2.3 shows the examples of these types of pores within shales/mudrocks.

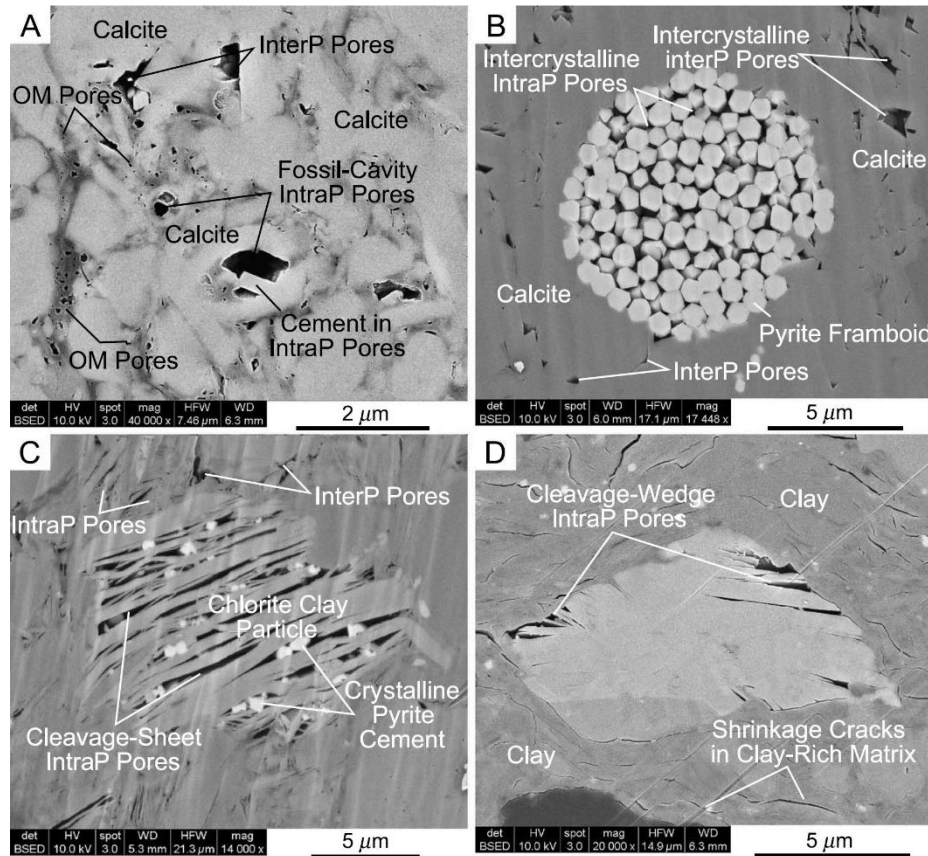


Figure 2.1: Examples of interparticle pores within various mudrocks (intraparticle pores and organic-matter pores are also labelled): A: Pearsall; B: Austin Chalk; C: Haynesville; D: Atoka. (Loucks et al., 2012)

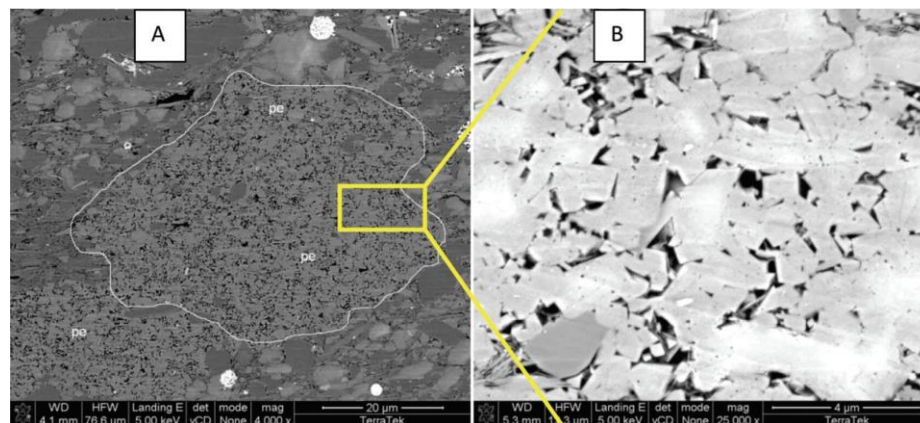


Figure 2.2: Example of intraparticle pores within Haynesville shale. (Milner et al., 2010)

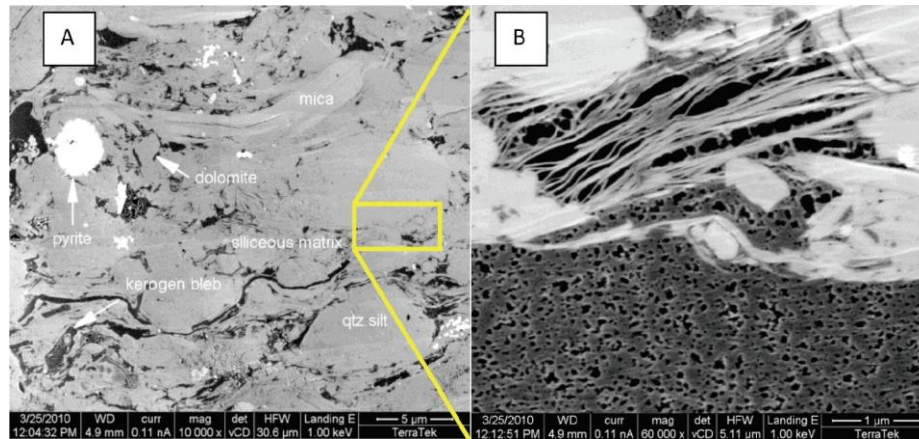


Figure 2.3: Example of organic-matter pores within Barnett shale. (Milner et al., 2010)

Organic matter is considered as the source of hydrocarbon and thus oil-wet; generated hydrocarbon can be adsorbed on the surface of organic-matter pores, or stored within these pores. It is believed that their pore structures are significantly affected by the total organic carbon (TOC) content (Milliken et al., 2013) and/or the thermal maturity (Milner et al., 2010; Curtis et al., 2010, 2012a). Nevertheless, majority of the organic-matter pores is believed to range from 5 to 100nm, while some big pores can be up to 750nm and serve as the pathways for hydrocarbon flow (Loucks et al., 2009).

Hydrocarbon can migrate and also be stored in the pores associated with the inorganic matrix. These pores are normally considered as water-wet, except the ones that have been contacted with polar compounds in oil and altered into oil-wet.

Therefore, shale is typically considered as mixed-wet.

## 2.2 HYDRAULIC FRACTURE AND FRACTURE NETWORK FOR FLUID FLOW

### 2.2.1 Dimensions of hydraulic fractures

Hydraulic fracturing creates a fracture network that extends the contact area with the formation and also provides a pathway for hydrocarbons to flow. The dimensions of

the growth of hydraulic fractures can be mapped through tracers, microseismic and microdeformation tools (Warpinski, 1996; Fisher and Warpinski, 2012). Fisher and Warpinski collected and showed the data on thousands of hydraulic-fracturing treatments in the Barnett, Woodford, Marcellus and Eagle Ford shale plays. They found the height of hydraulic fractures could be well constrained within the shale pay-zones, as long as they were not affected by the fault interceptions and bypassed into other layers (Fisher and Warpinski, 2012).

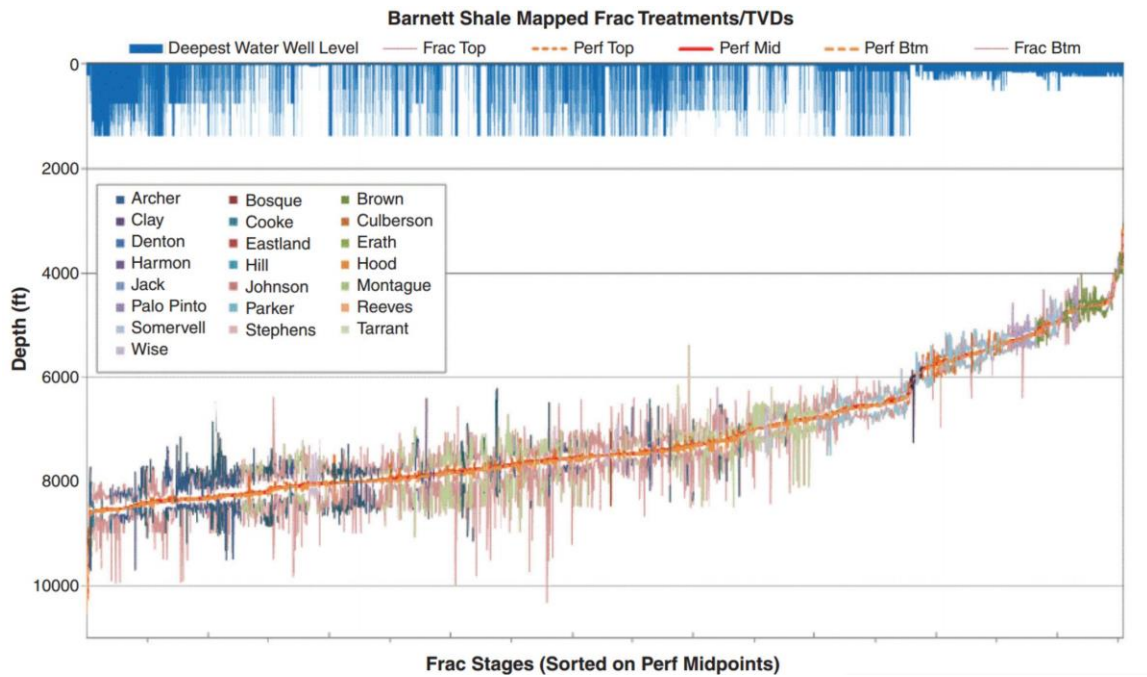


Figure 2.4: Hydraulic fracture height growths in Barnett shale. (Fisher and Warpinski, 2012)



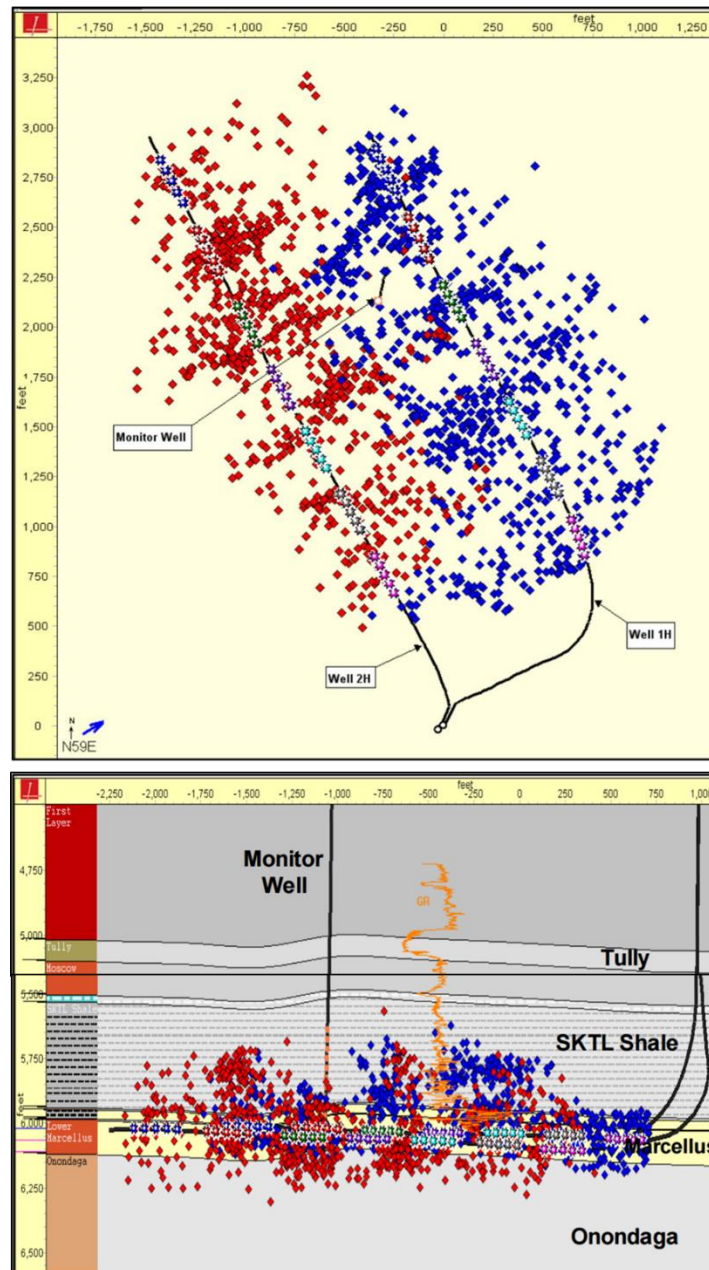


Figure 2.5: Microseismic mapping results for two adjacent wells in Marcellus shale.  
(Mayerhofer et al., 2011)

Besides the heights of hydraulic fractures, their lengths can also be mapped through similar methods. As shown in Figure 2.5, the average half wing length of hydraulic fracture was about 500ft and the height was about 250ft to 500ft in a “two-well, multi-stage, multi-perforation-clusters completion” in the Marcellus shale (Mayerhofer et al., 2011).

Due to the limitations of microseismic method, the dimensions of hydraulic fractures are also estimated through numerical simulations. It has been reported that the surface area of rock matrix exposed by the open fractures is approximately on the order of 0.2-10 million ft<sup>2</sup> depending on the location of the shale play (Yu and Sepehrnoori, 2014a; King, 2015; Simpson et al., 2016; Wang et al., 2016; Zuo et al., 2016).

### **2.2.2 Natural fractures**

Natural fractures, most are filled by cement, exist in shale reservoirs that can influence the growth of hydraulic fractures as well as the hydrocarbon production from originally low porosity and low permeability shales (Gale et al., 2014). It has been reported that hydraulic fractures can propagate along natural fractures based on the core sample tests and numerical simulation results (Lee et al., 2015, 2016; Wu and Olson, 2016). A field study has also shown that hydrocarbon production comes more from the stages with more natural fractures instead of ones with more microseismic detected events, as shown in Figure 2.6 (Moos et al., 2011). Secondly, it has also been reported from a digital rock physics workflow that hydrocarbon can flow along nanoscale grain boundary channels within the cemented natural fractures, resulting in an increase of rock permeability by more than one order of magnitude (Landry et al., 2016). If these two factors play parts in, the fracture network for hydrocarbon to flow is prone to propagate within the inorganic matrix which contains natural fractures.



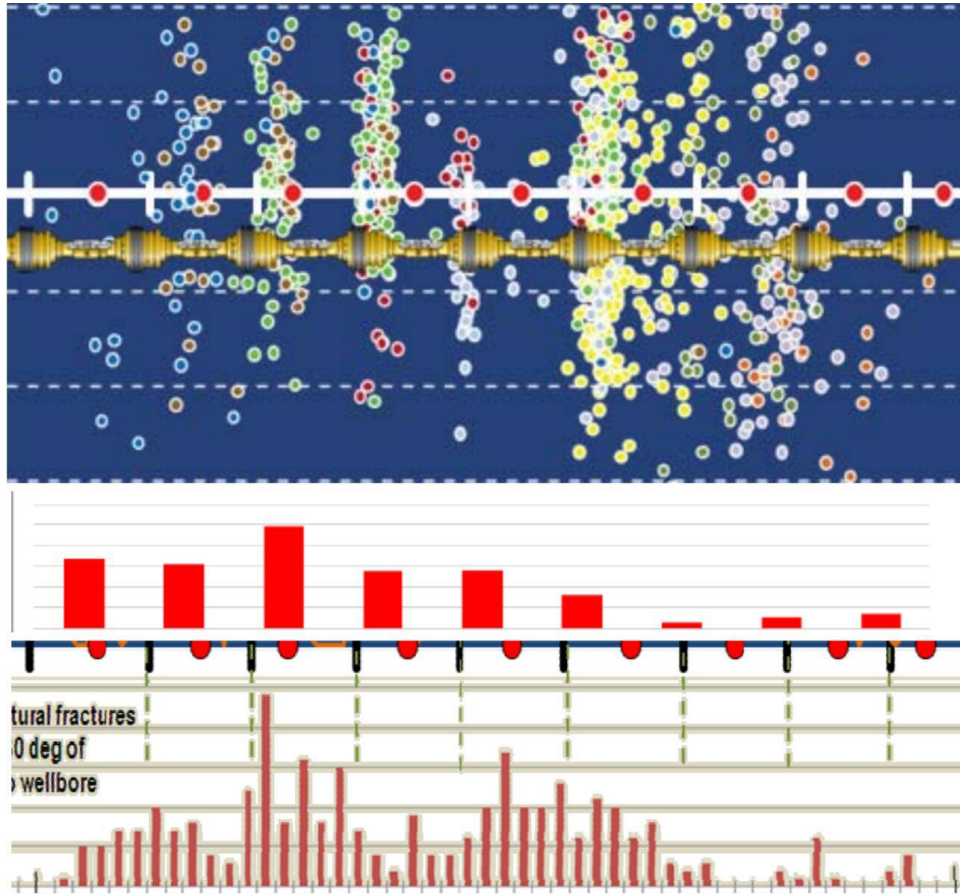


Figure 2.6: Comparison between relative contribution of hydrocarbon production (center), natural fracture frequency (bottom) and microseismic detected events (top) per stage of a well in an Upper Devonian shale gas reservoir. (Moos et al., 2011)

### 2.2.3 Fracture network and area contributes to total hydrocarbon production

Besides propagating along the natural fractures as introduced above, fracture network is likely to form within the inorganic matrix because of (1) the preferential Young's Modulus or brittleness ( $E/v$ ) (Paktinat et al., 2005; Ferrill et al., 2014; Far et al.,

2015) and (2) the minority of the organic matter (less than 20wt% for typical shales in the U.S. (DOE, 2009)).

Fracture network either directly connects the scattered organic matter or preexisting flow paths (e.g. natural fractures, continuous high-permeability layers (Curtis et al., 2010, 2012a) or big pores within the organic matter (Loucks et al., 2009; Milner et al., 2010; Milliken et al., 2013)), or creates extensive area that allows hydrocarbon stored in the adjacent inorganic or organic pores to flow to the production well. Due to the extremely low permeability of the rock, the flow of hydrocarbon therein can be considered as a linear flow perpendicular to the nearby open fractures (Patzek et al., 2013, 2014). Moreover, an interference time has been defined to characterize the time required for hydrocarbon production to spread over the space between two open fractures (i.e., one hydrocarbon molecule at the center of two open fractures reaches either fracture); this interference time was found to be around 5 years for wells in Barnett shale (Patzek et al., 2013) and 3.7 years for wells in Marcellus shale (Male et al., 2016). Therefore, it is assumed in this study that (1) hydrocarbon mainly flows linearly within rock matrix towards the nearby open fractures; (2) hydrocarbon from rock matrix adjacent to open fractures contributes to the major production in the prime of a well's life.

## **2.3 MECHANISMS GOVERNING WATER BLOCK AND PERMEABILITY REGAINING FROM VARIOUS ENHANCING METHODS**

### **2.3.1 Mechanisms governing water block**

As introduced in the previous section, pumped water creates the fracture network that allows the hydrocarbon stored in the adjacent matrix to flow into the production well. Therefore, from the viewpoint of multiphase flow, any trapped water within the matrix

would block the flow of hydrocarbon from the deeper reservoir rock and thus damage the overall well productivity. Water can be bypassed or trapped in the water-wet or oil-wet porous media depending on the competition between the viscous force and the capillary force (when gravity is negligible); and the residual water saturation in turn reduces the relative permeability to other phases (Lake et al., 2014).

For water-wet conditions, it has been reported that the mitigation of water block can be slowed down when the pressure drawdown is not significantly greater than the capillary pressure/capillary entry pressure, and thus the recovery of rock permeability to hydrocarbons (Abrams and Vinegar, 1985; Holditch, 1979; Mahadevan and Sharma, 2005; Parekh and Sharma, 2004). Under such a range of  $\Delta P$  to  $P_c$  ratios, the abrupt change of capillarity from the rock matrix to the fracture can cause extra water trapping therein and thus reduce the rock permeability to hydrocarbons. This is analogous to the capillary end effect described by the Rapoport-Leas number ( $N_{RL} = \mu u L / \sigma$ ) for the core-scale experiments (Rapoport and Leas, 1953); and an analytical study has shown that the steady state hydrocarbon permeability can be significantly reduced when the Rapoport-Leas number is not high enough (Huang and Honarpour, 1998a). A high value of Rapoport-Leas number is a criterion for conducting a good special core analysis that meets the typical conditions for the conventional reservoirs; however, unconventional tight reservoirs seem to be operated at conditions with low Rapoport-Leas numbers where such capillary discontinuity at the fracture face cannot be ignored. Since hydraulic fractures are very likely to propagate within the inorganic matrix (Section 2.2.3), which is typically water-wet, water block in such region of the formation can play a crucial role in hydrocarbon production. It is the primary focus of this study and the detailed mechanisms regarding the form, severity, time span and clean-up of water block under different reservoir/production conditions are elaborated in Chapters 3 and 4.

As introduced in Section 2.2.3, water can invade into big oil-wet pores during hydraulic fracturing. The detailed mechanism governing the water block in such part of the formation is elaborated in Chapter 8 and further compared with the mechanism under the water-wet state in the same porous media.

### **2.3.2 Permeability regaining from various enhancing methods**

As introduced in Chapter 1, various enhancing methods have already been proposed or applied in the field to solve water block so as to enhance the hydrocarbon production after hydraulic fracturing. Three major methods are (1) drawdown management, (2) shut-in/soaking treatment and (3) surfactant or volatile additive treatment.

#### ***2.3.2.1 Drawdown management***

Since water block arises from the phase trapping due to the insufficient viscous force over the capillary force, it has been proposed that increasing the pressure drawdown can mitigate this problem and enhance the production (Abrams and Vinegar, 1985; Holditch, 1979; Parekh and Sharma, 2004; Sharma and Agrawal, 2013). However, increasing the drawdown at the same time can cause the abrupt change in formation stress, resulting in the closure of propped fractures and thus a detrimental effect on hydrocarbon production (Okouma et al., 2011; Economides et al., 2012; Deen et al., 2015; Wilson, 2015). Therefore, other methods are indispensable when drawdown management is unable to achieve.

#### ***2.3.2.2 Shut-in/soaking treatment***

Although hydraulically fractured reservoirs are normally characterized by permeabilities of the order of microDarcies down to nanoDarcies (Section 2.1), several

studies have shown that the imbibition of water-based fluids can be significant even in shales (Pagels et al., 2013; Bostrom et al., 2014; Dutta et al., 2014; Lan et al., 2015).

High capillarity can generate the redistribution of the trapped water that cleans up water block within the rock matrix. This has been reported as the mechanism that regains the rock permeability after the shut-in/soaking treatment based on laboratory measurements or numerical simulations (Almulhim et al., 2014; Bertoncello et al., 2014; Cheng, 2012; Dutta et al., 2014; Le et al., 2012; Mahadevan et al., 2007; Odumabo et al., 2014; Taylor et al., 2010; Yan et al., 2015). In the field, enhancements of gas production after shut-in/soaking treatments have been reported in Marcellus (Yaich et al., 2015). On the contrary, two statistical studies on 80 Marcellus wells and 363 wells from six shale plays have shown that shut-in/soaking treatments were “generally harmful” to the production (Crafton and Noe, 2013; Noe and Crafton, 2013).

In any cases, shut-in/soaking treatment delays hydrocarbon production and meanwhile extends the contact time between the trapped fracturing fluid and the formation. The second issue may cause other types of formation damage: clay swelling (Madsen and Müller-Vonmoos, 1989; Caenn et al., 2011; Gupta et al., 2013), matrix softening and proppant embedment (Alramahi and Sundberg, 2012; Das et al., 2014), or fine migrant/clay dispersion (Bazin et al., 2009). Therefore, an in-depth study is required to understand the impact of shut-in/soaking treatment so that opposite observations from the field can be explained by one physical model. Besides, it is also beneficial to understand if shut-in/soaking treatment is necessary for low permeability reservoirs with such high capillary force; if the answer is yes, whether an optimal shut-in/soaking time does exist for a given reservoir/production condition.

### ***2.3.2.3 Surfactant or volatile additive treatment***

To chemically mitigate water block in shale or tight gas reservoirs, fracturing fluid additives are normally chosen based on three purposes. The first purpose is to make the water phase more volatile thus the invaded water can evaporate faster and carried out by the gas phase (Kamath and Laroche, 2003; Al-Anazi et al., 2005; Mahadevan and Sharma, 2005; Mahadevan et al., 2007). However, core samples recover their original permeability only after more than 10000 pore volumes (PV) of gas flow (Mahadevan and Sharma, 2005); this approach seems ineffective for shales since the distance between fractures can be as small as a few feet (I. Palmer et al., 2014). The second purpose is to reduce the surface tension between the fracturing fluid and gas thus the invaded water can be mobilized during the production (Howard et al., 2010; Zelenev et al., 2010; Penny et al., 2012; Noe and Crafton, 2013; Rostami and Nasr-El-Din, 2014). However, in this approach, pre-formed microemulsion system is typically used and thus its interaction with gas within the reservoir condition remains unclear, resulting in a difficulty to assess the benefits only from surface tension reduction. The third purpose is to alter the rock wettability from water-wet to intermediate-wet (Parekh and Sharma, 2004; Ahmadi et al., 2011; Sun et al., 2015). However, due to the complexity of mineralogical composition of shale, this approach is probably difficult to implement for shale reservoirs. Nevertheless, mitigating water block in gas reservoirs is not the main focus of this study; it is only briefly discussed in some of the chapters.

Oil recovery rate from shale or other tight formations is typically much lower than the gas rate (3-6% for shale oil vs. 15-25% for shale gas according to EIA (EIA, 2013)), even though the fracture spacing for oil cases is only half of that for gas cases (Morrill and Miskimins, 2012; Jin et al., 2013). Therefore, to understand and evaluate the potential impact of water block for oil cases is imperative, as well as its cleanup from using

surfactant additives. Surfactants are normally suggested to be used through either wettability alteration (for oil-wet pores) or interfacial tension (IFT) reduction. For wettability alteration, enhancements on oil production from various shale samples have been reported from the lab after altering the rock wettability to water-wet that generates the spontaneous imbibition (Wang et al., 2012; Alvarez and Schechter, 2015; Morsy and Sheng, 2015; Kim et al., 2016; Neog and Schechter, 2016). However, they were all conducted by the imbibition cells without any flow experiments showing the change of rock permeability to oil; secondly, wettability alteration was always accompanied with IFT reduction, hence their own enhancement mechanisms cannot be explored separately.

On the other hand, for IFT reduction, several types of surfactants have been discovered that could enhance the oil production, either in the lab or in the field. Firstly, weakly emulsifying surfactants have been shown to enhance the oil flow through tight pore throats in the lab using a microfluidic model (He et al., 2015) and enhancements on oil production have been reported from several wells in Eagle Ford and Mississippi Lime Shales after using such surfactants (Xu and Fu, 2012; He and Xu, 2015). Secondly, surfactants providing low to ultralow IFT have been shown to mobilize the oil droplets originally attached on rock surface in the lab, and they were suggested to be used in the field through “huff-n-puff” treatment (Bui et al., 2016; Shuler et al., 2016); however, no results from flow experiments have been provided to show the change of rock permeability due to the potentially formed emulsions/microemulsions. In this study, the mechanisms governing the enhancements from different surfactant approaches are thoroughly explored and compared, from which a screening criteria can be developed for various reservoir/production conditions.

## Chapter 3: Water Block within Fracturing Fluid Invaded Zone for Water-Wet Systems<sup>1</sup>

This chapter focuses on water block only within the water invaded zone for water-wet systems. An experimental platform is designed in the lab so that the impact of matrix-fracture interaction on permeability reduction can be evaluated. A new blocking mechanism is thus proposed that may give rise to the major permeability reduction in the low permeability water-wet rocks after hydraulic fracturing.

### 3.1 QUICK OVERVIEW OF THIS CHAPTER

Hydraulic fracturing is used to obtain the economical rates from tight and unconventional formations by increasing the surface area of the reservoir within flowing distance to a high conductivity pathway. However, a significant fraction of the fracturing fluid is never recovered and thus may reduce the hydrocarbon permeability near the fracture. Here, we experimentally mimic the water invasion process during fracturing, and measure the permeability reduction in a low permeability core. Measurements of water flowback and permeability as a function of interfacial tension, flow rate, and shut-in time suggest that water is being held at the fracture face due to the capillary discontinuity, i.e., when the water leaves the matrix and enters a space with minimal capillary pressure. This effect arises from the capillary interaction between the matrix and the fracture and is akin to the capillary end effect in coreflood experiments. The results show that this effect, while

---

<sup>1</sup> This chapter is based on the following two papers:

Longoria, R.A., **Liang, T.**, Huynh, U.T., Nguyen, Q.P., DiCarlo, D.A. Water Blocks in Tight Formations: The Role of Matrix-Fracture Interaction on Permeability Damage and Its Implications on the Use of EOR-Like Techniques. Submitted.

**Liang, T.**, Longoria, R.A., Lu, J., Huynh, U.T., Nguyen, Q.P., DiCarlo, D.A., 2015. The Applicability of Surfactants on Enhancing the Productivity in Tight Formations. SPE-178584-MS. doi:10.2118/178584-MS



only a laboratory experimental artifact for conventional reservoirs, can be a significant source of hydrocarbon permeability reduction by fracturing fluid invasion into the rock matrix in unconventional tight reservoirs.

### **3.2 INTRODUCTION**

Hydraulic fracturing where large volumes of water-based fluids are pumped into a low or ultralow permeability formation has emerged as the leading production stimulation approach in recent years. Although some of the fracturing fluid is recovered as flowback once the well is put into production, a significant fraction of the original volume used is lost to the formation and could hinder hydrocarbon production. Several mechanisms by which water trapping inside the formation takes place have been discussed in the past (Bennion et al., 1996). Furthermore, water invasion has been identified as a cause for permeability reduction in tight gas sandstones (Tannich, 1975; Abrams and Vinegar, 1985; Bennion et al., 2000). This permeability reduction due to fracturing fluid loss is known as “water block”.

The clean-up of water block has gathered significant attention in recent years (Kamath and Laroche, 2003; Mahadevan and Sharma, 2005; Bazin et al., 2010; Mirzaei-Paiaman et al., 2010; Le et al., 2012; Bertoncello et al., 2014) . In gas-bearing formations, the clean-up process can take place in two ways: viscous displacement and evaporative displacement. The former refers to the initial regime where the gas, as it is produced, pushes out some of the trapped water and it is recovered as flowback. After the initial flowback period has ended, gas will continue to flow and can aid the evaporation of the trapped water. Several laboratory and computational studies have shown that the addition of

volatile fluids, such as methanol, speeds up the evaporative process. Nevertheless, even when volatile fluids were used, samples regain full gas permeability only after more than 10,000 pore volumes (PV) of gas flowed through the core (Mahadevan and Sharma, 2005). Extremely large pore volumes of gas flowing through the shale are unlikely to be the general case for shale gas production where the effective distance between fractures can be as small as a few feet (I. D. Palmer et al., 2014). It is important to note that recovery of full gas permeability can only be achieved by reducing the water saturation to its initial value.

Abrams and Vinegar (Abrams and Vinegar, 1985) showed that permeability reduction from water block exists when the magnitude of the viscous force during production does not exceed a certain value. In principle, increasing the pressure drawdown would accomplish this goal; however, the lower the permeability of the rock, the higher the required pressure drawdown. Because the maximum pressure drawdown is often limited by well operational constraints, it might not be enough to overcome the large capillary forces characteristic of unconventional reservoirs.

Since such water block arise from capillary effects, reducing the surface/interfacial tension between the fracturing fluid and the hydrocarbon in place could be a solution to water block (Bennion et al., 1996). In conventional rocks, surfactant-based EOR is used to recover oil below its residual saturation. This oil is trapped by capillary forces and viscous forces alone are not sufficient to mobilize it. Similarly, the fracturing fluid causing a permeability block in unconventional rocks is trapped by capillary forces, and thus, one could imagine that reducing the interfacial tension can also lead to fracturing fluid recovery and the elimination, or mitigation, of water block. Although several recent studies showing

the enhancement of production by using specially formulated microemulsion additives have been reported (Zelenev and Ellena, 2009; Howard et al., 2010; Penny et al., 2012a; Rostami and Nasr-El-Din, 2014), none of them have focused on the actual mechanism responsible for the initial permeability reduction nor for the permeability improvement obtained after addition of surface/interfacial tension reducing agents, making it difficult to assess the benefits of using a surfactant formulation.

Understanding the physics of either removing or reducing the impact of water block requires performing, and correctly scaling, water block experiments. The scaling is required as economic flow rates in shales are only achieved by creating very large areas through hydraulic fracturing; the fluxes through the matrix are extremely low. To this end, there are two relevant scaling groups, or equivalently, dimensionless numbers. First, the capillary number,  $N_c = u\mu/\sigma$ , is the ratio of the viscous forces to the capillary forces at the pore scale (Hoffman, 1975; Lake et al., 2014). Here  $u$  is the fluid flux,  $\mu$  is the viscosity of the flowing fluid, and  $\sigma$  is the interfacial tension. For conventional reservoirs (assuming  $u \sim 0.01\text{-}1\text{ft/d}$ ,  $\mu \sim 1\text{-}10\text{cP}$ ,  $\sigma \sim 20\text{-}50\text{mN/m}$ ), the typical operating capillary number without surfactants is on the order of  $10^{-6}\text{-}10^{-9}$ ; at these values the capillary force dominates at the pore scale. If the capillary number is increased above the critical value of roughly  $10^{-4}$  and above, the viscous forces are then large enough to mobilize trapped phases (Lake et al., 2014). This process is known as capillary desaturation and is at the heart of conventional surfactant-based enhanced oil recovery where the capillary forces are reduced through ultralow interfacial tensions. Extending this to tight reservoirs, the operating capillary number is much lower due to the low/ultralow permeability and flow rates of tight

reservoirs (e.g.  $N_c \sim 10^{-12}$ - $10^{-10}$ ). Since even ultralow IFT surfactants only reduce the IFT by 4-5 orders of magnitude, any surfactant study for tight reservoirs needs to remain in the capillary dominated regime, i.e.  $N_c < 10^{-5}$ , and thus it is not clear how surfactants improve hydrocarbon permeability in such reservoirs even if surfactants that result in ultralow IFT were used. Nevertheless, as mentioned above, improvements have been reported even when the IFT was reduced by only a factor of 3 to 5 (Zelenev and Ellena, 2009; Penny et al., 2012a; Rostami and Nasr-El-Din, 2014). Therefore, developing an understanding of the mechanism by which surfactants work is imperative in order to design and optimize the use of surfactants in hydraulically fractured reservoirs.

The other scaling number relevant for hydraulically fractured reservoirs is the Rapoport-Leas number ( $N_{RL}$ ) (Rapoport and Leas, 1953),  $N_{RL} = \mu u L / \sigma$ , which is a ratio of the viscous and capillary forces at the *core* scale ( $L$  is the length of the core). While several mathematical definitions for the Rapoport-Leas number have been proposed (Lake et al., 2014) the simplest Rapoport-Leas number is proportional to the ratio between the pressure drop across the total length of flow through the porous media and the capillary pressure,  $\Delta P / P_c$  (Lake et al., 2014). This number is critical for good special core analysis; in conventional reservoir cores, care is taken to ensure that the Rapoport-Leas number is sufficiently high. This guarantees that viscous forces dominate at the core scale and capillary discontinuities at the core faces do not affect the coreflood measurements. Meeting this condition is appropriate for conventional reservoir core samples as the typical pressure drops applied in the field are several orders of magnitude larger than the capillary pressures characteristic of such rocks. Importantly, while the pressure drop between the

reservoir and the well during production in tight rocks are in the same order of magnitude as in conventional reservoirs, the capillary pressures characteristic of such low/ultralow permeability formations can be several orders of magnitude larger than for conventional reservoirs. Therefore, it is likely that tight reservoirs operate at low Rapoport-Leas number in the field. In this case, the capillary discontinuity between the reservoir and the fracture at the fracture face can play a significant role during production. A previous study on the impact of the capillary discontinuity during drainage shows that the final hydrocarbon permeability can be significantly reduced when the Rapoport-Leas number is not high enough (Huang and Honarpour, 1998b).

As mentioned above, for a particular saturation value, tight formations have much larger capillary pressures than conventional reservoirs. Thus, any water emplaced at the fracture face will result in a large capillary pressure gradient over the same zone. In the absence of hydrocarbon flow, the capillary forces will tend to redistribute the water back into the formation, effectively reducing the magnitude of water block, but when hydrocarbon is flowing towards the fracture face, there will be a large counterforce to push water back towards the face. Improvements in production following well shut-ins have been suggested (Le et al., 2012; Bertoncello et al., 2014), and studies show the improvement can be the result of mitigating water block due to fluid redistribution (Le et al., 2012; Bertoncello et al., 2014; Bostrom et al., 2014). Nevertheless, a direct comparison between the improvements obtained with shut-ins and those obtained with surfactants has not been specifically investigated and remains unknown.

To summarize, although the existence of water block has been documented in the past, a comprehensive study on the impact of water block, its controlling parameters and its minimization via surface/interfacial tension reducers is not available. In this work, we present an experimental study on the role of water block in hydrocarbon production from hydraulically fractured reservoirs and the effect of supplementing the fracturing fluids with interfacial tension reducing agents to minimize or eliminate water block. While the experiments are performed in a low permeability conventional rock ( $k_{abs} \sim 5\text{-}10\text{ mD}$ ), care was taken to ensure that the flooding conditions, mainly the capillary and the Rapoport-Leas number, are maintained in the regimes that are representative of tight and unconventional reservoirs. Our results show that significant permeability reduction occurs from the matrix-fracture interaction at the fracture face arising from the capillary discontinuity, and that improvements obtained with the use of interfacial tension reducing agents in tight and unconventional reservoirs are the result of an increase in the Rapoport-Leas number beyond the critical value.

### **3.3 MATERIALS AND METHODS**

#### **3.3.1 Field geometry and laboratory scaling**

This work focuses on the reservoir matrix region near the fracture face in a hydraulically fractured reservoir. Figure 3.1 shows a schematic of the field geometry and the volume of interest for this work. This geometry is captured in our laboratory experiments by a rock core in which one of the core faces represents the fracture face.

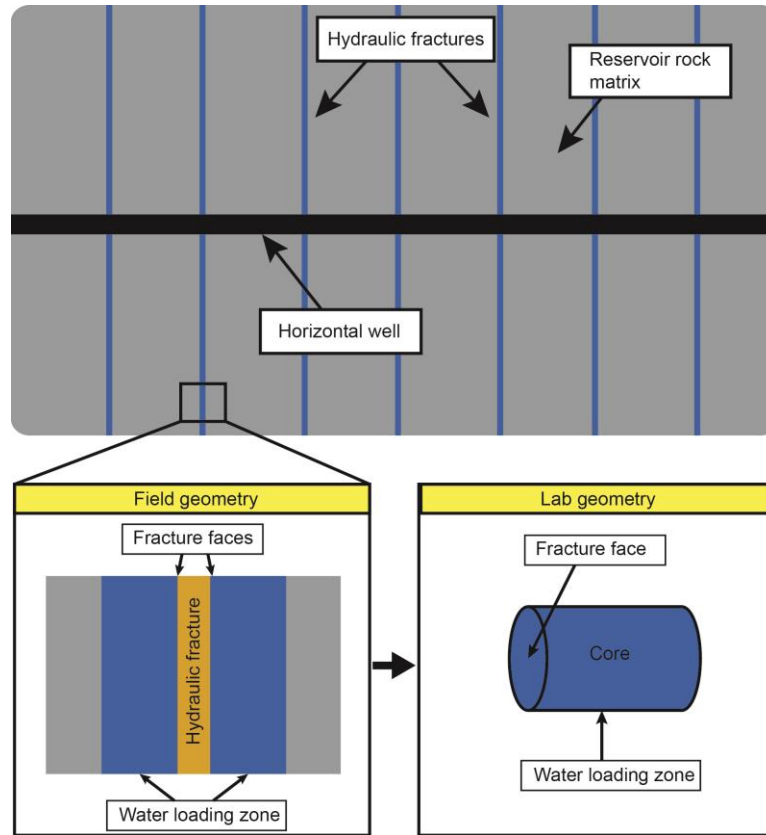


Figure 3.1: Schematic of field geometry and laboratory scaling. Fracturing fluid leaks off to the formation through the fracture face during hydraulic fracturing operations. This generates a water loading zone which can reduce the matrix permeability to the formation. This geometry is obtained in the lab by considering one of the faces of a core sample as the fracture face through which water penetrates the matrix and hydrocarbon flows out of it.

### 3.3.2 Core rock type and dimensions

We used outcrop Texas Cream Limestone as our rock sample. Cylindrical rock samples with dimensions of 1.5” in diameter and 9.5” in length were cored from an outcrop block. The absolute permeability for this rock type is listed between 5 and 10mD and has a porosity of ~21-25%. The sample here used is water-wet and the same core was used in

each one of the experiments. Before each experiment, the core was placed inside an oven at 105°C for at least 6 hours to evaporate the pentane, brine and/or methanol. The core was not reused after the surfactant injection. The porosity was calculated by subtracting the wet (water saturated) and dry weights of a 1” by 1” cylindrical core plug. The pore volume of the coreflood sample was then calculated from the dimensions of the large core by assuming the same porosity as the core plug.

### **3.3.3 Choice of hydrocarbon**

A low carbon number alkane was chosen as the hydrocarbon phase during coreflood experiments in order to represent a light hydrocarbon, as is likely the type of hydrocarbons produced from low permeability unconventional reservoirs. In all of the measurements here presented, n-pentane was used as the model hydrocarbon. It is important to note that n-pentane does not have the ability to change the wettability of the rock, and thus, throughout the experimental procedure the rock remains water-wet.

### **3.3.4 Fracturing fluids and interfacial tension reducers**

Experiments using brine or DI water as the fracturing fluid showed no permeability damage from the use of DI water. For simplicity, all the baseline experiments were performed with DI water as the fracturing fluid. Methanol and surfactant (a mixture of dioctyl sodium sulfosuccinate (AOT, (McFann and Johnston, 1993)) and dihexyl sodium sulfosuccinate) were used as interfacial tension reducers in this study. First, the surrogate fracturing fluid consisted of 20wt% methanol in DI water. The addition of methanol to water lowers the interfacial tension between this mixture and n-pentane (see Table 3.1). The viscosity of the mixture is 1.44 cP measured from a proRheo LS300 viscometer (Figure



3.2). In addition, a second surrogate fracturing fluid consisting of 1wt% of AOT in 3wt% NaCl brine was used (Liang et al., 2015b).

Fracturing fluid	IFT (mN/m)
Brine/DI water	50
with 20wt% MeOH	23
with 1wt% surfactant	0.048

Table 3.1: Interfacial tensions between pentane and different proxy fracturing fluids used.



Figure 3.2: proRheo LS300 viscometer.

### 3.3.5 Interfacial tension measurements

The pendant drop method was used to determine the interfacial tension between pentane and water for the baseline case (no additives) as well as for the methanol supplemented water. The interfacial tension between pentane and the surfactant formulation was estimated using the Chun Huh equation with constant  $C=0.3$  (Huh, 1979). The interfacial tensions measured are listed in Table 3.1.

### 3.3.6. Coreflood sequence and setup

A three-step coreflood sequence that simulates fracturing fluid invasion, flowback and hydrocarbon production from fractured reservoirs was developed. A schematic of the coreflood setup is shown in Figure 3.3. To accurately assess the impact of water block on permeability, both the pressure across the core and effluent fluid from the core (i.e., fluid recovered during flowback) were monitored as a function of time. The three-step sequence is as follows:

***Step-1 – Establish a hydrocarbon saturated reservoir.*** A dry and evacuated core is placed in a Hassler-type core holder. The confining pressure is set to 1500 psi and the core is flooded with pentane until full saturation is reached. The final state of the core represents a hydrocarbon-saturated formation. Clearly, the initial state of a reservoir does not correspond to  $S_{w0} = 0$ . While the times scales and impact of water block depend on the initial water saturation (Longoria et al., 2015), the underlying physics controlling the dynamics of water block is independent of this value. Therefore, for simplicity an initial hydrocarbon saturation of 100% was chosen. The single phase permeability of the core is measured during this step.

***Step-2 - Hydraulic fracturing fluid invasion.*** Fracturing fluid is pumped through the hydrocarbon saturated core. We are not interested in mimicking the fracturing process; instead we only measure the water saturation change and the final water permeability during fracturing fluid invasion. The water saturation in the core as a function of time is calculated from the effluent mass and the known injection flow rate. Unless otherwise noted, a flow rate of 0.075cc/min was used to inject 1PV of fracturing fluid during this step in all experiments.

***Step-3 - Fracturing fluid flowback and hydrocarbon production.*** Pentane is flooded through the core again at a specified rate. Some of the fracturing fluid emplaced during Step-2 is displaced by the hydrocarbon. The mass of the recovered fracturing fluid is measured as a function of time in addition to the pressure drop across the core. Since at the end of this step only pentane is flowing out of the core sample, the final permeability to pentane at the final water saturation  $S_{wf}$  can be calculated via Darcy's law using the known viscosity of pentane, and the core physical dimensions.. For shut-in experiments, the pentane pump was turned off at the end of Step-3 for a period of one hour after which the pump was turned on again. The pressure drop after the shut-in was used to calculate the new final permeability to pentane.

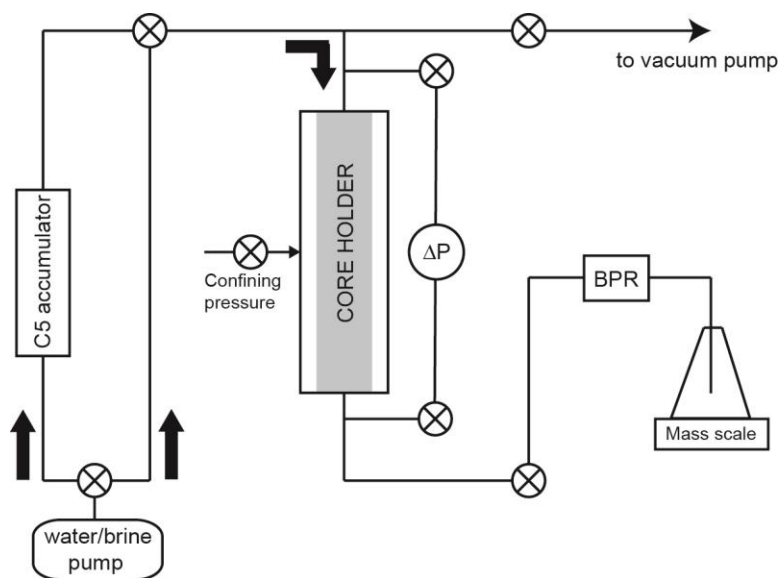


Figure 3.3: Schematic of experimental setup. A three-step coreflood sequence is used to simulate a hydrocarbon rich formation, fracturing fluid invasion and flowback, and hydrocarbon production. The pressure drop across the core and the effluent mass are recorded as a function of time.

### 3.4 RESULTS

The impact of water block on hydrocarbon production from low/ultralow permeability reservoirs was studied via a three-step coreflood sequence that simulates a hydrocarbon-saturated formation (Step-1), fracturing fluid invasion into the formation during the hydraulic fracturing process (Step-2), and fracturing fluid flowback and hydrocarbon production (Step-3). For more details refer to Materials and Methods (Section 3.3).

Figure 3.4 shows an example of flowback and pressure drop versus time for two different pentane flow rates during Step-3. Flowback increases with time and is larger with a higher flow rate. ( $2.1 \pm 0.2 \text{ ml}$  for  $Q_{\text{pentane}} = 0.05 \text{ ml/min}$  vs.  $3.2 \pm 0.2 \text{ ml}$  for

$Q_{\text{pentane}}=0.1\text{ml/min}$ ). The pressure drop shows a peak at early times due to multi-phase flow before plateauing to a final (steady-state) value. The final permeability to pentane (calculated using Darcy's law) depends on flow rate; it increases from 0.49mD (for  $Q_{\text{pentane}}=0.05\text{ml/min}$ ) to 0.68mD (for  $Q_{\text{pentane}}=0.1\text{ml/min}$ ). To investigate the dependence of the final permeability to pentane, this measurement was repeated for several flow rates.

Figure 3.5A shows the final relative permeability to pentane and the amount brine recovered as flowback for different pentane injection flow rates. For low flow rates, the final hydrocarbon permeability increases with flow rates, however, it reaches a plateau for larger values of flow rates. Increasing the injection flow rate amounts to larger viscous forces but does not affect capillary forces. The capillary number at the lowest flow rate is  $10^{-8}$ , while that for the highest flow rate is  $10^{-7}$ . Since these values are well below typical capillary desaturation values (at lowest  $10^{-5}$ ) it is unlikely that the observed improvements are due to the *pore* scale competition between viscous and capillary forces.

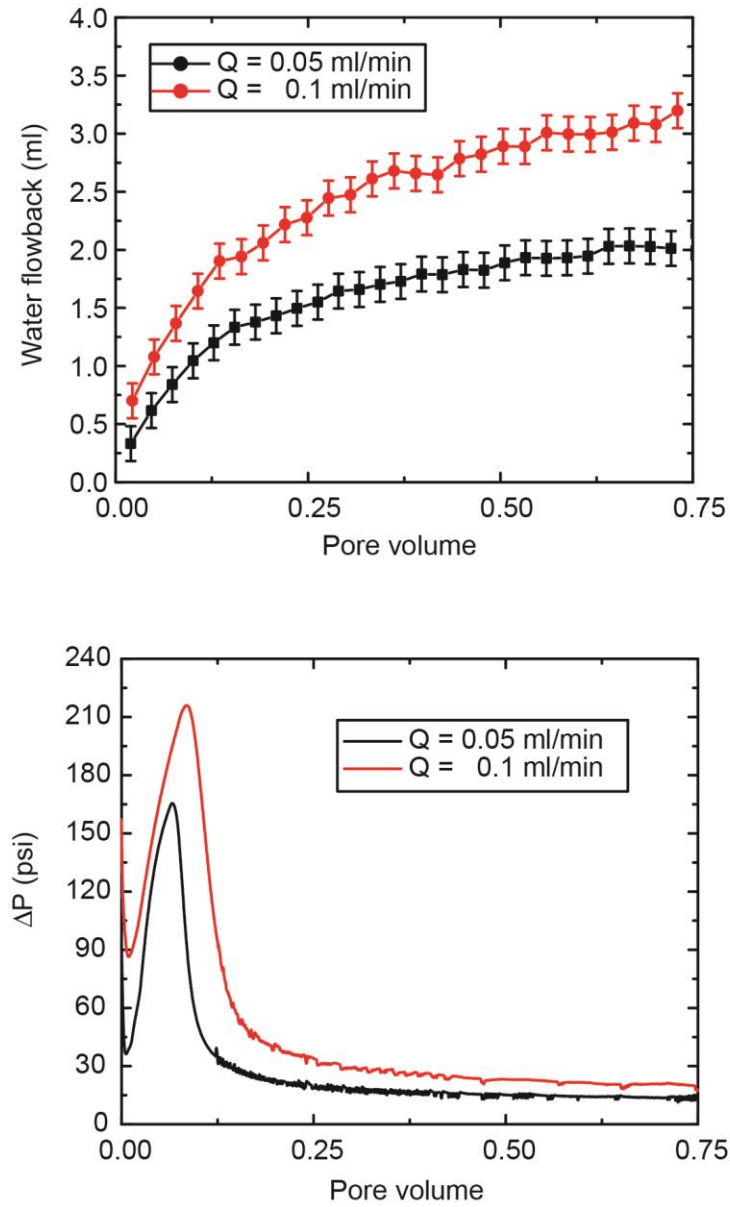


Figure 3.4: The amount of fracturing fluid recovered as flowback depends on the injection flow rate. At the end of Step-3 of the coreflood sequence only hydrocarbon flows out of the core. The pressure drop at the end of this flooding step is used to calculate the final relative permeability to pentane.

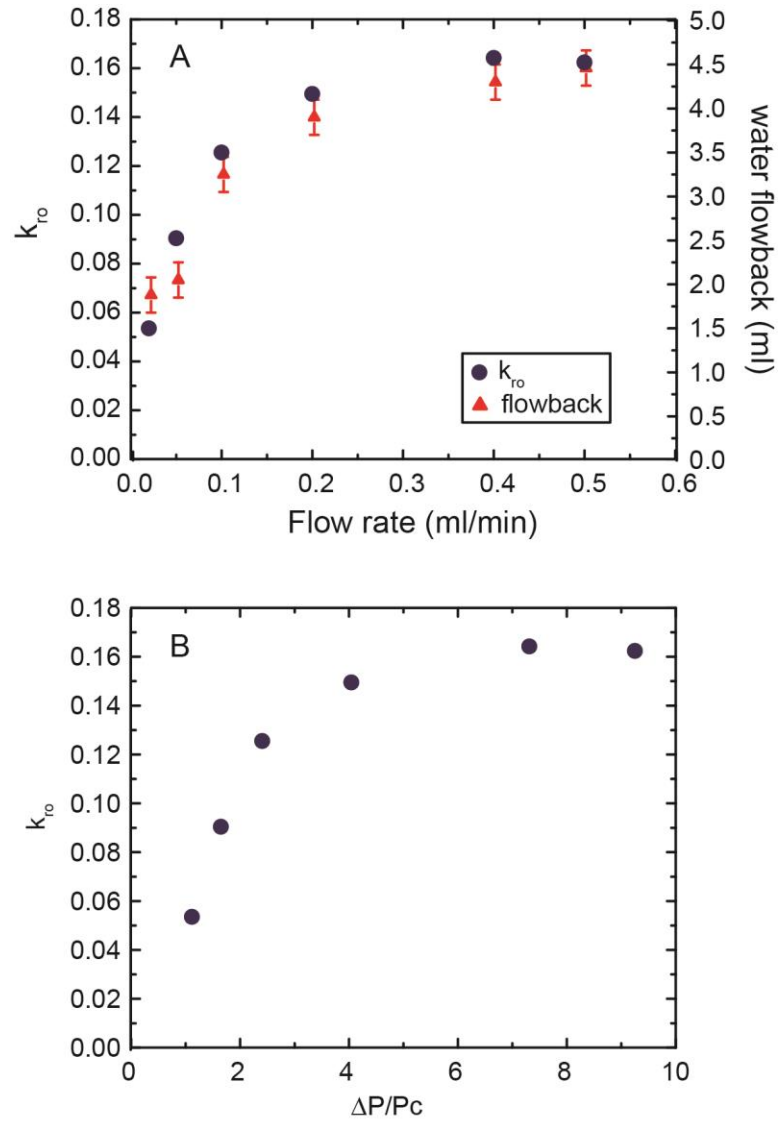


Figure 3.5: The final relative permeability to hydrocarbon increases as viscous forces, relative to capillary forces, increase. A) Final relative permeability to pentane increases for low hydrocarbon injection flow rates during the fluid flowback and hydrocarbon production steps of our experiment but reaches a plateau for higher injection rates. Similarly, water recovered during flowback increases with increasing hydrocarbon flow rate until it reaches a plateau. B) A more physically meaningful scaling for the x-axis is the ratio of viscous to capillary forces.  $\Delta P$  is the pressure drop across the core at the end of the flowback phase and  $P_c$  is a characteristic capillary pressure obtained from the  $P_c$  vs.  $S_w$  curve for our rock sample.

### 3.4.1 Capillary vs. viscous forces at core scale

As mentioned in the Introduction, the Rapoport-Leas number can be a relevant dimensionless quantity in low or ultralow permeability reservoirs. Therefore, instead of using the fluid flow rate as the independent variable, a more appropriate and physically meaningful parameter would be  $\Delta P/P_c$ . This ratio is representative of the competition between viscous and capillary forces at the core scale. Here, we use the pressure drop across the core at the end of Step-3 as  $\Delta P$ , and  $P_c$  is a characteristic capillary pressure obtained from the  $P_c$  vs.  $S_w$  curve; this capillary pressure depends linearly on the interfacial tension. It is important to note that the characteristic capillary pressure can be chosen arbitrarily as long as the selection criterion remains consistent. For example, Abrams and Vinegar (Abrams and Vinegar, 1985) used the capillary entry pressure as the characteristic capillary pressure. Here, we chose the value at the middle point of possible water saturations (see Figure 3.9 in the Supplemental material for more details and  $P_c$ -curve) as the characteristic capillary pressure. Figure 3.5B shows the same relative permeability data from Figure 3.5A with the x-axis rescaled to the corresponding  $\Delta P/P_c$ .

### 3.4.2 Effect of reduction of capillary forces

As shown above, the overall hydrocarbon permeability increases in the capillary dominated region with increasing  $\Delta P/P_c$ . While in the lab, the value of this ratio can be controlled by the injection flow rate; in the field, the pressure drop across the formation is determined by the difference between the reservoir and the pressure drawdown, potentially limiting the maximum  $\Delta P$  that can be achieved. In such a case, another way to increase the overall permeability is by decreasing the capillary pressures of the system. To test this experimentally, we supplemented the fracturing fluid with 20% methanol. Pendant drop measurements showed the addition of 20% methanol results in the reduction of the



interfacial tension (IFT) between pentane and water from 50mN/m to 23mN/m. Figure 3.6A shows the final relative permeability to pentane as a function of pressure drop across the core for the case when DI water alone was used as the fracturing fluid as well as when DI water was supplemented with methanol. Clearly, the addition of methanol increased the hydrocarbon permeability in the capillary dominated region. On the other hand, for higher pressure drops across the core, although the pentane relative permeability also reaches a plateau when methanol was used, the maximum value is lower than that without methanol. This may be due to the fact that, in addition to reducing the IFT between pentane and water, methanol increases the viscosity of the methanol/water mixture (Section 3.3.4) resulting in a more unfavorable displacement pattern due to viscous fingering (Lake et al., 2014).

An overlap of the curves obtained for methanol/water and that of pure water can be seen by scaling the data in each case by the corresponding characteristic  $P_c$  of each case indicating that any enhancements observed by reducing the capillary pressure of the system are the result of moving to higher  $\Delta P/P_c$  values on the curve shown in Figure 3.6B.

Reducing the IFT by three orders of magnitude was achieved using a surfactant formulation (Table 3.1). Although the flow rate used during Step-3 for this experiment was 0.1ml/min, the permeability to the hydrocarbon increased to the maximum value with the addition of the surfactant (Figure 3.8). The permeability to the hydrocarbon at this flow rate was higher when the surfactant was used when compared to the case of only DI water or that with 20wt% methanol.

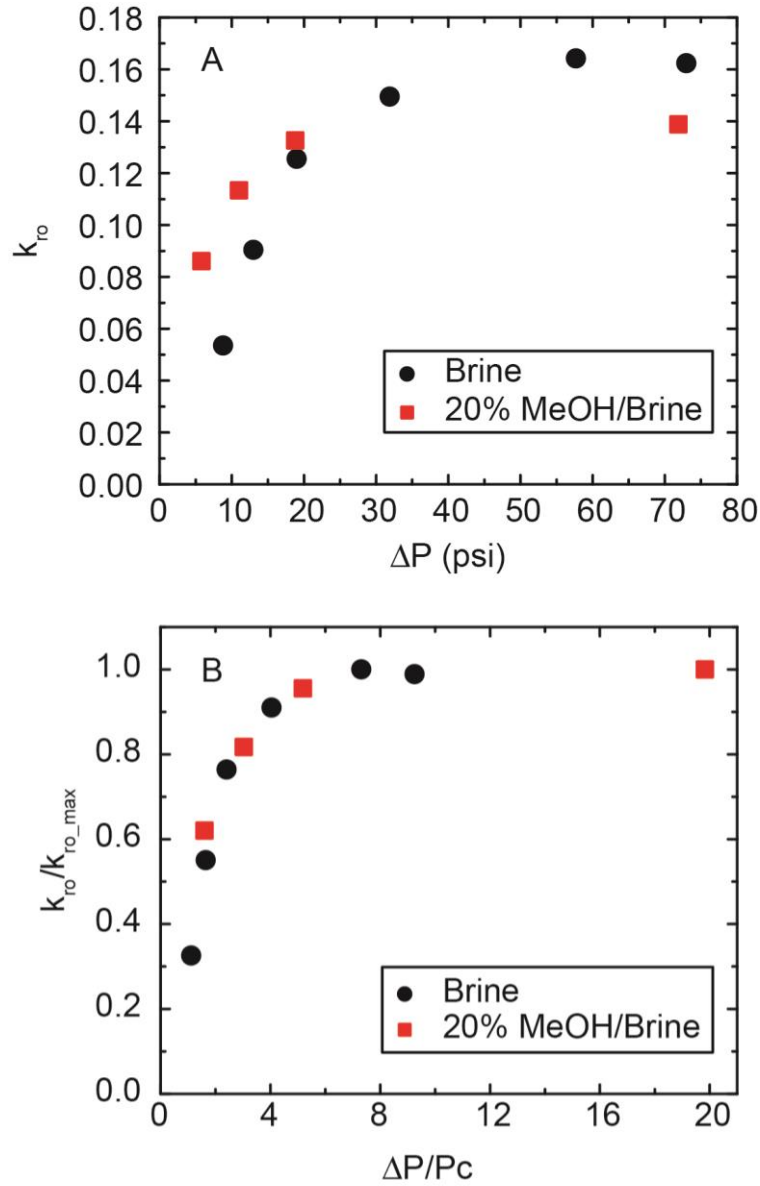


Figure 3.6: Reduction of IFT between fracturing fluid and hydrocarbon increases the hydrocarbon relative permeability in the capillary dominated region. A) Supplementing the fracturing fluid with methanol reduces the IFT between pentane and brine by a factor of about 2. This is sufficient to significantly enhance the final relative permeability to pentane during the production phase of our experiment. B) Rescaling the data by the corresponding  $P_c$  in each case results in the overlap of both curves indicating that a competition between viscous and capillary forces is the controlling parameter for the observed permeability reduction.

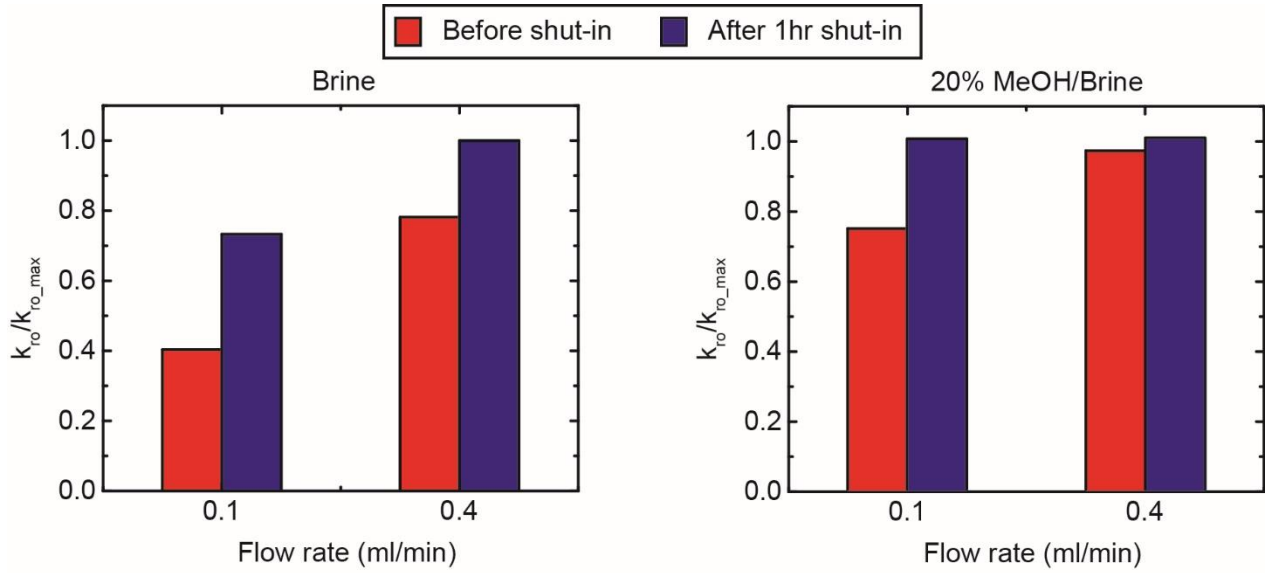


Figure 3.7: Shut-ins after the flowback phase ended result on capillarity dependent permeability increases. The largest enhancements of permeability take place when capillary forces dominate over viscous forces (e.g. at low flow rates such as 0.1 ml/min for our system) but decrease or completely disappear as capillarity plays a smaller role (high flow rates or lower IFT between brine and hydrocarbon). No additional fluid flowback was observed upon resuming flow after the shut-in suggesting that enhancements are due to a capillarity-driven redistribution of the fluid inside the core. The capillarity-mediated matrix fracture interaction leads to an increased brine saturation near the fracture face which in turn reduces the final relative permeability to the hydrocarbon. This interaction is reduced during the shut-in period resulting on the observed increase in permeability.

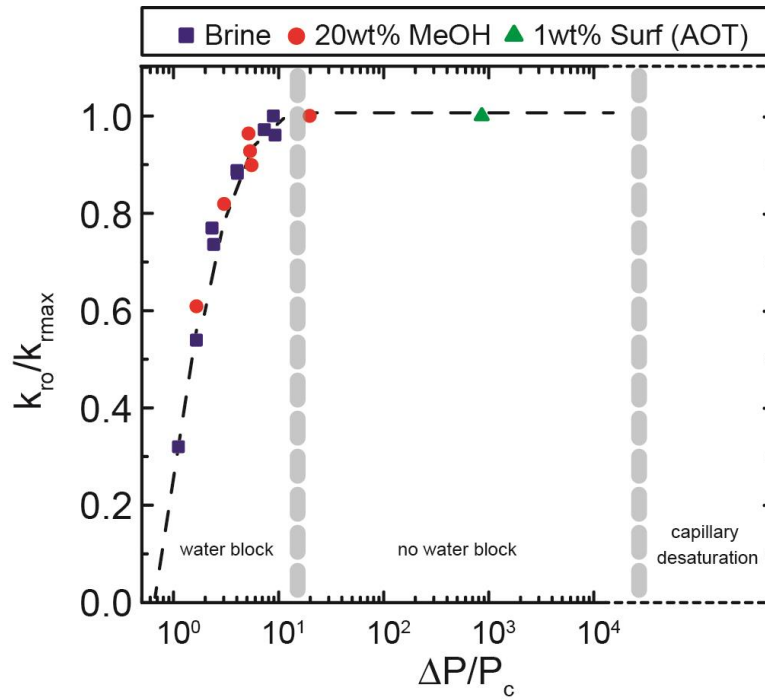


Figure 3.8: The capillary discontinuity between the matrix and the fracture at the fracture face is responsible for water block in unconventional reservoirs. Water block significantly affects production in formations where the pressure drawdown does not exceed a characteristic capillary pressure by at least 1 order of magnitude. Unconventional reservoirs fall in such a category. Interfacial tension reducers can help mitigate the impact of water block by reducing the capillary discontinuity between the matrix and the fracture rather than by capillary desaturation of the fracturing fluid lost to the formation.

### 3.4.3 Effect of shut-ins

A shut-in involves turning off the flow for a specified period of time. During a shut-in the fluid in the matrix responds only to capillary forces which allow redistribution within the rock. Since the overall pressure drop depends on both the overall water saturation and the particular saturation profile, this redistribution can potentially mitigate the permeability reduction.

We performed shut-in experiments by turning off the flow for one hour at the end of Step-3 before resuming the flow in order to investigate the nature and extent of these improvements. As shown in Figure 3.7, for low pentane flow rates (i.e., in the capillary dominated region of Figure 3.5), permeability enhancements were observed after a shut-in for both the case of DI water and methanol/water mixture as the fracturing fluids. The magnitude of the enhancement decreases as the flow rate increases and the maximum enhancement is limited to the plateau value shown in Figure 3.6A.

## 3.5 DISCUSSION

The experimental results from the three-step core flooding sequence can be summarized as follows:

1. Below a critical flow rate, the final permeability to the hydrocarbon decreases with decreasing flow rate.
2. Below the same critical flow rate, the amount of flow back of water decreases with decreasing flow rate.
3. By varying flow rates and IFTs, it is shown that the critical flow rate is a function of  $\Delta P/P_c$ .

4. When the flow rate is below the critical flow rate, shutting in the core improves the final hydrocarbon permeability to the value that is obtained for experiments above the critical flow rate.
5. There is no detectable fracturing fluid produced immediately after the shut-in.
6. Reducing IFT by three orders of magnitude does not improve the final hydrocarbon permeability, but it allows this permeability to be achieved at a lower flow rate.

We discuss the implication of these results as follows. It is unsurprising that the first two bullet points match up; in general, the less water in the porous medium, the higher the hydrocarbon permeability. But the critical flow rate shows that higher flow rates can only help remove water and increase permeability to a certain extent. More importantly, the third result shows that it is not really a flow rate effect, but a ratio of the pressure drop to the capillary pressure, or more specifically, to the interfacial tension. It is also unsurprising that the ratio of viscous pressure to capillary pressure plays a role as capillary pressure will tend to hold the water in a water-wet medium.

This suggests two different possibilities for the observed effects, capillary desaturation or a reduction in the capillary discontinuity at the matrix/fracture interface. Results 4 through 6 are integral in showing that it is the latter. First, if shut-ins alter the flow behavior, it implies that there are changes inside the medium during the shut-in, i.e., changes in the saturation distribution. This is to be expected due to the capillary discontinuity at the fracture face as the resulting distribution after the Step 3 (water

flowback) should have an increasing water saturation towards the fracture face (Huang and Honarpour, 1998b; Kianinejad et al., 2014). Once shut-in, this increasing water saturation profile towards the fracture face leads to a capillary pressure gradient that will act to dissipate the fracturing fluid emplaced in the matrix near the fracture face deeper into the rock. After this redistribution, the hydrocarbon permeability will be increased due to the concave nature of the hydrocarbon relative permeability curve. If the critical flow rate was caused by capillary desaturation, the profile would likely be uniform, and thus shut-ins would have no effect if no excess water was produced.

Likewise, this is the case for Result 6. Here, a three orders of magnitude reduction of capillary forces offers no improvement beyond the permeability value above the critical  $\Delta P/P_c$ . Capillary desaturation is known to continue with changes in the capillary number for several orders of magnitude (Lake et al., 2014).

Finally, the force ratio as shown in Figures 3.5 and 3.6 has the critical force ratio of  $\Delta P/P_c$  between 1 and 10. Simple scaling arguments show that this is where the Rapoport Leas number will transition (Rapoport and Leas, 1953; Huang and Honarpour, 1998b; Lake et al., 2014). As mentioned in the introduction, the capillary number is expected to be much lower than the critical value for capillary desaturation.

### **3.5.1 Implications for unconventional tight reservoirs**

While the experiments presented in this work are done with a conventional, low permeability core, the scaling of the permeability reduction shows that  $\Delta P/P_c$  is the relevant parameter when trying to study the effect of water block in any reservoir. This can thus be scaled to any rock in which multi-phase flow takes place. In order to illustrate the impact

of water block on the hydrocarbon permeability in both conventional and unconventional hydraulically fractured reservoirs, one can estimate the value of  $\Delta P/P_c$  by taking a typical pressure drop between the reservoir and the bottomhole pressure as a representative value for  $\Delta P$ , and using the Young-Laplace equation with a typical pore throat size to calculate a representative value for  $P_c$ . If the ratio of  $\Delta P/P_c$  does not exceed the critical value ( $\Delta P/P_c \sim 6$ , Figure 3.5B), then water block will exist. The magnitude of the permeability reduction due to water block is larger the smaller the ratio of  $\Delta P/P_c$ . For both conventional and unconventional reservoirs,  $\Delta P$  is in the order of  $10^3$  psi. On the other hand,  $P_c$  for a conventional rock is 1-10 psi (corresponding to pore throats around 1-10 $\mu$ m), while for unconventional rocks it will be around  $10^2$ - $10^4$  psi (corresponding to pore throats around 1-100nm). Thus, while for conventional reservoirs the value of  $\Delta P/P_c$  during production operations is  $\sim 10^2$ - $10^3$ , in unconventional or tight reservoirs  $\Delta P/P_c$  is  $\sim 0.1$ -10, implying that significant permeability reduction from water block can exist. This is summarized in Figure 3.8. As discussed above, to estimate if water block will exist in field operations, the pressure difference between the reservoir and the bottomhole pressure can be used as  $\Delta P$ , while the characteristic capillary pressure can be obtained via a special core analysis. If that is not available, value from a representative  $P_c$ -S curve can be used.

### **3.5.2 Implications for the use of surfactant-based EOR techniques in unconventional tight reservoirs**

As mentioned in the Introduction, production in unconventional reservoirs takes place at a very low capillary number, e.g.  $N_c < 10^{-10}$ . In these cases, even if ultralow interfacial tensions were achieved via surfactants, the increase in capillary number would likely not be sufficient to capillary desaturate the water phase. On the other hand, a reduction of the capillary pressures by 3-5 orders of magnitude can be sufficient to increase



the Rapoport-Leas number (here represented by  $\Delta P/P_c$ ) beyond the critical value and thus to increase the final permeability to the hydrocarbon to its maximum value. As shown in Figure 3.8, when a surfactant formulation which lowers the interfacial tension between pentane and brine by three orders of magnitude was used, the impact of water block is completely eliminated.

The permeability improvements observed in this work are the result of a decrease, or in the best case a complete clean-up, of the matrix-fracture interaction. It is important to note that while in conventional chemical EOR no improvements are obtained with modest reductions in IFT, any reduction in IFT will result in enhancements of the hydrocarbon permeability when the matrix-fracture interaction is the cause of the permeability reduction, as shown by the addition of methanol to our surrogate fracturing fluid (Figure 3.6). This provides a mechanistic explanation for the enhancements observed when surfactants that reduced the surface tension by only a factor of 3-5 were used (Zelenev and Ellena, 2009; G. S. Penny et al., 2012a; Rostami and Nasr-El-Din, 2014). On the other hand, since the use of surfactants in unconventional rocks does not completely eliminate capillary pressures, it is possible that some fluid redistribution through capillary suction still takes place. Indeed, differences in the dynamics have been observed when surfactant-supplemented fracturing fluids are used (Liang et al., 2016); however, the details of how the fracturing fluid redistributes by capillary suction are beyond the scope of this work. However, these can play a significant role in the ability of the surfactant to penetrate the rock matrix. Additional effects, such as molecular diffusion or osmotic driven flow (Bryndzia, 2012; Fakcharoenphol et al., 2014; Zhou et al., 2016) could also play a role.

Nevertheless, the framework presented in this work (e.g. estimating  $\Delta P/P_c$ ) provides a tool that can be used to determine if water block will impact the production of hydrocarbons, as well as to estimate the improvements expected from the use of a surfactant formulation given its reduction in IFT.

### **3.5.3 Role of reservoir rock wettability**

All the results presented here were obtained in a strongly water-wet rock. However, unconventional reservoirs, in particular shales, are known to have pores in both an inorganic (typically assumed to be water wet) and an organic (oil-wet) network. Since these shales do spontaneously imbibe water (Dehghanpour et al., 2012, 2013; Bostrom et al., 2014), the water-wet network is connected, just like the samples studied here, and thus we expect similar blocking results for this portion of the network. No spontaneous imbibition is expected into the oil-wet network, but if the connections between the networks are extensive in the media, the overall blocking should work in similar manner although possibly to a different extent.

## **3.6 CONCLUSIONS**

We present a three-step coreflood sequence that simulates fracturing fluid invasion, flowback and hydrocarbon production from hydraulically fractured reservoirs. This experimental sequence was used to study the permeability reduction due to the capillary mediated matrix-fracture interaction in tight and unconventional reservoirs. Our results show that the capillary discontinuity at the fracture face can give rise to significant permeability reduction in hydraulically fractured reservoirs after fracturing fluid invasion.

We present a scaling function that could serve as a tool to estimate enhancements on permeability via modest reductions of capillary pressures or well shut-ins. Furthermore, our results show that the maximum enhancement achieved via a shut-in is identical to that obtained with the use of a surfactant that reduces the IFT significantly.

### 3.7 SUPPLEMENTAL MATERIAL (CHARACTERISTIC CAPILLARY PRESSURE)

Due to the capillary discontinuity at the fracture face (in our experiment, the outlet core face), a non-uniform water saturation profile will exist during drainage. The water saturations can vary from  $1-S_{or}$  at the outlet face to  $S_{w,irr}$  at the inlet face. This leads to a capillary pressure distribution along the length of the core. Although the  $P_c-S$  curve relevant during flowback is not a primary drainage curve, the characteristic capillary pressure introduced in this work is only a normalizing parameter. For that reason, it can be chosen arbitrarily as long as the selection remains consistent between comparisons of different fluids (i.e., different IFTs). Here, we take as the characteristic capillary pressure the capillary pressure at the middle point between  $S_{w,irr}$  and  $1-S_{or}$ . The upper water saturation limit is obtained from mass balance, while the lower limit is estimated from the extrapolation of Corey-type relative permeability curves obtained from history-matching a core-scale drainage finite-difference calculation. The value of the characteristic capillary pressure is then obtained from rescaling MICP (during mercury extrusion) data to a pentane/water and to a pentane/water-methanol system using the Leverett J-function with the appropriate value for interfacial tension. An example of the determination of the characteristic  $P_c$  is shown in Figure 3.9.

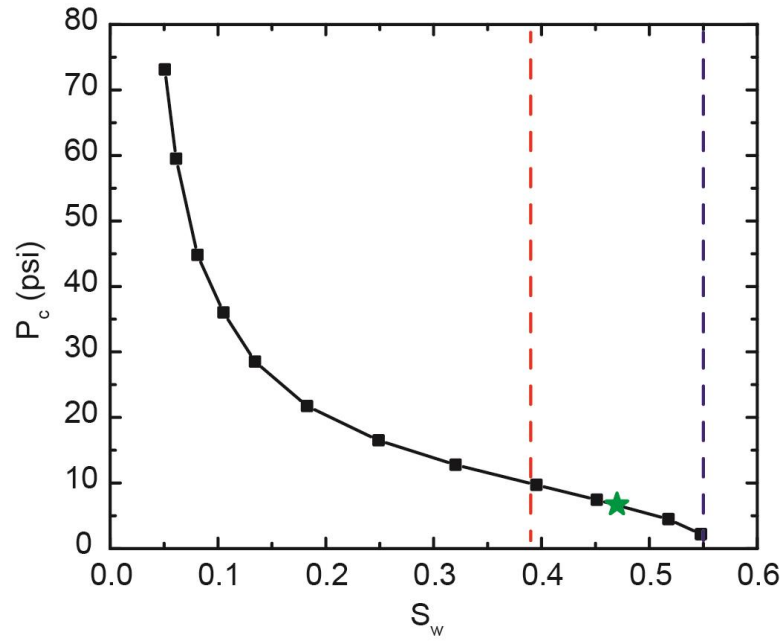


Figure 3.9: Mercury extrusion capillary pressure curve for Texas Cream Limestone scaled to the pentane/water system using Leverett J-function equation. The dashed lines show the possible water saturations. The green star indicates the characteristic capillary pressure for this case. The value of IFT between pentane and water and the contact angle used are 50mN/m and 18°, respectively.

## **Chapter 4: Water Block within the Entire Rock Matrix Adjacent to the Propped Fractures for Water-Wet Systems<sup>2</sup>**

This chapter extends the focus to the entire body of rock matrix adjacent to the propped fractures, both the water invaded and uninvaded zones; this region is believed to primarily contribute to the hydrocarbon production. The impact of the water invaded zone on the effective rock permeability to hydrocarbon is studied as a function of time and absolute rock permeability.

### **4.1 QUICK OVERVIEW OF THIS CHAPTER**

Invaded fracturing fluid into the rock matrix can potentially reduce the hydrocarbon production in low permeability reservoirs. To supplement the previous studies, CT scans were applied during this work to provide deeper understandings on different forms of water block in the low permeability rocks. Moreover, core samples with different bedding angles, thus different permeabilities, were drilled from the same batch of rock to compare the duration of water block; this helped to establish the scaling of water block for even tighter rocks.

### **4.2 INTRODUCTION**

Horizontal drilling and hydraulic fracturing are widely applied to economically produce hydrocarbons from shales or other tight reservoirs. During hydraulic fracturing, a large volume of fracturing fluid is pumped into the formation to create a complex fracture

---

<sup>2</sup> This chapter is based on the following paper:

**Liang, T.**, Luo, X., Nguyen, Q.P., DiCarlo, D.A. CT Measurements of Water Block in Low Permeability Rocks – Scaling and Clearing of Permeability Impairment. In Preparation.

network; this network maximizes the contact area with the formation and meanwhile provides the pathway for hydrocarbons to flow. Water-based fracturing fluids are typically used in North America, and it has been reported that only 5% to 50% of the pumped water can be recovered as “flowback” after the fracturing (Penny and Pursley, 2007; Zelenev and Ellena, 2009; King, 2012; Wasylshen and Fulton, 2012). Besides a small portion filled in the propped fractures and the wellbore, more than 90% of the fracturing fluid (i.e., water) is believed to be trapped within the induced unpropped fractures and the rock matrix (Sharma and Manchanda, 2015). Closed unpropped fractures have low conductivity and the trapped water therein can result in a further reduction due to multiphase flow; therefore, hydrocarbon production through this region likely has minor contribution to the total production especially during the early time. For rock matrix of shale or other tight reservoirs, the permeability is normally believed on the order of microDarcies down to nanoDarcies (DOE, 2009; Nelson, 2009) and therefore the water invasion might be restricted. However, it has been found that water imbibition can be significant even into the shales because of the existence of water-wet pores and their high capillary pressure generated by small pores/pore throats (Pagels et al., 2013; Bostrom et al., 2014; Dutta et al., 2014; Engelder et al., 2014; Lan et al., 2014). Moreover, considering that the surface area of rock matrix exposed by the open fractures is approximately on the order of 0.2-10 million ft<sup>2</sup> depending on the location of the shale play as well as the stimulation job (Yu and Sepehrnoori, 2014a, 2014b; King, 2015; Simpson et al., 2016; Wang et al., 2016; Zuo et al., 2016), the trapped water into the rock matrix can have great impact on hydrocarbon production. In shales, propped fracture network can also connect the pre-existing pathways, which are more likely affected by the invaded water, to the horizontal well; these preexisting pathways can be natural fractures, continuous high-permeability layers (Curtis et al., 2010, 2012a) or big pores within the organic matter that are typically observed in the

mature shales (Loucks et al., 2009). In short, any trapped water within the matrix adjacent to the propped fracture network would block the flow of hydrocarbon from the deeper reservoir rock and thus damage the well productivity for shales or tight sandstone reservoirs.

Low permeability rocks have small pore bodies and pore throats, which generate high capillarity that can result in the permeability reduction due to water block. It has been reported that the mitigation of water block in tight gas reservoirs would be slowed down when the pressure drawdown is not significantly greater than the capillary pressure/capillary entry pressure, and thus the recovery of rock permeability (Abrams and Vinegar, 1985; Holditch, 1979; Parekh and Sharma, 2004; Mahadevan and Sharma, 2005). Under the similar production conditions, our previous studies have shown that capillary discontinuity at the fracture face, which is analogous to capillary end effect in the core scale, may be mainly in charge of the water block after hydraulic fracturing; the water saturation profile, instead of the total water saturation, determines the level of permeability regaining through shut-in treatment (Liang et al., 2015a, 2015b; Longoria et al., Submitted). However, this hypothesis was only supported by the pressure drop/permeability recovery measurements as well as the mass balance measurements; therefore, more straightforward characterization method with high precision is needed.

CT scans have been used in some of the above studies to show the migration of the invasion front as well as the decrease of water saturation in the originally invaded region because of the material balance. However, the phase changes due to capillary discontinuity near the fracture face/core outlet have not been captured as proposed, and this is likely because that the gas was used to displace the trapped water and the evaporation effect/wicking effect near the core outlet cancels out the buildup of water (Mahadevan et al., 2007; Le et al., 2012). The impact of capillary discontinuity in low permeability rocks

is needed to be studied for the gas-water system at the early time that evaporation has not begun to play a role, as well as the entire period of time for the oil-water system that evaporation is negligible. Besides, three studies using CT scans conducted by the same research group reported that the imbibition and the permeability regaining during flowback behaved inconsistently for 5mD sandstone, 5μD shale and 100nD shale, and they attributed this inconsistency to the lithology and clay swelling (Odumabo et al., 2014; Chakraborty and Karpyn, 2015; Yan et al., 2015). Nevertheless, a continuous CT monitoring is necessary to capture the subtle phase saturation changes during flowback and hydrocarbon production, thus the governing physics behind the regaining of rock permeability can be well understood.

In this study, we present an experimental platform that simulates the fracturing fluid invasion as well as the flowback during hydrocarbon production occurring in the reservoir rock near the fracture face. Regaining of the rock permeability to hydrocarbon is obtained and compared with the changes of phase saturations in real-time by CT scans for the entire period of the experiment. This shows the existence of trapped water near the fracture face due to capillary discontinuity, as well as its significant impact on the permeability reduction. Permeability regaining is further compared on rock samples within a range of permeability; we thereby demonstrate that the duration of water block due to capillary discontinuity scales as  $\left(\sqrt{k/\phi}\right)^{-1}$ , thus tighter rocks experience longer period of water block. The second finding also explains the discrepancy observed by Odumabo et al., Yan et al. and Chakraborty et al.



### 4.3 MATERIALS AND METHODS

Hydraulic fracturing creates complex fracture network that provides the pathway for hydrocarbon to flow. It is very likely that most of the production, especially at the early time, is contributed by the formation rock adjacent to the fracture face, which might be seriously affected by the invaded fracturing fluid at the same time. Therefore, this region in the field was focused in this study and it was mimicked in the lab by using a core sample (Figure 4.1). An open space was created by one face of this core sample to simulate the fracture face, while the other side of the core represented the deeper uninvaded region of the formation rock. Invasion of the fracturing fluid and its recovery along with hydrocarbon production occurring through this region were simulated through a three-step coreflood experiment (Figure 4.2). The proxy fracturing fluid and hydrocarbon were injected into the core sample from its opposite faces during different steps of the experiment. Details on proxy fluids, rock samples and the design of coreflood experiments will be elaborated in the following sections.

The in-situ water saturation profile was acquired in real time by a Universal System HD-350 modified medical CT scanner. The CT scans were conducted every 30min, with 2mm slice thickness, 5mm slice intervals and 2s exposure time per slice. Each scan started at 1mm from the “frac face” of the core sample, and consisted of 47 slices that provided the water saturation profile within the sample at that moment. For each slice, the image resolution was approximately 210 $\mu$ m. In the meantime, pressure drop across the core was continuously recorded by a pressure transducer with a range of -200psi to 200psi for the entire period of coreflood; it gave the change of rock permeability due to the change of water saturation since the fluid injection rate was kept at a constant in each step of the coreflood.

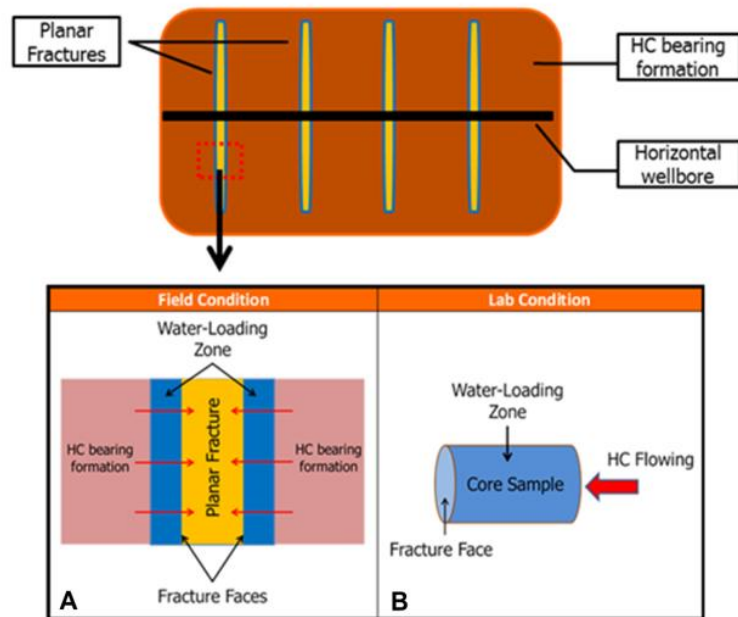


Figure 4.1: Field geometry (A) comparing to the lab model (B).

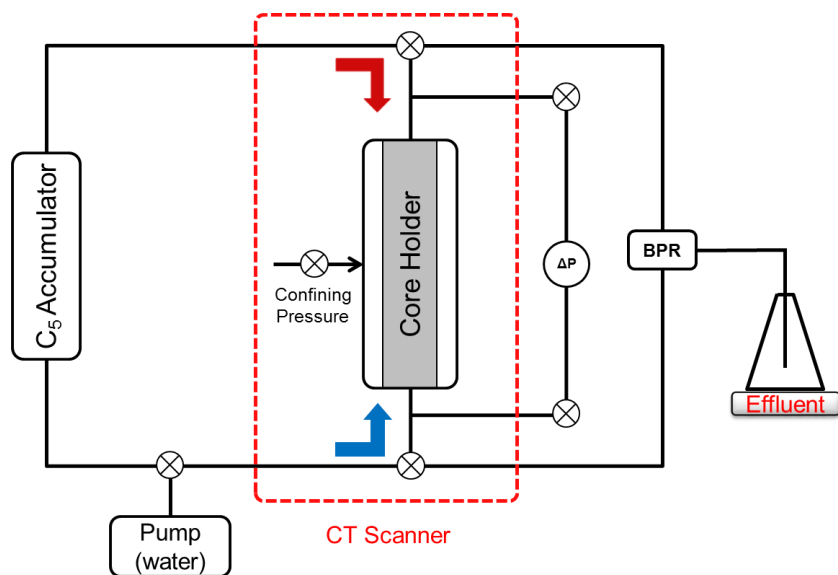


Figure 4.2: Coreflood setup in the lab.

#### **4.3.1 Proxy fluids**

Oil produced from shale or other tight reservoirs are typically low carbon number hydrocarbons. They have low density and thus low viscosity, which generates small resistant to flowing through the formation rock with a low/ultralow permeability. In view of this, n-pentane was chosen as the proxy hydrocarbon in this study. Its high mobility relative to water can also make many findings from this study be extrapolated to the gas reservoir cases.

Pure DI-water was used to mimic the fracturing fluid in this study. DI-water shows no adverse effects on the particular cores used in this study as is detailed below.

#### **4.3.2 Rock samples**

Indiana Limestone outcrop was chosen as the rock sample in this study. It is a water-wet carbonate, which mimicked the water-wet part of shales/tight rocks that is mainly affected by the invaded fracturing fluid. Since pure DI-water would be injected into the core samples during the experiments, multiple wetting and drying cycles with DI-water in this type of rock was conducted beforehand. No change on rock permeability was observed, and this indicated that the content of water-sensitive minerals is negligible in this type of rock.

Totally three core samples were drilled from two Indiana Limestone outcrop blocks from the same batch and then used in four coreflood experiments for comparison (Table 4.1). Core samples were all cylindrical in shape with identical dimensions: 3 inches in diameter and 10 inches in length. Core IND#1-1 was drilled from the block #1 and it had a permeability of 7.52mD and porosity of 0.161. Core IND#2-1 and IND#2-2 were both drilled from the block #2 but along different directions: the former one was parallel to the bedding planes while the latter one was perpendicular to the bedding planes. This

difference in stratification leads to their different permeability along the core direction, which was 14.1mD for IND#2-1 and 3.71mD for IND#2-2. Their permeabilities were measured from steady state coreflood experiments and their porosities were measured from CT scans. Although their permeabilities were well above the tight rocks or shales, the ratio of the viscous driving force to the capillary force was carefully designed in the coreflood experiment for capturing the relevant physics playing in tight formations during the fracturing fluid invasion and flowback. After tested in the coreflood experiment, each core sample could be restored by drying at 85°C for at least 8 hours in an oven to remove the contained pentane and water; this allowed the repetitive or comparative experiments to be conducted on the same sample. More details refer to Table 4.1 shown below.

Coreflood Number	Core Sample Name	Permeability (mD)	Porosity	Coreflood Schemes
#1	IND#2-1	14.4	0.168	DI water invasion; immediately production for 15hr
#2				DI water invasion; shut-in 15hr then production for 15hr
#3	IND#1-1	7.52	0.161	DI water invasion; immediately production for 15hr
#4	IND#2-2	3.71	0.174	DI water invasion; immediately production for 15hr

Table 4.1: Information of core samples and coreflood experiments (Corefloods #1-#2 are Corefloods #11-#12 in Chapter 5 (see Table 5.2), and results of Coreflood #2 will be shown in Chapter 5).

### 4.3.3 Coreflood schemes

The three-step coreflood experiment was started from a dry and vacuumed core sample that was loaded inside an aluminum Hassler coreholder with a confining pressure of 1500psi. An aluminum spacer, which was also X-ray transparent, was used by one core face to mimic the open fracture.

To choose an appropriate hydrocarbon flow rate that captures the governing physics during flowback and production in the field, the Rapoport and Leas number was used for scaling the competition between capillary force and viscous force (Rapoport and Leas, 1953; Lake et al., 2014).

$$N_{RL} = \left(\frac{\varphi}{k}\right)^{1/2} \frac{\mu u L}{k_r^0 \varphi \sigma \cos \theta} = \left(\frac{1}{k\varphi}\right)^{1/2} \frac{\mu u L}{k_r^0 \sigma \cos \theta}$$

For Bakken and Eagle Ford Shales, according to the published history-matching studies, oil superficial velocity (i.e., Darcy velocity) during early-time production is around 0.002-0.005ft/day for rock permeability of around 0.5-10μD and porosity of around 5-15% (Tran et al., 2011; Yu and Sepehrnoori, 2014b; Simpson et al., 2016). In the lab, to capture the similar impact from capillary force using the rock with permeability of 3-15mD and porosity of around 17%, the Darcy velocity was estimated by maintaining the same  $N_{RL}$  as follows.

$$u_{lab} \approx u_{field} \times \sqrt{\frac{k_{lab}}{k_{field}} \times \frac{\varphi_{lab}}{\varphi_{field}}} \approx 0.002\text{ft/day} \times 55 = 0.11\text{ft/day}$$

***Step-1: Initiation of a hydrocarbon-rich formation rock.*** To simplify the problem, no connate water was assigned initially into the core sample, and it was fully saturated with pentane as the initial reservoir condition. Unless otherwise specified, the downstream pressure was always kept at 500psi with a back pressure regulator (BPR). During this step, pentane was injected into the core at a constant flow rate; once steady state flowing

condition was reached, the absolute permeability of this core was determined through Darcy's Law.

***Step-2: Invasion of the fracturing fluid.*** A predetermined volume (0.160PV) of the DI-water was injected at a constant flow rate (0.4cc/min) into the core sample. During this step, as mentioned already, water was injected from the face that represented the fracture face in order to simulate the loss of fracturing fluid into the matrix adjacent to the open fracture network. At the end of this step, the core sample captured the change of water saturation from the fracture face to the deeper uninvaded region of the formation rock after the hydraulic fracturing.

***Step-3: Flowback of the fracturing fluid during hydrocarbon production.*** This step simulated the hydrocarbon production through the fracturing fluid invaded region into the open fracture network. To do so, pentane was flooded through the core from the other face at a constant flow rate (0.1cc/min, i.e., 0.11ft/day), which mimicked the production from the deeper region of formation rock. The changes of water saturation profile as well as the pressure drop across the core were both recorded with time in order to trace the trapped fracturing fluid and also to quantify the permeability regaining due to that.

## **4.4 RESULTS**

### **4.4.1 Change during water invasion (Step-2)**

A controlled volume of DI water was injected into the pentane-saturated core at 0.4cc/min for 75min during this step, which resulted in the overall water saturation of 16% (i.e., 0.160PV). Figure 4.3 (top) shows the water saturation profiles within the core sample acquired from CT scans at different time slices. The advance of sharp water saturation front can be noticed, which was indicative of a piston-like displacement by virtue of the

favorable mobility ratio during the invasion. As could also be seen in this figure, water saturation plateaus uniformly at about 40% within the invaded part of the core, where 60% of pentane remained undisplaced. Figure 4.3 (bottom) shows the side views of water distribution within the core sample at different time slices. Water was uniformly distributed within the invaded region of the core; no gravity segregation was observed although this coreflood was conducted horizontally in the CT scanner. In this case, capillary smearing was not obvious at the invasion front, which suggested a slower spontaneous imbibition comparing to the viscous-driven displacement.

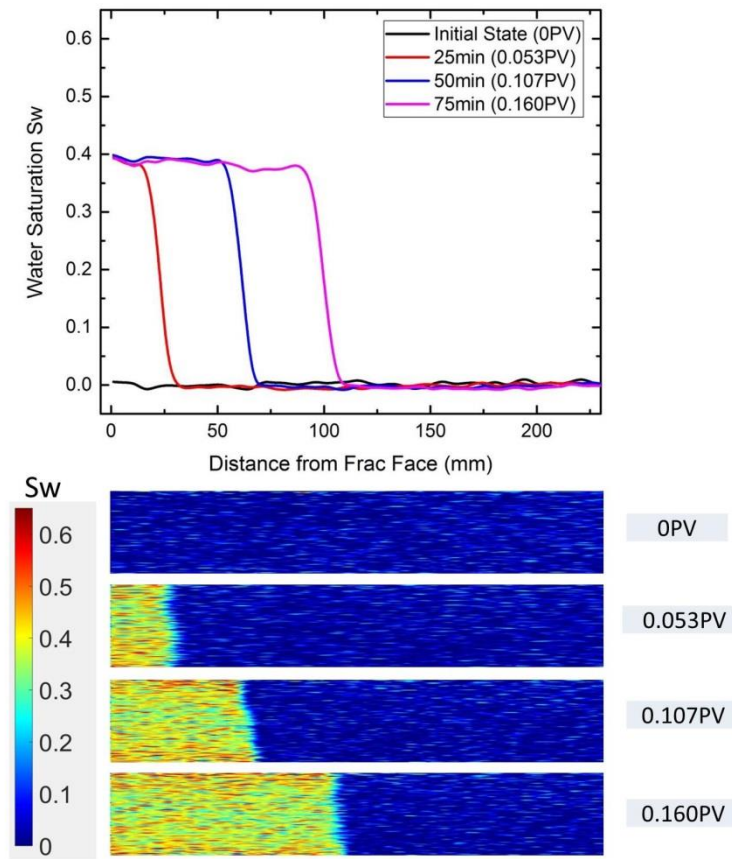


Figure 4.3: Change of water saturation profile (top) and side views of water distribution within the core sample at different time slices (bottom) during DI water invasion.

Although not shown here, the pressure drop across the core sample increased linearly with time under the constant injection rate. This also suggests that the invasion process was a piston-like displacement with a favorable mobility ratio. Details of similar pressure data can be found in the previous work (Liang et al., 2016).

#### **4.4.2 Change during flowback and hydrocarbon production (Step-3)**

When moved to Step-3, pentane was injected into the core sample from the other face at a constant flow rate of 0.1cc/min for 15hr (i.e., 0.481PV). As mentioned already, this step simulated the flowback of fracturing fluid during the constant rate hydrocarbon production. Figure 4.4 shows the change of water saturation profile with time both in flooded PV and real time. From this figure, two clear changes can be observed during this treatment. First, the invasion front migrated deeper into the rock (towards the right-hand side of Figure 4.4) over time, resulting in the increased water saturation within the originally uninvaded region of the rock (i.e., beyond 100mm from the fracture face). Second, water saturation decreased within the originally invaded region (i.e., within 0-100mm from the fracture face).

From the changes over time, it can be observed that most of the change in the originally invaded region happened within the first 3hr/0.096PV of the flood during Step-3; besides, water saturation at the fracture face remained high for the first 5hr/0.160PV, after which it decreased slightly and eventually the water saturation profile was levelled off towards the fracture face. The buildup of water saturation near the outlet of the flow at earlier time slices is evidence showing the capillary end effect due to the capillary discontinuity from the porous media (i.e., formation rock) to an open space (i.e., fracture). This discontinuity was defined as “*matrix-fracture interaction*” in Chapter 3.



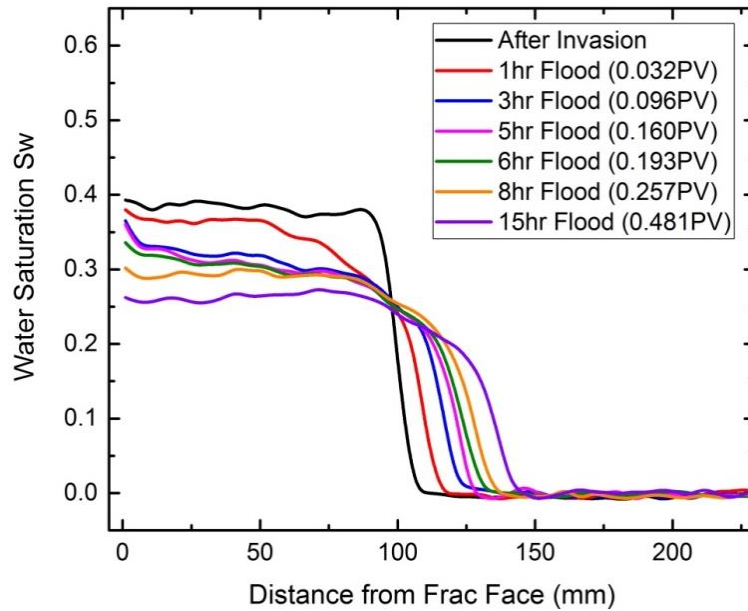


Figure 4.4: Change of water saturation profile within the core sample at different time slices during flowback and hydrocarbon production in Coreflood #1.

By integrating the water saturation profile at each time slice, the overall water saturation inside the core sample was determined as shown in Figure 4.5 (blue discrete data points). From this figure, it can be noticed that most of the flowback was produced within the first 3hr/0.096PV, after which no more change happened along the pentane flooding. Therefore, the clean-up of water trapped near the fracture face after 5hr/0.160PV shown in Figure 4.4 was likely due to the redistribution of water saturation profile through imbibition, instead of being recovered out of the rock. Figure 4.5 also shows the pressure drop across the core (black curve) during this flowback. An early time plateau was observed between 2.5hr/0.080PV and 5hr/0.096PV of pentane flooding. This plateau then decreased to a lower plateau and stayed almost the same for the rest of the flooding (after 6.5hr/0.208PV). The end-point relative permeability to pentane was calculated from the pressure drop, which was around 0.4 (i.e.,  $k_{ro}=0.4$ ). By comparing to the change of overall water saturation (blue discrete data points in Figure 4.5), it can be found that the decrease

of the pressure drop before 2.5hr/0.080PV was attributed to the flowback of invaded water out of the core sample. By further comparing to the change of water saturation profile (Figure 4.4), it can also be found that the decrease of the early time plateau was attributed to the clean-up of fluid trapped by matrix-fracture interaction; once this portion of trapped water was cleaned up, longer redistribution of water saturation did not provide an additional enhancement on the matrix permeability to pentane. CT results from this study provide the direct evidence proving the hypothesis made in the previous work (Liang et al., 2015a). For better understanding, the pressure drops were calculated using the water saturation profiles at different time slices and the fitted Corey-type permeability curves (red discrete points in Figure 4.5); this calculation will be elaborated in the following section.

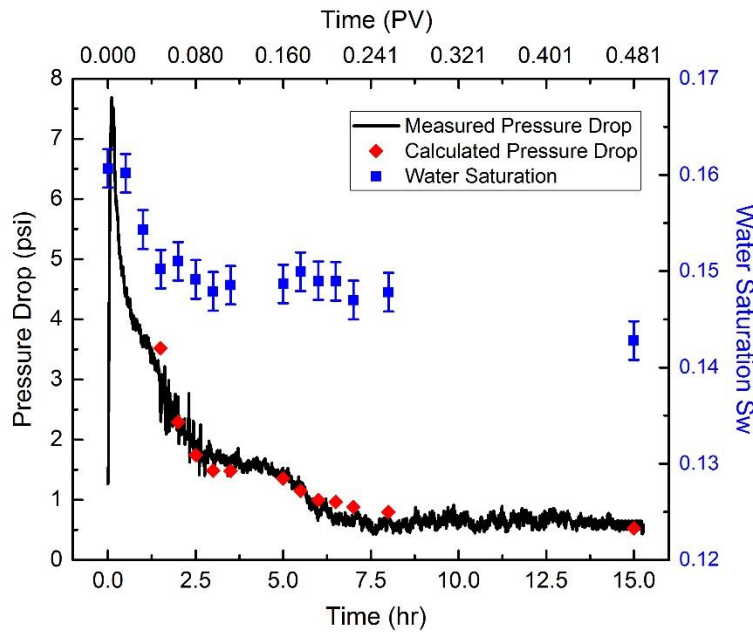


Figure 4.5: Changes of the overall water saturation inside the core sample (blue discrete data points) and the measured pressure drop across the core (black curve) during flowback and hydrocarbon production in Coreflood #1; red discrete data points shows the calculated pressure drops at different time slices through the fitted Corey-type relative permeability curves.

#### 4.4.3 Understand the formation and mitigation of water block through calculation

To better understand the permeability reduction due to the matrix-fracture interaction, water saturation profile at each time slice after the breakthrough of pentane in Step-3 of coreflood #1 was used to calculate the pressure drop across the core from Darcy's law. Corey-type relative permeability curves were applied and tuned for matching the pressure drop history measured in the lab. Table 4.2 (left two columns) lists all parameters of core samples and coreflood settings, which were required for calculating the pressure drop. Table 4.2 (right two columns) lists the Corey-type coefficients obtained from the coreflood measurement and history-matching.  $k_{rw}^o$  and  $S_{or}$  were measured from a separate coreflood by injecting water through a pentane-saturated core drilled from the same Indiana Limestone block;  $S_{wr}$  was estimated from end time CT scans in coreflood #1 as shown in Figure 4.5.  $k_{ro}^o$  and  $n_o$  were parameters tuned to match the pressure drop history acquired from coreflood #1, as shown in red in Table 4.2.  $n_w$  required other measurements and it was not shown here; nevertheless, it did not affect the history-matching of the pressure drop curve after pentane was the continuous phase. Figure 4.5 shows the comparison between the calculated pressure drops at different time slices (red discrete data points) and the recorded experimental data during the flowback from coreflood #1 (black curve).

History-matching confirms that the small portion of trapped water near the fracture face was the reason causing the early-time plateau during the flowback, and its clean-up generated further regaining (25% in this case) on the matrix permeability to hydrocarbon. In the end of Coreflood #1, 60% of matrix permeability remained unrecovered; this was due to the residual water in the rock that blocks some of the pathway for pentane to flow.

Core and Coreflood Information		Corey-Type Coefficients	
$k$ (mD)	14.4	$k_{ro}^o$	0.4
$\varphi$	0.168	$k_{rw}^o$	0.045
$A$ (m <sup>2</sup> )	0.0044	$S_{or}$	0.61
$L$ (m)	0.24	$S_{wr}$	0.25
$\mu_o$ (Pa · s)	2.4e-4	$n_o$	2.3
$u_o$ (m/s)	3.8e-7	$n_w$	/

Table 4.2: Parameters for history-matching the pressure drop curve during flowback of Coreflood #1.

Furthermore, it can be also found that once water invades into the rock during hydraulic fracturing, the water saturation profile, instead of the total water saturation, causes the major permeability reduction for the water-wet system. Matrix-fracture interaction, which is analogous to capillary end effect in the core-scale, would retain high water saturation in the matrix at the fracture face. This results in an extra permeability reduction and can last for a long period of time. However, this type of water block can be cured by itself through the imbibition: water saturation gradient generates a capillary force gradient, which drives water towards the deeper uninvaded region of the rock; this redistribution of water saturation profile cleans up the water block due to matrix-fracture interaction and enhances the rock permeability to hydrocarbon.

Since the length of early-time plateau is curial to hydrocarbon production and the permeability of the core sample used in Coreflood #1 might not reflect the case for tight rocks very well, a series of rock samples with a range of permeabilities were then tested in order to understand the physics so as to scale this length of water block for shale or other tight reservoirs.

#### 4.4.4 Permeability reduction and regaining as a function of rock permeability

The following results were obtained from the Coreflood #1, #3 and #4, and details about these three experiments refer to Table 4.1. Identical coreflood scheme was applied on three different Indiana Limestone core samples with different permeabilities. This comparison was designed to study how the duration of permeability reduction due to water block changes when the reservoir rock becomes tighter.

Figure 4.6 compares the changes of pressure drop across the core during flowback and hydrocarbon production when cores with different permeabilities were tested in the coreflood experiments. Early time plateaus were observed in all three cases; the tighter of the core sample, the longer this plateau would last: it increased from 5.2hr to 10.3hr when rock permeability decreased from 14.4mD to 3.7mD. Therefore, for the same size of water invasion, tighter rock undergoes a longer time to naturally cure the water block due to the trapped water near the fracture face and regain the matrix permeability to hydrocarbon.

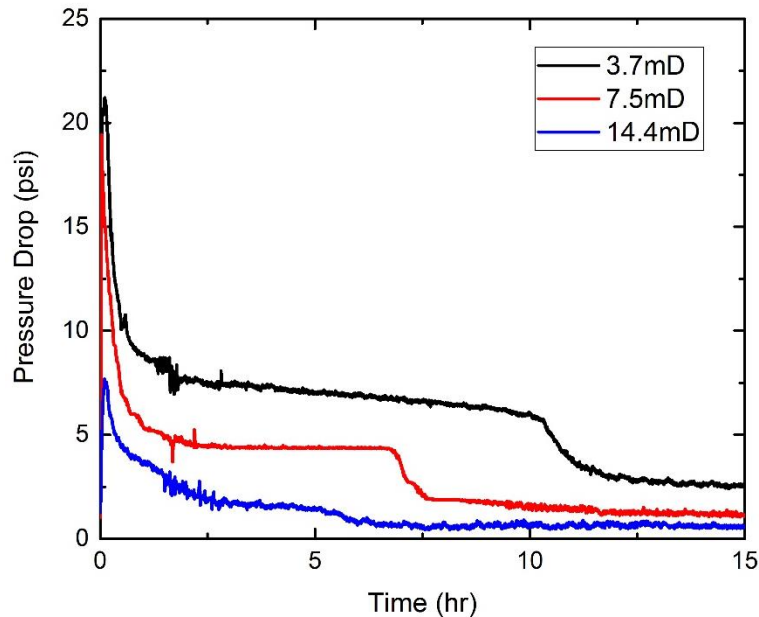


Figure 4.6: Comparison of changes of the pressure drop across the core during flowback and hydrocarbon production on three different core samples with different permeabilities (Coreflood #1, #3 and #4).

Since mitigating this type of water block was attributed to the capillary-driven imbibition, and  $\sqrt{k/\phi}$  was normally used to scale up the imbibition process (Zhang et al., 1996), this ratio was calculated for each core sample and then plotted versus the length of early time plateau as in Figure 4.7. Table 4.3 lists the petrophysical properties of each core sample for calculating its scaling factor. The linearity of data points shows the potential of this scaling factor on estimating the duration of such water block for tighter rocks. Qualitatively speaking, the tighter the formation rock, the longer the regaining of rock permeability to hydrocarbon is impeded by water block.

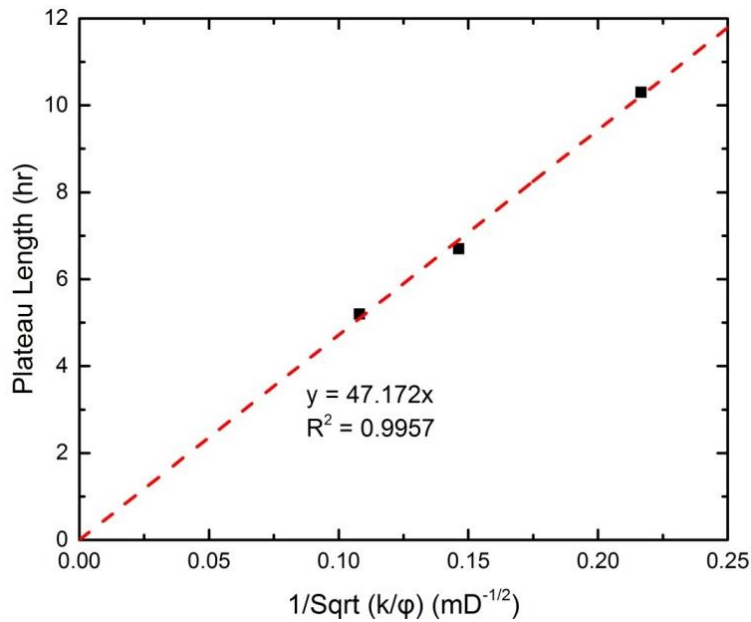


Figure 4.7: Duration of water block for rocks with different petrophysical properties.

<b>Coreflood Number</b>	<b>k (mD)</b>	<b><math>\phi</math></b>	<b><math>1/\text{Sqrt}(k/\phi) \text{ (mD}^{-1/2}\text{)}</math></b>	<b>Plateau Length (hr)</b>
#1	14.4	0.168	0.108	5.2
#3	7.52	0.161	0.146	6.7
#4	3.71	0.174	0.217	10.3

Table 4.3: Petrophysical properties for scaling/extrapolating the duration of water block.

## 4.5 DISCUSSION

### 4.5.1 Permeability reduction due to different types of water block

For the water-wet rock containing the light oil or gas, water invasion is a favorable/piston-like displacement while its flowback is not. This is very likely the case for the water-wet part of the productive shale or tight reservoirs. Piston-like invasion results in more water invading in the matrix near the fracture face; during the flowback, high mobility hydrocarbon fingers through the water invaded region, leaving a large portion of water behind due to a poor mobility ratio. From the point of view of multiphase flow, increase in water saturation would lead to low relative permeability to hydrocarbon. However, based on the experimental results of this study, it has been found that although the permeability damage due to the poor mobility ratio might affect a long period of hydrocarbon production, most of the damage is recovered along with the breakthrough of hydrocarbon. The major permeability reduction for the long term seems to be caused by the other two reasons: (a) water trapped near the fracture face due to matrix-fracture interaction; (b) water invasion into the desiccated part of formation rock whose initial water saturation is below the residual.

Coreflood #1 shows the major changes expected to happen during the flowback: a fast breakthrough of pentane, an early time plateau due to water trapped near the fracture face (reason (a)), and then a quasi-steady state when residual water saturation is reached within the originally invaded region (reason (b)). According to Figure 4.5, it took less than 1.2hr/0.038PV for pentane to breakthrough, which gave rise to about 15% regaining in its relative permeability; then matrix permeability to pentane was mainly damaged by the trapped water near the fracture face up to 6.5hr/0.208PV, and its clean-up gave rise to another 25% regaining in the relative permeability; matrix permeability stayed at 40% regaining for the rest of coreflood, when a residual water saturation of 26% was observed within the originally invaded region. This second type of water block (reason (b)) would play a significant role in initially-desiccated reservoirs whose water saturation is below its residual at the flow condition. Trapped water might imbibe into the deeper region of the rock after an extremely long period of production or be remobilized through the surfactant treatment. However, this is beyond the scope of this study.

#### **4.5.2 Influence of oil-wet part on mitigation of water block**

This work was done on a water-wet system. It was found that water block is mainly caused by matrix-fracture interaction; meanwhile capillary-driven imbibition of water can help to clean it up, although this process would be slow for low permeability rocks. Knowledge acquired from this work can be easily applied to most of the tight hydrocarbon formations, which are water-wet as well.

Shale varies from basin to basin; however, it is generally considered to be mixed-wet. Pores in shales are both observed within the inorganic matrix (which is mainly water-wet) as well as the scattered organic matter (which is mainly oil-wet). Due to the



preferential Young's Modulus or brittleness ( $E/v$ ), fracture network is likely formed mainly within the inorganic matrix (Paktinat et al., 2005; Ferrill et al., 2014; Far et al., 2015); it then links the organic matter to the production well and provides flow paths for hydrocarbon. If this is the case, same types of water block would also occur in the mix-wet system and impair the permeability to hydrocarbon. Water block in the oil-wet organic matter, if it happens, is mainly due to the increase of water saturation that reduces the relative permeability to hydrocarbon; damage due to matrix-fracture interaction is likely negligible. Under this scenario, water (non-wetting phase) is trapped in the center of organic pores, and the migration of hydrocarbon (wetting phase) during the production might not be able to clean up the water block. Therefore, using surfactant might be one of the most effective methods to mobilize the residual water and further regain the rock permeability to hydrocarbon; in-depth studies on this topic will be shown in later chapters.

#### **4.6 CONCLUSIONS**

An experimental platform was developed in this work that simulated the fracturing fluid invasion as well as the flowback during hydrocarbon production occurring in the reservoir rock near the fracture face. Regaining of rock permeability to hydrocarbon was obtained and compared with changes of phase saturations in real-time by CT scans for the entire period of experiment. It was found that matrix-fracture interaction causes the majority of permeability reduction for the water-wet system; the saturation profile within the invaded zone, instead of the total water saturation, determines the permeability reduction. However, it can be self-cured over time through the imbibition; while the tighter the rock, the longer time this self-curing process would take.

## **Chapter 5: Evaluation of Shut-In/Soaking Treatment on Mitigating Water Block for Different Initial Reservoir Conditions<sup>3</sup>**

This chapter evaluates the shut-in/soaking treatment for different reservoir conditions with different initial water saturation, i.e., non-desiccated reservoir with mobile water or desiccated reservoir without any mobile water. This study is focusing on the impact of this treatment from view of multiphase flow.

### **5.1 QUICK OVERVIEW OF THIS CHAPTER**

Fracturing fluid loss into the formation can potentially damage hydrocarbon production in shale or other tight reservoirs. Well shut-ins are commonly used in the field as a way to dissipate the lost water into the matrix adjacent to fracture faces. Unconventional tight reservoirs can differ significantly from one another, which could make this technique effective in some cases while not in others. We present an experimental investigation based on a coreflood sequence that simulates fluid invasion, flowback, and hydrocarbon production from hydraulically-fractured reservoirs. In this work, we evaluate the benefits from different lengths of shut-ins on regaining the rock permeability to hydrocarbon; then we elaborate the regaining mechanism behind this treatment, which can provide a guide for designing an effective shut-in/soaking treatment after hydraulic fracturing.

---

<sup>3</sup> This chapter is based on the following two papers:

**Liang, T.,** Longoria, R.A., Lu, J., Nguyen, Q.P., DiCarlo, D.A., 2015. Enhancing Hydrocarbon Permeability after Hydraulic Fracturing: Laboratory Evaluations of Shut-Ins and Surfactant Additives. SPE-175101-MS. doi:10.2118/175101-MS

**Liang, T.,** Luo, X., Nguyen, Q.P., DiCarlo, D.A. CT Measurements of Water Block in Low Permeability Rocks – Scaling and Clearing of Permeability Impairment. In Preparation.

## 5.2 INTRODUCTION

In order to economically produce hydrocarbon from shale or tight reservoirs, a large volume of fracturing fluid is injected to create a fracture network that maximizes the contact area with the formation. Water-based fracturing fluids are commonly used to fracture tight reservoirs in North America (DOE, 2009; Wasylishen and Fulton, 2012), and it has been reported that only 5% to 50% of the injected fluid is typically recovered as “flowback” (Penny and Pursley, 2007; Zelenev and Ellena, 2009; King, 2012; Wasylishen and Fulton, 2012). Water loss into the formation can have detrimental effects on the hydrocarbon flow from chemical and mechanical damage, for example clay swelling or rock softening (Abrams and Vinegar, 1985; Alramahi and Sundberg, 2012; Das et al., 2014; Zhang et al., 2015), and/or relative permeability reduction due to capillary trapping of the water phase. The second effect of permeability reduction is the focus of this study (i.e., “water block”) and its mechanism has been discussed in details in Chapters 3 and 4. In short, for water-wet media, water is held by capillary force; the mitigation of water block can be slowed down when the pressure drawdown is not significantly greater than the capillary pressure/capillary entry pressure, and thus the recovery of rock permeability (Holditch, 1979; Abrams and Vinegar, 1985; Parekh and Sharma, 2004; Mahadevan and Sharma, 2005). Under the similar production conditions, Chapters 3 and 4 have also shown that capillary discontinuity at the fracture face, which is analogous to capillary end effect in the core scale, is likely in charge of the water block after hydraulic fracturing; the water saturation profile, instead of the total water saturation, determines the degree of permeability reduction due to the invaded water (Liang et al., 2015a, 2015b; Longoria et al., Submitted).

Although hydraulically fractured reservoirs are normally characterized by permeabilities of the order of microDarcies down to nanoDarcies (DOE, 2009; Nelson,

2009), several studies have shown that water imbibition can play a role both in creating and mitigating water block (Pagels et al., 2013; Bostrom et al., 2014; Dutta et al., 2014): the creation of water block can arise from the initial fracturing fluid loss into the formation through spontaneous imbibition; while the mitigation of water block can arise from imbibition-driven water redistribution that essentially removes such water block. This has been reported as the mechanism that regains the rock permeability after the shut-in/soaking treatment based on laboratory measurements or numerical simulations (Taylor et al., 2010; Cheng, 2012; Le et al., 2012; Almulhim et al., 2014; Bertoncello et al., 2014; Dutta et al., 2014; Odumabo et al., 2014; Yan et al., 2015). In the field, enhancements of gas production after shut-in/soaking treatments have been reported in Marcellus (Yaich et al., 2015). On the contrary, two statistical studies on 80 Marcellus wells and 363 wells from six shale plays have also shown that shut-in/soaking treatments were “generally harmful” (Crafton and Noe, 2013; Noe and Crafton, 2013). In any cases, shut-in/soaking treatment delays hydrocarbon production; meanwhile, it extends the contact time between the trapped fracturing fluid and the formation, which can cause the first type of formation damage introduced earlier. Therefore, an in-depth study is required to understand the impact of shut-in/soaking treatment so that opposite observations from the field can be explained by one physical model. Besides, it is also beneficial to understand if shut-in/soaking treatment is necessary for low permeability reservoirs with such high capillary force; if the answer is yes, whether an optimal shut-in/soaking time does exist for a given reservoir/production condition.

In this chapter, similar experimental methods as introduced already in Chapters 3 and 4 are applied; shut-ins are carried out by delaying the hydrocarbon injection (i.e., Step-3) after water injection (i.e., Step-2) for a predetermined amount of time. We thereby demonstrate that shut-in can enhance the initial hydrocarbon production rate but it cannot

enhance the total production (i.e., total recovery); on the contrary, it might slow down the redistribution process that naturally cures water block.

### **5.3 MATERIALS AND METHODS**

When hydraulic fracturing fluid is applied to stimulate the tight formations, a portion of the injected fluid invades into the matrix from the fractures through imbibition; this can affect the hydrocarbon production during later life cycle of the well. The essential change that takes place in the matrix near the fracture faces during hydraulic fracturing or flowback process is captured and simulated through a three-step coreflood sequence in the lab, as introduced in details in Chapters 3 and 4. In this chapter, the study focused on evaluating the enhancements from shut-in/soaking treatment for different initial reservoir conditions and for different lengths of treatment time as well.

Initial reservoir condition determines key petrophysical properties of the rock that can impact the imbibition process and thus the shut-in treatment; for a specific rock sample at the laboratory environment, the initial water saturation seems to be a major factor. Therefore, two extreme initial water saturation were tested and compared in this study: (1) at the residual oil saturation where water is mobile across the whole rock (i.e., IRC-1), and (2) at 100% oil saturation where no mobile water presents (i.e., IRC-2).

To evaluate different lengths of treatment time, hydrocarbon injection (i.e., Step-3) was delayed for a predetermined amount of time after water injection (i.e., Step-2), as described in Section 5.3.3.

### **5.3.1 Proxy fluids**

N-pentane was also chosen here to mimic the low carbon number alkanes that are typically produced from shale or tight reservoirs.

To only focus on the physics of water block, pure DI water was chosen to mimic the water-based fracturing fluid. No detectable adverse effects were observed on the particular rocks used in this study as is detailed below.

### **5.3.2 Rock samples**

Austin Chalk and Indiana Limestone outcrops were chosen as the rock samples in this study. Both rocks are natively water-wet carbonates, which were used to mimic the water-wet portion of shales or other tight rocks that is mainly affected by the invaded water. Since pure DI-water would be injected into the core samples during the experiments, multiple wetting and drying cycles with DI-water in both types of rocks were conducted beforehand. No detectable change on rock permeability was observed, and this indicated that the content of water-sensitive minerals is negligible in both types of rocks.

As shown in Table 5.1, AUS#1 and AUS#2 were drilled from the same block of Austin Chalk outcrop, with permeability around 8.5mD and porosity around 0.26. Both core samples were cylindrical in shape with the identical dimensions: 3 inches in diameter and 10 inches in length. IND#2-1 was drilled from a block of Indiana Limestone outcrop, with permeability around 14.4mD and porosity around 0.17. It had a bigger diameter since CT scanner was used to monitor its phase change during the three-step coreflood experiment and such a big dimension ensured a good quality of CT results.

<b>Core Sample Name</b>	<b>Permeability (mD)</b>	<b>Porosity</b>	<b>Diameter (inch)</b>	<b>Length (inch)</b>
AUC#1	8.6	0.26	1.5	9.5
AUC#2	8.5	0.26	1.5	9.5
IND#2-1	14.4	0.17	3	10

Table 5.1: Information of core samples used in this study.

Although their permeabilities were well above the tight rocks or shales, the ratio of the viscous driving force to the capillary force was carefully designed in the coreflood experiment for capturing the relevant physics playing in tight formations during the fracturing fluid invasion and flowback (see Chapter 3). After tested in the coreflood experiment, each core sample could be restored by drying at 85°C for at least 8 hours in an oven to remove the contained pentane and water; this allowed the repetitive or comparative experiments to be conducted on the same sample. More details refer to Table 5.2 shown below.

### 5.3.3 Coreflood schemes

In this study, a similar three-step coreflood experiment was applied as shown in Chapters 3 and 4; by varying the parameters of each of these steps (e.g. amount of fluid injected, hydrocarbon injection rate, delays between steps, etc.), we can create different reservoir conditions (IRC-1 and IRC-2) and simulate different production schemes (including applying different production rates or performing different lengths of shut-ins). Detailed coreflood schemes are shown in Table 5.2.

Coreflood Number	Core Sample Name	Mimicked IRC	Sw after Invasion	pre-production shut-ins	HC Production Rate (cc/min)	post-production shut-ins
#1	AUC#1	IRC-1	0.55	/	0.1	/
#2						2hr
#3					0.4	/
#4						2hr
#5					0.6	/
#6						2hr
#7	AUC#2	IRC-2	0.20	/	0.1	2hr
#8				200min		
#9				400min		
#10				24hr		
#11	IND#2-1		0.16	/		
#12				15hr		

Table 5.2: List of corefloods conducted in this study (Corefloods #11-#12 are Corefloods #1-#2 in Chapter 4; more details refer to Table 4.1).



To simulate IRC-1, the pentane-saturated core was flooded with 1 pore volume (PV) of water during Step-2. Since the mobility of water was lower than that of the hydrocarbon, water saturation at the end of Step-2 was uniform across the core and approximately  $1-S_{or}$  ( $S_{or}$  is the residual oil saturation that oil does not mobilize, which was 0.45 in this case (i.e.,  $1-S_{or}=0.55$ )). Water was mobile everywhere within the core, and longer water invasion did not change the saturation.

To simulate IRC-2, a slug of water (0.20PV for Austin Chalk cores and 0.16PV for Indiana Limestone core) was injected into the pentane-saturated core at a constant flow rate during Step-2, which was less than the amount that required for reaching  $S_{wr}$  of the core ( $S_{wr}$  is the residual water saturation that water does not mobilize). In this condition, water only presented within the invaded zone.

To create different production processes, we varied the flow rate and/or the duration of the shut-in before or after the initial production (Step-3). The flow rate of hydrocarbon was controlled through the pump during Step-3 to study the impact of drawdown of shut-ins (Corefloods #1-#6); in general, the flow rate cannot be varied directly in the field, but can be controlled by the pressure drawdown, e.g. the lower the bottom-hole pressure with respect to the reservoir pressure, the higher the flow rate. To explore the effects of shut-ins, the pump was turned off for pre-designed lengths of time before or during Step-3. For IRC-1, we mainly focused on post-production shut-ins where the pump was stopped for 2 hours after 1 PV of hydrocarbon production (Corefloods #1-#6). For IRC-2, we mainly focused on pre-production shut-ins with different lengths of time before starting the flowback and hydrocarbon production (Corefloods #7-#12); post-production shut-ins were also conducted for 2 hours for comparison. Pre-production shut-ins are not tested for IRC-1; this was because at the end of Step-2, the water saturation is fairly uniform along the core and thus no capillary pressure gradient exists to generate spontaneous imbibition.

The key evaluation for each experiment is the permeability reduction due to the invaded water from the measured pressure drop across the core in Step-3. This pressure drop is converted to hydrocarbon permeability using the known flow rate and Darcy's Law. For corefloods using AUS#1 or AUS#2, the change of average water saturation within the core was determined by measuring the volume of flowback water from the effluent; while for corefloods on IND#2-1, changes of the average water saturation as well as the water saturation profile were both recorded through CT scans, as described in details in Section 4.3.3.

## 5.4 RESULTS

Figure 5.1 shows examples of the typical pressure drop profiles for Step-2 and Step-3 of the coreflood sequence for IRC-1&2 both conducted on Austin Chalk cores. For IRC-1, 1PV of fracturing fluid was injected into the core during Step-2, followed by 1PV of hydrocarbon injection during Step-3. Then, shut-in was performed by stopping the pump for 2 hours and resuming the hydrocarbon flow for another 2 hours (Figure 5.1A). For IRC-2, a slug of water (0.20PV in this case) was injected during Step-2 and the overall water saturation inside the core was kept below the residual of this rock type (Figure 5.1B). Since the pumping direction was reversed after Step-2, the pressure drop across the core changes the sign between Step-2 and Step-3. During water invasion (Step-2), pressure drop across the core linearly increases within time until it reaches a plateau (Figure 5.1A); this is indicative of a piston-like/favorable displacement in this step. In Step-3, however, an initial pressure peak in either case is indicative of an unfavorable displacement of water by the hydrocarbon. Due to the higher mobility of pentane with respect to water, pentane breaks through in a short amount of time and pressure drop across the core reaches an initial

plateau. When water production is not detectable anymore, the pressure drop across the core can be used to estimate the relative permeability to the hydrocarbon by applying single phase Darcy's Law. Here, we use the pressure drop after 1PV of hydrocarbon flowed through during Step-3 for both IRC-1 and IRC-2; and the hydrocarbon permeability calculated using this pressure drop is called *late-time relative permeability*.

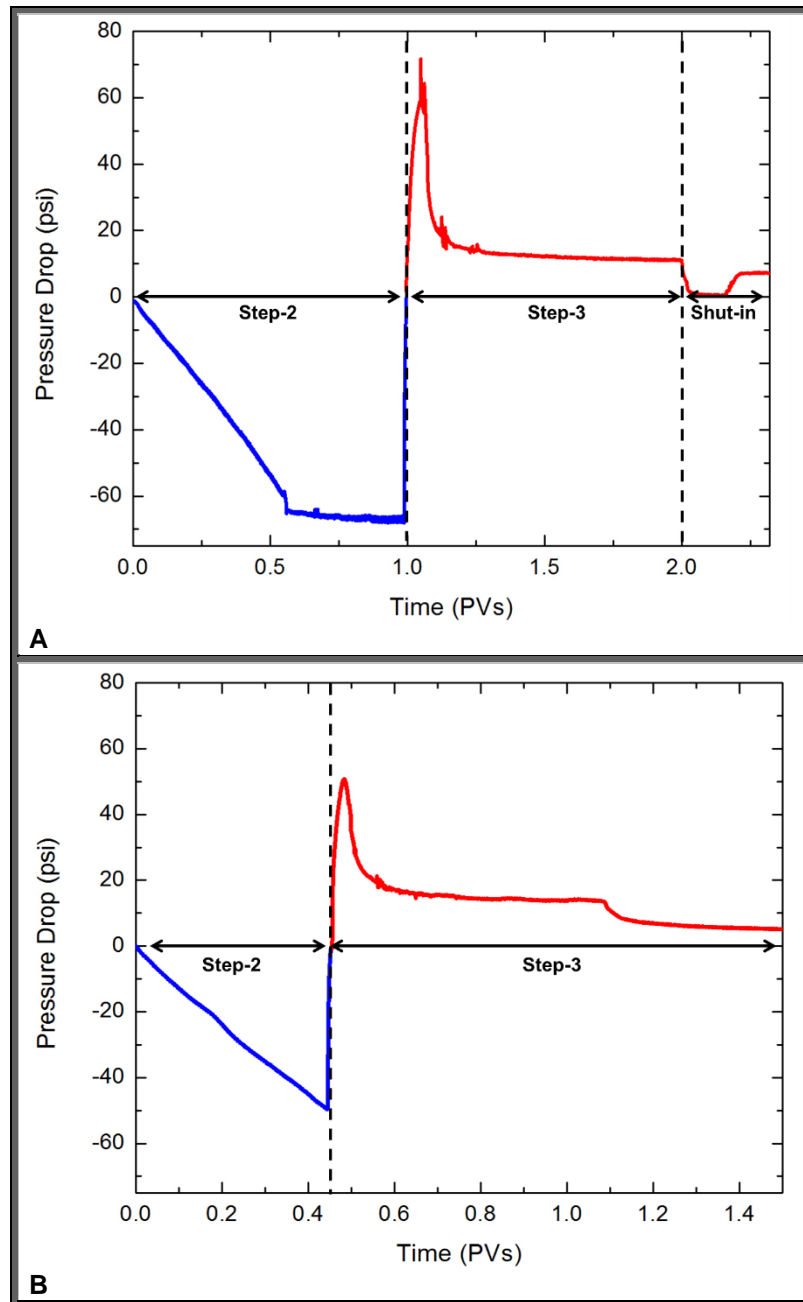


Figure 5.1: Pressure drop across the core as a function of time (in PV) during water invasion and flowback for IRC-1 (A) or IRC-2 (B). Post-production shut-in is performed after Step-3 for all IRC-1 cases.

### 5.4.1 Shut-ins for IRC-1

We first discuss how post-production shut-ins affect the late-time relative permeability to hydrocarbon for IRC-1. Pressure drop across the core was measured before and after the shut-in to quantify the improvement on hydrocarbon permeability. Red and blue columns in Figure 5.2 show the late-time relative permeability to pentane under different pentane flow rates (in Step-3) before and after the post-production shut-in; orange diamond dots in Figure 5.2 show the total volume of water flowed back after 1PV pentane flood, and no detectable volume of flowback is observed after the flood is resumed for another 0.25PV (not shown here).

At the lowest flow rates, the reduction of matrix permeability is more pronounced while the improvement after a shut-in is the greatest. In particular, the relative permeability to hydrocarbon increases by a factor of 2 after the shut-in in the case with a flow rate of 0.1cc/min. With increasing flow rate, the relative permeability to hydrocarbon plateaus and the improvement due to the shut-in becomes insignificant. These results show that shut-ins can enhance permeability when the viscous force is not enough to eliminate the water block hold by capillary force. A similar trend is observed for the volume of flowback water: it increases with pentane flow rate and reaches a plateau at high flow rates. This data can be used to calculate the change of overall water saturation within the core through material balance. Table 5.3 tabulates the changes before and after shut-ins under various flow rate conditions. The comparison of data indicates the enhancement of relative permeability after a shut-in is attributed to the change of water saturation profile, but not to the change of total water saturation within the core.

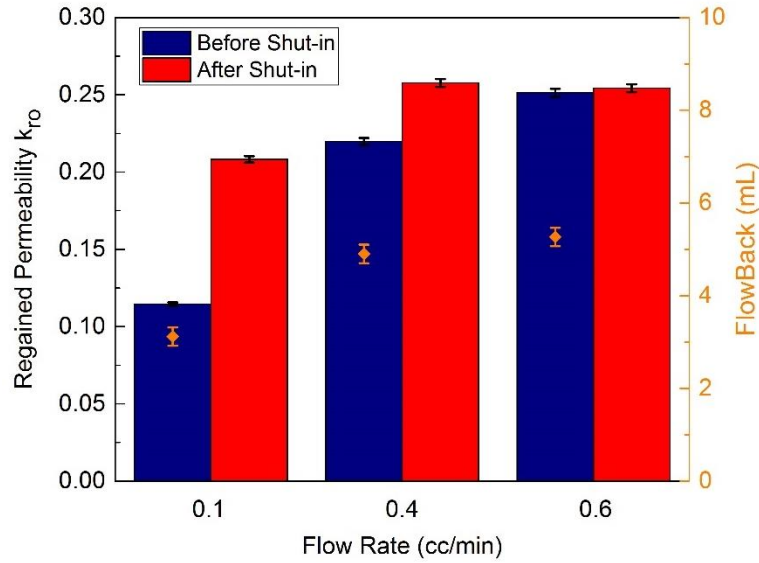


Figure 5.2: Regained relative permeabilities to hydrocarbon before (blue columns) and after (red columns) performing shut-ins at various flow rates. The volume of flowback water in each case is shown as the orange diamond dot; no detectable change was observed after performing the shut-in (Corefloods #1-#6).

Flow Rates	$\overline{S}_w$ before HC Flood	$\overline{S}_w$ after 1PV Flood	$\overline{S}_w$ after 2hr Shut-in
0.1 cc/min ( $u=1.51E-6m/s$ )	0.55	$0.51 \pm 0.01$	$0.51 \pm 0.01$
0.4 cc/min ( $u=6.04E-6m/s$ )	0.55	$0.49 \pm 0.01$	$0.49 \pm 0.01$
0.6 cc/min ( $u=9.06E-6m/s$ )	0.55	$0.48 \pm 0.01$	$0.48 \pm 0.01$

Table 5.3: Changes of the total water saturation within the core under various flow rates for IRC-1 (Corefloods #1-#6).

## 5.4.2 Shut-ins for IRC-2

### 5.4.2.1 Mitigation of water block after various lengths of shut-ins

For IRC-2, a slug of water was injected into the core during Step-2 (0.20PV for Corefloods #7-#10 and 0.16PV for Corefloods #11-#12), after which the overall water saturation of the core was still below the residual level to the hydrocarbon flow. Afterwards, different shut-in times were performed before starting hydrocarbon production in Step 3. Figure 5.3 shows the pressure drop across the core in Step-3 as a function of hydrocarbon flooding time (in PV) after pre-production shut-ins of different durations (i.e., step-3 in Corefloods #7-#10). These four experiments were performed at the same flow rate and on the same core, as shown in Table 5.2. Their flowback data is not presented here since no detectable water was measured from the effluent; therefore, all changes in rock permeability therein likely resulted from the change of water saturation profile, not from the change of total water saturation within the core sample. As can be seen in Figure 5.3, the hydrocarbon permeability after 1PV hydrocarbon flood (i.e., late-time relative permeability) is the same for all the cases tested; however, higher pressure drops (and thus, lower relative permeabilities) at early times are observed for shorter shut-in times. Without any shut-in (black curve), a high initial pressure drop appears, which then reaches a first plateau (before 200-minute or 0.29PV), after which the pressure drop across the core decreases to a second plateau. When a 200-minute shut-in was performed (red curve), the initial pressure drop is lower and the duration of the first plateau is shorter than that in the no-shut-in case; when a 400-minute shut-in was performed (blue curve), both of the initial pressure drop and the first plateau were dramatically reduced. After a 24-hour shut-in (green curve), the initial peak as well as the first plateau in the pressure drop all completely disappeared. It is important to note that the late-time hydrocarbon relative permeability converges to the same value in all cases. In short, these experiments show that while shut-

ins can enhance the matrix permeability, the magnitude of the early-time improvements depend on the duration of the shut-in; however, the late-time improvements seem independent of the durations.

Post-production shut-ins were also conducted for these cases, and no detectable change in the pressure drop across the core was observed (not shown here). This observation also supports that the identical late-time values shown in Figure 5.3 represents the maximum improvements one could expect from a shut-in treatment.

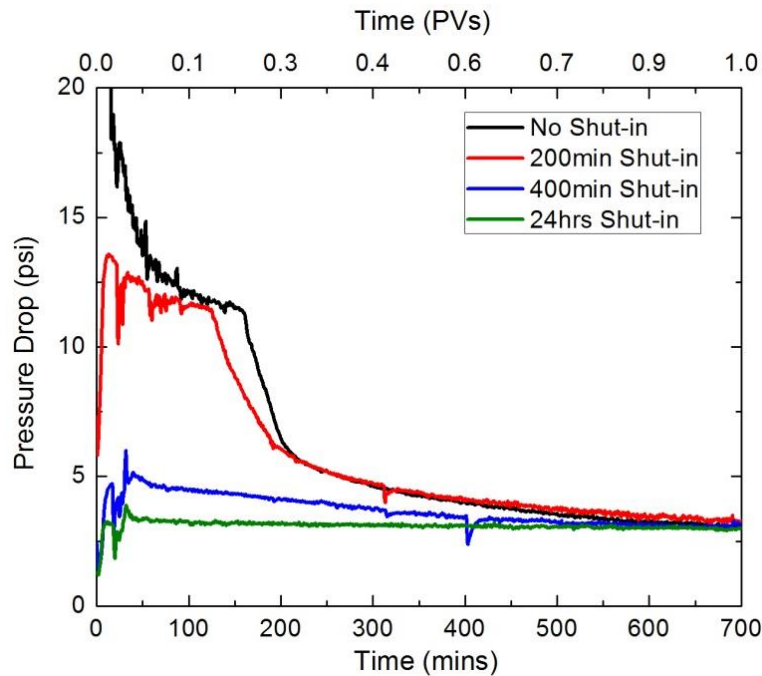


Figure 5.3: Pressure drop across the core during flowback and hydrocarbon production (Step-3) as a function of time (in PV) after different shut-in time spans after water invasion (Step-2). All the comparisons are conducted on the same core sample (Corefloods #7-#10).



#### 5.4.2.2 Observing the mitigation of water block during shut-in treatment through CT scans

CT scanner was then applied to visualize the change of water saturation profile during the shut-in treatment as well as the post-shut-in production (Corefloods #11-#12). Coreflood #11 was the baseline test without any shut-in treatment, and all its results have been shown in Chapter 4, including the changes of water saturation profile, total water saturation within the core and pressure drop across the core (Figures 4.3, 4.4 and 4.5).

For Coreflood #12 that tested the shut-in treatment, the injection pump was turned off for 15hr after 0.16PV of water injected into IND#2-1 during Step-2. Since shut-in treatment did not affect the invasion process, its results on Step-2 were identical to the case without the shut-in treatment, and they are not shown here.

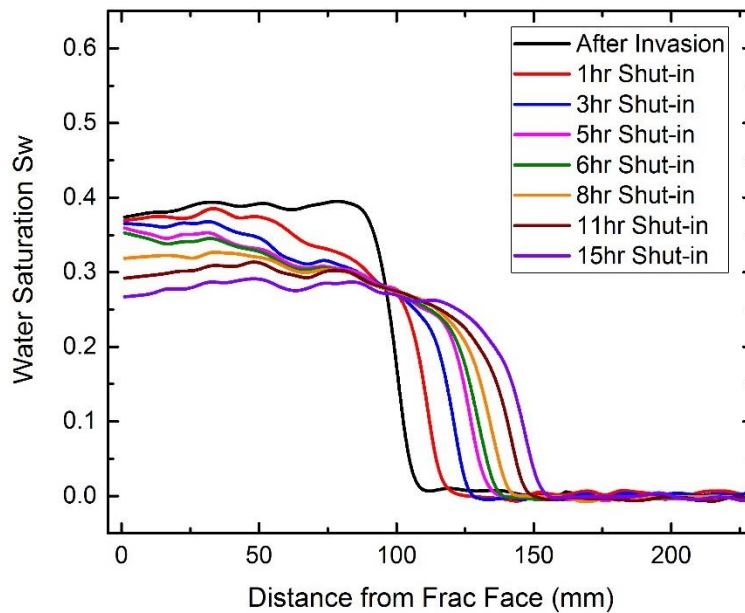


Figure 5.4: Change of water saturation profile within the core sample at different time slices during the shut-in treatment (Coreflood #12).

Figure 5.4 shows the change of water saturation profile within the core during this 15hr-shut-in treatment. From this figure, two similar changes can be noticed during this treatment, as ones happened with pentane flood for 15hr (Figure 4.4). Firstly, the invasion front migrated deeper into the core sample over time, resulting in the increased water saturation within the originally uninvaded region of the rock (i.e., beyond 100mm from the fracture face). Secondly, since the overall water saturation inside the core sample remained the same during this shut-in treatment, the migration of the invasion front pulled down the water saturation within the originally invaded region (i.e., within 0-100mm from the fracture face). The reduction of water saturation was faster near the invasion front and gradually levelled off near the core inlet (i.e., fracture face). However, different from the changes when hydrocarbon was flowing, water did not remain high at the fracture face and it uniformly dropped over time within the originally invaded region of the rock.

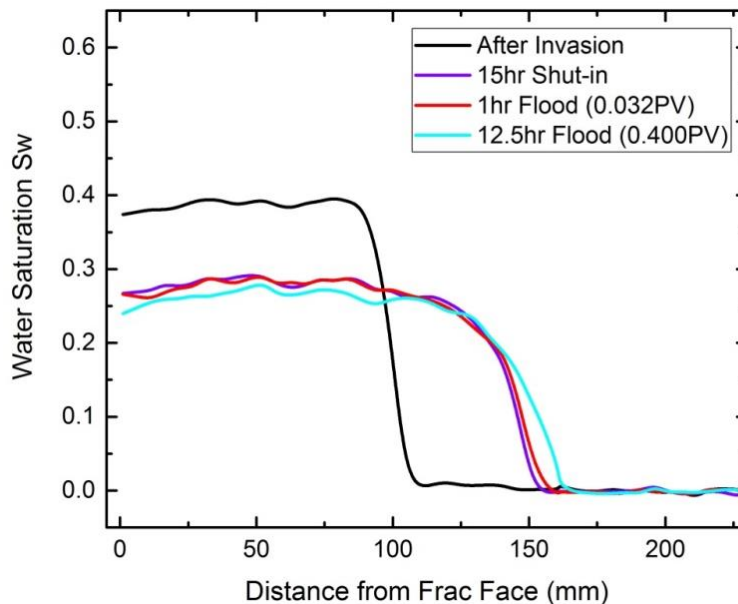


Figure 5.5: Change of water saturation profile within the core sample at different time slices during flowback and hydrocarbon production after 15hr-shut-in treatment (Coreflood #12).

Figure 5.5 shows the change of water saturation profile after pentane was flowed back through the core sample after 15hr-shut-in treatment. Comparing to the water saturation profile right after the treatment (purple curve in Figure 5.5), change during the flowback was very subtle. Water saturation within the originally invaded region remained at around 26% even after 12.5hr/0.4PV of pentane flooding, which was almost identical as the baseline case without shut-in (Figure 4.4). Figure 5.6 shows changes of the overall water saturation inside the core sample (blue discrete data points) as well as the pressure drop across the core (black curve) during this step. It also shows the calculated pressure drops (red discrete data points) using water saturation profiles at different time slices and the same fitted Corey-type relative permeability curves (Table 4.2).

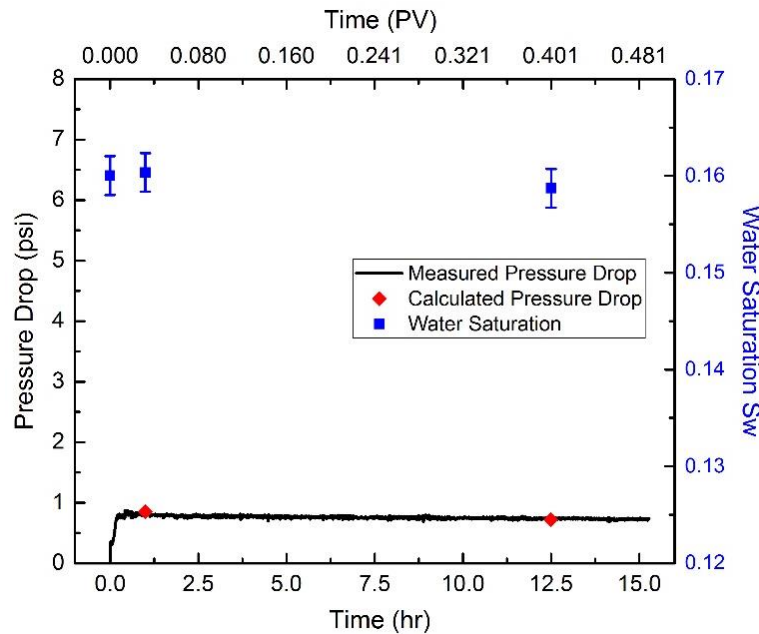


Figure 5.6: Changes of the overall water saturation inside the core sample (blue discrete data points) and the measured pressure drop across the core (black curve) during flowback and hydrocarbon production after 15hr-shut-in treatment; red discrete data points shows the calculated pressure drops at different time slices through the fitted Corey-type relative permeability curves (Coreflood #12).

As can be observed in Figure 5.6, neither the flowback of invaded water nor the enhancement on matrix permeability to pentane changed since pentane started to flow through the core sample. In addition, the late time water saturation profile and pressure drop across the core in this case were found as similar as those in the baseline case, and in-depth comparisons will be provided in the Discussion section. 26% water saturation within the originally invaded region might be indicative of the residual water saturation of this rock under the current production condition, resulting in the regaining of matrix permeability up to 40% (i.e.,  $k_{ro}=0.4$ ).

## 5.5 DISCUSSION

Figures 5.2 and 5.3 show that when water block created by capillary discontinuity exists at the fracture face, shut-ins can help remove such water block, for reservoirs that fall into both IRC-1 and IRC-2 conditions. However, the specific dynamics of mitigating water block differ between these two scenarios. After 1PV of pentane flood for the IRC-1, a saturation gradient may exist between the near fracture region and deeper in the reservoir, as introduced above. However, the viscous force acting on the water balances out the capillary suction, and therefore the permeability reduction due to water block is static as long as the hydrocarbon is flowing out. Once the hydrocarbon flow is stopped, i.e. a post-production shut-in is performed, the viscous force disappears and the capillary pressure gradient can now redistribute the water into the rock. The enhancements obtained with the shut-in depend on the severity of water block, with larger enhancements for the case with more significant permeability reduction before the shut-in (Figure 5.2). Nevertheless, although an enhancement on hydrocarbon permeability was observed after the shut-in in IRC-1 cases, this enhancement might not be long lasting: as long as the water saturation is

above the residual saturation in the formation, water can be mobilized by the flow of hydrocarbon and then accumulate at the fracture face after the shut-in. This gives rise to the rebuild of such water block that reduces the hydrocarbon permeability. However, further experimental studies are needed to fully understand this mechanism.

In contrast, for the IRC-2 cases (Figure 5.3), once capillary suction removes the water from the near fracture region, the water block due to capillary discontinuity is permanently eliminated and the permeability enhancement is not transient. It is important to note that in the IRC-2 cases, the viscous force acting on the water during hydrocarbon production is not enough to overcome the capillary force, which is resulted from the capillary pressure gradient between the near fracture region and the deeper reservoir. Therefore, in these cases, capillary suction can remove such water block even without a shut-in. However, in such cases, a large pressure difference (e.g. high drawdown) is needed during early time production as seen by the high initial pressure drop in Figure 5.3 for the case without any shut-in. A pre-production shut-in allows capillary suction to dissipate, at least part of, the lost fracturing fluid further into the formation; this gives rise to a much lower pressure drawdown required to achieve the same production rates. By comparing the results of the different shut-in durations shown in Figure 5.3, it is clear that the longer the shut-in, the more the dissipation of water block and thus, the lower pressure differential required for a given hydrocarbon flow rate. For example, the maximum pressure drop observed for the case with a 200-minute shut-in was more than twice as big as that observed for a shut-in twice as long. However, from our data, it is clear that there is an optimum shut-in duration, as the improvements obtained with a 24-hour shut-in are not very different from those obtained with the much shorter 400-minute shut-in.

As also presented in Figure 5.3, the early-time plateau in the pressure drop dramatically reduces around 200 minutes and starts to form the late-time plateau around

400 minutes in the case without the shut-in. These two changes led to the designs of conducting the tests by performing 200-minute shut-in and 400-minute shut-in before starting hydrocarbon production. 200-minute shut-in helps eliminate the very early time pressure drop but its overall improvement is very limited; while 400-minute shut-in almost clears the water block and eliminates the early-time plateau in the pressure drop.

Permeability enhancement during the shut-in is attributed to the clean-up of trapped water towards the deeper region of the rock through imbibition, which is time-dependent. Therefore, pressure drops after different durations of shut-ins are then shifted respective to their durations in order to compare the enhancement at the same time point after the mimicked “fracturing” (Step-2) was done in each case (Figure 5.7).

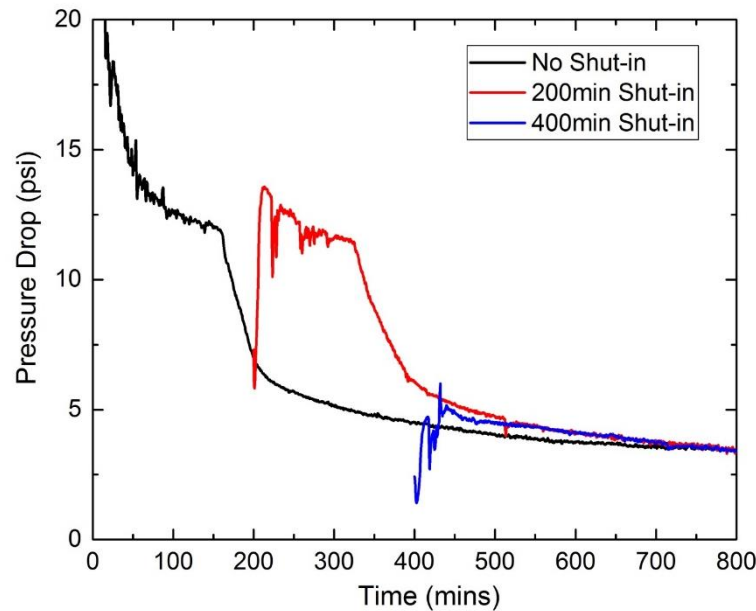


Figure 5.7: Pressure drop across the core during flowback and hydrocarbon production (Step-3) as a function of time (in PV) after different shut-in time spans after water invasion (Step-2). Pressure drops are shifted to compare the permeability enhancement at the same time since the end of invasion process. This figure is modified from Figure 5.3 shown above.

From this comparison, it can be noticed that although each case performs differently at the early time, their late time pressure drops end up with the same value. This suggests that (1) the speed of mitigating water block through imbibition is not obviously accelerated by the shut-in treatment, as seen in IRC-1; (2) for desiccated water-wet rocks, imbibition would redistribute the invaded fracturing fluid over time so as to mitigate water block, and shut-in treatment does not enhance the hydrocarbon production in the long term.

By further comparing the changes of water saturation profile with and without the shut-in from Corefloods #11-#12 (Figure 4.4 and Figure 5.4), it was found that the speed of mitigating water block was actually slowed down during the shut-in treatment. Pentane flowing in the opposite direction can push out a portion of water (Figure 4.5) that generates a saturation gradient; this saturation gradient can further generate a capillary pressure gradient that accelerates the imbibition process. Figure 5.8 compares the changes of regained relative permeability to hydrocarbon after hydrocarbon started to flow through the core (i.e., Step-3 began) during these two corefloods. Shut-in treatment enhanced the initial regained permeability by allowing the redistribution of water saturation profile to occur before the production started; however, it did not provide an extra enhancement than the capillarity itself could do. On the contrary, comparing to the baseline without any shut-in treatment, the overall regained relative permeability to pentane was actually lower when the shut-in treatment was applied (around 27% less). This was due to the little more portion of water invaded into the core during the treatment and it agrees with the CT results as compared in Figure 5.9.

In a short conclusion, shut-in treatment is not suggested only from the perspective of multiphase flow within the rock, especially the tight rocks: (1) it delays the production and it seems unnecessary for regaining the matrix permeability; (2) it allows more water

imbibed into the matrix before flowback; (3) it slows down the imbibition rate that helps to remove the trapped water near the fracture face.

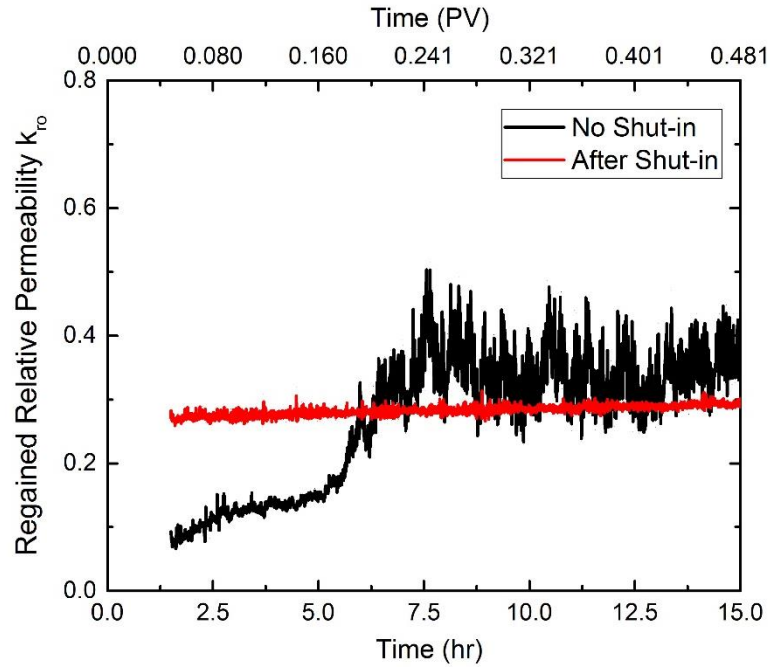


Figure 5.8: Comparison of the regained relative permeability to pentane during flowback and hydrocarbon production after 15hr-shut-in treatment was performed or not (Corefloods #11-#12).

Moreover, shut-in delays hydrocarbon production and meanwhile extends the contact time between the trapped fracturing fluid and the formation. The second issue may cause other types of formation damage: clay swelling (Madsen and Müller-Vonmoos, 1989; Caenn et al., 2011; Gupta et al., 2013), matrix softening and proppant embedment (Alramahi and Sundberg, 2012; Das et al., 2014), or fine migrant/clay dispersion (Bazin et al., 2009). Moreover, resuming hydrocarbon production after the shut-in can also cause an abrupt change in the drawdown and thus the formation stress; this can result in the closure of propped fractures and thus a detrimental effect on hydrocarbon production (Okouma et



al., 2011; Economides et al., 2012; Deen et al., 2015; Wilson, 2015). The permeability reduction people observed in the field after shut-in/soaking treatment is likely attributed to these factors.

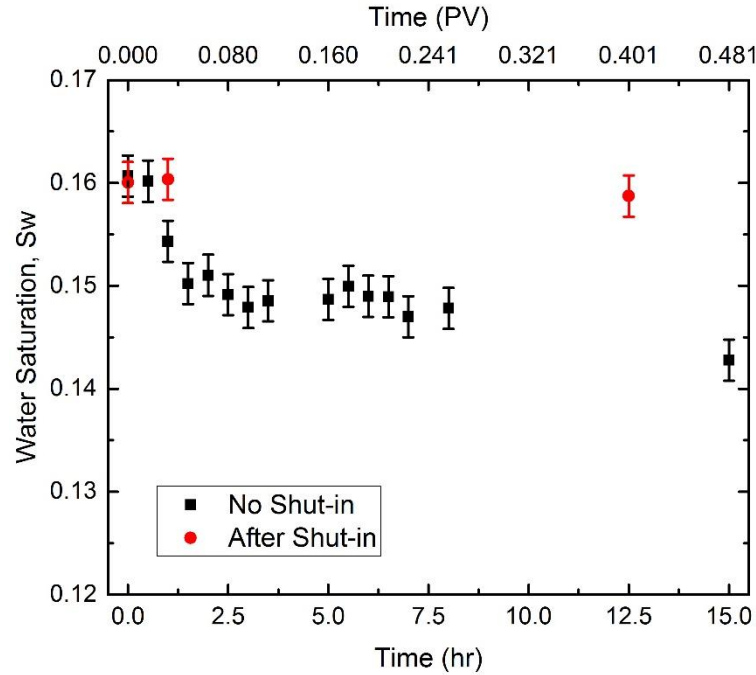


Figure 5.9: Comparison of the change of water saturation within the core during flowback and hydrocarbon production after 15hr-shut-in treatment was performed or not (Corefloods #11-#12).

## 5.6 CONCLUSIONS

Well shut-ins is one of the main methods currently used to overcome the permeability reduction caused by the fracturing fluid and enhance the hydrocarbon production in hydraulically-fractured tight formations. In order to determine detailed mechanisms, we established an experimental investigation based on a coreflood sequence that simulates fracturing fluid invasion, flowback and hydrocarbon production. As

proposed in our previous studies, reduction of matrix permeability due to the invaded water is mainly attributed to the capillary discontinuity at the fracture face.

By varying the details of coreflood sequence, we can simulate and compare different reservoir conditions and production managements (e.g., drawdown or shut-ins). We find that shut-ins remove the trapped water, especially the one hold by capillary discontinuity, through capillary suction (i.e., spontaneous imbibition into deeper formation rock); this results in an enhanced hydrocarbon permeability after the treatment. However, for the ultimate recovery rate, different initial reservoir conditions (e.g., water saturation) can create different capillarity gradient that affects the effectiveness of this treatment.

For non-desiccated reservoirs (IRC-1, with initial mobile water), the capillarity gradient between the invaded zone and the uninvaded zone is possibly weak, thus the permeability reduction due to water block can be long-lasting if shut-in treatment is not performed. However, for desiccated reservoir (IRC-2, without initial mobile water), this capillarity gradient is large that the mitigation of water block is a naturally-triggered process. Under such circumstance, shut-in treatment does not enhance the ultimate hydrocarbon production, and it instead slows down the mitigation of water block that can harm the hydrocarbon production.

## Chapter 6: Evaluation of IFT Reduction on Mitigating Water Block for Water-Wet Systems<sup>4</sup>

This chapter provides the evaluation of surfactant treatment for a range of interfacial tension (IFT) reductions. For surfactants generate the ultralow IFT reductions, a range of salinities is tested to compare the effect of various Winsor-type microemulsions on the efficiency of water flowback as well as the improvement of rock permeability to hydrocarbon.

### 6.1 QUICK OVERVIEW OF THIS CHAPTER

Significant amount of fracturing fluid is lost after hydraulic fracturing, and it is believed that the loss of fluid into the matrix can hinder the hydrocarbon production. One way to reduce this damage is to use the surfactants. Robust surfactant formulations have been developed for chemical enhanced oil recovery (CEOR); similar ideas are introduced in this study to mitigate water block in low permeability reservoirs. Here we present an experimental investigation based on a coreflood sequence that simulates fluid invasion, flowback, and hydrocarbon production within the rock near the fracture face. Real-time CT scans are applied to visualize the change of water saturation profile, which is then compared with the regaining of rock permeability. Different surfactants are used to test the effect of IFT reductions and formation of microemulsions; these are further compared in order to explore the best condition that maximizes the permeability enhancement. From

---

<sup>4</sup> This chapter is based on the following two papers:

**Liang, T.**, Longoria, R.A., Lu, J., Nguyen, Q.P., DiCarlo, D.A., 2015. Enhancing Hydrocarbon Permeability after Hydraulic Fracturing: Laboratory Evaluations of Shut-Ins and Surfactant Additives. SPE-175101-MS. doi:10.2118/175101-MS

**Liang, T.**, Achour, S.H., Longoria, R.A., DiCarlo, D.A., Nguyen, Q.P., 2016. Identifying and Evaluating Surfactant Additives to Reduce Water Block after Hydraulic Fracturing for Low Permeability Reservoirs. SPE-179601-MS. doi:10.2118/179601-MS

this work, we recognize the mechanism responsible for the permeability damage in matrix, and we suggest criteria to optimize the performance of surfactant additives so as to enhance the hydrocarbon production from low permeability gas/oil reservoirs after hydraulic fracturing.

## **6.2 INTRODUCTION**

Hydraulic fracturing is normally applied to stimulate low/ultralow permeability reservoirs in order to obtain an economical hydrocarbon production rate. However, only 5 to 50% of the injected fluid is typically reported to be recovered as “flowback” (Penny and Pursley, 2007; Zelenev and Ellena, 2009; King, 2012; Wasylishen and Fulton, 2012). Because of this, there is concern that the remaining fracture fluid can hinder hydrocarbon production; this all depends on where the fluid ends up being emplaced in the subsurface. Some fraction of the fluid is trapped within or leaks through the closed induced unpropped fractures (Sharma and Manchanda, 2015); however, this water would likely not impact hydrocarbon production at the early time. On the other hand, leak-off into the matrix that is near the open/propped fractures can harm the matrix permeability due to multiphase flow.

Shales or tight sandstones normally have pore throat sizes ranging from tens to hundreds of nanometers (DOE, 2009; Nelson, 2009), which generate large capillary pressures and can trap the invaded fracturing fluid. It has been reported that the mitigation of water block in tight gas reservoirs would be slowed down when the pressure drawdown is not significantly greater than the capillary pressure/capillary entry pressure (Holditch, 1979; Abrams and Vinegar, 1985; Parekh and Sharma, 2004; Mahadevan and Sharma, 2005; Le et al., 2012). In particular, we reported that matrix-fracture interaction, one form

of capillarity, could be mainly responsible for the water block and thus cause significant damage on matrix permeability in such reservoirs which are produced at low flow rates (Liang et al., 2015a, 2015b; Longoria et al., Submitted).

Supplementing fracturing fluids with surfactants that reduce capillary trapping of water has been recognized as a potential solution to permeability reduction due to water block (Bennion et al., 2000). Several studies have investigated the use of surfactant-based fluid additives to enhance flowback and regain matrix gas permeability (Penny and Pursley, 2007; Zelenev and Ellena, 2009; Rostami and Nasr-El-Din, 2014). As opposed to the traditional chemical enhanced oil recovery (CEOR) approach where surfactants are injected into the formation with the intent of forming an *in-situ* microemulsion between the injected water and the reservoir hydrocarbon, these studies developed microemulsions between the fracturing fluid and a solvent/oil before injection into the reservoir. These fracturing fluids with pre-formed (*ex-situ*) microemulsions are commonly known as “nanofluids”. In addition to improvements observed in laboratory experiments, several field studies report improved fracturing fluid clean-up and production in tight sandstone or shale gas reservoirs upon the use of nanofluids (Paktinat et al., 2005; Agee et al., 2010; Noe and Crafton, 2013). Despite these studies, several questions remain regarding the use of surfactants as fracturing fluid additives in unconventional plays. For example, it is not clear why nanofluids appear to enhance hydrocarbon permeability, while the addition of surfactants (without the *ex-situ* microemulsion) to the fracturing fluid lead to further permeability damage even though the surfactant reduces the surface tension between the gas and the water (Rostami and Nasr-El-Din, 2014). Furthermore, recent studies have shown that hydrocarbon regained permeability increases with reduction in capillary pressures, and therefore with reduction in interfacial/surface tension (Liang et al., 2015b). However, all of the nanofluid studies were done with gas as a model hydrocarbon phase

and in such cases, only limited reductions in surface tensions were achieved (e.g. the surface tension between gas and water was reduced to about a third of its original value with the use of nanofluids). No study has been done so far to explore the possibility of using surfactants within tight oil or shale oil reservoirs where ultralow interfacial tensions can be reached and *in-situ* microemulsions can be formed.

There has been major progress in how to screen robust surfactants to generate ultralow IFT reductions that mobilizes the residual oil and thus achieve successful ternary recoveries for conventional oil reservoirs (Levitt et al., 2009; Yang et al., 2010; Hirasaki et al., 2011; Lake et al., 2014; Lu et al., 2014). Here, similar ideas are introduced for choosing surfactants as fracturing fluid additives to mobilize the residual invaded water so as to regain the matrix permeability after hydraulic fracturing. A previous study has shown that forming *in-situ* microemulsions by using appropriate surfactants can enhance the hydrocarbon permeability (Liang et al., 2015b). However, it is still unclear (i) how different levels of IFT reductions affect the flowback of fracturing fluid and the regaining of matrix permeability; (ii) how different types of *in-situ* formed Winsor type microemulsions affect the maximum enhancement of matrix permeability.

In this study, we design an experimental method that simulates reservoir rock near the fracture face undergoing fracturing fluid invasion as well as flowback during hydrocarbon production. Experiments are conducted within a CT scanner to visualize the *in-situ* change of phase saturations. Using this method, we evaluate the performance of two different oil-water IFT modifiers that provide two levels of IFT reductions: methanol and an anionic surfactant formulation. Oil-water microemulsion phase behavior tests are conducted on the surfactant formulation to determine respective salinity conditions for the formation of Winsor type-I, II and III microemulsions (Winsor, 1948). Then, the effect of microemulsion type on the efficiency of water flowback as well as the improvement of

matrix permeability is quantified and compared with the microemulsion-free oil-methanol solution system. Our results show that methanol, the additive that only moderate reduces oil-water IFT, seems to have a negative impact on mitigating water block; while surfactant additives that form *in-situ* microemulsions, in particular type-I and type-III ones, are promising candidates to mitigate water block after hydraulic fracturing.

## **6.3 MATERIALS AND METHODS**

### **6.3.1 Rock samples**

All the core samples used in this study were drilled from a block of Indiana Limestone outcrop (IND#1) and they are all cylindrical in shape with dimensions of 3 inches in diameter and 9 inches in length. Indiana Limestone is a homogenous water-wet carbonate rock with permeability around 3.7mD and porosity around 17.7%. Although the permeability of this type of rock is well above tight rocks or shales, the ratio of the viscous driving force to the capillary force was well chosen to ensure that experimental conditions could capture the relevant physics playing in tight formations during fracturing flood invasion and flowback. As long as the core sample has not contacted with the surfactant, the core properties were restored by drying in an oven at 85°C for at least 6 hours to remove contained pentane, water, or methanol. Three core samples were used in this study for additive comparison, whose detailed information is shown in Table 6.2 below.

### **6.3.2 Choice of hydrocarbon**

Hydrocarbons from productive shale or tight oil reservoirs are normally composed of low carbon number alkanes, which are light and mobile in low/ultralow permeability porous media. In view of this, n-pentane was chosen as the proxy hydrocarbon in all

coreflood experiments conducted in this study. Since it is in liquid phase under ambient temperature and pressure, a wide range of IFT reduction could be achieved between pentane and water through various IFT modifiers. Furthermore, its high mobility relative to water could make many findings of this study be extrapolated to the gas reservoir cases.

### **6.3.3 Fracturing fluid additives**

In order to identify and evaluate surfactants to mitigate water block after hydraulic fracturing, two levels of IFT reductions were investigated as the first half of this study: (1) moderate reduction that is representative of a gas/water system or the best scenario of oil/water systems when low molecular weight alcohols are used without forming viscous macroemulsions; (2) low/ultralow IFT that is representative of an oil/water system when an optimized surfactant formulation is used and thermodynamically stable microemulsions are formed. 20wt% methanol was chosen as the additive for the first case, which reduces the IFT between pentane and water only by a factor of 2 as shown in Table 6.1. For the second case, 1wt% surfactant mixture (1wt% Surf) was applied as the mimicked fracturing fluid; it was a mixture of an internal olefin sulfonate (IOS) and an alcohol propoxy sulfate (APS), as well as isobutyl alcohol (IBA) as the cosolvent (more details refer to **Appendix C**). Cosolvent was added for two reasons: to increase the equilibrium time of microemulsions as well as to reduce the viscosity of microemulsions. With the increase in the salinity of surfactant solution, different Winsor type microemulsions are formed once mixed with pentane. This study further compared the effectiveness of different surfactant solutions at various conditions when three Winsor type microemulsions were formed as shown in Table 6.2. 1wt% Surf (type-I) has a salinity of 50000ppm, 1wt% Surf (type-III) has a salinity of 54500ppm while 1wt% Surf (type-II) has a salinity of 59000ppm; except



for the salinity, all other contents were the same among these three mimicked fracturing fluids.

<b>Mimicked Fracturing Fluid</b>	<b>IFT (mN/m)</b>
DI Water (Control Group)	50
20wt% Methanol in DI Water	23
1wt% Surf (Type-III)	4.8E-4 (ME/oil) 1.5E-3 (ME/water)
1wt% Surf (Type-I)	1.3E-3 (ME/oil)
1wt% Surf (Type-II)	3E-3 (ME/water)

Table 6.1: Interfacial Tension (IFT) by Various Fracturing Fluid Additives.

Phase behavior tests between surfactant solutions and pentane were conducted with 1:1 water-to-oil ratio in graduated 5mL borosilicate pipettes (Levitt et al., 2009), as shown in Figure 6.1. Black arrows indicate interfaces of aqueous phase and oleic phase before mixing, while red arrows indicate interfaces after mixing and equilibrated at room temperature. In the cases of DI water and 20wt% methanol, no other phases formed after mixing and interfaces remained the same by observation. When Winsor type-III microemulsion was formed, parts of the aqueous phase and oleic phase formed a bicontinuous middle phase, which gave two interfaces as pointed by red arrows. At a lower salinity, Winsor type-I microemulsion was formed where oil-in-water microemulsions coexisted with the excess oleic phase; at a higher salinity, Winsor type-II microemulsion was formed where water-in-oil microemulsions coexisted with the excess aqueous phase. From the phase behavior results, solubilization ratios of both oleic and aqueous phases in microemulsions could be recorded so as to determine oil-water IFT through Chun Huh

equation (Huh, 1979). As could be seen in Table 6.1, 1wt% Surf reduced the IFT between water and pentane around 4 orders of magnitude once different Winsor type microemulsions were formed.

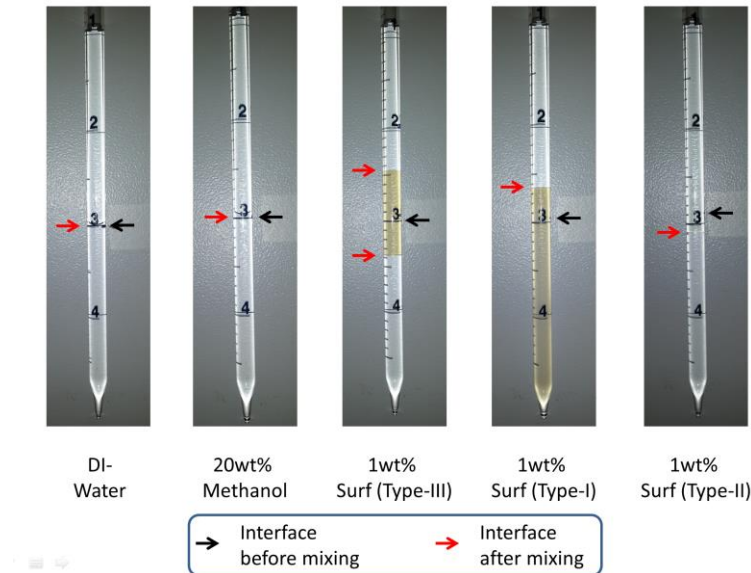


Figure 6.1: Phase behavior tests between pentane and various fracturing fluid additives. 2mL pentane and 2mL mimicked fracturing fluid were added in each pipette, gently shaken several times, and then allowed to equilibrate at 25°C. Black arrow points to the interfaces before mixing and red arrows points to the interfaces after mixing.

These mimicked fracturing fluids with various additives were tested and compared through 7 coreflood experiments, which are listed in sequence in Table 6.2. Since the core sample could not be restored to its initial state by heated in an oven once it was contacted with 1wt% Surf, three core samples from the same rock block were used to test three conditions that forms Winsor type-I, II and III microemulsions. DI water was always used to establish a baseline for the following additive tests to compare with (Corefloods #1, #4 and #6). Further details can be found in our previous reported work (Liang et al., 2015a and 2015b).

Coreflood Number	Core Sample Name	Permeability (mD)	Porosity	Fracturing Fluid Additive Tested
#1	IND#1 CT-4	3.88	0.178	DI Water (Baseline)
#2				20wt% Methanol
#3				1wt% Surf (Type-III)
#4	IND#1 CT-3	3.69	0.176	DI Water (Baseline)
#5				1wt% Surf (Type-I)
#6	IND#1 CT-2	3.55	0.176	DI Water (Baseline)
#7				1wt% Surf (Type-II)

Table 6.2: Schedule of Coreflood Experiments.

#### 6.3.4 Coreflood schemes

Invasion of fracturing fluid and its recovery along with hydrocarbon production were simulated in the lab through a three-step coreflood experiment. The mimicked fracturing fluid and hydrocarbon were injected into the core sample from its opposite faces during different steps of the experiment. The core sample was tested horizontally in the system to simulate the flows perpendicular to fracture faces in the reservoir (Figure 6.2). An open space was created by one face of the core sample in order to use that core face to simulate the fracture face. The *in-situ* water saturation profile was acquired in real time by a Universal System HD-350 modified medical CT scanner. CT scans were conducted every 30min, with 2mm slice thickness, 5mm slice intervals and 2s exposure time per slice. Each scan started at 1mm from the “frac face” of the core sample, and consisted of 45 slices that

provided the water saturation profile within the sample at that moment. For each slice, the image resolution was approximately  $210\mu\text{m}$ . In the meantime, pressure drop across the core was continuously recorded by a pressure transducer with a range of -200psi to 200psi for the entire period of coreflood; it gave the change of rock permeability due to the change of water saturation since the fluid injection rate was kept at a constant in each step of the coreflood.

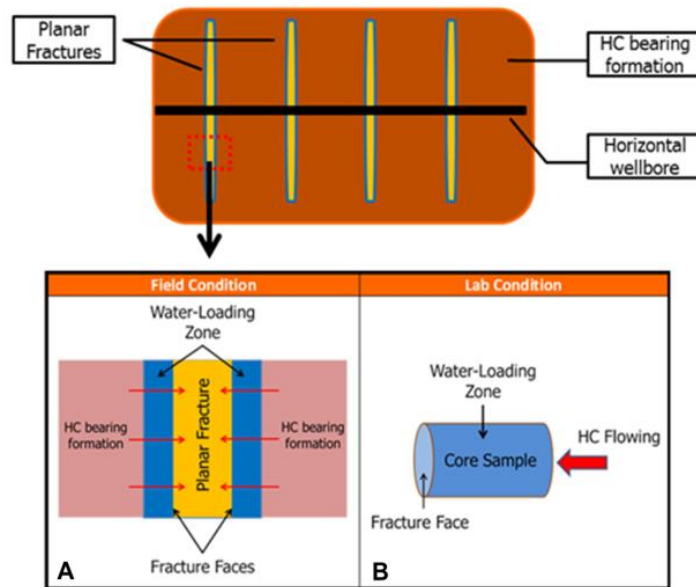


Figure 6.2: Field geometry (A) comparing to the lab model (B).

A dry Indiana Limestone core sample was loaded into an aluminum Hassler coreholder with an aluminum spacer by the face that simulated the fracture face, both of which were X-ray transparent. The core was then vacuumed to reach at least -28inHg before undergone the three-step coreflood sequence within the CT scanner as follows.

**Step-1: Reservoir saturated with hydrocarbon.** The core was fully saturated with pentane to simulate the initial reservoir condition. The confining pressure of the coreholder

was kept at 1500psi and the downstream pressure was kept at 500psi with a back pressure regulator (BPR) for all tests conducted. Once the core was fully saturated with pentane, the pressure drop across the core was measured under different flow rates, from which the absolute permeability of the core was determined through Darcy's law.

***Step-2: Fracturing fluid invasion.*** A controlled amount of mimicked fracturing fluid (0.173PV) was injected at a constant flow rate (0.4cc/min, about 0.43ft/day) into the core from the face that represented the fracture face. This step simulated the loss of fracturing fluid into the matrix since the hydraulic fracturing process and before the hydrocarbon production. Among all 7 coreflood experiments done in this study (Table 6.2), the amount of fluid invaded into the core and the fluid injection rate were all kept the same, while the only difference was the type of the mimicked fluid with different additives used during this step. At the end of this step, the core sample captured the water saturation change from the fracture face to the deeper uninvaded region of the formation rock after the hydraulic fracturing.

***Step-3: Fracturing fluid flowback during hydrocarbon production.*** Once invasion process was done, pentane was flooded through the core from the other face at a constant flow rate of 0.1cc/min (about 0.11ft/day), which simulated the hydrocarbon production from the deeper region of the formation rock. The water saturation profile and the pressure drop across the core were both recorded with time in order to locate the trapped fracturing fluid and also to quantify the permeability damage due to that.

## 6.4 RESULTS

### 6.4.1 Simulation of fracturing fluid invasion (Step-2)

#### 6.4.1.1 Water invasion without additives

DI water was used to simulate the fracturing fluid without any additives. This test was designed to establish a baseline for evaluating the performance of various additives. DI water was injected at 0.4cc/min for 78min, which resulted in the overall water saturation of 17.3% (0.173PV). Figure 6.3A shows water saturation profiles determined from CT results at different time slices during water invasion. As shown in this figure, the water saturation was uniform in space until it dropped quickly. In this paper, we refer to the position where the water saturation changes abruptly in space as *the invasion front*, and the portion of the core sample that is from the fracture face (0mm) till this invasion front as *the invaded region*. The invasion front advanced with time, which indicates a piston-like displacement of pentane by virtue of viscous force dominated flow. At the end of water invasion, water saturation plateaus uniformly at about 40% within the invaded zone (i.e., 60% of pentane remained undisplaced).

Figure 6.3B shows the change of pressure drop across the core during this step. Since the flow direction of pentane was designed to yield the positive pressure drop, the injection of water in the opposite direction resulted in a negative pressure drop. The pressure drop increased linearly with time as the region invaded by water increased linearly with time. This result also suggests that the invasion process was a piston-like displacement.

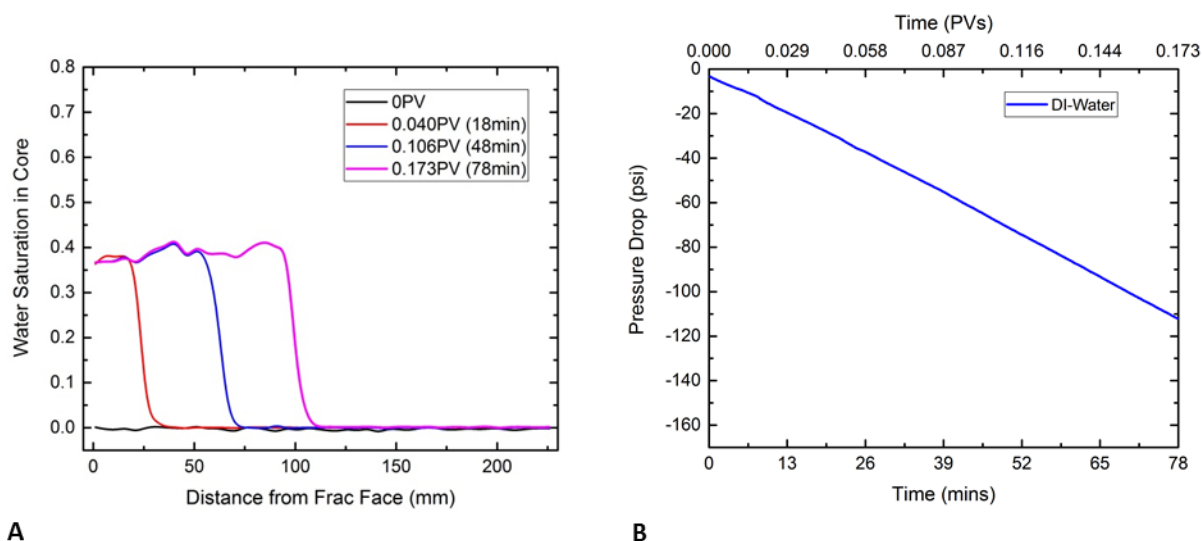


Figure 6.3: Changes of water saturation profile (A) and the pressure drop across the core (B) during fracturing fluid invasion in the baseline case (Coreflood #1).

#### 6.4.1.2 Water invasion with methanol as a moderate IFT modifier

20wt% methanol reduces the oil-water IFT from 50 to 23mN/m (Table 6.1). When agitated with pentane in the graduated pipette, it generated unstable macroemulsions that completely separated into visually unchanged aqueous and oleic phases within 15min (Figure). The viscosity of 20wt% methanol solution was measured by a proRheo LS300 viscometer (Figure 3.2), and it is about 1.44 times higher than that of DI water.

Figure 6.4A shows the change of water saturation profile within the core during the invasion of 20wt% methanol solution. Comparing with the baseline (Figure 6.3A), water saturation profiles at each time slice were almost the same. Since the pump was kept at the constant injection rate, the final overall water saturation inside the core was the same as the baseline, which was 17.3%.

Figure 6.4B shows the change of pressure drop across the core during the invasion for methanol. In this case, the pressure drop began to increase faster than the baseline after about 0.058PV (26min), which ended up with a higher pressure drop across the core, which was about -161psi. Comparing to the end point pressure drop of the baseline, which was about -112psi (Figure 6.3B), it was found that the ratio of two pressure drops was identical to the ratio of two fluid viscosities.

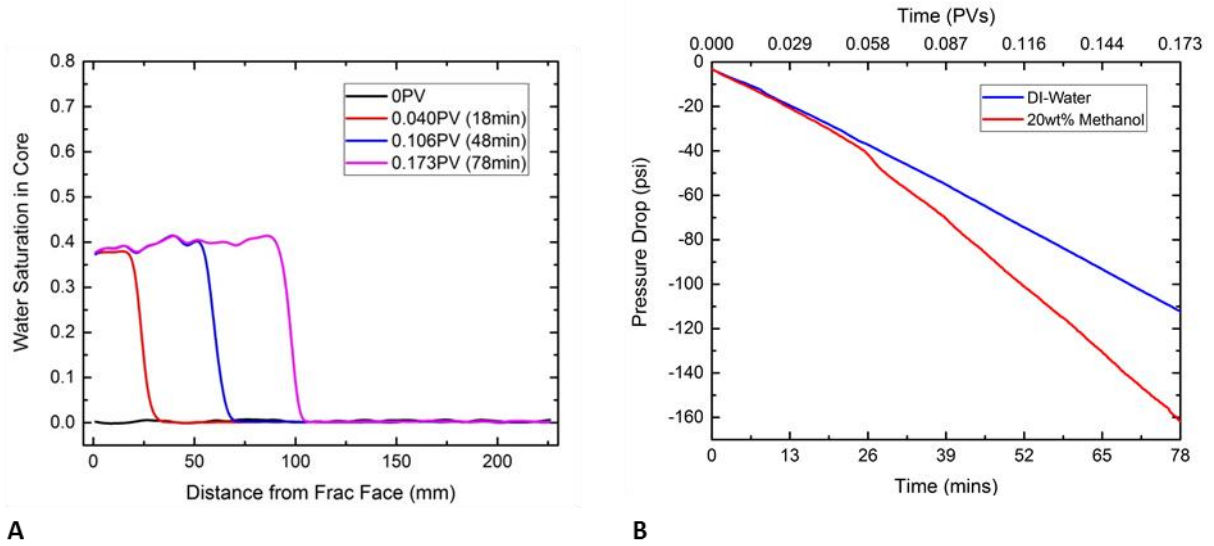


Figure 6.4: Changes of water saturation profile (A) and the pressure drop across the core (with comparison to the baseline) (B) during fracturing fluid invasion in the methanol case (Coreflood #2).

#### 6.4.1.3 Water invasion with surfactant as a strong IFT modifier

Figure 6.5 (right column) shows the changes of water saturation profile during the invasion process when different surfactant solutions that form different types of microemulsions were applied as the fluid additives. Since different cores were used for these surfactant corefloods, the baseline corefloods with DI water were also conducted before each surfactant run. To improve our interpretation on surfactant performance, the



change of water saturation profile at identical time slices for each baseline is also shown in Figure 6.5 (left column).

By comparing to the baseline, it is found that the invasion region was separated into two relatively distinct regions called *the adjacent region* (including the fracture face) and *the intermediate region*. In the adjacent region, although it evolved with time during the invasion, the water saturation was obviously higher than the baseline (up to  $S_w \sim 0.7$ ); while in the intermediate region, the water saturation remained the same as the baseline ( $S_w \sim 0.4$ ). It can also be noticed that the depth of invasion was slightly shallower in the surfactant cases due primarily to the increased water saturation in the adjacent region. Since the pump was kept at the constant injection rate for the same amount of time, the final overall water saturations inside the core in all cases were the same with a value of 17.3%.

Figure 6.6 compares the pressure drop across the core for the surfactant solutions for three respective microemulsion types. The pressure drop in the baseline increased linearly with time (only one baseline shown as they were all within 0.4% of the pressure drop); in contrast, for the three surfactant cases the pressure drop increased non-linearly. When the surfactant formed type-I and type-II microemulsions the pressure drops were lower than the baseline; when the salinity was such that it formed a type-III microemulsion, the pressure drop increased to more than the baseline after 0.116PV (52min).

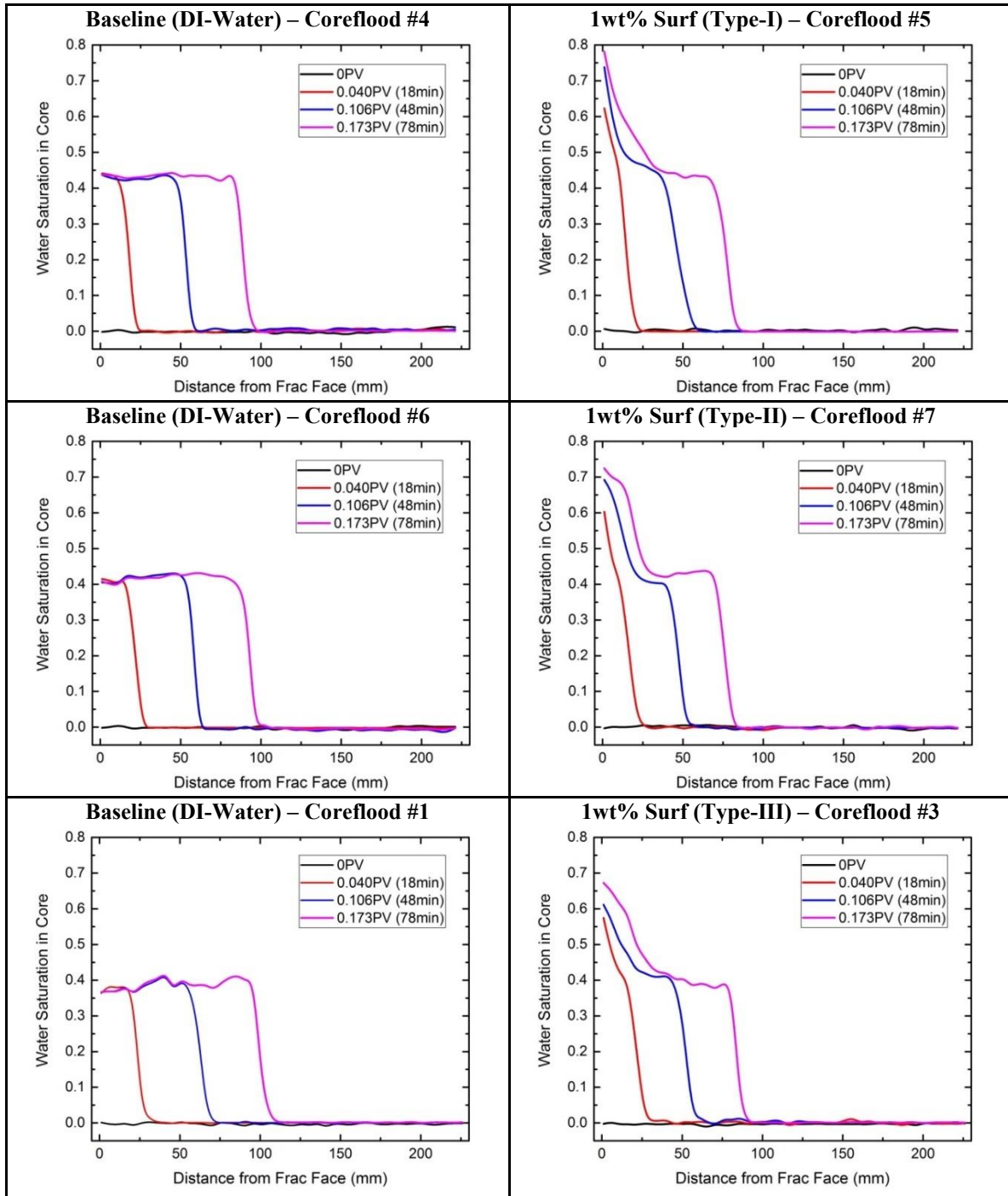


Figure 6.5: Comparison of changes of water saturation profile during fracturing fluid invasion in various surfactant cases (Left column: baselines; right column (from top to bottom): conditions that form Winsor type-I, type-II and type-III microemulsions).

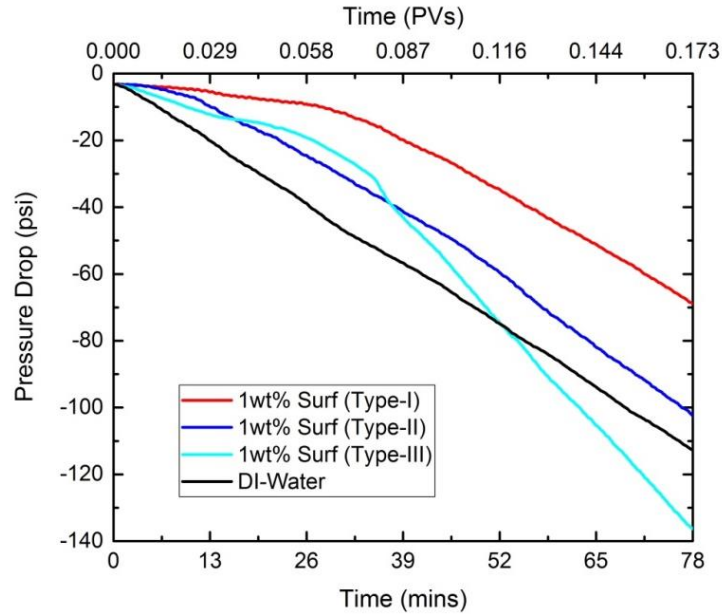


Figure 6.6: Comparison of changes of pressure drop across the core during fracturing fluid invasion among various surfactant cases (Corefloods #1, #3, #5 and #7).

## 6.4.2 Simulation of fracturing fluid flowback (Step-3)

### 6.4.2.1 Flowback without additives

Figure 6.7 shows the change of water saturation profile with time both in PV and real time after pentane was flowed back through the core. During the flowback, the water saturation profile decreased in the invaded region. This is followed with the propagation of the invasion front further into the core that resulted in an increase of water saturation in this region; we refer this region as *the imbibition region* (as shown in Figure 6.7). In addition, the water saturation at the fracture face (0mm) was constant for the first 0.35PV (10.5hrs), after which it decreased slightly. The overall water saturation in the core at a given point in time was determined by integrating the water saturation profile, as shown in Figure 6.8 (blue discrete data points). From the change of overall water saturation, it is

noticeable that the major change happened within the first 1hr of the flowback. Moreover, it is also found that no more invaded water was recovered out of the core after 0.083PV (2.5hrs) of pentane flooding. Thus the clean-up of water trapped near the fracture face was due to the redistribution of water saturation profile, instead of being recovered out of the core.

Figure 6.8 also shows the pressure drop across the core (black curve) for water flowback. An early time plateau was observed after 0.167PV (5hrs) of pentane flooding; it decreased after 0.333PV (10hrs) to a lower plateau. This dual plateau profile was previously reported and attributed to the clean-up of fluid trapped by matrix-fracture interaction (Liang et al., 2015b). This is confirmed in this study by comparing this dual plateau pressure drop profile to the saturation data shown in Figures 6.7 and 6.8 (blue discrete data points). In addition, this comparison also shows that the further redistribution of water saturation did not provide an additional enhancement of matrix permeability to pentane.

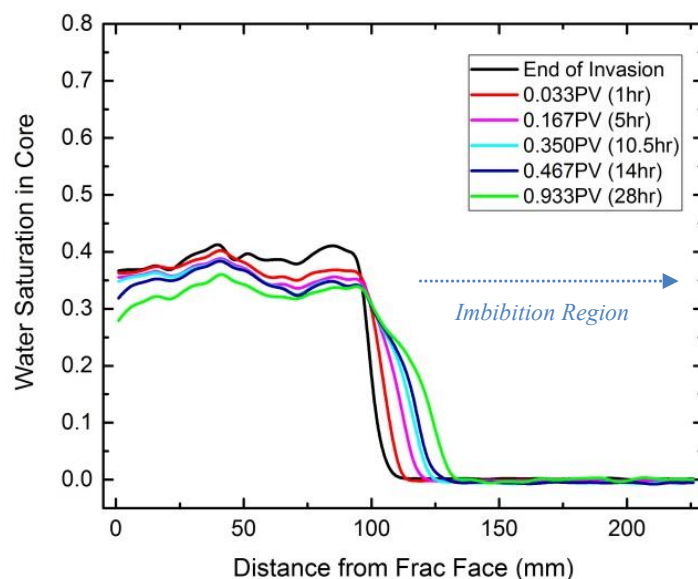


Figure 6.7: Change of water saturation profile during flowback and hydrocarbon production the baseline case (Coreflood #1).

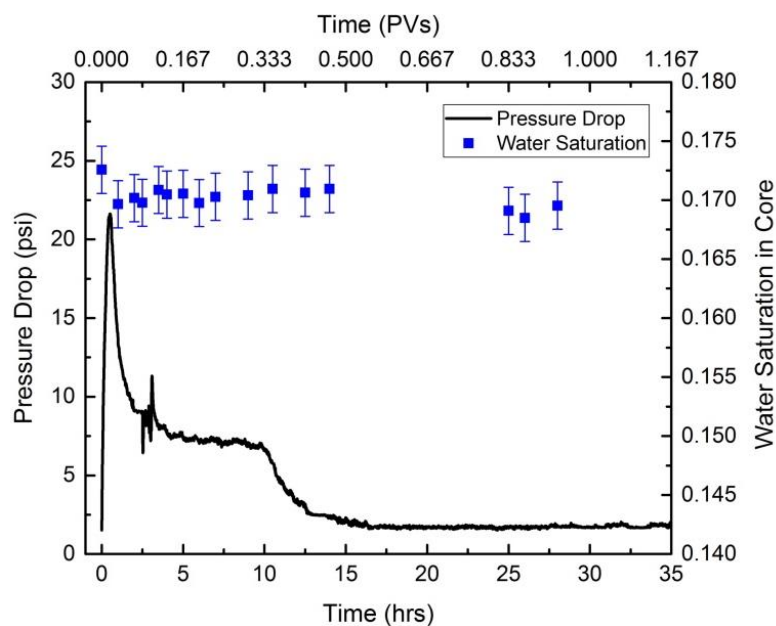


Figure 6.8: Changes of the overall water saturation inside the core (blue discrete data points) and the pressure drop across the core (black curve) during flowback and hydrocarbon production the baseline case (Coreflood #1).

#### **6.4.2.2 Flowback with methanol**

Figure 6.9 shows the change of water saturation profile after pentane was flowed back through the core with 20wt% methanol solution. The same two changes in water saturation were observed: the decrease of water saturation in the invaded region and the migration of the invasion front within the imbibition region. Water trapping at the fracture face was also noticed in this case. It started to dissipate after 0.833PV (25hrs) of pentane flooding, which was more delayed than the baseline. Moreover, the invasion front imbibed slower into the uninvaded region of the core comparing to the baseline, and this was corresponding to the IFT reduction with methanol. The change of overall water saturation in this case is compared with the baseline as in Figure 6.10. It shows that the length of flowback was extended from 1hr to 10hrs, resulting in three times more produced water when 20wt% methanol was used as the fluid additive.

Figure 6.11 shows the pressure drop across the core for water flowback with methanol. Comparing to the baseline, the early time plateau still occurred, but it was delayed to around 0.77PV (23hrs). Similar to the baseline, the CT data showed that this plateau occurred when water at the fracture face started to dissipate (Figure 6.9). The second plateau was reached after 1PV (30hrs) flooding, which was slightly higher than the baseline.

In summary, although adding methanol resulted in higher flowback, its moderate reduction on oil-water IFT resulted in a slowdown of capillary-driven imbibition that is in charge of mitigating water block.

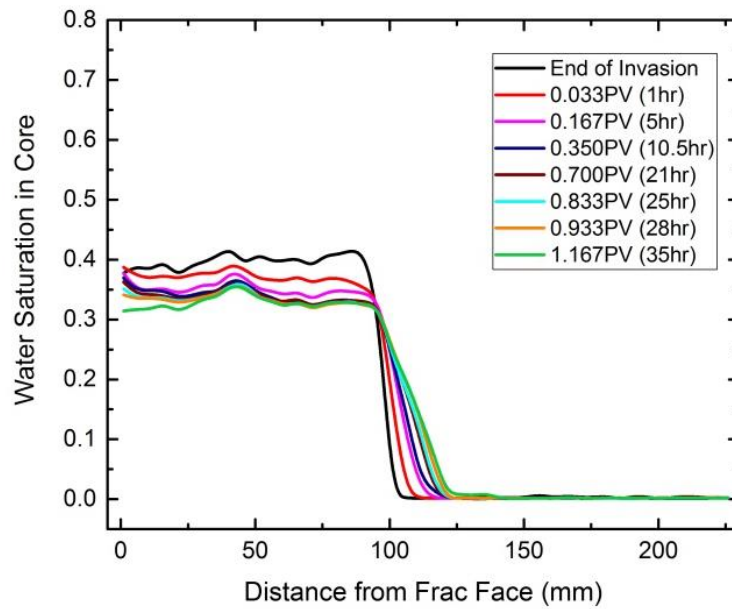


Figure 6.9: Change of water saturation profile during flowback and hydrocarbon production the methanol case (Coreflood #2).

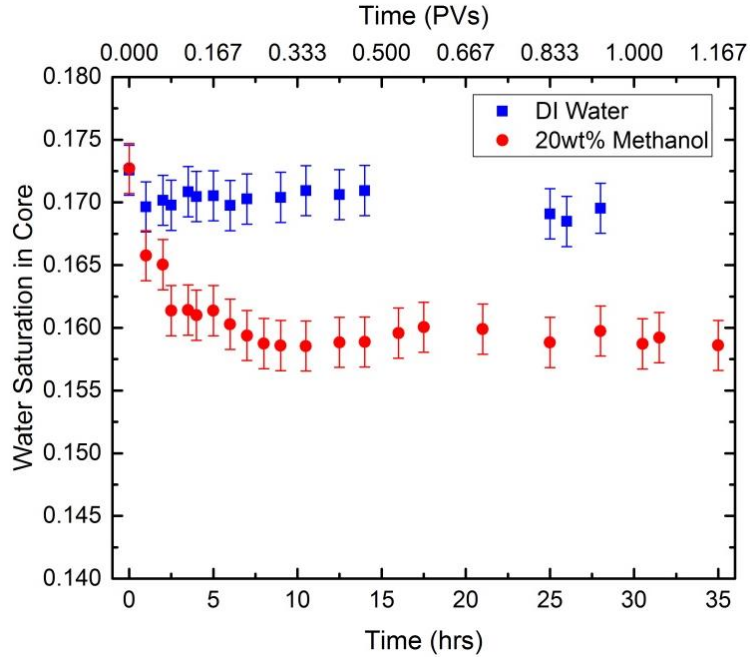


Figure 6.10: Comparison of changes of the overall water saturation inside the core between the methanol and baseline cases (Coreflood #2).

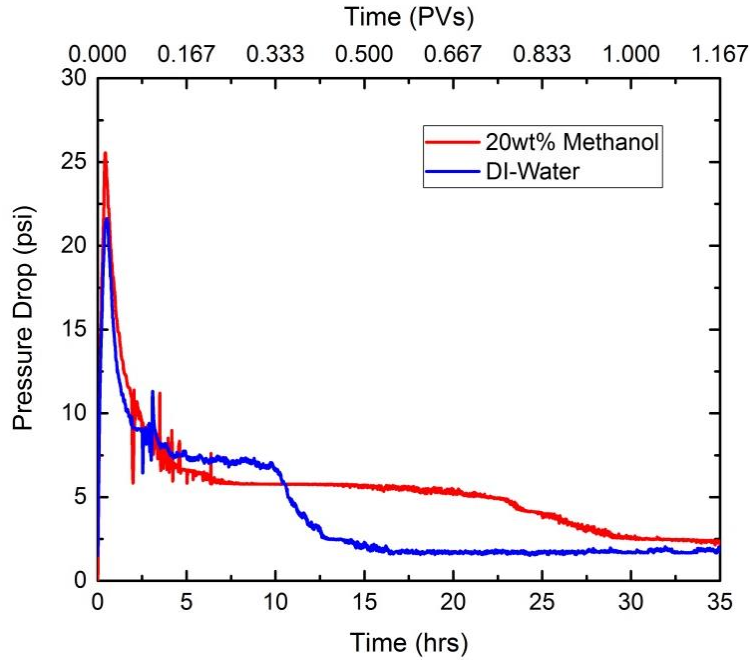


Figure 6.11: Comparison of changes of pressure drop across the core between the methanol and baseline cases (Coreflood #2).

#### 6.4.2.3 Flowback with surfactant

Figure 6.12 shows the changes of water saturation profile during water flowback for different surfactant solutions. Again, all three baselines are shown here to improve our interpretation on surfactant performance.

In all surfactant cases, the imbibition region ( $>75\text{mm}$ ) was observed as in the baseline, in addition to *the adjacent region* (0-50mm) and *the intermediate region* (50-75mm). It can be noticed that the changes with time in the imbibition region were very similar to the case where no surfactant was added – the water was seen to invade further into the core at a similar rate (i.e. compare Figure 6.7 with Figure 6.12). This suggests that the IFT was high there even in the surfactant case, suggesting that the surfactant concentration in the imbibition region was low.



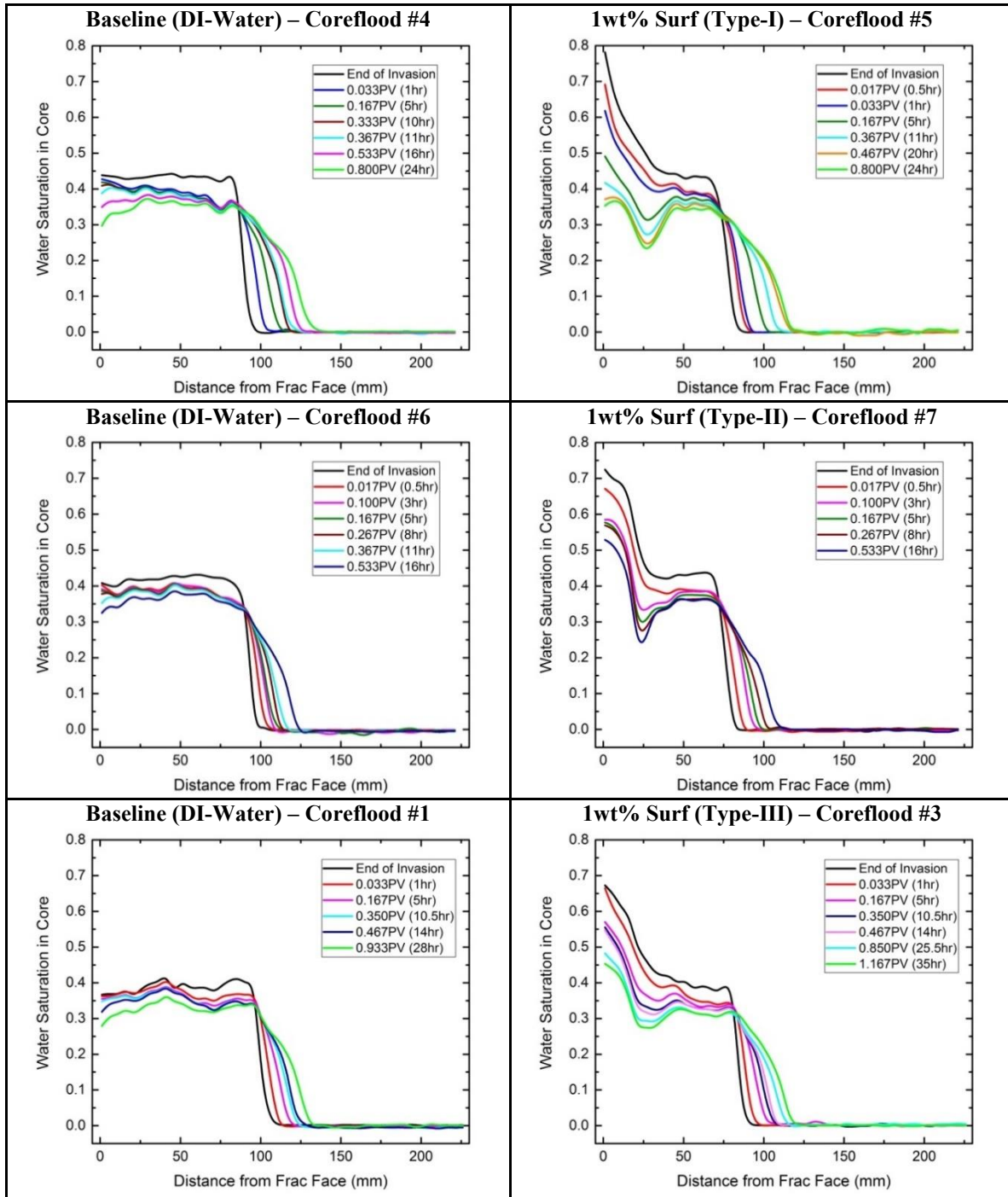


Figure 6.12: Comparison of changes of water saturation profile during flowback and hydrocarbon production among various surfactant cases (Left column: baselines; right column (from top to bottom): conditions that form Winsor type-I, type-II or type-III microemulsions).

From the comparison in Figure 6.12, it can also be noticed that the changes of water saturation profiles in all three surfactant cases behave similarly within the intermediate region and the imbibition region; however, they behave distinctly within the adjacent region, where surfactant concentration is likely high. Upon flowback, for Winsor type-I and type-II microemulsions, significant reductions in water saturation were observed within the adjacent region around 25mm; however, between these two cases, type-I microemulsion caused a faster reduction in water saturation close to the fracture face (0-25mm). For Winsor type-III microemulsion, the water saturation decreased uniformly in space within the adjacent region. Comparing to the other two types of microemulsions, the reduction of water saturation within the adjacent region (25-50mm) was smaller even though this case went through a much longer flooding time (i.e., 1.167PV (35hrs) in total).

Figure 6.13 compares the overall water saturation inside the core (left column) and the pressure drop across the core (right column) during water flowback for different surfactant solutions. For all three baselines, water was mainly recovered within the first hour, after which the overall water saturation in the core remained the same. However, when 1wt% surfactant was used, the overall water saturation continuously decreased for a longer period of time, resulting in a larger amount of flowback. Among all three surfactant cases, type-I microemulsion triggers the most flowback.

For the pressure drop, an early time plateau appeared till 0.333PV (10hrs) of pentane flooding when no additive was used. This early time plateau decreased to a second one after about 0.5PV (15hrs) of the flooding. For type-I microemulsion, no early time plateau was observed and the pressure drop levelled off at a value lower than the baseline. This indicates the enhancement of matrix permeability to hydrocarbon due to surfactant. For type-II microemulsion, no early time plateau was observed, but the pressure drop levelled off at a value higher than the second plateau in the baseline. This indicates a lower

relative mobility to pentane during the late time of hydrocarbon production. For type-III microemulsion, the pressure drop monotonically decreased to a plateau that was as same as the second plateau in the baseline. Since its pressure drop crosses over the baseline at around 0.4PV (12hrs), this type of additive gave an enhanced matrix permeability at only the early time of hydrocarbon production.

In summary, the surfactant additive forming type-I microemulsion gave permanent enhancement on hydrocarbon production after hydraulic fracturing fluid invasion; the ones forming type-III or type-II microemulsions gave temporary enhancement only during the early production. Between type-III and type-II microemulsions, the former one would produce a higher matrix permeability to hydrocarbon in longer time scales.

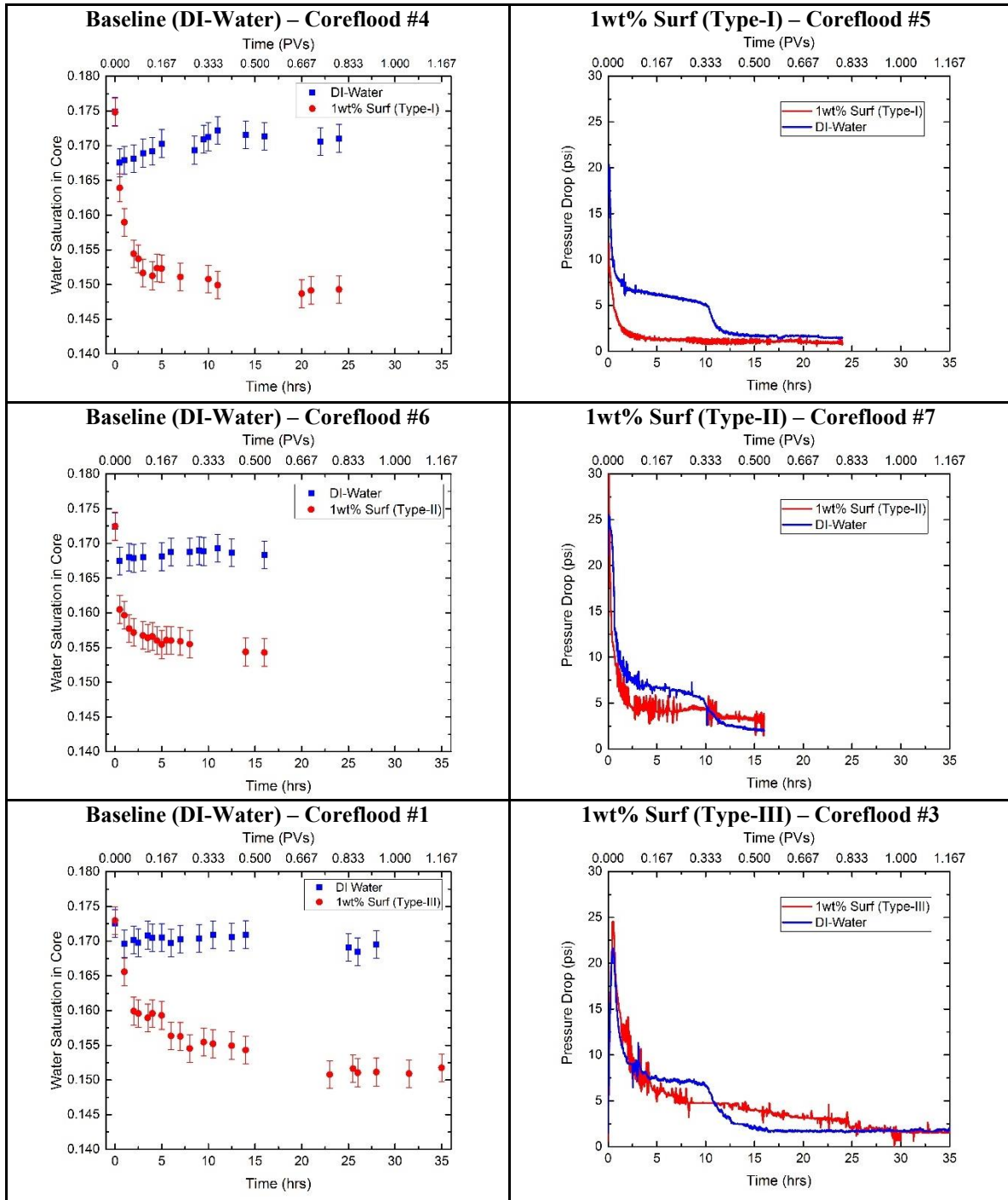


Figure 6.13: Comparison of changes of the overall water saturation within the core (left column) and the pressure drop across the core (right column) during flowback among various surfactant cases (From top to bottom: conditions that form Winsor type-I, type-II or type-III microemulsions).

## 6.5 DISCUSSION

From the CT and pressure results, the main observations of this study are summarized as follows.

1. Water invasion was a piston-like displacement while flowback was not.
2. During invasion, 20wt% methanol did not cause any noticeable change in water saturation comparing to the baseline.
3. During invasion, all three types of surfactant solutions gave rise to higher water saturation in the adjacent region; however, at the intermediate region the water saturation showed the same value and structure as the baseline even though the water did not propagate as far into the matrix.
4. During flowback, matrix permeability improved significantly after an early time plateau in the baseline and 20wt% methanol cases; while this early time plateau was longer for the methanol case. No plateau was observed for the surfactant cases; the improvement of permeability was immediate.
5. During flowback, CT scans showed the end of the early time plateau was correlated with the clean-up of water at the fracture face.
6. During flowback, CT scans showed that water imbibed further into the core even though the main flow was the other direction. This imbibition was equal in the surfactant and baseline cases but less in the methanol case.
7. When surfactants were used, more flowback was observed during the production step. When Winsor type-I microemulsions was formed, water recovery rate appeared the fastest in the adjacent region among all three conditions.
8. In terms of matrix permeability enhancement, type-I microemulsion gave permanent enhancement from the beginning of hydrocarbon production, while

type-II or type-III microemulsions only enhanced the production at the early stage comparing to the baseline.

### **6.5.1 Fracturing fluid invasion**

Observations 1 and 2 show that both water and the 20wt% methanol solution produced almost identical shock invasion profiles. In the water invaded region, the saturation was constant in space. This is the expected profile for a mobility favorable displacement, not surprising for a viscosity ratio of 4.2 in a water-wet system. In addition, viscosity dominates as we did not see capillary smearing at the front (the flow rate was fast enough), nor any desaturation behind the front (but not too fast to cause desaturation). The water invasion front was sharper for 20wt% methanol because the capillary-driven imbibition was reduced due to the reduction of oil-water IFT by methanol.

Observation 3 shows that water saturation at the invasion front for different surfactant solutions was the same as the baseline (Figure 6.14). Since the presence of surfactant would reduce the oil-water IFT so as to change the residual oil saturation, this observation may indicate the change of surfactant concentration from the adjacent region to the intermediate region. In particular, surfactant concentration could be reduced towards the invasion front, which can be caused by the adsorption of surfactant on rock surface and/or the formation of microemulsions that retarded the surfactant along the displacement front. Two water saturation shocks is standard behavior for a low-tension water flood as explained by fractional flow theory (Pope, 1980). According to this theory, the first shock is determined by the fractional flow curve of the pure water and oil, while the second one is determined by the fractional flow curve of the low tension water and oil, causing the retardation of the surfactant front.

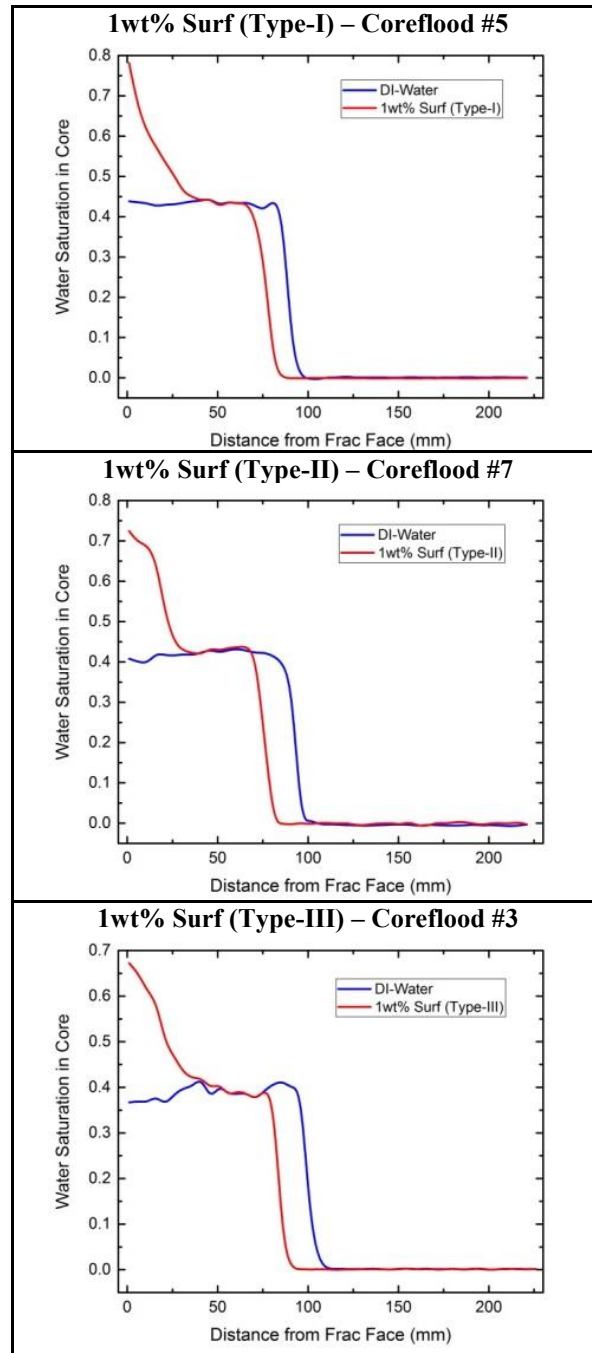


Figure 6.14: Comparison of water saturation profile at the end of fracturing fluid invasion among various surfactant cases (From left to right: conditions that form Winsor type-I, type-II or type-III microemulsions)

As also mentioned in observation 3, there was a big increase in the water saturation within the adjacent region. This is most likely caused by capillary desaturation with a low IFT being achieved in this portion of the core. Since only a small slug of fluid (0.173PV) was injected into the core during this step, only the second saturation shock was observed (Figure 6.14). A longer slug of injection is needed to observe the second plateau so as to determine the degree of capillary desaturation due to different surfactant solutions; however, this is beyond the scope of this study.

When surfactants were used as the additives, the pressure drops were not linear with time, but instead curved at around 0.073PV (33mins) (Figure 6.6). By comparing to the change of water saturation profile during the invasion (Figure 6.5), 0.073PV (33min) appeared to be the moment when water saturation started increasing from the short invasion front according to CT scans. In addition, the pressure data in Figure 6.6 is different for each different surfactant solution. This is likely related to the formation of different microemulsions as observed in the phase behavior tests (Figure 6.1). A potential explanation of how the different microemulsions are expressed in the pressure behavior is as follows.

For the type-I microemulsion, the pentane is emulsified in the water phase, thus the increase in water saturation within the adjacent region is connected water, and the pressure drop is smaller than the baseline case. For the type-II microemulsion, the water is emulsified in the pentane phase, thus the increase in water saturation within the adjacent region is disconnected water, which does not contribute to the flow, and the pressure drop is similar to the baseline case. For the type-III microemulsion, the pentane and water form a third phase, thus the increase in water saturation within the adjacent region consists of the third phase which is more viscous than the other two, making the pressure drop larger with time (Lu et al., 2014).



## **6.5.2 Flowback/hydrocarbon production**

### ***6.5.2.1 Permeability recovery without additives***

Observation 4 shows that the permeability reduction caused by the water invasion eventually cleaned up with time, even without using any additive. Observations 5 and 6 show the changes of water saturation profile that occurred during the flowback.

As shown in Figure 6.7, during the pentane flowback, the water saturation profile decreased slightly in the intermediate region while water invasion front migrated further into the uninvaded region of the core. Meanwhile, very little water was removed from the core. This is consistent with the previously proposed mechanism that capillary pressure gradient drives the water into the uninvaded region of the rock, instead of being recovered out of the core (Liang et al., 2015a, 2015b).

Importantly, the water saturation at the fracture face ( $< 10\text{mm}$ ) does not decrease like the rest of the invaded region. This can be seen in the close up in Figure 6.7. At the fracture face, it takes a relatively long time (10hrs in this study), before the water saturation here finally begins to decrease. At roughly the same time, the pressure drop across the core started to decrease from the early time plateau, indicating higher matrix permeability (Figure 6.8). This suggests that the change in water saturation at the fracture face causes the increased permeability to pentane. A simple reason for the time delay, or plateau, is that it just takes a finite amount of time for the capillary pressure gradient (which causes the imbibition) to reach the fracture face.

#### ***6.5.2.2 Permeability recovery with additives that moderately reduce IFT***

Observation 4 also shows the change of the pressure drop, thus the change of matrix permeability, when methanol was used. Observation 6 relates this change in permeability to the change of water saturation within the core occurring at the same time.

As mentioned above, if capillarity is responsible for the cleaning-up of trapped fluid near the fracture face through counter-current imbibition, then reducing oil-water IFT will extend the time required to clean up the trapped fluid. This was observed when 20wt% methanol was used, and this time was more than doubled as the baseline (23hrs in the methanol case vs. 10hrs in the baseline) (Figure 6.11). It is almost exactly the ratio of IFT change by adding methanol. This suggests that moderately reducing oil-water IFT prevents the capillary force from redistributing the water saturation profile effectively reducing the overall relative permeability to pentane during early time in the production.

#### ***6.5.2.3 Permeability recovery with additives that provide ultralow IFT***

As discussed above in the invasion section, two different invaded regions were formed when surfactant solutions were used. They were: a region with constant water saturation that was low in surfactant concentration (the intermediate region), and a region with increased water saturation further upstream where microemulsions were likely formed (the adjacent region). However, different surfactant additives performed differently during the flowback and hydrocarbon production.

Using an additive that forms a type-I microemulsion, there was a relatively rapid decrease in water saturation within the adjacent region. This indicates that the invaded water was easy to flow back under this condition. It might benefit from the structure of this type of microemulsions, which is oil-in-water. Oleic phase is emulsified to form the scattered droplets within the continuous aqueous phase; therefore, more water can be

displaced out of the rock when pentane flows through this region. Ultralow IFT may also cause lower residual water saturation as well as larger relative permeability, either one of which helps to accelerate the flowback process.

Using an additive that forms a type-II microemulsion, the water saturation profile changes in a similar way like the type-I condition, but it decreased much slower with time compared to the type-I condition. For this type of microemulsions, the aqueous phase is emulsified to form the scattered droplets within the continuous oleic phase; therefore, pentane might finger through this region much easier, bypassing more invaded water.

Using an additive that forms a type-III microemulsion, the water saturation profile decreased uniformly in space within the adjacent region. In this case, no sudden change in water saturation was observed around 25mm to 50mm from the fracture face as shown in type-I and type-II. In this type of microemulsions, a bicontinuous middle phase is formed between the oleic and aqueous phases. Since the viscosity of this middle phase is about 3.5 times larger than the pure water, displacement becomes less favorable which slows down the flowback of trapped fracturing fluid. However, on the bright side, water and hydrocarbon are miscible within type-III microemulsions, therefore the trapped water could still be brought out slowly by the flowing hydrocarbon phase.

In terms of the matrix permeability recovery attained from the pressure drop results, the lack of plateau in time suggests that the water block due to matrix-fracture interaction was cleaned up in all three surfactant cases. When 1wt% Surf (type-I) was applied, the enhancement of matrix permeability was observed from the beginning of hydrocarbon production till the end. By comparing with the CT results of water saturation profile, this enhancement was attributed to the fast clean-up of the invaded fracturing fluid, especially in the region close to the fracture face. When 1wt% Surf (type-III or type-II) was applied, although there was no plateau, the final pressure drop was higher than the type-I case. This

limited enhancement respect to type-I condition is likely to be due to the high water saturation near the fracture face which was cleaned very slowly with time during the production. As mentioned already, this is a result of unfavorable displacement in both cases, instead of water trapping due to matrix-fracture interaction.

In addition, another explanation on their difference on cleaning up the water block can be relevant to the fact that surfactant becomes more and more soluble in the oleic phase with the increase in salinity. From Winsor type-I to type-III and then to type-II, the salinity of surfactant solution increases; thus surfactant becomes more prone to stay with the oil. Consequently, the loss of surfactant from the trapped water into the flowing pentane can result in the decreased clean-up rate as observed in Figures 6.12 and 6.13.

### **6.5.3 Influence of oil-wet pores or small pores**

This experimental work has been performed in a water-wet porous media. There is evidence in shales and other tight formations that they are mixed-wet with some fraction of the pore space being oil-wet; this oil-wet portion is either pores that are in the organic matter, or inorganic pores that have come in long-time contact with polar compounds (Curtis et al., 2010; Milner et al., 2010; Loucks et al., 2010, 2012). In contrast to the water-wet pores, these oil-wet pores are unlikely to be invaded by water as capillary forces resist the movement of water in the oil-wet case. Since much of the results of this work are consistent with capillary forces either holding water and/or imbibing water, future experimental work will concentrate on the effect of wettability on permeability reduction caused by water block.

Likely, the key factor is the percentage of oil-wet pores, and how these pores are oriented to form a network. There are suggestions that there exists both a water-wet

network (through the inorganic parts of the matrix) and an oil-wet network, with various connections between the two (Section 2.2.3). If the water-wet network is a significant part of the flow network, then it can be expected that the above results still apply. But again, the effect of wettability will be determined in future experiments, most likely using similar arguments from the water-wet case for the physics of the permeability damage.

On a separate note, the very small pores in tight rocks may affect/inhibit the formation of microemulsions if considering their sizes typically range from 1-100nm (Hou et al., 1988; Morales et al., 2003; Goddeeris et al., 2006; Wang et al., 2008). This is an interesting phenomenon, however the aim of using surfactants in this study is to understand how lowering the oil-water IFT affects the permeability reduction via cleaning up the capillary trapped water. From this point of view, (1) surfactants do not need to go deep into the rock matrix to clean up the majority of permeability reduction; (2) as long as IFT is reduced between oil and water, microemulsions are not necessary to form within the matrix. If microemulsions form, type-I condition seems to be the best option to choose according to this study. All of these findings are distinct from the criteria of screening surfactants for Chemical-EOR. For oil-wet rocks, surfactants may also be helpful on mobilizing the invaded fracturing fluid into the matrix. However, they can be applied through two different approaches: altering rock wettability into water-wet or reducing the oil-water IFT. Nevertheless, these ideas are outside the scope of this study, but can be lines of future research.

## **6.6 CONCLUSIONS**

Our results show that using additives that provide moderate reductions on IFT seems to have negative impacts on mitigating water block. They reduce the capillary force,

which would slow down the imbibition process, thus extend the length of water block. For additives that provide the ultralow IFT, matrix-fracture interaction could be eliminated while the enhancement of matrix permeability is mainly determined by the recovery rate of the trapped fluid and/or the formed microemulsion phase. type-I condition gives the fastest recovery rate which results in the best enhancement on matrix permeability to hydrocarbon.

## **Chapter 7: Evaluation of Microemulsion-Forming Surfactant Additives on Mitigating Water Block through a Glass Microfluidic Model<sup>5</sup>**

This chapter provides an in-depth study on the effect of surfactants, which generate ultralow oil-water IFT, on mitigating water block through a 2.5D (i.e., pseudo-three-dimensional) glass microfluidic model. The phase changes of oil-water system during fracturing fluid invasion and flowback can be directly visualized and then compared with the coreflood results shown in Chapter 6.

### **7.1 INTRODUCTION**

In Chapter 6, the effect of microemulsion-forming surfactants on mitigating water block has been studied through coreflood experiments with CT scans. The regaining of rock permeability to hydrocarbon has been observed especially when ultralow IFT is achieved between the mimicked reservoir oil and the invaded fracturing fluid. However, the degree of this enhancement has been found to be a function of the generated microemulsion phase; different performance of mitigating water block and regaining rock permeability have been observed when different Winsor types of microemulsions are formed. The most prominent observation is: among three conditions when Winsor type-I, type-II and type-III microemulsions are formed respectively, invaded water recovery and rock permeability regaining show the best performance under the type-I condition, then the type-III condition, while the worst under the type-II condition.

---

<sup>5</sup> This chapter is based on the following paper:

**Liang, T.**, Xu, K., Lu, J., Nguyen, Q.P., DiCarlo, D.A. Evaluating the Performance of Surfactants on Enhancing Flowback and Permeability Regaining after Hydraulic Fracturing through a Microfluidic Model. In Preparation.

Two conjectures have been proposed to explain such different performance as follows.

The first conjecture is that surfactant becomes more and more soluble in oil with increase in salinity, i.e., type-II condition > type-III condition > type-I condition. After surfactant-aided fluid invades the rock, the surfactant under the type-II condition starts partitioning into the oil phase. When the flowback occurs, the surfactant can be carried out by the oil, resulting in water being trapped without surfactant. Instead, while under the type-I condition, the surfactant stays with the invaded water, continuously keeping a low IFT and helping to mobilize with the oil phase.

The second conjecture is that water is more dispersed within oil under the type-II condition where water-in-oil microemulsion is formed, thus it is likely to be bypassed by oil and then left behind; while water is more continuous under the type-I condition where oil-in-water microemulsion is formed, thus most of it can be displaced by oil during the flowback. Similarly, water is bi-continuous with oil under the type-III condition, thus a portion of it can be bypassed and then left behind.

Nevertheless, both conjecture assume that all types of microemulsion phases form between the bulk aqueous phase and the bulk oleic phase where the surfactant-aided fluid initially meets oil during the invasion. This was suggested based on observations of sandpack experiments (Lu et al., 2014). Moreover, both conjectures are proposed based on CT scans acquired during coreflood experiments (which only provides local water saturation, Figures 6.12) as well as the phase behavior results observed in the pipettes (Figure 6.1). More straightforward measurement or direct observation is required, which can provide the information regarding *in-situ* phase changes during mixing in porous media, so that both conjectures can be tested or verified.



In this study, an equivalent three-step “chipflood” sequence, as the three-step coreflood sequence introduced in Chapter 6 (Section 6.3.4), is conducted on a novel 2.5D glass microfluidic model. This ensures that the phase changes during the mimicked fracturing fluid invasion and the flowback can be directly observed and further compared when different types of microemulsion are forms in porous media.

## **7.2 MATERIALS AND METHODS**

### **7.2.1 Microfluidic model**

A novel 2.5D glass microfluidic model is fabricated by utilizing an isotropic HF etching (Ke Xu et al., Submitted); its sketch and microscopic characterization are shown in Figure 7.1. In this glass chip model, the dimension of pore throats is smaller than that of pore bodies, not only in two horizontal directions, but also in the vertical direction. Figure 7.2 shows a sketch of the cross-sectional view of pore-throat structure; this novel 2.5D fabrication technique provides 3D feature at the pore throats to a traditionally-fabricated 2D microfluidic model. The pore-throat geometry matches the requirement of capturing the important feature of “capillary snap-off” in regular rocks (Roof, 1970; Conn et al., 2014; Ke Xu et al., Submitted). The detailed geometric dimensions of this microfluidic model are listed in Table 7.1.

As also shown in Figure 7.1, there are three ports (i.e., either as an inlet or outlet) connecting to this microfluidic model. In this study, oil was always injected from port A towards port B, with port C sealed; while water (either DI water or surfactant solution) was always injected from port A towards port C, with port B sealed. More details about the experimental schemes are shown in Section 7.2.4.

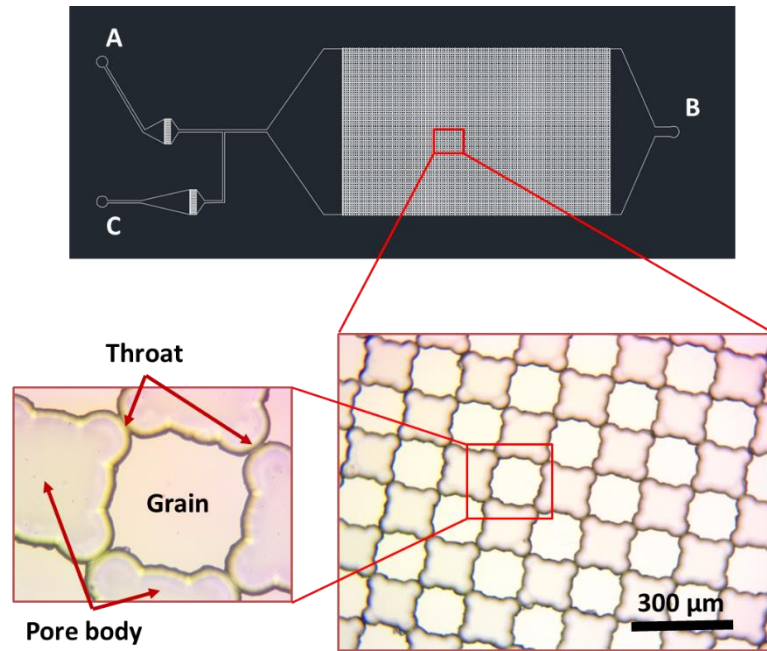


Figure 7.1: Sketch and microscopic characterization of 2.5D glass microfluidic model (Ke Xu et al., Submitted).

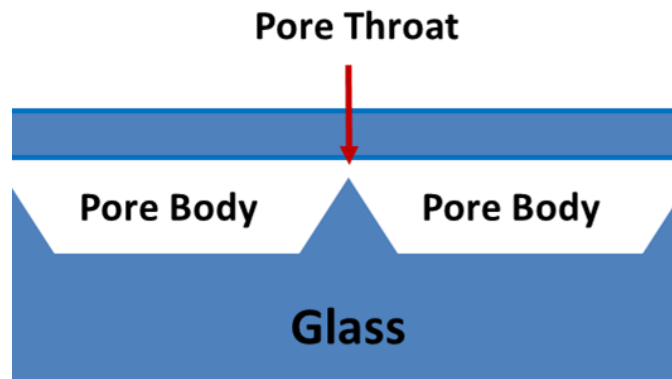


Figure 7.2: Sketch of cross-sectional view of 2.5D pore-throat structure (Ke Xu et al., Submitted).

<b>Geometric Dimensions of Microfluidic Model</b>			
Pore Diameter	200 $\mu$ m	Matrix Length	2.4cm
Pore Depth	20.3 $\mu$ m	Matrix Width	1.5cm
Throat Width	23 $\mu$ m	Pore Volume	7 $\mu$ L
Throat Depth	3.2 $\mu$ m	Matrix Wettability	Water-Wet

Table 7.1: Geometric dimensions of 2.5D glass microfluidic model (Ke Xu et al., Submitted).

### 7.2.2 Choice of hydrocarbon

In this study, n-pentane and n-hexane were chosen to mimic the light oil typically produced from the productive shale or other tight oil reservoirs. The boiling point of n-pentane is 36.1°C at atmosphere pressure, while that of n-hexane is 68°C. Therefore, special cooling treatments are required to prevent the evaporation of n-pentane when it is tested in the microfluidic chip, while n-hexane does not need. In this study, these cooling treatments included pre-cooling the chip before experiment, continuously applying ethanol to the top surface of the chip, and turning off the illumination system of microscope when photo/film shooting was finished. It has been experimentally tested that n-pentane can stay in the microfluidic chip without evaporation for at least 4 hours when these treatments are conducted; while n-hexane can stay without evaporation for at least 12 hours when no cooling treatment is required.

### 7.2.3 Surfactant-aided fracturing fluid

The identical surfactant formulation as introduced in Chapter 6 was applied in this study; it is a mixture of an internal olefin sulfonate (IOS), an alcohol propoxy sulfate (APS)

and isobutyl alcohol (IBA), with the total concentration of 1wt% in DI water (i.e., 1wt% Surf). NaCl was used to tune the salinity of surfactant solution so that different Winsor type microemulsion can be formed. Through pipette phase behavior tests, it was found that 1wt% Surf with a salinity of 50000ppm generated Winsor type-I microemulsion with n-hexane, 1wt% Surf with a salinity of 60000ppm generated Winsor type-III microemulsion with n-hexane, while 1wt% Surf with a salinity of 57500ppm generated Winsor type-II microemulsion with n-pentane. Since the salinity for this surfactant formulation to generate Winsor type-II microemulsion with n-hexane is beyond the salinity limitation ensuring the aqueous stability without precipitation, n-pentane was used as the hydrocarbon to test the type-II condition. Figure 7.3 shows the results of pipette phase behavior tests.

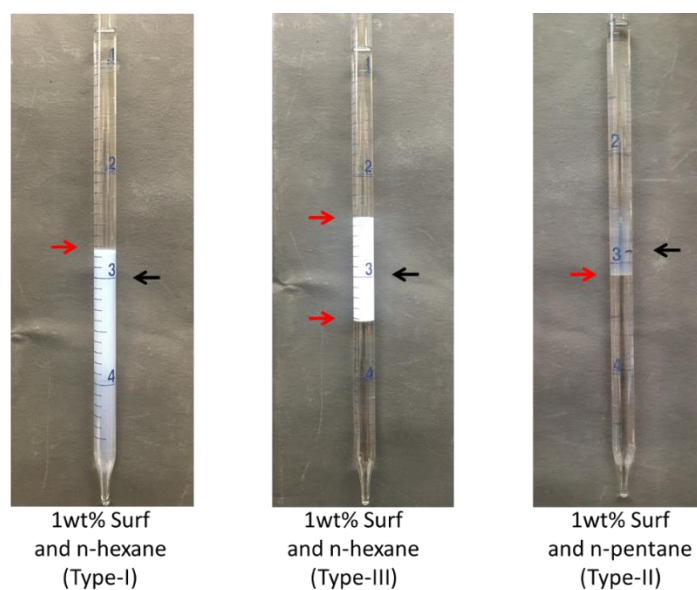


Figure 7.3: Results of phase behavior tests between various surfactant solutions and n-pentane or n-hexane at room temperature. 2mL hydrocarbon and 2mL surfactant solution were added in each pipette, gently shaken several times, and then allowed to equilibrate at 25°C. Black arrow points to the interfaces before mixing and red arrows points to the interfaces after mixing. All surfactant solutions passed the aqueous stability tests without any precipitation at their assigned salinities.

### 7.2.4 Flood schemes

An equivalent three-step “chipflood” sequence, as the three-step coreflood sequence introduced in Chapter 6 (Section 6.3.4), is conducted on the glass microfluidic chip to mimic the invasion of fracturing fluid as well as its recovery along with hydrocarbon production. The whole experimental process, including the formation and clean-up of microemulsions when surfactants were used, was directly recorded by a microscope that was equipped with a digital camera (Figure 7.4).

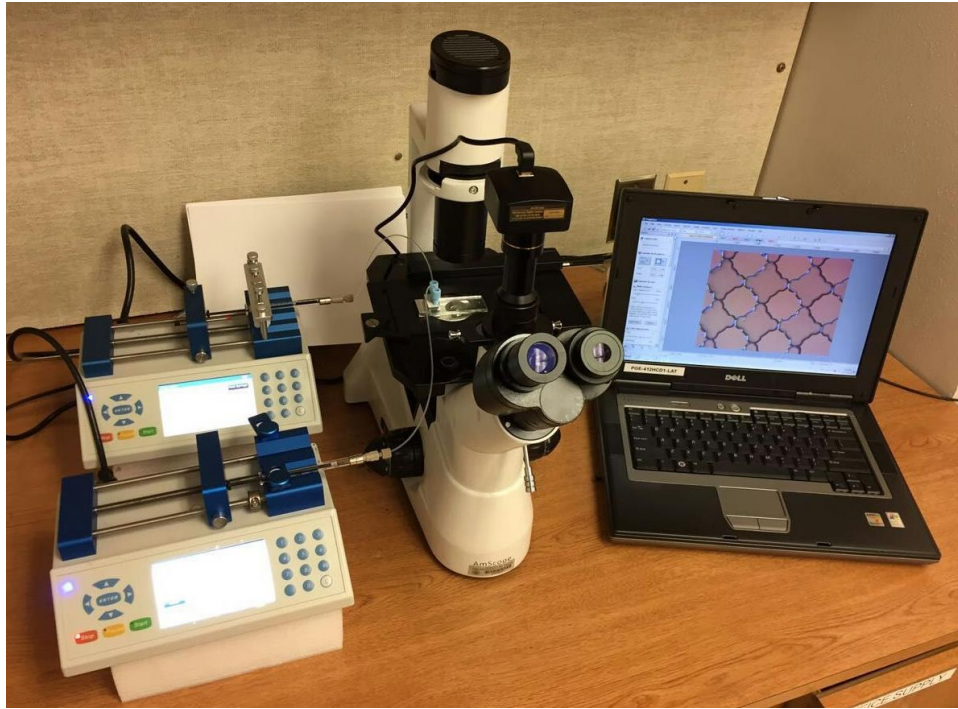


Figure 7.4: Experimental platform for observing the phase change during surfactant-aided water invasion and flowback in a 2.5D glass microfluidic model. Two Fusion 400 syringe pumps are used to inject oil and water separately into this model; the microscope is equipped with a digital camera that all images and videos are directly recorded by a computer.

Before each experiment, the glass chip was rinsed with DI water, then ethanol, and at last the hydrocarbon that would be tested (i.e., n-hexane or n-pentane). Once this was

done, the chip was dried at 100-120°C. Afterwards, hydrocarbon and the mimicked fracturing fluid were injected into the glass chip from the opposite ports during different steps of this “chipflood” sequence, which are described as follows.

***Step-1: Reservoir saturated with hydrocarbon.*** After the glass chip cooled down, hydrocarbon (either n-hexane or n-pentane) was injected from port A (see Figure 7.1). At the beginning, both port B and port C were open for purging; once the glass chip and all tubings were fully saturated with hydrocarbon, port A was closed and port B was connected to a water injection pump.

***Step-2: Fracturing fluid invasion.*** The mimicked fracturing fluid (either pure DI water or surfactant solution, both dyed into blue) was injected into the glass chip from port B towards port C; this step was stopped after the fluid swept two-third of the matrix (i.e., invasion depth was kept constant for DI water and surfactant solution, not the invasion volume). The injection rate was 30 $\mu$ L/hr during this step, which was about four times that of Step-3 (see below); this matched with the procedure followed in Chapter 6 (Section 6.3.4). Again, this step simulates the loss of fracturing fluid into the matrix as well as its interaction with the hydrocarbon before flowback and production starts.

***Step-3: Fracturing fluid flowback during hydrocarbon production.*** Once the invasion process was done, port B was switched to an outlet and port C was sealed. Hydrocarbon (either n-hexane or n-pentane) was flooded through the glass chip from port A at a constant flow rate of 7 $\mu$ L/hr, which was around 1.9ft/day. This flow rate was about one order of magnitude higher than the corefloods shown in Chapter 6 (Section 6.3.4) due to the limitation of current experimental setup; however, capillary trapping was still captured after this change (see more details in Section 7.3). The injection was continued for at least 2.5PV for the microscopic observation. Again, this step simulates the

hydrocarbon production from the deeper region of the formation rock towards the open fracture.

### **7.3 RESULTS AND DISCUSSION**

Before testing the surfactant additives, a three-step “chipflood” experiment with dyed DI water as the mimicked fracturing fluid was conducted to establish a baseline for later comparison. Its results obtained from Step-2 and Step-3 are shown in Sections 7.3.1.1 and 7.3.2.1 as follows.

#### **7.3.1 Simulation of fracturing fluid invasion (Step-2)**

As introduced in Section 7.2.4, Step-2 simulates the invasion of fracturing fluid into rock matrix during hydraulic fracturing. In this step, the mimicked fracturing fluid (either DI water or surfactant solution, both dyed into blue) was injected at a constant flow rate into the hydrocarbon saturated microfluidic model from the right-hand side to the left-hand side.

##### ***7.3.1.1 Water invasion without surfactant***

This section shows results from the baseline measurement, in which DI water invaded the hexane saturated microfluid model. Figure 7.5 (left column) shows the change of local phase saturations within 20 seconds (i.e., 0.024PV) during this step. It can be observed that water (blue fluid) migrates along the wall/edges of pore bodies and pore throats, resulting in lots of bypassed oil (white fluid) in the centers of pore bodies. Although the local invasion profile is irregular, the overall water front is almost flat from a macroscopic view; this agrees with the viscosity ratio (mobility ratio) that generates a favorable displacement.

Since this microfluidic model is water-wet, spontaneous imbibition can happen, which drives water to migrate along the wall/edges of this porous media, and create a similar invasion profile. To test the impact of this driving force, the pump was turned off after the designed volume of water invaded the matrix, while the water source was still connected with the injection port; this allowed the spontaneous imbibition occur by itself within the porous media. Figure 7.5 (right column) shows the change of local phase saturations during this process also within 20 seconds. Although water migration through spontaneous imbibition was observed at the local water invasion fronts, its speed was much slower than that of the invasion in Step-2 (left column of Figure 7.5). Therefore, the imbibition profile observed in Step-2 was mainly driven by the viscous force, and it was not an artifact of spontaneous imbibition in water-wet porous media.

Moreover, it can also be observed from the spontaneous imbibition results (right column of Figure 7.5) that water saturation at the local water invasion fronts was slightly higher than that within the swept region. This was also likely due to the redistribution of the invaded water towards the originally uninvaded region through spontaneous imbibition.

Figure 7.6 shows the change of local water saturation across the lateral space of the glass microfluidic model at the end of invasion (Step-2): from the invasion front (top figure), to the middle range of the invasion body (center figure) and then to the invasion tail at the inlet of the porous media (bottom figure). Local water saturation was found higher within the invasion front and the invasion tail. Both can be attributed to the redistributed water from the neighboring regions through spontaneous imbibition, either from the following invasion body or from the open space in front of the matrix inlet.



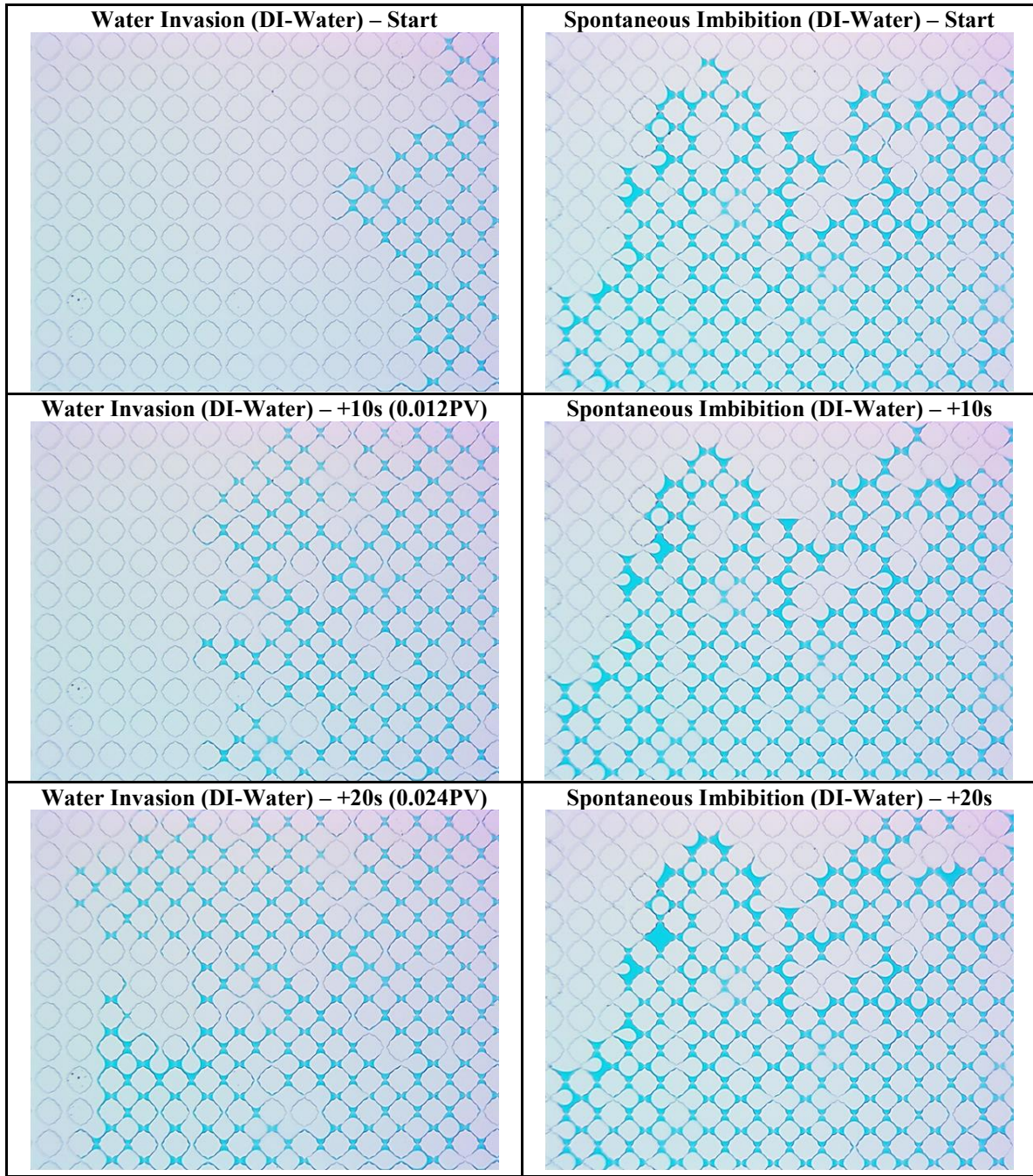


Figure 7.5: Changes of local phase saturations during water invasion (left column) or pump shut-in (right column) within 20 seconds. Closed transparent circles are solid grains of the microfluidic model, and the rest space is the porous media; dyed DI water is blue while n-hexane is white.

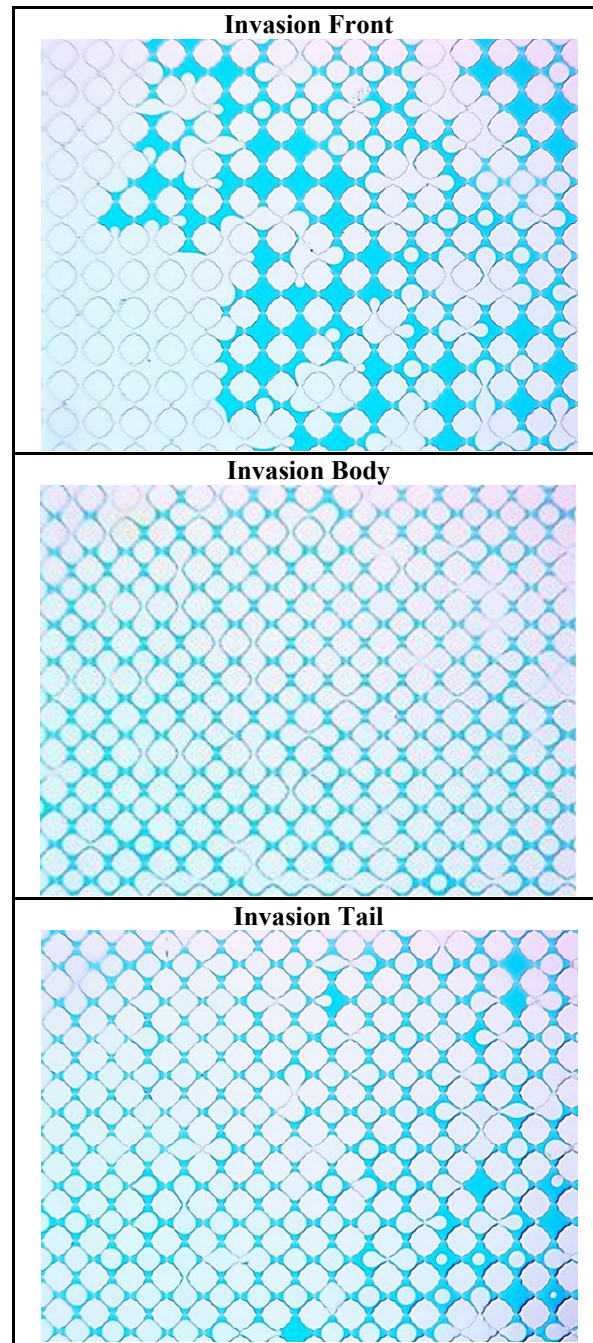


Figure 7.6: Local water saturation at the invasion front (top), within the middle range of the invasion body (center), or at the invasion tail near the inlet of the porous media (bottom) after DI water invaded the microfluidic model from the right-hand side.

### ***7.3.1.2 Water invasion with surfactant at Winsor type-I condition***

Figure 7.7 shows the change of local phase saturations when type-I surfactant solution invaded the hexane saturated microfluidic model; the invasion front migrated uniformly with time from the right-hand side to the left-hand side of this model. In detail, when this surfactant was applied in the aqueous phase, residual oil saturation was greatly reduced comparing to the baseline (Figure 7.5); meanwhile, lots of small oil droplets were observed to form within the invaded region.

Figure 7.8 shows the change of local water saturation across the lateral space of the glass microfluidic model at the end of invasion (Step-2): from the invasion front (top figure), to the middle range of the invasion body (center figure) and then to the invasion tail at the inlet of the porous media (bottom figure). Small oil droplets were found to form within the entire invaded region; however, edges of oil droplets near the invasion front were found to be fuzzier than those near the invasion tail. A close-up view of oil droplets within the near-invasion-front region is shown in Figure 7.9. Sub-micro sized oil droplets (i.e., diameter  $< 1\mu\text{m}$ ) can be observed accompanied with the blur interface between the oleic phase (in white) and the aqueous phase (in blue); both are likely the evidence showing the formation of microemulsions. This agrees with the expectation that microemulsion forms at the invasion front where the oleic phase and the aqueous phase initially mix with each other.



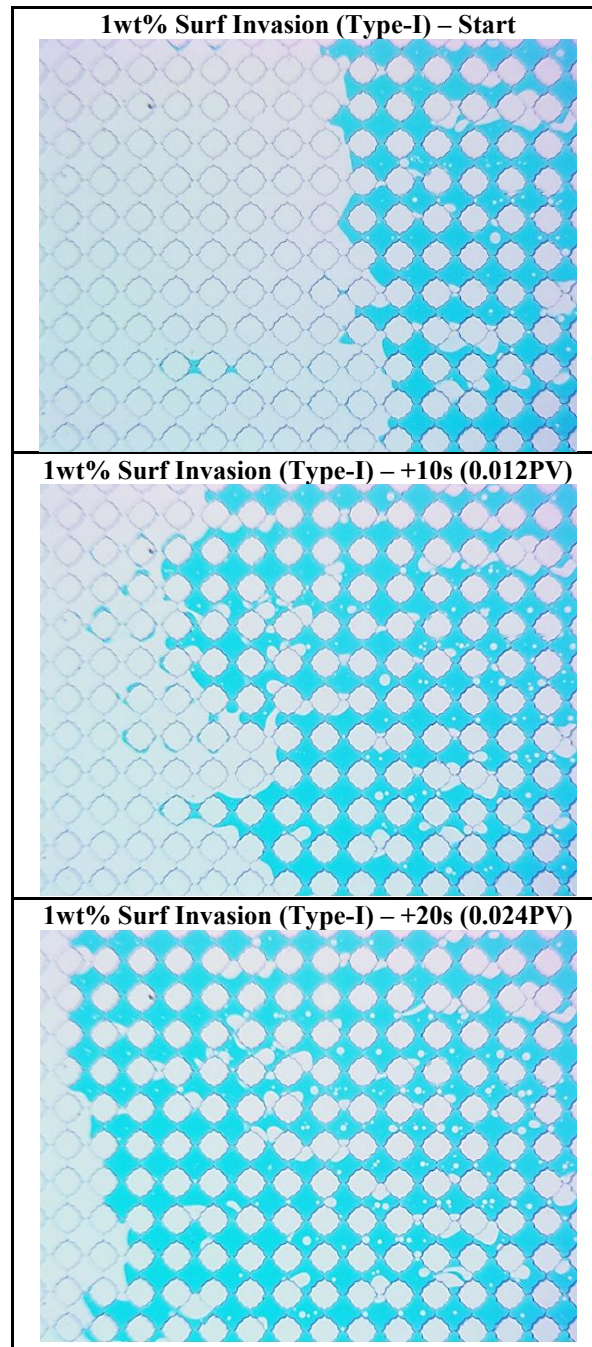


Figure 7.7: Changes of local phase saturations during type-I surfactant solution invasion within 20 seconds. Closed transparent circles are solid grains of the microfluidic model, and the rest space is the porous media; dyed DI water is blue while n-hexane is white.

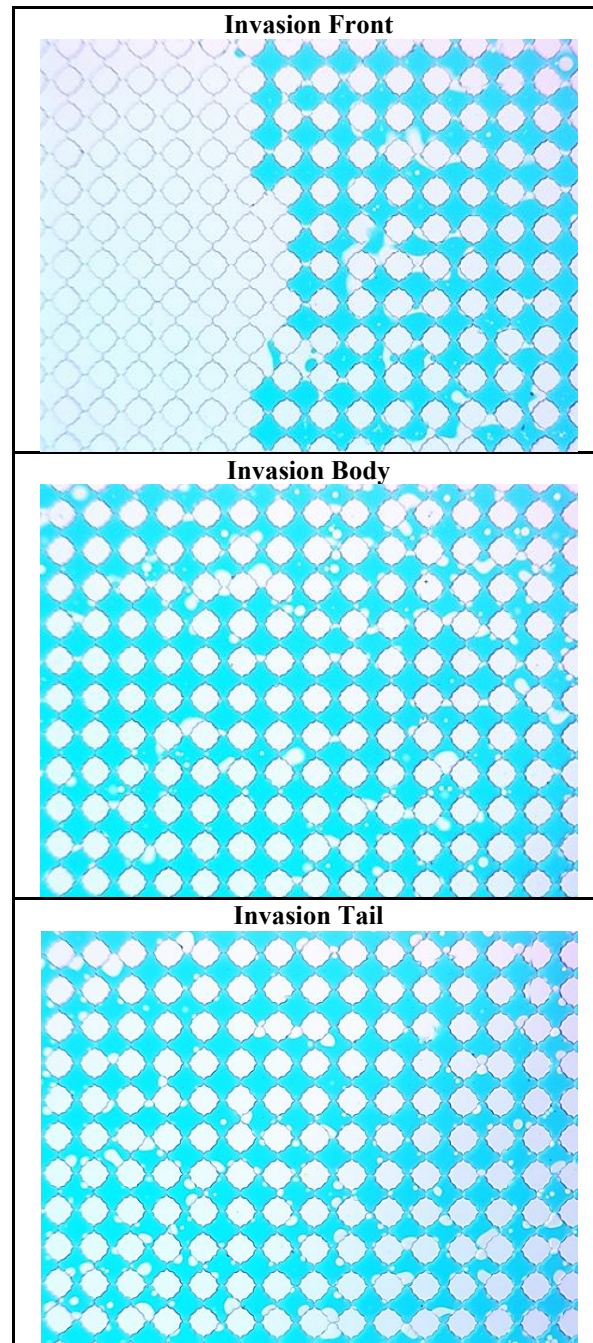


Figure 7.8: Local water saturation at the invasion front (top), within the middle range of the invasion body (center), or the invasion tail near the inlet of the porous media (bottom) after type-I surfactant solution invaded the microfluidic model from the right-hand side.

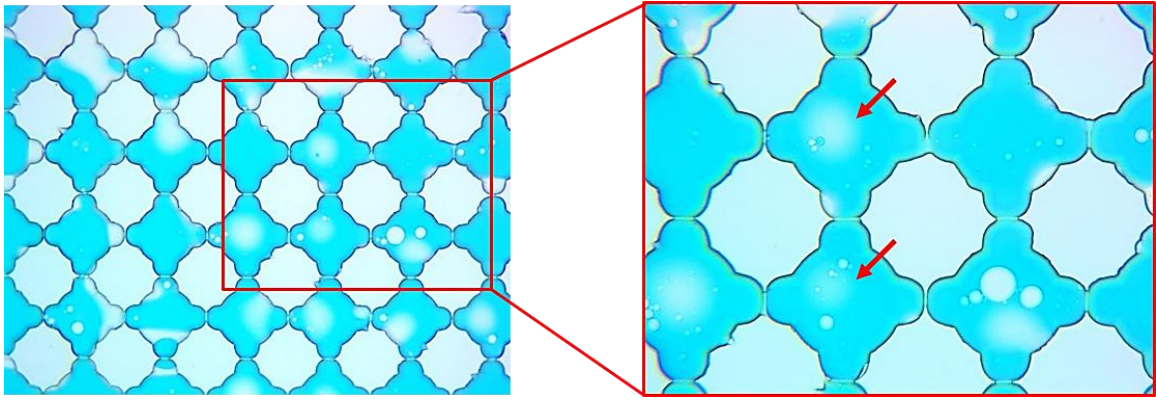


Figure 7.9: Close-up view of the near-invasion-front region after type-I surfactant solution invaded the microfluidic model. Red arrows point the fuzzy clusters that are likely the microemulsions.

### **7.3.1.3 Water invasion with surfactant at Winsor type-III condition**

Figure 7.10 shows the change of local phase saturations when type-III surfactant solution invaded the hexane saturated microfluidic model; the invasion front also migrated uniformly with time from the right-hand side to the left-hand side of this model. Similar to the type-I condition (Figure 7.7), reduced residual oil saturation and lots of small oil droplets were both observed within the invaded region in this surfactant condition.

Figure 7.11 shows the change of local water saturation across the lateral space of the glass microfluidic model at the end of invasion (Step-2): from the invasion front (top figure), to the middle range of the invasion body (center figure) and then to the invasion tail at the inlet of the porous media (bottom figure). Unlike the type-I condition (Figure 7.8), small oil droplets were found only within the first two-third of region behind the invasion front; in the rest region that was near the matrix inlet (i.e., the invasion tail), elongated blur mixed phase was observed. Figure 7.12 provides a close-up view of this mixed phase within such near-invasion-tail region. It can be clearly seen that the blur mixed phase (in light blue) was elongated with the flowing aqueous phase (in blue), forming like a belt. Accompanied with this mixed phase, sub-micro sized oil droplets (i.e., diameter < 1 $\mu$ m) were also observed within this region (Figure 7.12). These observations likely indicate that the type-III microemulsion form near the invasion tail where the mixing is sufficient; this is completely different from the expectation that microemulsion forms at the invasion front where the oleic phase and the aqueous phase initially mix with each other.

To explore this phenomenon more deeply, a repeat experiment was conducted to mainly focus on the phase change within the invasion tail. As pointed by red arrows in Figure 7.13, residual oil droplets were observed behind the solid grains of the microfluidic model (closed transparent circles) after around 0.3PV of surfactant solution flood (top left

figure). After the following 0.3PV of flood, these oil droplets were gradually sheared by the flowing surfactant solution and eventually disappeared; meanwhile, the belt-like mixed phase was formed. These observations indicate that the formation of type-III microemulsion is likely both time-dependent and shear-dependent; it does not form during the initial mixing between the surfactant solution and the hydrocarbon. In the end, the residual oil saturation, in form of either residual oil droplets or the mixed phase, was almost zero; this was expected for such an ultralow IFT condition.



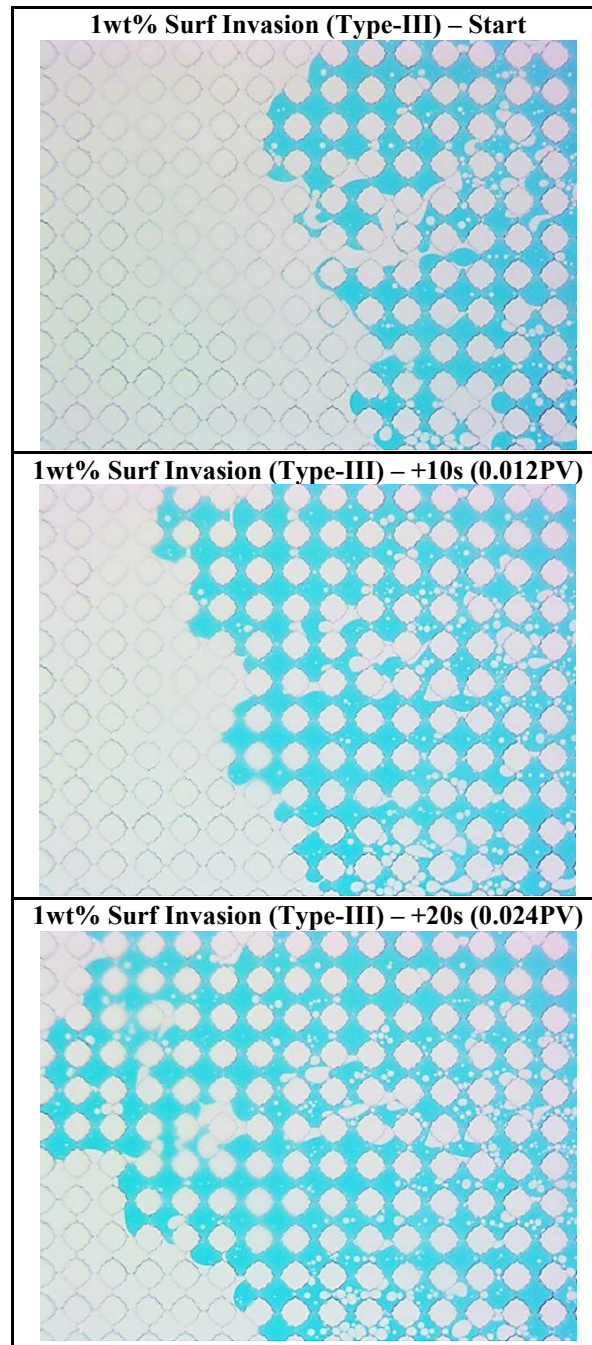


Figure 7.10: Changes of local phase saturations during type-III surfactant solution invasion within 20 seconds. Closed transparent circles are solid grains of the microfluidic model, and the rest space is the porous media; dyed DI water is blue while n-hexane is white.

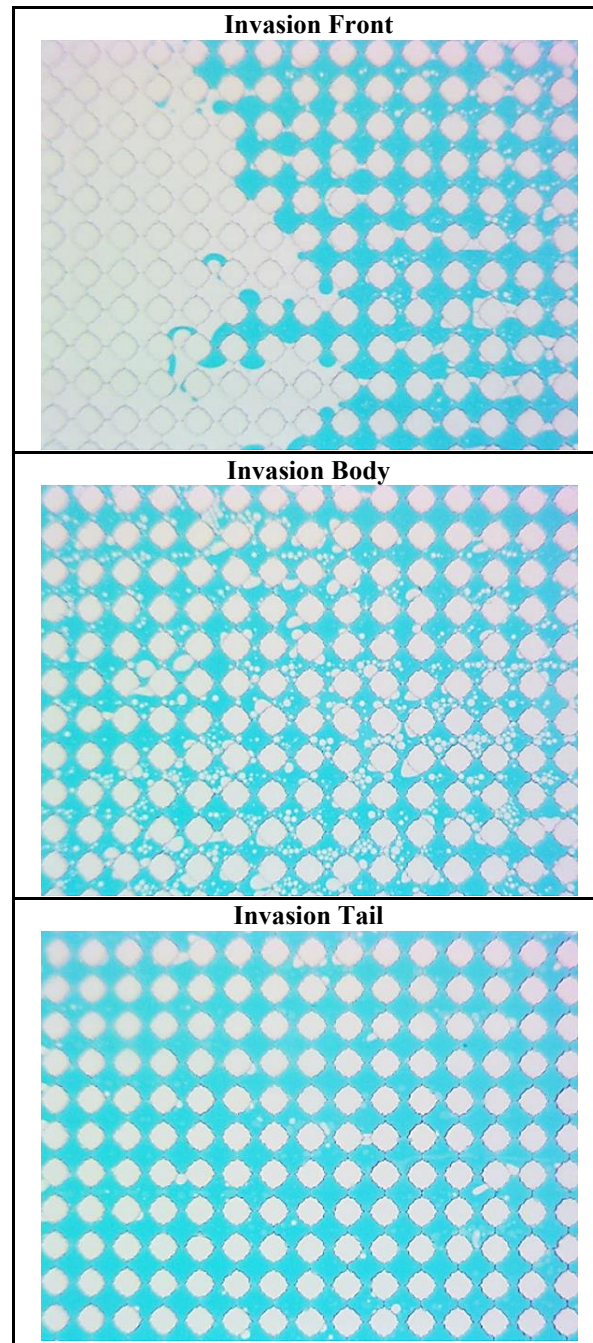


Figure 7.11: Local water saturation at the invasion front (top), within the middle range of the invasion body (center), or the invasion tail near the inlet of the porous media (bottom) after type-III surfactant solution invaded the microfluidic model from the right-hand side.

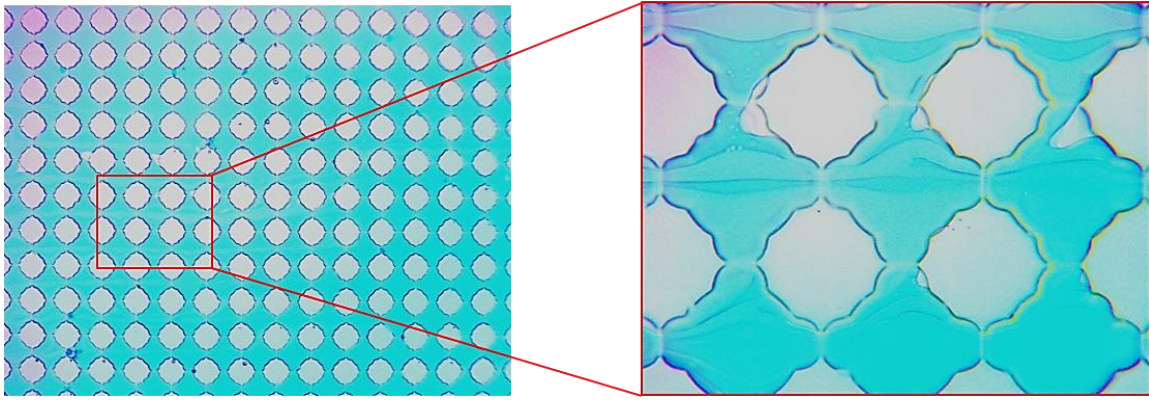


Figure 7.12: Close-up view of the near-invasion-tail region after type-III surfactant solution invaded the microfluidic model. Red arrows point the fuzzy clusters that are likely the microemulsions.



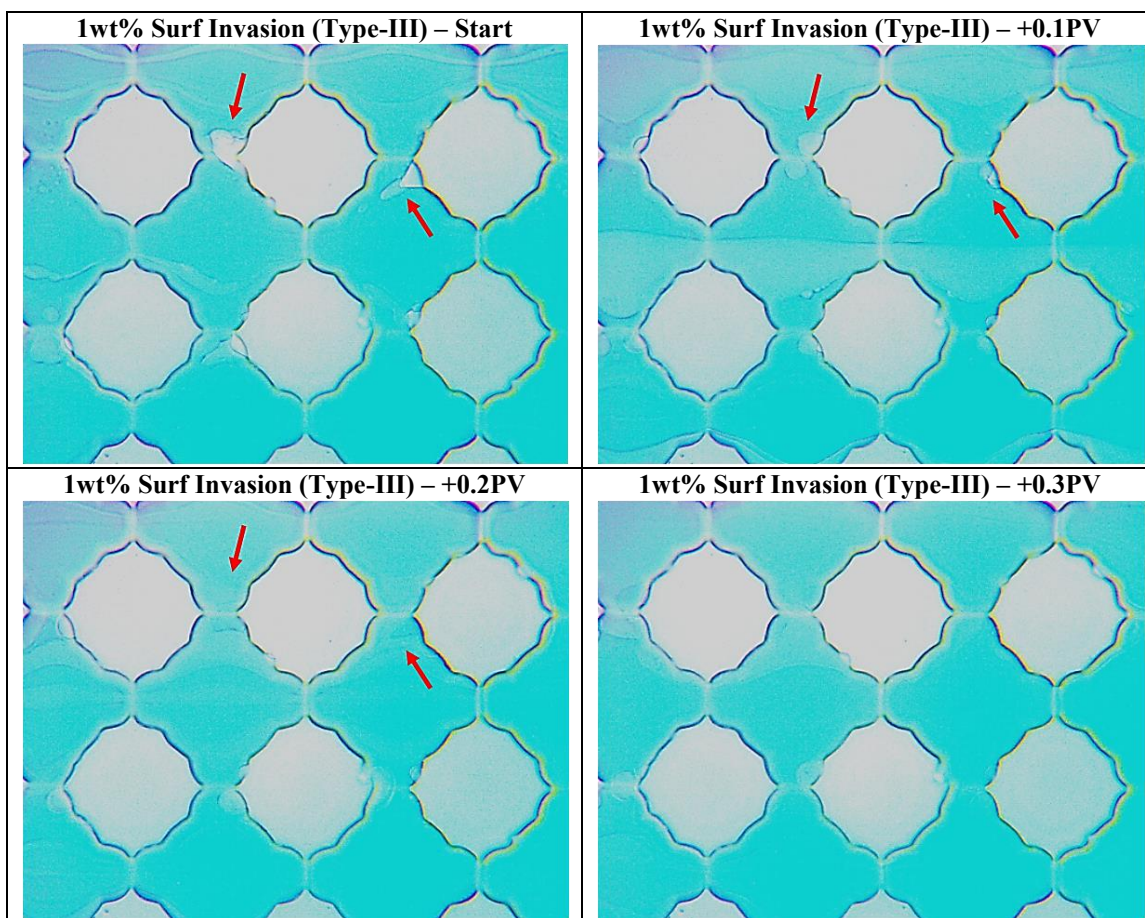


Figure 7.13: Close-up view of the formation of type-III microemulsions. Red arrows point the residual oil droplets that were gradually sheared to form the microemulsions and carried away by the surfactant solution.

#### ***7.3.1.4 Water invasion with surfactant at Winsor type-II condition***

Figure 7.14 shows the change of local phase saturations when type-II surfactant solution invaded the pentane saturated microfluidic model; the invasion front also migrated uniformly with time from the right-hand side to the left-hand side of this model. Unlike the type-I and type-III conditions (Figures 7.7 and 7.10), an extensive mixed phase (in light blue) immediately formed behind the invasion front. Figure 7.15 provides a close-up view of the formation of this new phase during the invasion. Right after the surfactant solution invaded the hydrocarbon-saturated pores, two fluids mixed with each other and formed a relatively homogeneous phase. Compared with the previous two surfactant conditions, this new phase is very likely the microemulsion phase. In this condition, small scattered oil droplets were not observed.

Figure 7.16 shows the change of local water saturation across the lateral space of the glass microfluidic model at the end of invasion (Step-2): from the invasion front (top figure), to the middle range of the invasion body (center figure) and then to the invasion tail at the inlet of the porous media (bottom figure). The microemulsion phase (in light blue) was found to extend from the invasion front to the invasion tail, spreading across the entire invaded region. Clear oil droplets, as ones in type-I and type-III conditions, were not observed within the invaded region; residual oil was only in form of the mixed microemulsion phase. With the decrease of the volume percentage of the mixed microemulsion phase from the invasion front to the invasion tail, the residual oil saturation also decreased. This trend agrees with the CT results of corefloods shown in Figure 6.5.

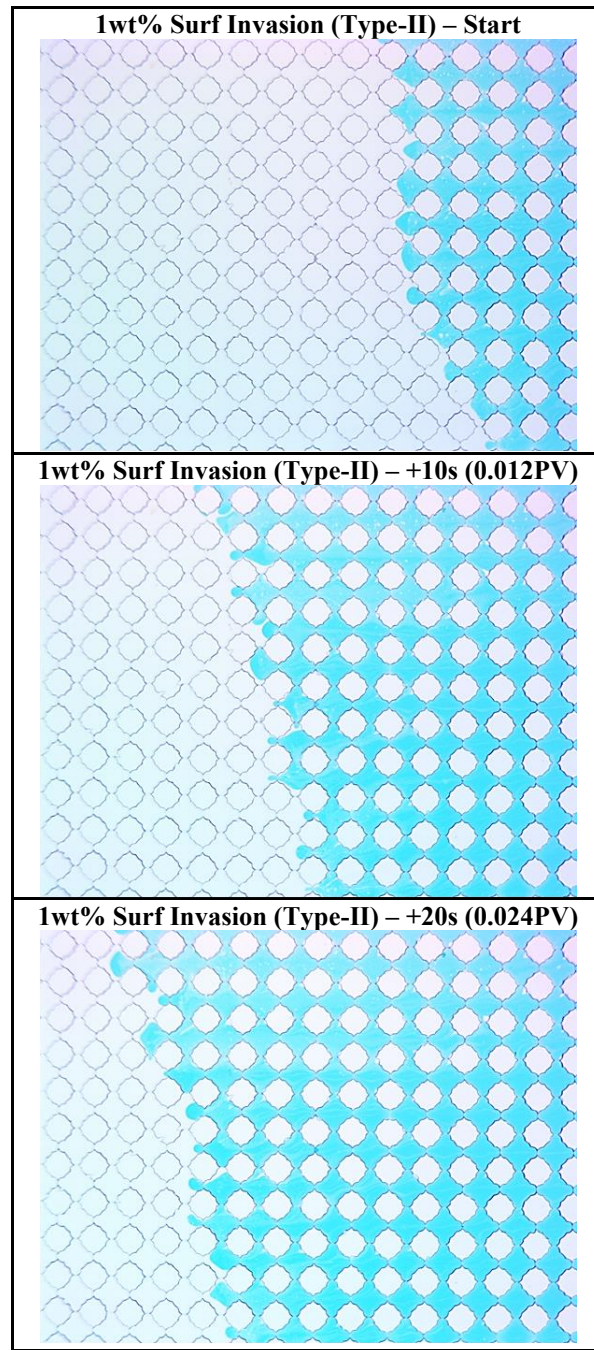


Figure 7.14: Changes of local phase saturations during type-II surfactant solution invasion within 20 seconds. Closed transparent circles are solid grains of the microfluidic model, and the rest space is the porous media; dyed DI water is blue while n-pentane is white.

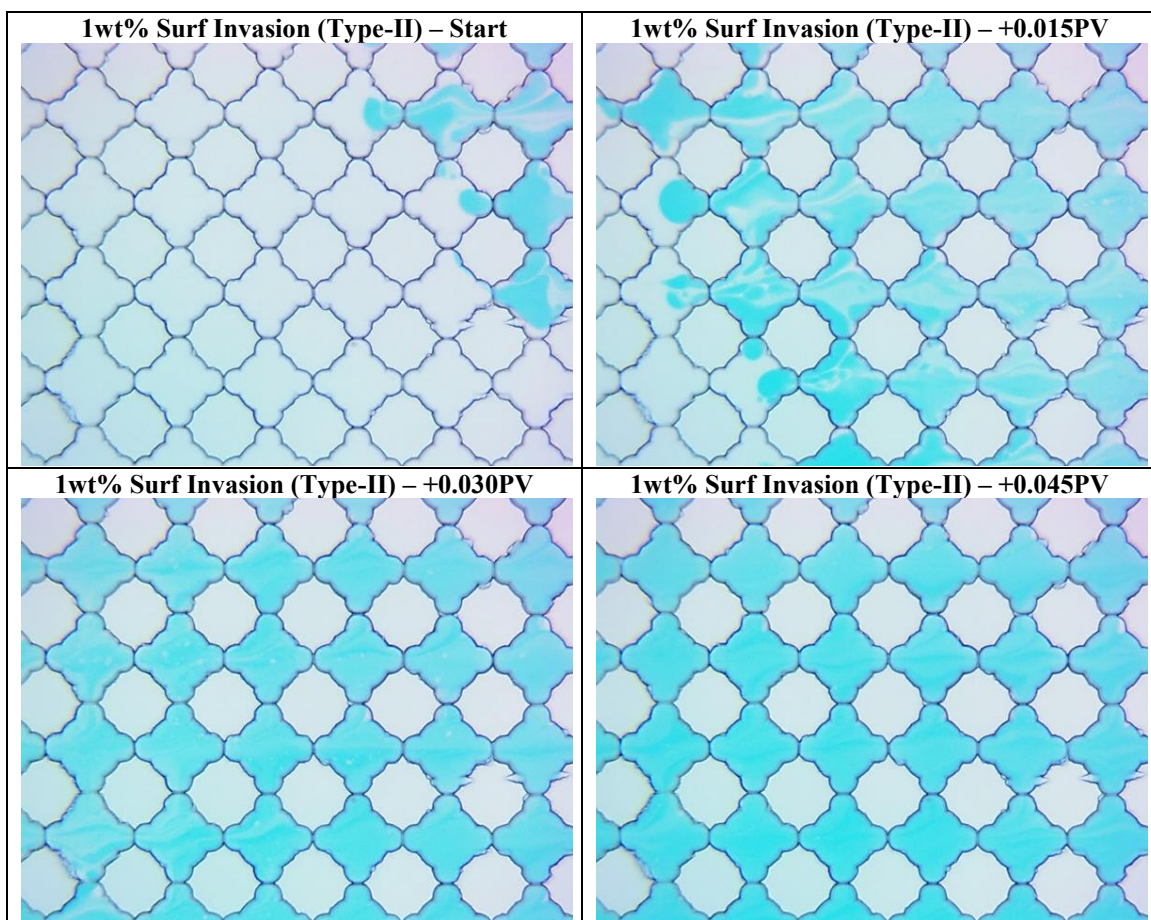


Figure 7.15: Close-up view of the formation of type-II microemulsions during the initial mixing at the invasion front. Dyed DI water is blue while n-pentane is white; the light blue fluid formed during the mixing is very likely the type-II microemulsion.



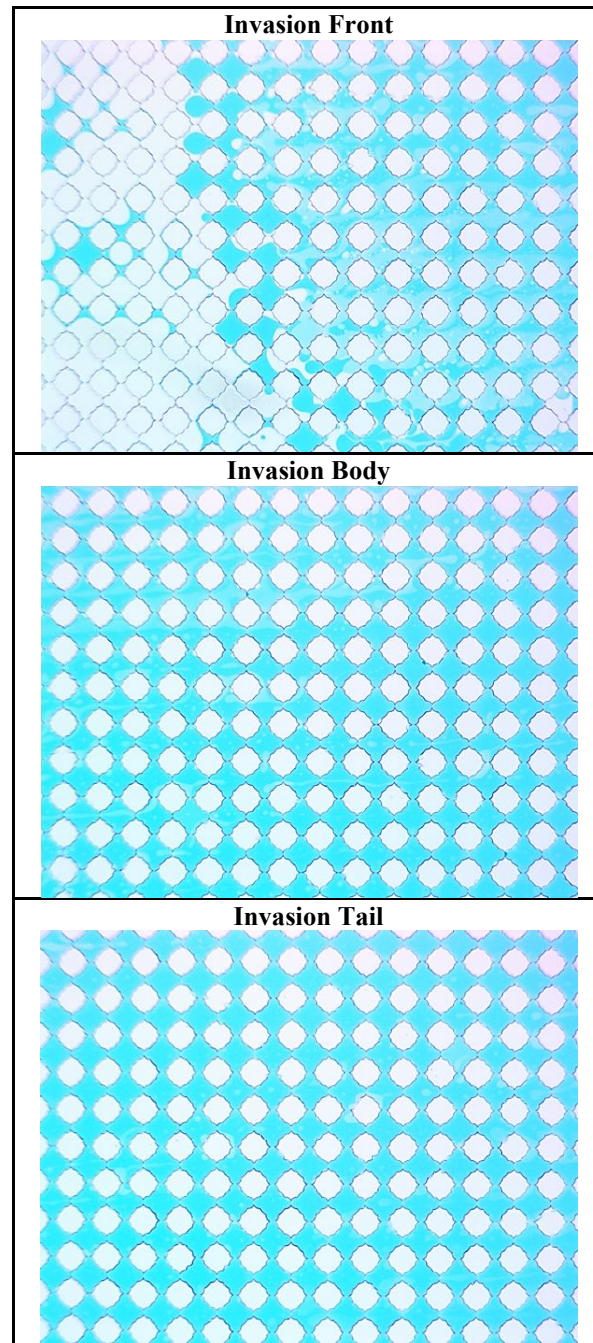


Figure 7.16: Local water saturation at the invasion front (top), within the middle range of the invasion body (center), or the invasion tail near the inlet of the porous media (bottom) after type-II surfactant solution invaded the microfluidic model from the right-hand side.



### 7.3.2 Simulation of fracturing fluid flowback (Step-3)

After water invasion (Step-2) was finished, hydrocarbon was injected at a constant flow rate into the microfluidic model from the left-hand side to the right-hand side; as introduced in Section 7.2.4, this Step-3 simulates the flowback and hydrocarbon production through water-invaded rock adjacent to the open fracture.

#### 7.3.2.1 Flowback without surfactant

This section shows the results from the baseline measurement, in which hexane flowed through the DI water invaded microfluid model. Figure 7.17 shows the changes of local phase saturations within 180 seconds (i.e., 0.05PV) during this step. It can be observed that hydrocarbon (white fluid) fingered through the invaded water (blue fluid) and resulted in a lump of water being bypassed in the end. This agrees with the expectation for the low viscosity fluid (hexane) displacing the high viscosity fluid (water).

Figure 7.18 shows the change of local water saturation across the lateral space of the entire invaded region after 0.5PV of hexane flood through the microfluidic model: from the original invasion front (top figure), to the middle range of the invasion body (center figure) and then to the invasion tail which was now the outlet of the porous media (bottom figure). Lumps of bypassed/trapped water can be observed almost everywhere; they were likely to remain trapped since hydrocarbon had broken through the water invaded region and created the preferred flow paths. Moreover, it can also be observed that an extra volume of water was trapped at the outlet of the porous media due to capillary end effect; hydrocarbon snapped off through this water layer and then into the following open space (bottom figure). This is also expected for such a water-wet system where capillary discontinuity at the outlet of the porous media prevents the wetting phase to leave. This can cause an extra permeability reduction to rock matrix, and it has been elaborated in the previous chapters.

It is worth mentioning that the flow rate applied in this “chipflood” experiment was one order of magnitude higher than the coreflood experiments conducted for Chapter 6 (1.9ft/day vs. 0.1ft/day, as detailed in Section 7.2.4). When hydrocarbon flow rate decreases and the viscous force is less supreme to the capillary force, the displacement efficiency would likely become worse that more invaded water can be trapped in the porous media during flowback and hydrocarbon production.

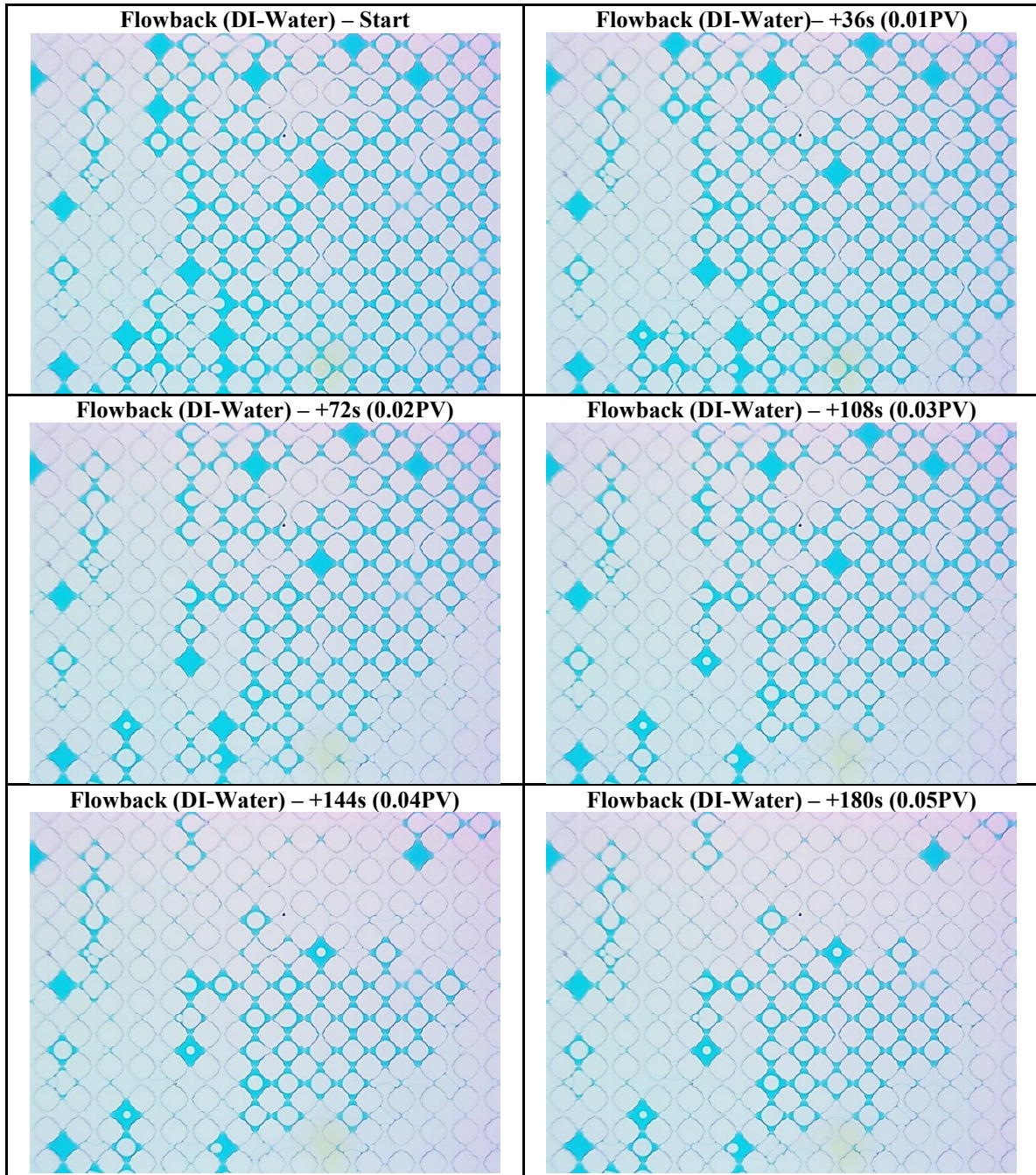


Figure 7.17: Changes of local phase saturations during flowback and hydrocarbon production from the DI water invaded microfluidic model for 180s (0.05PV). Closed transparent circles are solid grains of the microfluidic model, and the rest space is the porous media; dyed DI water is blue while n-hexane is white.

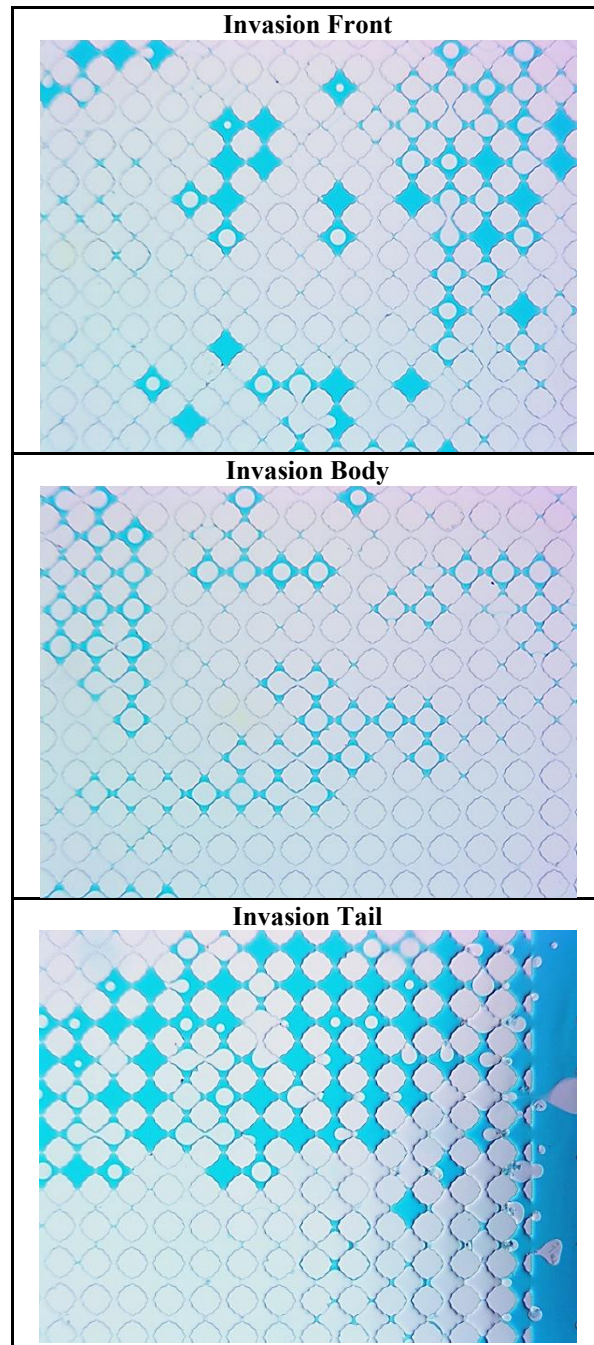


Figure 7.18: Changes of local water saturation at the invasion front (top), within the middle range of the invasion body (center), or at the invasion tail (bottom) after 0.5PV of hexane flood through the DI water invaded microfluidic model.

### ***7.3.2.2 Flowback with surfactant at Winsor type-I condition***

This section shows the results when hexane flowed through the microfluid model invaded by the type-I surfactant solution. Figure 7.19 shows the changes of local phase saturations within 360 seconds (i.e., 0.10PV) during this step. Unlike the baseline case, majority of the trapped water was mobilized by hydrocarbon; the form of water changed from small spherical droplets scattered in water to bigger bubbles wrapped in water. These bubbles kept growing with time when less water was left behind in form of the bubble films. In this case, viscous fingering was not observed and most bubbles were mobile before the breakthrough of hydrocarbon.

Figure 7.20 shows the change of local water saturation across the lateral space of the entire invaded region after 0.5PV of hexane flood through the microfluidic model: from the original invasion front (top figure), to the middle range of the invasion body (center figure) and then to the invasion tail which was now the outlet of the porous media (bottom figure). Residual water was observed in the region near the original invasion front, mainly attached to the wall/edges of pore bodies and pore throats (top figure). This was likely due to the retardation of surfactant during the invasion, resulting in trace surfactant concentration near the invasion front; the same phenomenon has been reported from CT measurements in Chapter 6. Moving towards the matrix outlet, oil bubbles were observed, and almost all residual water was in form of very thin films between oil bubbles. Although the sizes of these oil bubbles were bigger than the pore throat, they could easily squeeze through the matrix without phase separation (i.e., bubble burst) (bottom figure).

Some oil bubbles can be bypassed and trapped within the matrix; however, bubble bursts were observed from the near-invasion-front region towards the matrix outlet. Figure 7.21 shows the changes of trapped bubbles within 108 seconds (i.e., 0.03PV). It can be observed that bubbles started to burst from the contact where a lump of bubbles met with

the flow of hydrocarbon (pointed by red arrows in figures). Trapped bubbles could block the flow of hydrocarbon, meanwhile, they were likely to experience the force from hydrocarbon that could cause their bursts. These bursts were unlikely due to the solubilization/loss of surfactants into hydrocarbon, and this can be found out by comparing with the case under the type-III condition (Figure 7.24). This will be elaborated in the following section (Section 7.3.2.3). Moreover, along with the bursts of bubbles, aqueous phase and oleic phase were separated, resulting in the formation of small water droplets; some of them stayed in pore bodies while the others were mobilized by hydrocarbon.

Figure 7.22 shows the change of local water saturation across the lateral space of the entire invaded region after 3.5PV of hexane flood through the microfluidic model. Residual water was still observed in the region near the original invasion front, mainly attached to the wall/edges of pore bodies and pore throats (Figure 7.22(a)). Due to the lack of surfactant in this region (a), the trapped water could not be mobilized by hydrocarbon, like the case in the baseline. Behind this region (Figures 7.22(b-f)), distinct phase change can be noticed that almost all oil bubbles disappeared at this moment; they might burst or be displaced by hydrocarbon. Scattered tiny water droplets were observed in the center of pore bodies within regions (b-f); as seen in Figure 7.21, they were originated from the separated aqueous phase from burst bubbles. Among these regions, residual water saturation in region (b) was found the lowest, which might indicate these separated water droplets could still be mobilized by hydrocarbon over time (Figure 7.22(b)). This observation agrees with the CT results from Coreflood #5 shown in Chapter 6: water saturation profile decreased and then increased from the invasion front to the rock outlet, and it decreased relatively fast with time (Figure 6.12). Moreover, water trapping due to capillary end effect was not observed near the outlet of this microfluidic model (Figure



7.22(f)). This is expected for a reduction in IFT that eliminate the capillary discontinuity across the matrix outlet.

In general, surfactant additive at the type-I condition can effectively clean up the water block caused by invaded fracturing fluid. This microfluidic model test complements and further supports the new physics proposed in Chapter 6.

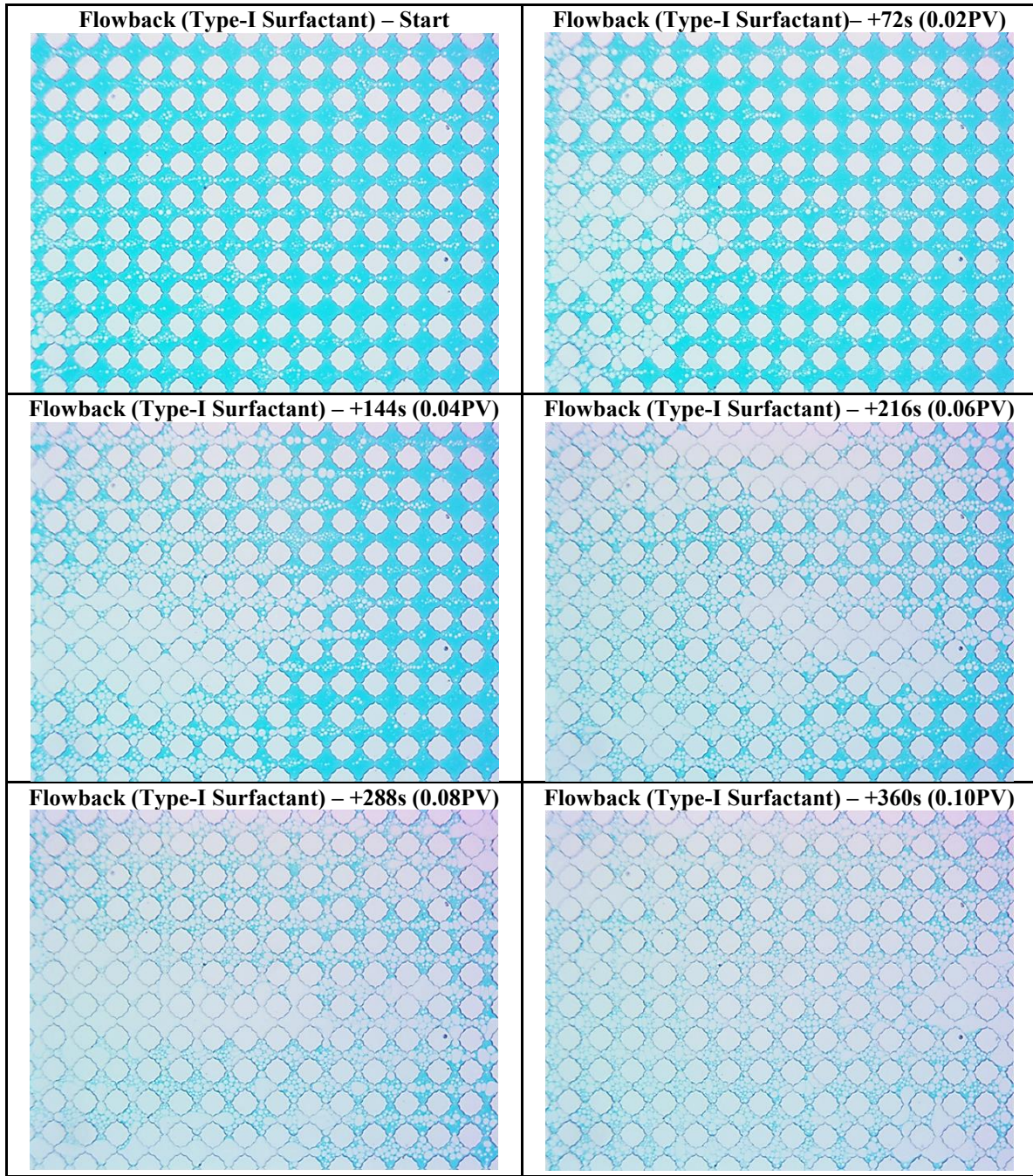


Figure 7.19: Changes of local phase saturations during flowback and hydrocarbon production from the type-I surfactant solution invaded microfluidic model for 360s (0.10PV). Closed transparent circles are solid grains of the microfluidic model, and the rest space is the porous media; dyed DI water is blue while n-hexane is white.



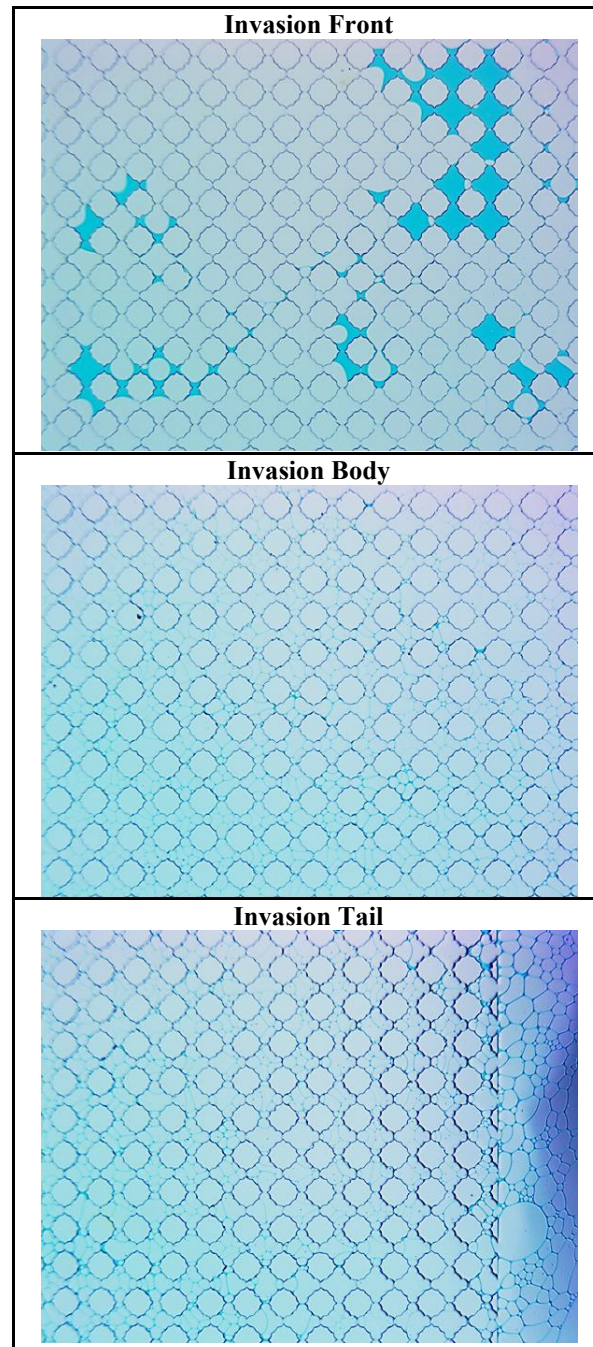


Figure 7.20: Changes of local water saturation at the invasion front (top), within the middle range of the invasion body (center), or at the invasion tail (bottom) after 0.5PV of hexane flood through the type-I surfactant solution invaded microfluidic model.

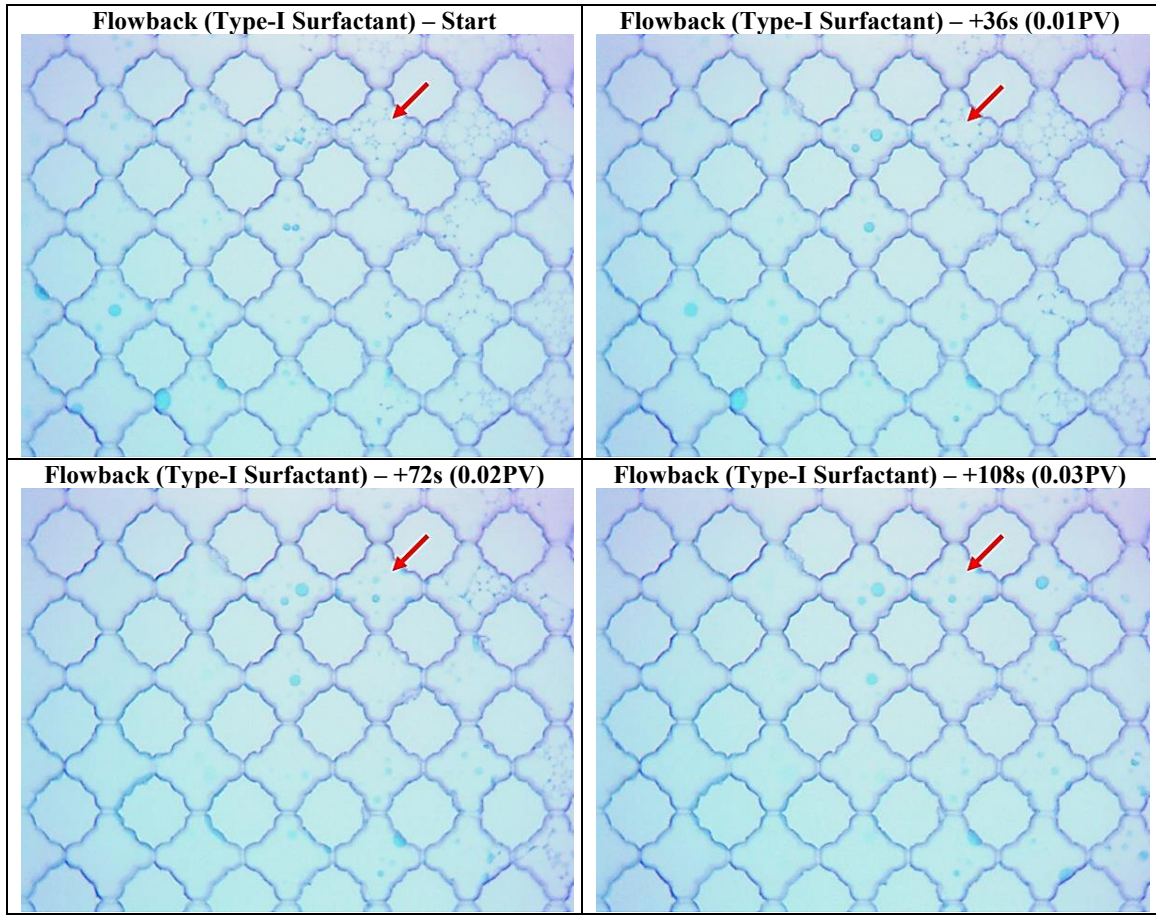


Figure 7.21: Changes of the trapped bubbles for 108s (0.03PV) after 0.5PV of hexane flood through the type-I surfactant solution invaded microfluidic model. Red arrows point the change within the same pore at different time slices.



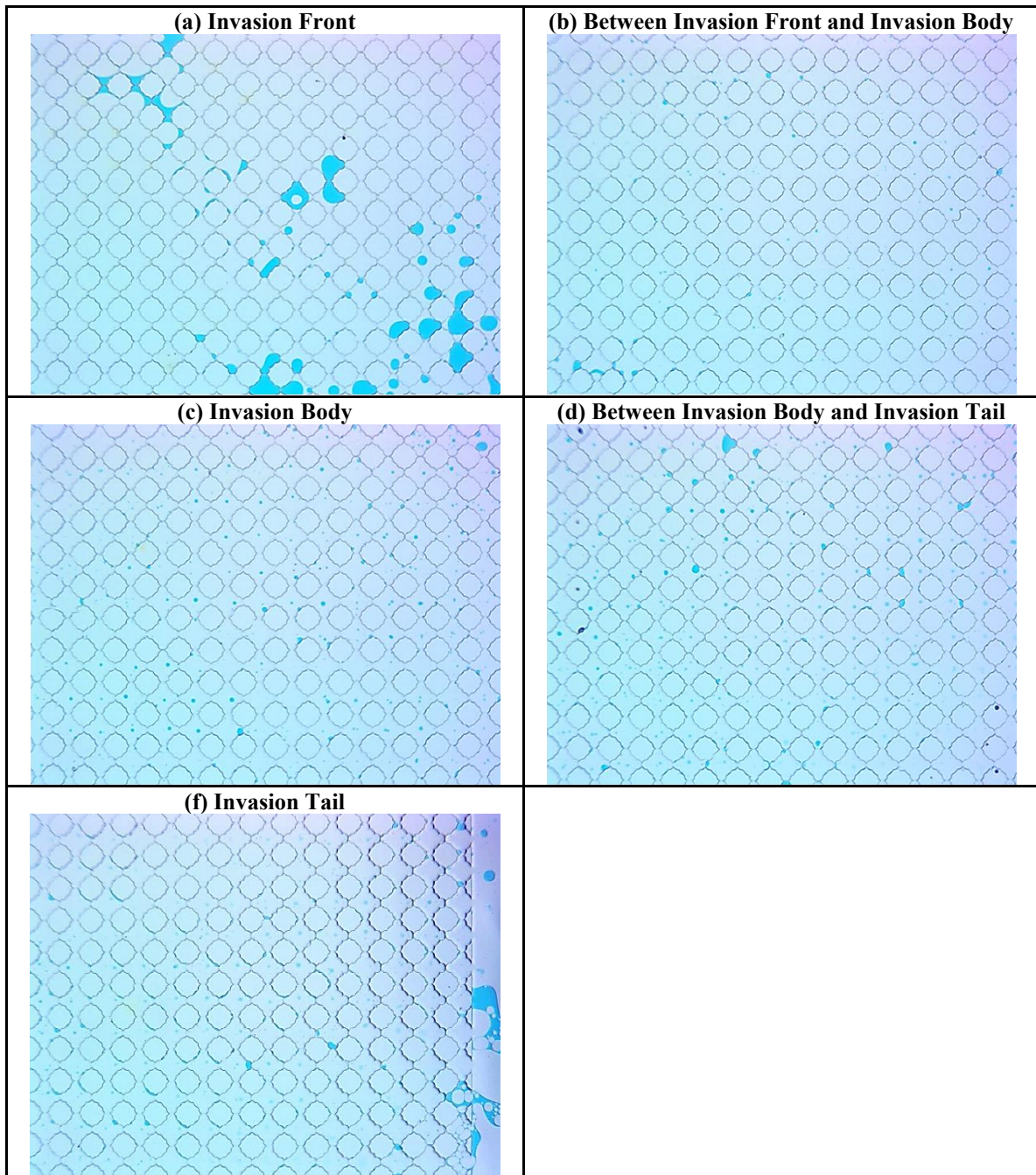


Figure 7.22: Changes of local water saturation across the invaded region (from the original invasion front to the invasion tail) after 3.5PV of hexane flood through the type-I surfactant solution invaded microfluidic model.

### **7.3.2.3 Flowback with surfactant at Winsor type-III condition**

This section shows the results when hexane flowed through the microfluid model invaded by the type-III surfactant solution. Figure 7.23 shows the changes of local phase saturations within 360 seconds (i.e., 0.10PV) during this step. Similar to the type-I condition (Figure 7.19), majority of the trapped water was mobilized by hydrocarbon; the form of water changed from small spherical droplets scattered in water to bigger bubbles wrapped in water. However, oil bubbles in this condition were less homogeneous than the type-I condition while big lumps of oil can be observed; water films between oil bubbles were also thicker than the ones in the type-I condition.

Figure 7.24 shows the change of local water saturation across the lateral space of the entire invaded region after 0.5PV of hexane flood through the microfluidic model: from the original invasion front (top figure), to the middle range of the invasion body (center figure) and then to the invasion tail which was now the outlet of the porous media (bottom figure). Similar to the type-I condition, residual water attached to the wall/edges of pore bodies/throats was also observed in the region near the original invasion front due to surfactant retardation (top figure). After this region, water was in form of films between oil bubbles; however, in this case, more water was trapped among the oil bubbles, resulting in a slower migration of oil bubbles towards the matrix outlet.

In this case, bursts of oil bubbles were also observed from the near-invasion-front region towards the matrix outlet; however, the speed of burst was much slower than that in the type-I condition. Figure 7.25 shows the changes of trapped bubbles within 432 seconds (i.e., 0.12PV). Unlike the type-I condition, some oil bubbles changed to smaller bubbles with higher water-to-oil ratio; complete phase separation was not ubiquitous in such type-III condition. This was likely attributed to the ultralow oil-water IFT in this condition where the mixed phase was stable regardless of hydrocarbon flow. Therefore, the relatively fast

burst speed of bubbles observed in the type-I condition (Figure 7.21) was likely due to the weakly stabilized oil-water interface, rather than to the loss of surfactants in hydrocarbon.

Figure 7.26 shows the change of local water saturation across the lateral space of the entire invaded region after 2.5PV of hexane flood through the microfluidic model. In region (a) where surfactant concentration was low due to the retardation happened during the invasion, residual water was attached on the wall/edges of pore bodies and pore throats (Figure 7.26(a)). Without changing the viscous force/pressure drawdown, this trapped water is unlikely to move with hydrocarbon. From the rear section of region (a) to the front section of region (c), tiny water droplets from burst bubbles and small bubbles without complete phase separation were both observed (Figure 7.26(a-c)); the phase separation was likely to continue, although it happened slowly due to the ultralow oil-water IFT that stabilized the mixed phase. In the following regions (i.e., the rear section of region(c) to region(f)), unbroken bubbles were observed (Figure 7.26(c-f)). This poor clean-up efficiency was likely due to the high water-to-oil ratio of the bubbles that increased their viscosity and thus slowed down their migration velocity. Moreover, this observation agrees with the CT results from Coreflood #3 shown in Chapter 6: water saturation decreased almost uniformly with time from the invasion front to the rock outlet (Figure 6.12). Like the type-I condition, water trapping due to capillary end effect was not observed near the matrix outlet because of the IFT reduction (Figure 7.26(f)). Preferred flow paths might exist, but they were not as clearly detected as those in the type-II condition (see more details in Section 7.3.2.4).

In general, a further reduction in IFT (type-III condition) did not improve the efficiency on cleaning up water block; it can create stable/long-lasting mixed phase that possibly impedes the flow of hydrocarbon. This also supports the physics proposed in Chapter 6.



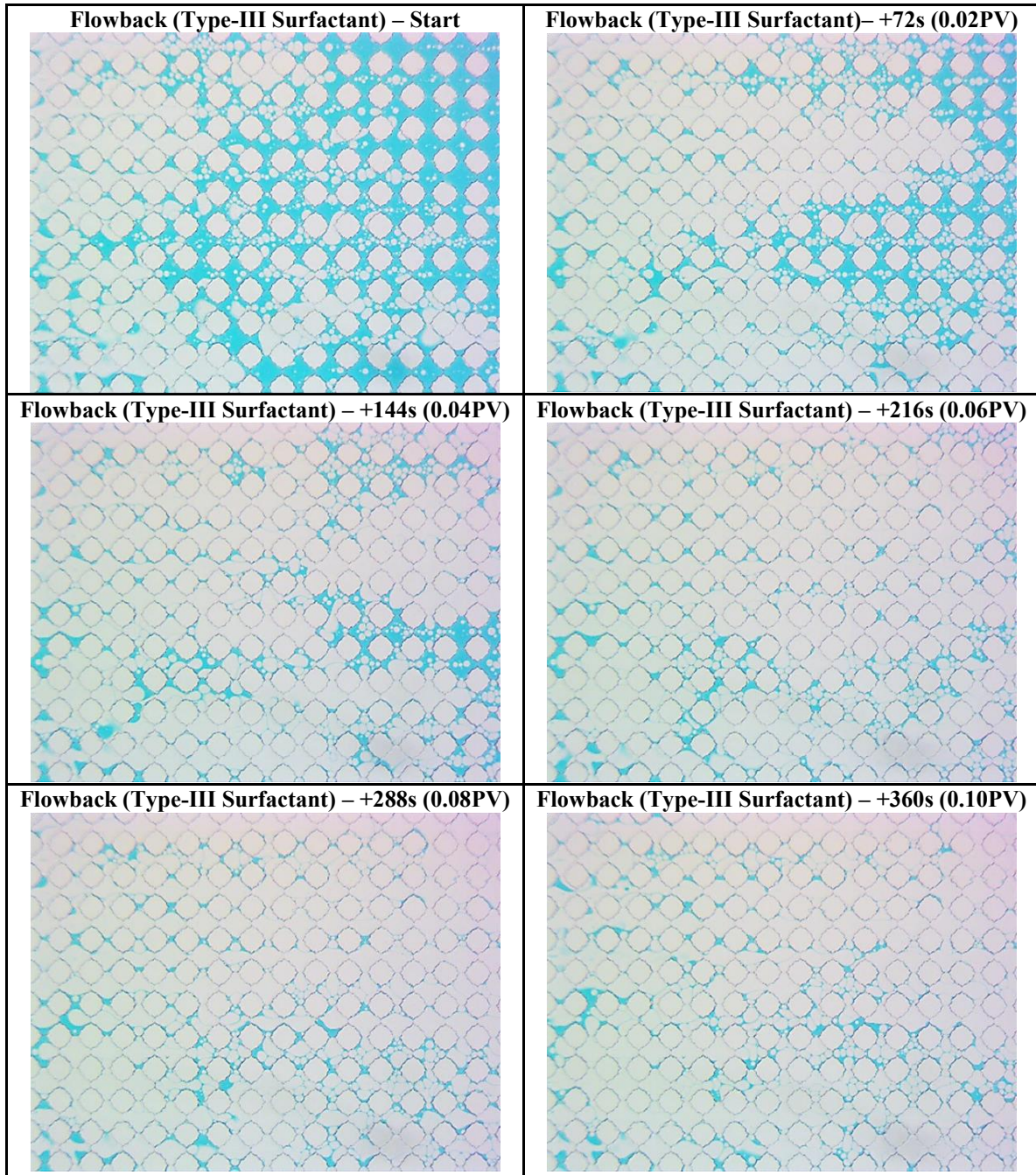


Figure 7.23: Changes of local phase saturations during flowback and hydrocarbon production from the type-III surfactant solution invaded microfluidic model for 360s (0.10PV). Closed transparent circles are solid grains of the microfluidic model, and the rest space is the porous media; dyed DI water is blue while n-hexane is white.

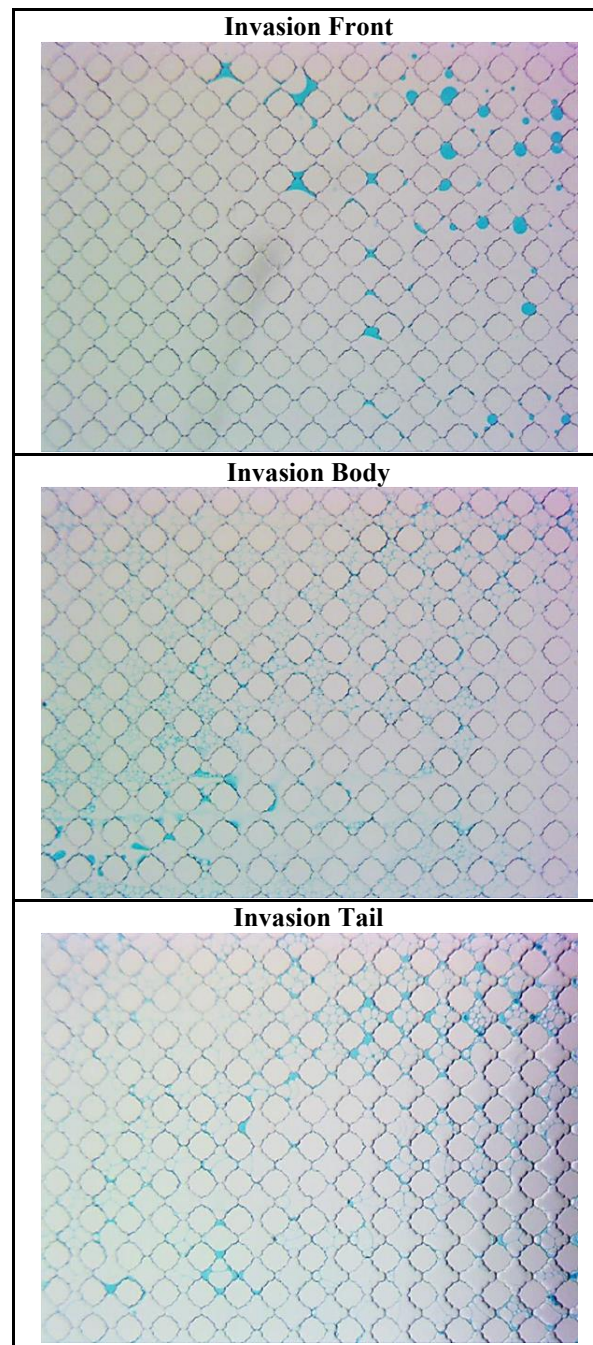


Figure 7.24: Changes of local water saturation at the invasion front (top), within the middle range of the invasion body (center), or at the invasion tail (bottom) after 0.5PV of hexane flood through the type-III surfactant solution invaded microfluidic model.



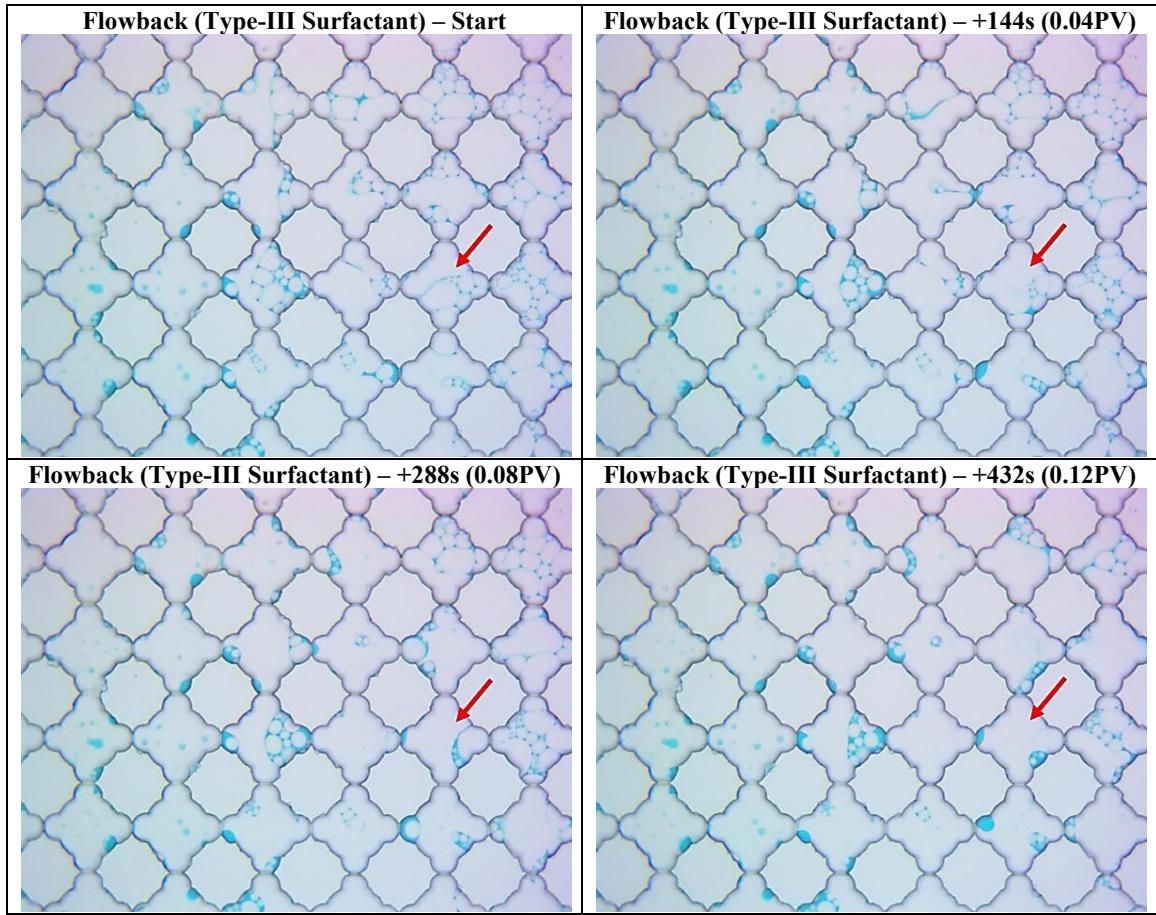


Figure 7.25: Changes of the trapped bubbles for 432s (0.12PV) after 0.5PV of hexane flood through the type-III surfactant solution invaded microfluidic model. Red arrows point the change within the same pore at different time slices.



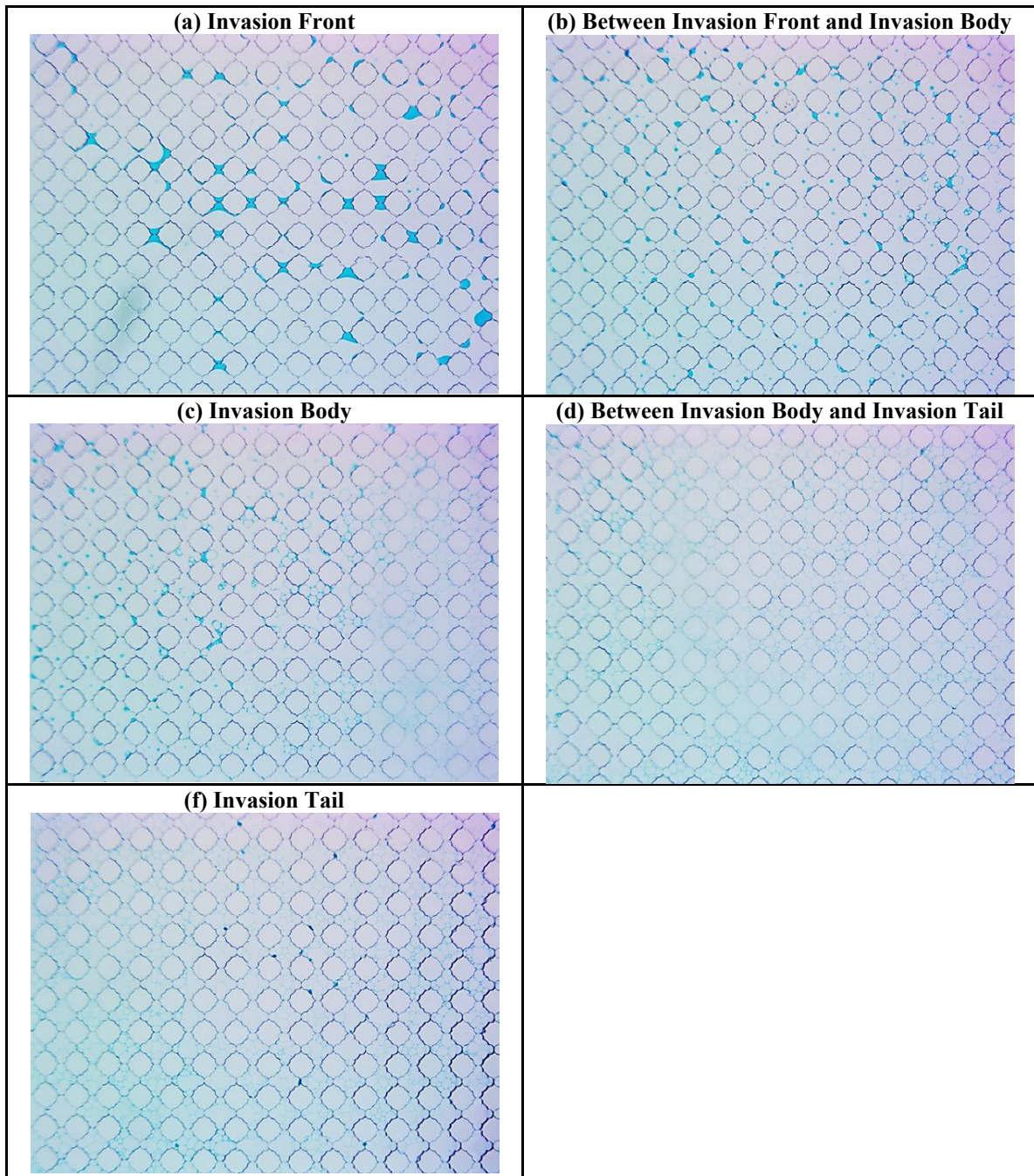


Figure 7.26: Changes of local water saturation across the invaded region (from the original invasion front to the invasion tail) after 2.5PV of hexane flood through the type-III surfactant solution invaded microfluidic model.

#### ***7.3.2.4 Flowback with surfactant at Winsor type-II condition***

This section shows the results when pentane flowed through the microfluid model invaded by the type-II surfactant solution. Figure 7.27 shows the changes of local phase saturations within 360 seconds (i.e., 0.10PV) during this step. The invaded water (blue fluid) and the previously formed microemulsion phase (light blue fluid) were both mobilized by hydrocarbon and gradually transformed to oil bubbles wrapped in water. Similar to the type-I condition (Figure 7.19), these oil bubbles kept growing with time when less water was left behind in form of the bubble films.

Figure 7.28 shows the change of local water saturation across the lateral space of the entire invaded region after 0.5PV of pentane flood through the microfluidic model: from the original invasion front (top figure), to the middle range of the invasion body (center figure) and then to the invasion tail which was now the outlet of the porous media (bottom figure). Similar to the type-I and type-III conditions, residual water attached to the wall/edges of pore bodies/throats was observed in the region near the original invasion front where surfactant concentration was low (top figure). After this region, water was in form of films between oil bubbles; however, in this case, distinct preferred flow paths were observed that bypassed a lump of oil bubbles (center figure).

Figure 7.29 provides a close-up view on the formation of preferred flow paths in this region within 108 seconds (0.03PV). As pointed by two red arrows, preferred flow paths were created, on which oil bubbles burst relatively fast; separated water droplets from the burst bubbles were continuously mobilized by hydrocarbon, leaving a lump of oil bubbles unchanged between these two preferred flow paths. Bursts of bubbles were found to start from the contact with the flow of hydrocarbon, as explained for the type-I condition (Section 7.3.2.2); however, the speed of bubble burst seemed to be faster in this case, which

was likely enhanced by the solubilization/loss of surfactant in hydrocarbon in such a high salinity environment.

Figure 7.30 shows the change of local water saturation near the matrix outlet across the matrix width after 2.5PV of pentane flood. Two major preferred flow paths can be observed, which was accompanied with separated water droplets. For other area, water remained being trapped as films between oil bubbles. Once preferred flow paths formed, hydrocarbon was likely to keep flowing away from the trapped oil bubbles; this resulted in a poor clean-up efficiency on invaded water, possibly being even poorer than the type-III condition. Nevertheless, water trapping due to capillary end effect was not observed in this region because of the IFT reduction.

In general, observations from this microfluidic model test agrees very well with the CT results from Coreflood #7 shown in Chapter 6: water saturation profile decreased and then increased from the invasion front to the rock outlet as the type-I condition, while it decreased much slower with time (Figure 6.12).



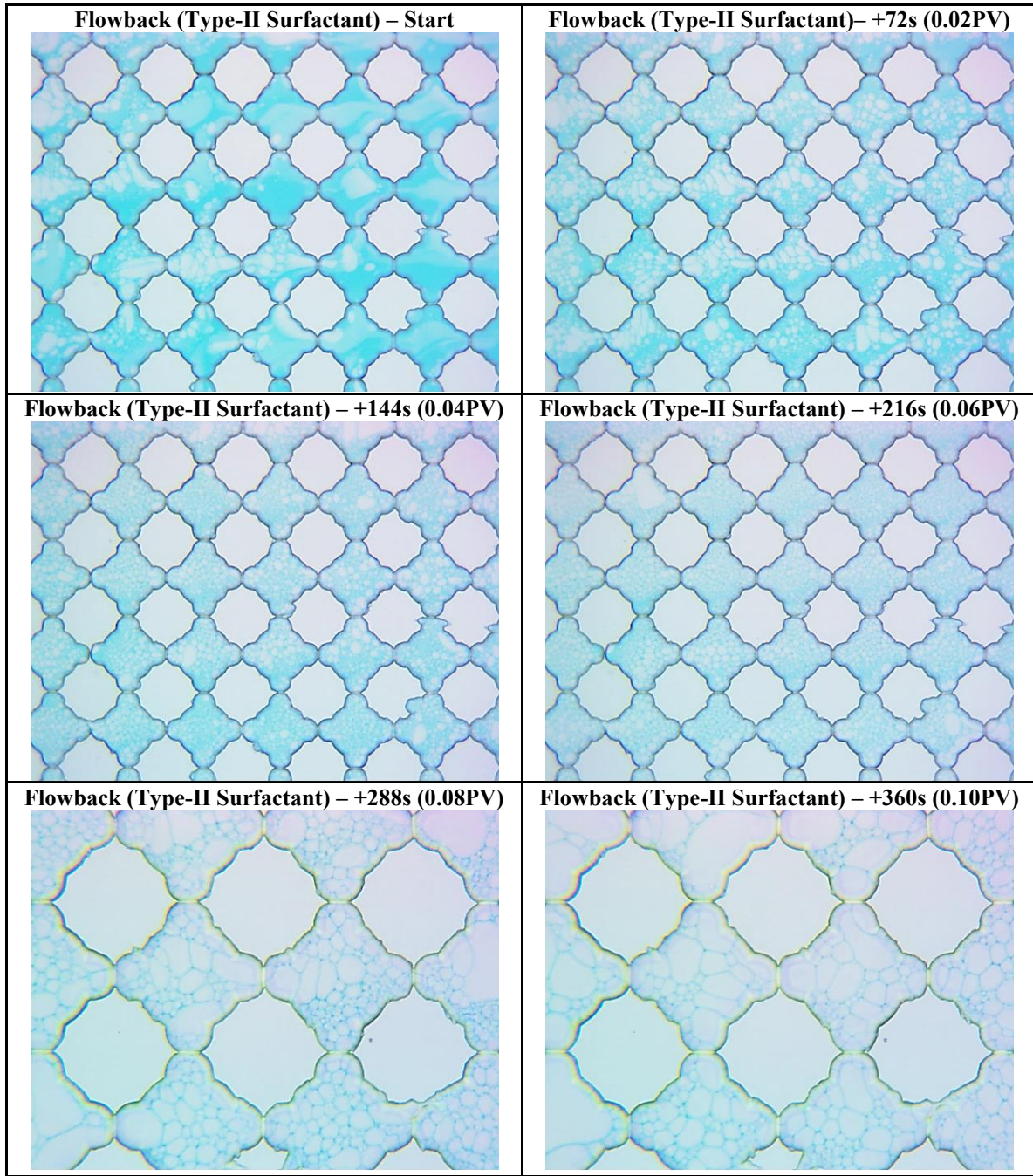


Figure 7.27: Changes of local phase saturations during flowback and hydrocarbon production from the type-II surfactant solution invaded microfluidic model for 360s (0.10PV). Closed transparent circles are solid grains of the microfluidic model, and the rest space is the porous media; dyed DI water is blue while n-pentane is white.

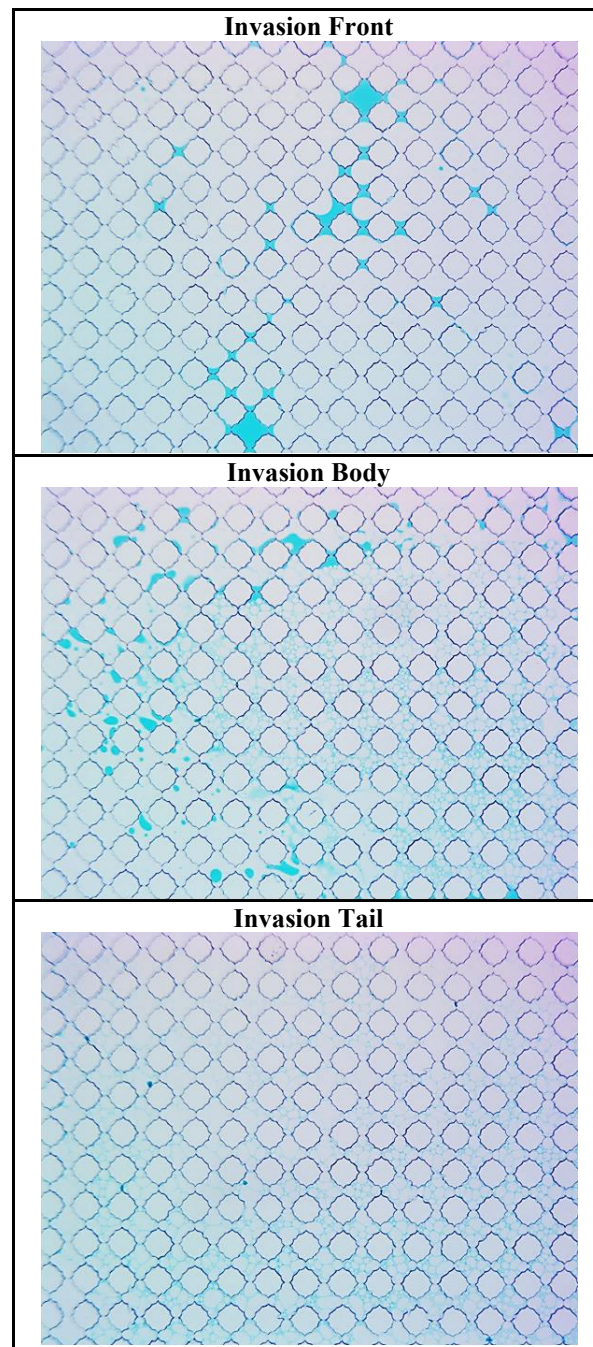


Figure 7.28: Changes of local water saturation at the invasion front (top), within the middle range of the invasion body (center), or at the invasion tail (bottom) after 0.5PV of pentane flood through the type-II surfactant solution invaded microfluidic model.



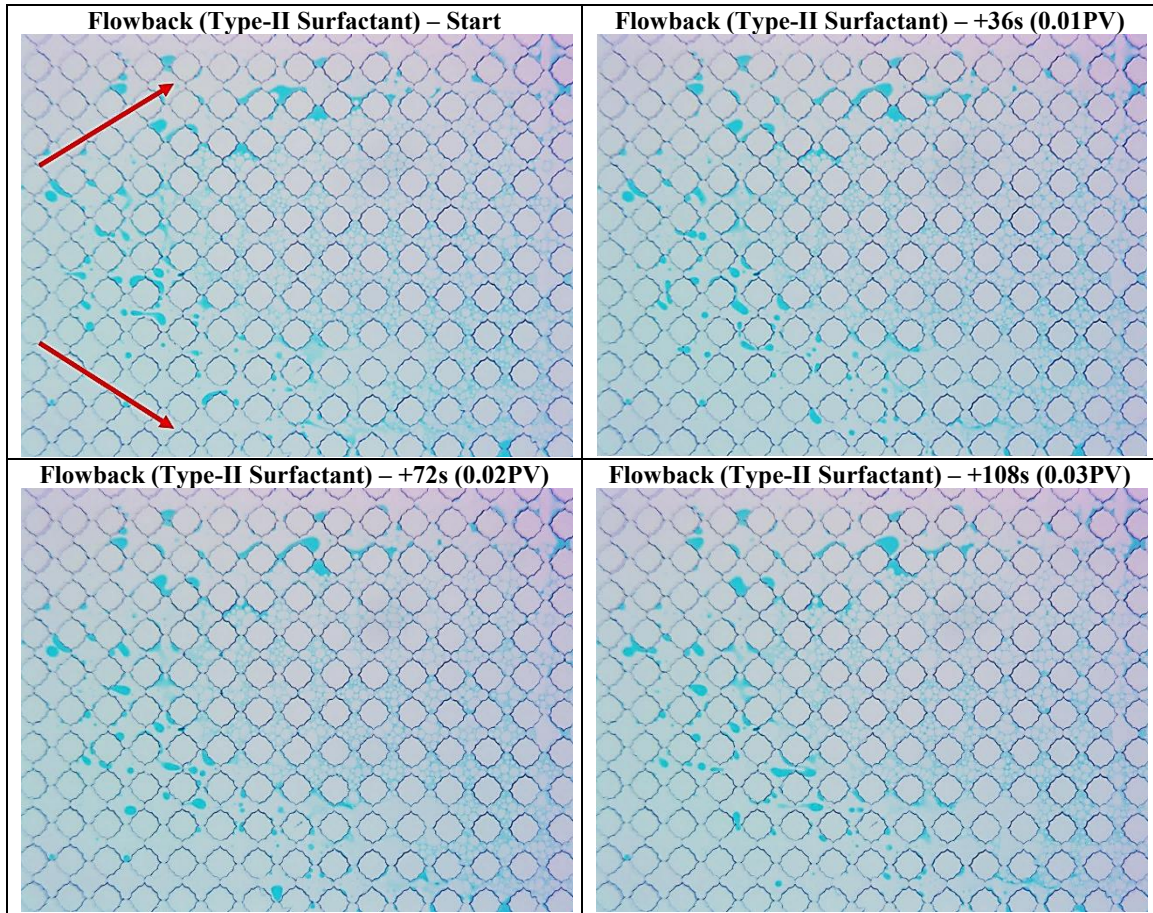


Figure 7.29: Changes of the trapped bubbles for 108s (0.03PV) after 0.5PV of pentane flood through the type-II surfactant solution invaded microfluidic model. Red arrows point the formation of two preferred flow paths with time.

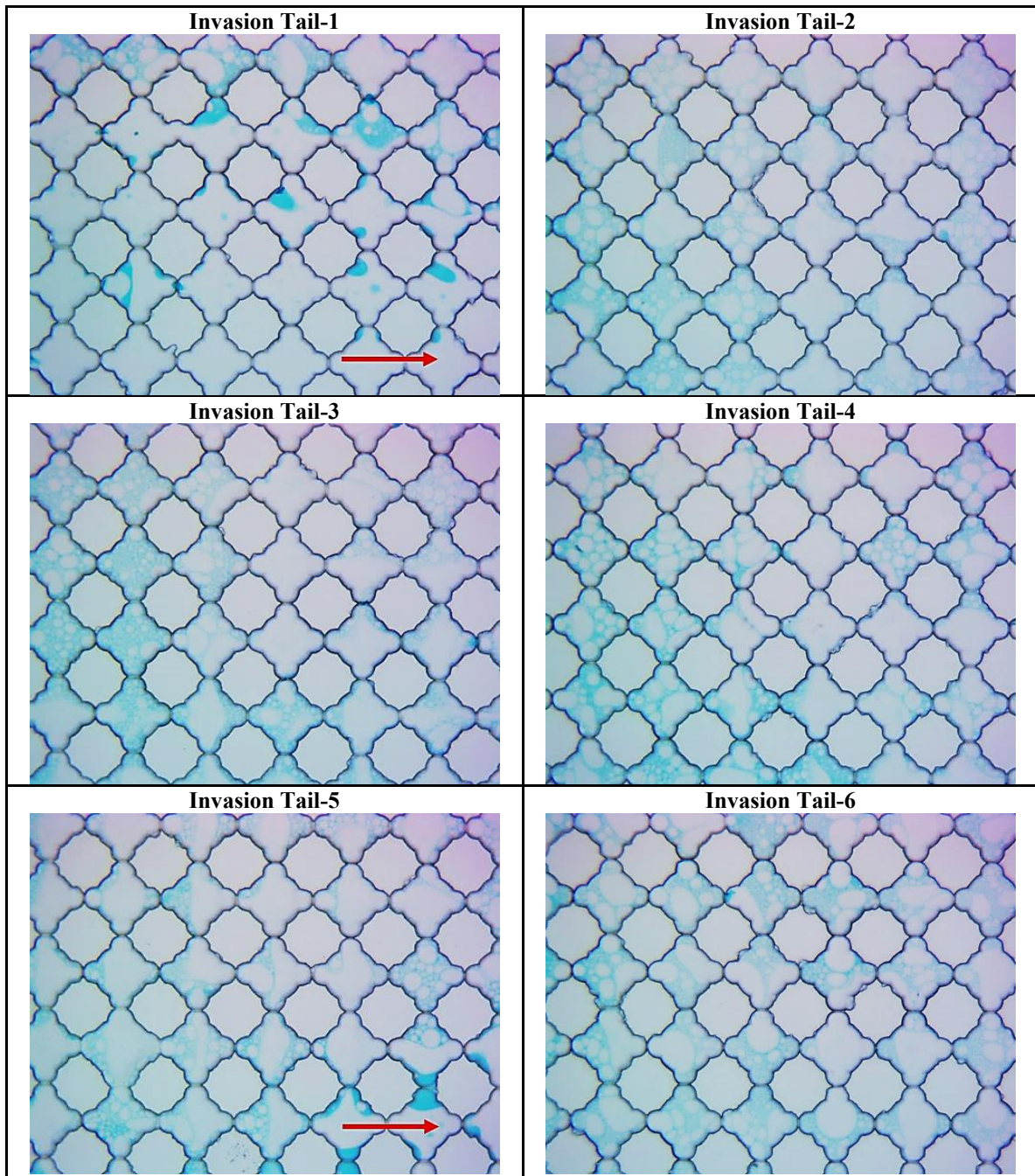


Figure 7.30: Changes of local water saturation at the invasion tail (i.e., the matrix outlet) across the matrix width after 2.5PV of pentane flood through the type-II surfactant solution invaded microfluidic model. Red arrows point the formed preferred flow paths.

## 7.4 CONCLUSIONS

In the study shown in this chapter, microemulsion-forming surfactants are tested through an equivalent three-step “chipflood” sequence on a novel 2.5D glass microfluidic model. This ensures that the phase changes during the mimicked fracturing fluid invasion and the flowback can be directly observed and further compared when different types of microemulsion are formed in porous media. In general, the observation results agree very well with CT scan results shown in Chapter 6; they complement and further support the new physics proposed in the previous chapters.

The major findings are listed as follows.

1. During the mimicked surfactant-aided fracturing fluid invasion, microemulsions are mainly formed near the invasion front where hydrocarbon and surfactant solution initially mix with each other in the type-I and type-II conditions; however, for the type-III condition, microemulsions are formed far behind the invasion front where sufficient mixing is required.
2. During flowback and hydrocarbon production, the type-I condition provides the best clean-up efficiency on the invaded fluid. The mixed phase between hydrocarbon and water (i.e., bubbles) is mobile and the bypassed/trapped one, if any, can break with time at a decent rate.
3. During flowback and hydrocarbon production, thicker water films are formed within the mixed phase in the type-III condition; this can increase the viscosity of the phase and thus result in a poor clean-up efficiency. Bypassed/trapped bubbles are relatively stable due to the ultralow oil-water IFT in this condition.
4. During flowback and hydrocarbon production, distinct preferred flow paths are created in the type-II condition; more water is left behind in form of films of the bypassed/trapped bubbles between these preferred flow paths.



## **Chapter 8: Evaluation of Wettability Alteration and IFT Reduction on Mitigating Water Block for Oil-Wet Systems<sup>6</sup>**

This chapter extends the study of water block to the oil-wet systems. Surfactant treatment is evaluated in the lab to understand the underlying physics. In specific, since wettability alteration and IFT reduction are two typical approaches people proposed to solve the water block in oil-wet systems, they are compared on the same porous media for enhancing the rock permeability to hydrocarbon.

### **8.1 QUICK OVERVIEW OF THIS CHAPTER**

Significant amount of water is lost into shale reservoirs after hydraulic fracturing, and this can cause the permeability reduction that hinders hydrocarbon production. A similar coreflood setup, as introduced in previous chapters, was used in this study to explore the mechanisms behind the formation and mitigation of water block in rock matrix. Since shale is typically considered as mixed-wet, one core sample was altered from native water-wet into oil-wet and tested through an identical experimental procedure; this provided a straightforward comparison of water block in water-wet and oil-wet states. Recently, surfactants have been widely proposed to enhance the oil production from shales, through either wettability alteration or IFT reduction. A microemulsion-forming surfactant was then tested in the core sample at the oil-wet state, also through the identical experimental procedure; this provided another straightforward comparison on rock permeability regaining from either one of these two approaches on the same porous media.

---

<sup>6</sup> This chapter is based on the following paper:

**Liang, T.,** Luo, X., Nguyen, Q.P., DiCarlo, D.A. Water Block under Different Wetting States and Effectiveness of Surfactant-Aided Fracturing Fluid through Different Approaches. In Preparation.

Our results showed the regaining of rock permeability to hydrocarbon is a naturally-triggered process under the water-wet condition, where higher drawdown delays the regaining; however, it is a drawdown-driven process under the oil-wet condition, where higher drawdown promotes the regaining of permeability. Moreover, when oil-wet rock is altered into water-wet, regained permeability at the late time will be enhanced but the amount of flowback water will be significantly reduced. However, permeability reduction due to matrix-fracture interaction may take place at the early time, the degree of which depends on the level of IFT reduction. For low permeability rocks that the steady state requires long time to achieve, using surfactants that give ultralow IFT reductions might be a better option.

## **8.2 INTRODUCTION**

In the United States, tight/shale oil contribute to approximately 1/3 of technically recoverable oil resources (EIA, 2015). To economically produce hydrocarbon from such low/ultralow permeability reservoirs, horizontal drilling and multistage hydraulic fracturing must be applied to maximize the contact area with the reservoir. However, it is usually reported that only less than 5-50% of water can be recovered as “flowback” (Penny and Pursley, 2007; Zelenev and Ellena, 2009; King, 2012; Wasylishen and Fulton, 2012). Water creates extensive surface area of rock matrix that allows more hydrocarbon to flow out to the well; meanwhile, any trapped water therein can hinder hydrocarbon production and well productivity.

Shale is normally considered as mixed-wet, and this is attributed to its three types of pores: interparticle pores and intraparticle pores associated with the inorganic matrix, as well as pores associated with the organic matter (Curtis et al., 2010; Milner et al., 2010;

Loucks et al., 2010, 2012). Inorganic matrix is normally considered as water-wet, and thus can imbibe water. On the other hand, organic matter is considered as the source of hydrocarbon and thus oil-wet. The sizes of organic pores are found to be affected by the total organic carbon (TOC) content (Milliken et al., 2013) and/or the thermal maturity (Milner et al., 2010; Curtis et al., 2010, 2012a); therefore, although the majority of organic pores is believed to range from 5 to 100nm, some big pores up to 750nm can exist and serve as hydrocarbon pathways (Loucks et al., 2009). For these big pores, water can invade in by the high pressure generated during hydraulic fracturing. In general, for pores with different wettabilities, increase in water saturation both reduces the rock permeability to hydrocarbon due to multiphase flow; however, the detailed mechanisms behind the formation and mitigation of water block are distinct between two wetting states and need to be elaborated.

Shale is typically very tight; its small pores generate low/ultralow permeability of the order of microDarcies down to nanoDarcies (DOE, 2009; Nelson, 2009). At the same time, small pores also generate high capillary force. For water-wet pores, this force may result in the imbibition of water-based fracturing fluid, and it has been reported that this imbibition can be significant in shale (Odusina et al., 2011; Dehghanpour et al., 2013; Bostrom et al., 2014; Dutta et al., 2014; Sun et al., 2015). Once water invades in, high capillary force keeps the water in the rock and hinders the rock permeability being recovered (i.e., forms water block); this phenomenon becomes more significant when production drawdown is not significantly greater than the capillary force, which is typically the case for shales (Holditch, 1979; Abrams and Vinegar, 1985; Parekh and Sharma, 2004; Mahadevan and Sharma, 2005). Under the similar production conditions, our previous studies have revealed that capillary discontinuity at the fracture face may be mainly responsible for the water block in water-wet systems; water saturation profile, instead of

the total water saturation, determines the degree of permeability reduction due to the invaded water (Liang et al., 2015b, 2016). On the other hand, for oil-wet systems, bypassed water due to capillary trapping is likely the main reason causing water block: the lower the trapping number/capillary number (Pope et al., 2000), the more the residual water after flowback and thus the larger the reduction of rock permeability. The detailed mechanism for the oil-wet state was explored in this study and further compared with that for the water-wet state on an identical porous media and at an identical production condition. This was achieved by conducting identical experiments on one core sample before and after its wettability was altered from natively water-wet into oil-wet. Moreover, impacts of production drawdown were also studied for both wetting states, aiming at better understandings on their mitigation mechanisms.

To reduce such water block due to capillarity for shale oil reservoirs, surfactants are normally suggested to be used as the fracturing fluid additives, through either wettability alteration or interfacial tension (IFT) reduction. For wettability alteration, enhancements on oil production from various shale samples have been reported from the lab after altering the rock wettability to water-wet that generates the spontaneous imbibition (Wang et al., 2012; Alvarez and Schechter, 2015; Morsy and Sheng, 2015; Kim et al., 2016; Neog and Schechter, 2016). However, they were all conducted by the imbibition cells without any flow experiments showing the change of rock permeability to oil; secondly, wettability alteration was always accompanied with IFT reduction, hence their own enhancement mechanisms cannot be separately explored. For IFT reduction, several types of surfactants have been discovered that could enhance the oil production, some of which have been tested in the field. Firstly, weakly emulsifying surfactants have been shown to enhance the oil flow through tight pore throats in the lab using a microfluidic model (He et al., 2015) and enhancements on oil production have been reported from

several wells in Eagle Ford and Mississippi Lime Shales after the use of such surfactants (Xu and Fu, 2012; He and Xu, 2015). Secondly, surfactants providing low to ultralow IFT have been shown to mobilize the oil droplets originally attached on rock surface in the lab, and they were suggested to be used in the field through “huff-n-puff” treatment (Bui et al., 2016; Shuler et al., 2016); however, no results from flow experiments have been provided to show the change of rock permeability due to the potentially formed emulsions/microemulsions. Thirdly, based on our previous studies, microemulsion-forming surfactants can effectively remove the water block at the fracture face due to matrix-fracture interaction, and thus remarkably enhance rock permeability at the early time of hydrocarbon production; they do not need to invade deep into the reservoir rock to react (Liang et al., 2015a, 2015b, 2016). However, understandings on microemulsion-forming surfactants were limited to only water-wet systems, and more studies are required for the oil-wet systems. Nevertheless, no study has been done, at least experimentally in the lab, to give a straightforward comparison on both surfactant approaches on oil-wet tight rocks, so as to elucidate the permeability enhancement from either one of them during flowback.

In this study, we used a coreflood sequence that simulated fracturing fluid invasion, flowback and hydrocarbon production. The change of *in-situ* water saturation profile within the core was recorded through CT scans; while the permeability reduction during fluid invasion and the permeability regaining during flowback were both quantified from pressure drop measurements. One core sample was altered from native water-wet into oil-wet and tested through an identical experimental procedure; this allowed the mechanisms behind the formation and mitigation of water block can be explored and compared for both wetting states. Furthermore, a microemulsion-forming surfactant was then tested in the core sample at the oil-wet state, also through the identical experimental procedure; this

allowed a direct comparison on rock permeability regaining from either wettability alteration or IFT reduction on the same porous media.

## **8.3 MATERIALS**

### **8.3.1 Rock and hydrocarbon proxies**

Indiana Limestone was chosen as the rock sample for all the experiments conducted in this work. The specific block of Indiana Limestone outcrop is homogeneous and originally water-wet; it does not contain water sensitive minerals. It has permeability around 3.2mD and porosity around 16.8%. One small core plug from this rock block was ground into powders for testing the effect of the wettability alteration agent; another two small core plugs with dimensions of 1.5-inch in diameter and 2-inch or 2.5-inch in length were drilled for the imbibition cell tests. One bigger core sample with dimensions of 3-inch (7.6cm) in diameter and 9.5-inch (24.1cm) in length was drilled for all five coreflood experiments conducted in this study.

N-pentane was chosen to mimic the light oil produced from the typical shale or other tight reservoirs. Since it has a low boiling point (36.1°C at atmosphere pressure), residual pentane in the rock after each coreflood test can be removed with water by drying in an oven. Moreover, pentane does not affect the rock wettability, either before or after the rock wettability is altered by the agent introduced later. Therefore, an identical core sample can be used for a series of comparative experiments in this study.

### **8.3.2 Wettability alteration agent**

It has been found that naphthenic acids can adsorb on the carbonate rock to alter the rock wettability from water-wet to oil-wet (Wu et al., 2008). For experimental purposes,

1.5wt% cyclohexanepentanoic acid in n-decane has been used in the lab to alter the originally water-wet Texas Cream Limestone into oil-wet. (Gupta and Mohanty, 2011). Inspired by them, we applied 1.5wt% cyclohexanepentanoic acid in n-pentane in this study to alter the Indiana Limestone core into oil-wet. Detailed procedure on testing this agent on the rock is provided in the later section. Table 8.1 shows the molecular structure of this agent, as well as some of its physical properties provided by the vendor.

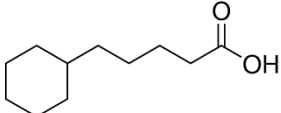
Molecular Structure	Molar Mass (g/mol)	Boiling Point (°C)	Melting Point (°C)
	184.28	126~127	16~17

Table 8.1: Basic Information about Cyclohexanepentanoic Acid (by Sigma-Aldrich).

### 8.3.3 Surfactant formulation for IFT reduction

A surfactant formulation has been successfully discovered that gives ultralow IFT between water and n-pentane, and it forms Winsor type microemulsions within a range of salinities (Liang et al., 2015a). Since it has been shown that the salinity forming Winsor type-I microemulsion gives the best performance on mitigating water block (Liang et al., 2016), a salinity of 47500ppm was chosen in this study to mimic the low tension fracturing fluid. Figure shows the phase behavior result between 1wt% of this surfactant solution and n-pentane after mixed and equilibrated at the room temperature. The red arrow in this figure points the original oil-water contact before mixing; from the change of oil-water contact, the reduced IFT can be estimated through Chun Huh equation, which was found to be 0.003mN/m.



Figure 8.1: Phase behavior test between n-pentane and 1wt% surfactant solution at a salinity of 47500ppm. Red arrow points the original oil-water contact before mixing.

#### 8.4 METHODS

A three-step coreflood system was developed in the lab to evaluate rock permeability reduction due to the invaded water under different wetting states. This system was then applied to evaluate the permeability regaining under different production drawdowns or after IFT reduction by surfactant. Firstly, two baseline measurements were established on the originally water-wet core sample to compare the permeability regaining under two different drawdowns. Secondly, this core sample was altered into oil-wet by the wettability alteration agent introduced above. Thirdly, another two baseline measurements with different drawdowns were conducted under such oil-wet state for comparison. In the



end, the microemulsion-forming surfactant was tested on this core sample to evaluate the enhancement of rock permeability regaining from IFT reduction.

Table 8.2 lists the order of five coreflood experiments conducted in this study on an identical porous media. As shown in this table, Corefloods #1-#4 compared the rock permeability reduction under oil-wet and water-wet states, as well as the permeability regaining under different drawdowns for both wetting states. Moreover, this study also compared the enhancements of hydrocarbon production from low permeability oil-wet reservoirs through two typical surfactant approaches: altering rock wettability (Coreflood #3 vs. Coreflood #1) and achieving ultralow oil-water IFT (Coreflood #3 vs. Coreflood #5).

<b>Coreflood Number</b>	<b>Core Wetting State</b>	<b>Mimicked Fracturing Fluid</b>	<b>Fluid Invaded Volume (PV)</b>	<b>Hydrocarbon Flow Rate (cc/min)</b>
<b>#1</b>	Water-Wet	DI-Water	0.171	0.2
<b>#2</b>	Water-Wet	DI-Water	0.171	0.1
<b>#3</b>	Oil-Wet	DI-Water	0.171	0.2
<b>#4</b>	Oil-Wet	DI-Water	0.171	0.1
<b>#5</b>	Oil-Wet	Surfactant Solution	0.171	0.2

*\*Note: The core sample was altered from water-wet into oil-wet after Coreflood #2.*

Table 8.2: Schedule of Coreflood Experiments in Sequence.

#### **8.4.1 Wettability alteration tests**

To examine the effectiveness of the wettability alteration agent, two tests were conducted before the agent was applied to the core sample used in five corefloods. These tests were imbibition cell test and grinded sample test.

##### ***8.4.1.1 Imbibition cell test***

1. A short Indiana Limestone core plug was loaded into a clean and dry imbibition cell, and then vacuumed for reaching at least -27inHg;
2. The bottom port of the imbibition cell was connected to either pure n-pentane or 1.5wt% cyclohexanepentanoic acid in n-pentane, and then let the core plug be submerged;
3. The core plug was aged in the fluid for 48hr;
4. DI water was injected from the bottom port of the imbibition cell until it displaced the oil and submerged the core plug, and then all valves were closed;
5. The oil-water contact and the total fluid height were labeled for the record;
6. The cell was placed for observation.

##### ***8.4.1.2 Grinded sample test***

1. A short core plug was grinded into powders in a mortar;
2. Powders were dried in an oven at 70°C for 12hr, and then cooled down at the room temperature;
3. Powers were split into two 20mL borosilicate glass vials, each with 2.5g;
4. One vial was filled by 1.5wt% cyclohexanepentanoic acid in n-pentane, while the other vial was filled by pure n-pentane as a control; both vials was placed in an ultrasonic bath for 24hr;

5. Two vials were transferred into an oven without caps and dried at 126°C (bubble point of the agent) for 2hr, followed by 70°C for 8hr;
6. When two vials cooled down, 8mL DI water (with blue dye) was slowly injected into them, followed by 8mL n-pentane (with red dye);
7. Two vials were intensively mixed and then placed for observation.

#### **8.4.2 Coreflood schemes**

Three-step coreflood system was designed to simulate the fracturing fluid invasion and its flowback during hydrocarbon production occurring within the tight rock matrix adjacent to the hydraulically induced open fractures. The 9.5-inch-long core sample was tested in an aluminum Hassler coreholder, which is X-ray transparent; an aluminum spacer was attached to one side of the core sample, and the core face on this side represented the matrix outlet to an open fracture (i.e., fracture face or “frac face” in short). Each coreflood was conducted under a modified medical CT scanner, which measured the change of water saturation profile within the core sample in real time. The CT scans were conducted every 30min, with 2mm slice thickness, 5mm slice intervals and 2s exposure time per slice. Each scan started at 1mm from the “frac face” of the core sample, and consisted of 46 slices that provided the water saturation profile within the sample at that moment. For each slice, the image resolution was approximately 210 $\mu$ m. In the meantime, pressure drop across the core was continuously recorded by a pressure transducer with a range of -200psi to 200psi for the entire period of coreflood; it gave the change of rock permeability due to the change of water saturation since the fluid injection rate was kept at a constant in each step of the coreflood.

These three steps included: establishing the initial reservoir condition (Step-1), mimicked fracturing fluid invasion (Step-2) and mimicked flowback during hydrocarbon production (Step-3); more details have been elaborated in authors' previous studies (Liang et al., 2015a, 2016). In this study, except for testing the surfactant, pure DI water was used as the mimicked fracturing fluid for all corefloods. Brine with the same salinity as the surfactant solution (i.e., 47500ppm) was not chosen because: (1) the same core sample was reused to test the consistency and reproducibility of the measurements, in addition to the listed corefloods shown in Table 8.2, and any introduced salt could result in the measurement uncertainty; (2) no detectable difference in core permeability was previously detected when brine or DI water was used as the mimicked fracturing fluid.

As shown in Figure 8.2, the core sample was fully saturated by pentane during Step-1, and the initial water saturation before water invasion was set at zero (i.e.,  $S_{wi}=0$ ) for ease of analysis. During Step-2 and Step-3, water and pentane were injected into the core respectively from the opposite sides, which resulted in the opposite signs of the measured pressure drop data as can be seen later. Water injection rate was 0.4cc/min for all corefloods, while pentane injection rate varied among various corefloods as shown in Table 8.2.

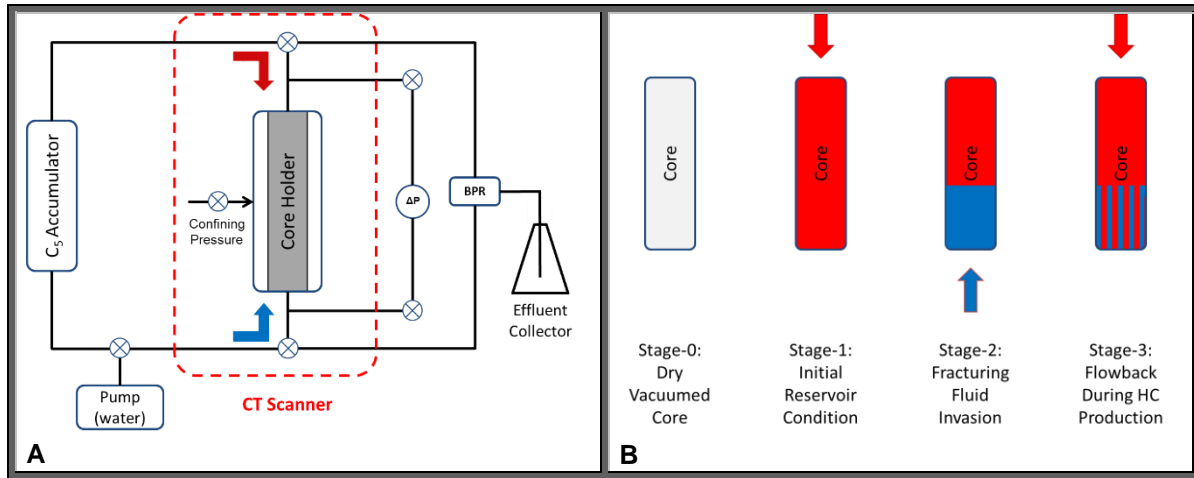


Figure 8.2: Schematic of the coreflood setup (A) and three-step coreflood sequence (B) (Modified from (Liang et al., 2015a, 2016)).

## 8.5 RESULTS

### 8.5.1 Wettability alteration tests

#### 8.5.1.1 Imbibition cell test

Imbibition started once DI water replaced the oil and submerged the core plug within the imbibition cell. Daily changes in each cell were recorded through a camera. Figure 8.3 shows the comparison of changes after 30-day imbibition when the core plug was treated by the wettability alteration agent (Figure 8.3A) or not (Figure 8.3B). In each figure, the black short line labeled on the imbibition cell shows the original oil-water contact; the black dotted-line arrow points the oil-water contact after 30-day imbibition, and the red solid-line arrow points the oil droplet(s) displaced out of the core sample within these 30 days.

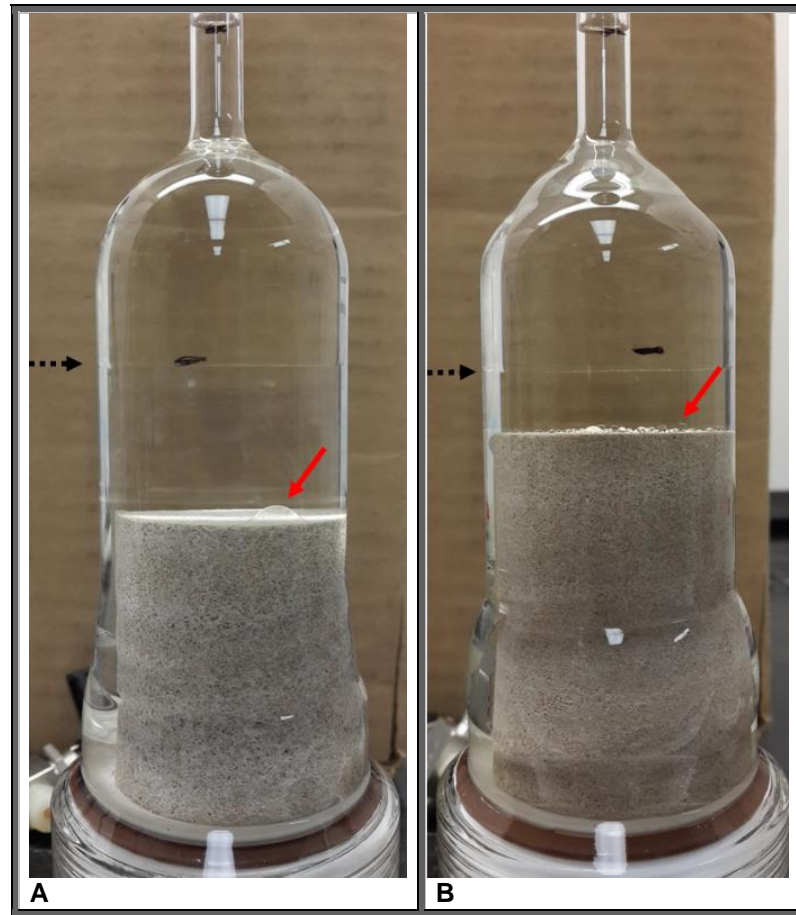


Figure 8.3: Results of imbibition cell tests after 30 days when the wettability alteration agent was applied (A) or not applied (B). In each figure, the black short line labeled on the imbibition cell shows the original oil-water contact; the black dotted-line arrow points the oil-water contact after 30 days, and the red solid-line arrow points the oil droplet(s) displaced out of the core sample within these 30 days.

For the agent-treated core plug (Figure 8.3A), the change of oil-water contact was imperceptible; this indicates only trace amount of water imbibed into the core plug within 30 days. One oil droplet can be observed on the top surface of this core plug (pointed by a red arrow in the figure). From the contact angle of this droplet, as well as the almost unchanged saturation, one may tell that the rock has been altered into oil-wet by the wettability alteration agent.

For the untreated core plug (Figure 8.3B), the change of oil-water contact was observed; this indicates some water imbibed into the originally pentane saturated core. Multiply pentane droplets left the core plug from its top surface (pointed by a red arrow in the figure) and they are almost all spherical in shape. Both two observations confirm that this type of rock was originally water-wet.

#### ***8.5.1.2 Grinded powder test***

Figure 8.4 shows the comparison of changes after 15 days when the grinded powders were treated by the wettability alteration agent (left) or not (right). For the agent-treated rock powders (left), they clung to each other and floated within the water. This observation indicates that the powders very likely became oil-wet and tended to reduce the total surface area in the water. Meanwhile, for the untreated rock powders (right), they sank to the bottom of water in the glass vial as being expected.

This result also shows the wettability alteration agent was chemically bonded on rock surface; drying the treated rock sample at a moderate to high temperature (126°C for 2hr or 70°C for 8hr) does not destroy this bond. Therefore, pentane and water can be removed from the core sample by heating in an oven after each coreflood, without affecting the rock wettability.

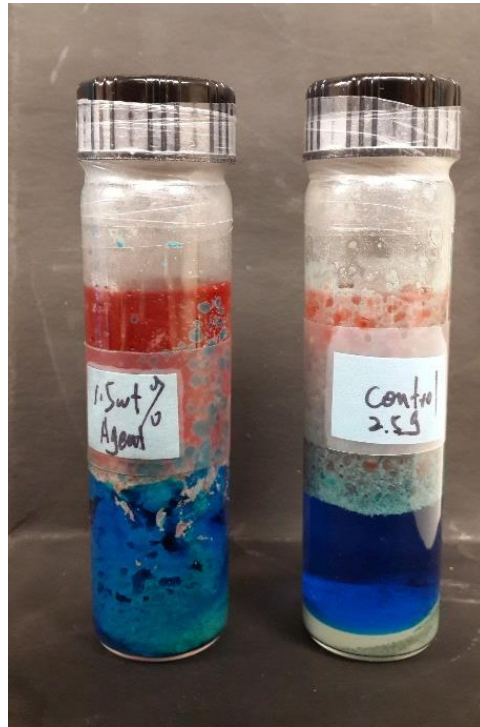


Figure 8.4: Results of grinded powder tests after 15 days when the wettability alteration agent was applied (left) or not applied (right).

### 8.5.2 Water block vs. wettability and IFT at the same hydrocarbon flow rate

In this section, results from Corefloods #1, #3 and #5 are shown to compare the water block at the different wetting states and oil-water IFTs. Among these three corefloods, the same amount of water invaded the same core sample, followed by the flowback and hydrocarbon production at the same flow rate. The only difference was the wetting state of the core sample or the type of water used during the invasion process. Detailed information has been provided in Table 8.2. The target of this comparison was the changes of water saturation and pressure drop across the core in Step-3 of each coreflood; it can reveal the water block during flowback and hydrocarbon production under various conditions.



#### **8.5.2.1 Water invasion (Step-2) at different wetting states and oil-water IFTs**

In Step-2, DI water was injected into the core sample at a constant flow rate (0.4cc/min) to simulate the fracturing fluid invasion into rock matrix. The invasion process lasted for 75min, resulting in the final water saturation of 17.1% (0.171PV). CT scans were conducted at 0min (0PV), 15min (0.34PV), 45min (0.103PV) and 75min (0.171PV) with the scanning parameters introduced in the section of “coreflood schemes” (Section 8.4.2).

##### **(1) Water invasion into water-wet rock without IFT reduction (Coreflood #1)**

In this coreflood, the core sample was at its native water-wet state. Figure 8.5 shows the change of water saturation profile measured from CT scans at different time slices during DI water invasion. As can be observed in this figure, water saturation increased with time from the fracture face where water flowed in; it became almost uniform in space until it dropped quickly to zero, which was  $S_{wi}$  of this test. For convenience, the following names are given to refer to the specific sections of the water saturation profile, as shown in Figure 8.5: the position where water saturation changes abruptly in space is named as *the invasion front*; the portion of the core sample that is from the fracture face (0mm) till the invasion front is named as *the invaded region*; the portion of the core sample that has not contacted with water as named as *the uninvaded region*.

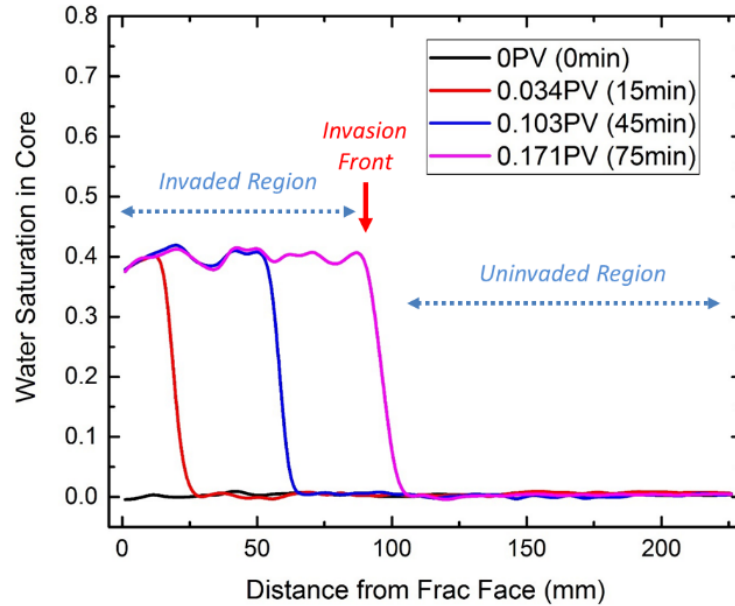


Figure 8.5: Change of water saturation profile during DI water invasion into the core sample at the water-wet state (Step-2, Coreflood #1).

When DI water displaced pentane in such a water-wet system, the invasion front advanced with time, leaving a relatively uniform water saturation in the invaded region; this indicates a piston-like/favorable displacement by virtue of the viscous force dominated flow. At the end of the invasion, water saturation plateaued at about 40% within the invaded zone (i.e., 60% of pentane remained undisplaced).

The black line in Figure 8.6 shows the pressure drop across the core during this invasion process, while the other two lines will be discussed in later sections. Since the pressure drop for pentane injection was designed as the positive direction, water injection from the opposite direction gave a negative pressure drop as shown in this figure. The pressure drop across the core linearly increased with time as the region invaded by water linearly increased with time (Figure 8.5); this also indicates that water invasion was a piston-like/favorable displacement.

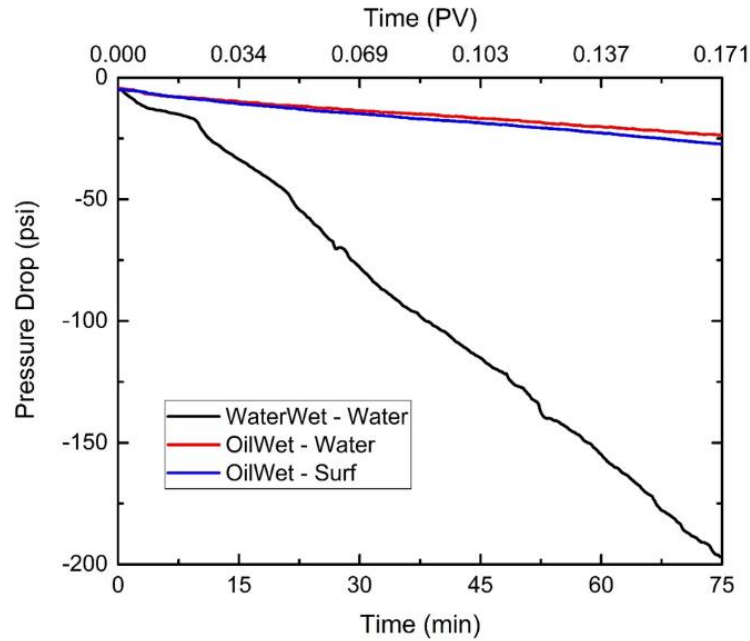


Figure 8.6: Comparison of changes of pressure drop across the core during fracturing fluid invasion under various conditions (Step-2, Corefloods #1, #3 and #5).

### (2) Water invasion into oil-wet rock without IFT reduction (Coreflood #3)

Prior to this coreflood, the core sample was aged in 1.5wt% cyclohexanepentanoic acid and altered into oil-wet. The identical coreflood sequence was conducted as in Coreflood #1, and Figure 8.7 shows the change of water saturation profile at different time slices during the step of DI water invasion. Comparing to the ones for the water-wet state, water saturation profiles for the oil-wet state were not uniform in space, indicating this step was no longer a favorable displacement. Water saturation increased up to 50% in the end of the invaded region (<5mm from the fracture face). These observations are consistent with the change of rock wettability: when water becomes the non-wetting phase, it tends to flow in bigger pores; therefore, water permeability is increased as well as the mobility ratio, resulting in an unfavorable displacement to pentane.

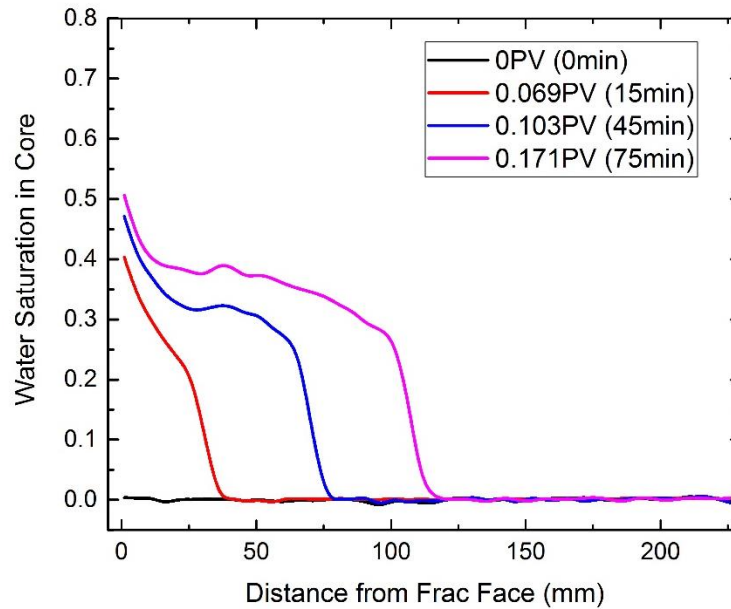


Figure 8.7: Change of water saturation profile during DI water invasion into the core sample at the oil-wet state (Step-2, Coreflood #3).

The pressure drop across the core during water invasion for the oil-wet state is shown by the red line in Figure 8.6. It was 7 times smaller than the one for the water-wet state. This also indicates the increase of water permeability as well as the mobility ratio once the core sample was altered from water-wet into oil-wet.

### (3) Water invasion into oil-wet rock with IFT reduction (Coreflood #5)

In this coreflood, 1wt% surfactant solution, instead of DI water, was used as the mimicked fracturing fluid. Figure 8.8 shows the change of water saturation profile at different time slices when surfactant solution invaded the oil-wet core sample. In this case, water saturation near the invasion front (>25mm from the fracture face) behaved similar to the case when only DI-water was used as the mimicked fracturing fluid (Figure 8.7). Within the invaded zone, water saturation profile discontinued at around 25mm from the fracture face; behind this point (towards the fracture face), water saturation increased from 35% to

around 77%. These changes in water saturation profile were analogous to the case when the same surfactant solution was used for the water-wet systems (Liang et al., 2016); in that work, they were attributed to the retardation of surfactant ( $>25\text{mm}$  from the fracture face) and capillary desaturation of oil phase ( $<25\text{mm}$  from the fracture face). In addition, since the residual oil saturation within the invaded zone was reduced, the total invasion depth was also reduced when the same amount of fluid invaded the core sample.

The pressure drop across the core during surfactant solution invasion for the oil-wet state is shown by the blue line in Figure 8.6. It was only slightly larger than the DI water invasion under the same wetting state (27.5psi vs. 23.6psi). The formation of Winsor type-I microemulsion and the increase of local water saturation did not obviously affect the pressure drop in this step.

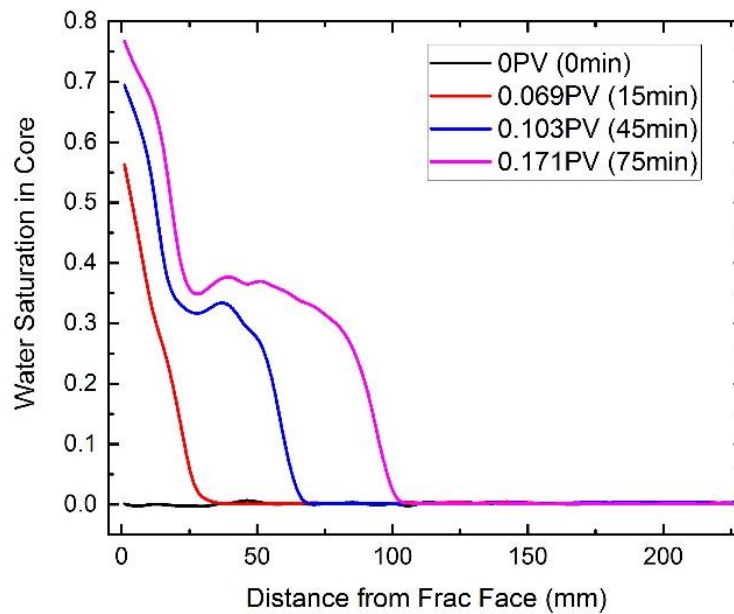


Figure 8.8: Change of water saturation profile during surfactant solution invasion into the core sample at the oil-wet state (Step-2, Coreflood #5).

#### ***8.5.2.2 Flowback and hydrocarbon production (Step-3) at different wetting states and oil-water IFTs***

After invasion step (Step-2) was finished, pentane was injected into the core sample at a constant flow rate (0.2cc/min) to simulate the flowback during hydrocarbon production (Step-3). This step lasted for 36hr (2.469PV), and the changes of water saturation profile as well as the pressure drop across the core were recorded to explore the regaining of rock permeability to hydrocarbon under various conditions.

##### **(1) Flowback from water-wet rock without IFT reduction (Coreflood #1)**

Figure 8.9 shows the change of water saturation profile with time (in PV or real time) after pentane flowed back through the core sample at the water-wet state. During the flowback, water saturation decreased with time within the invaded region (0-100mm from the fracture face in this case); meanwhile, the invasion front propagated further into the originally uninvaded region (>100mm from the fracture face in this case). In addition, it can be noticed that water saturation was retained at a high level (around 35% in this case) near the outlet (<10mm from the fracture face in this case) at least for 0.823PV (12hr), after which it decreased with time. Similar observations have been reported in authors' previous work; water trapping at the fracture face has been attributed to matrix-fracture interaction, and it can dissipate with time through countercurrent imbibition in the water-wet system (Liang et al., 2016).

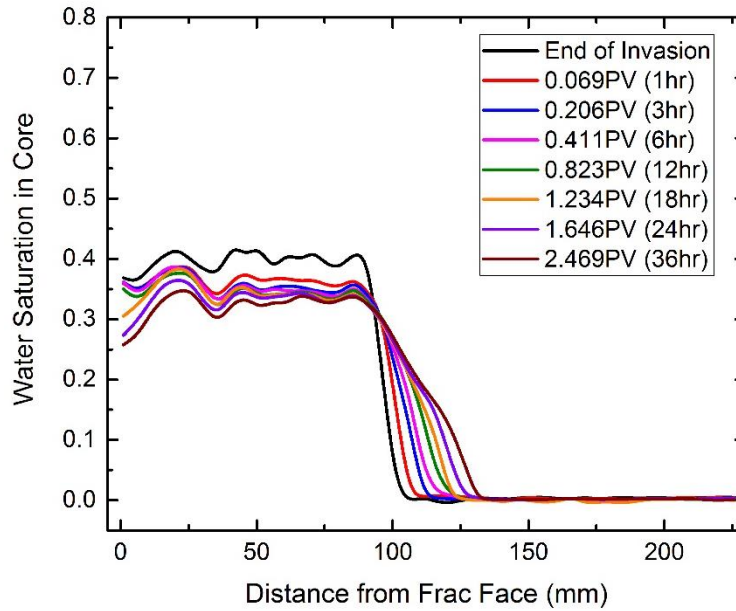


Figure 8.9: Change of water saturation profile during flowback after DI-water invasion into the core sample at the water-wet state (Step-3, Coreflood #1).

By integrating the water saturation profile at a given time shown in Figure 8.9, the total water saturation within the core can be determined at that time. The black discrete data points in Figure 8.10A show the change of the total water saturation within the core after pentane started to flow back during Coreflood #1. It can be noticed that most water was recovered out of the core sample within the first 1.5hr of the flowback, resulting in only around 5% change in water saturation (17.1% to 16.2%).

The black curve in Figure 8.10B shows the change of the pressure drop across the core for the flowback step of Coreflood #1. It can be noticed that the curve abruptly decreased from an early time plateau to another after around 14.5hr (1PV) of pentane flood. Comparing to the results shown in Figure 8.9 and Figure 8.10A, this discontinuous change of the pressure drop was attributed to the clean-up of trapped water at the fracture face through countercurrent imbibition, instead of being recovered out of the core sample.

Both observations agree on authors' previous work as well, and more detailed analysis on water-wet system can be found there (Liang et al., 2016). The other two cases also shown in Figure 8.10 will be discussed in later sections.

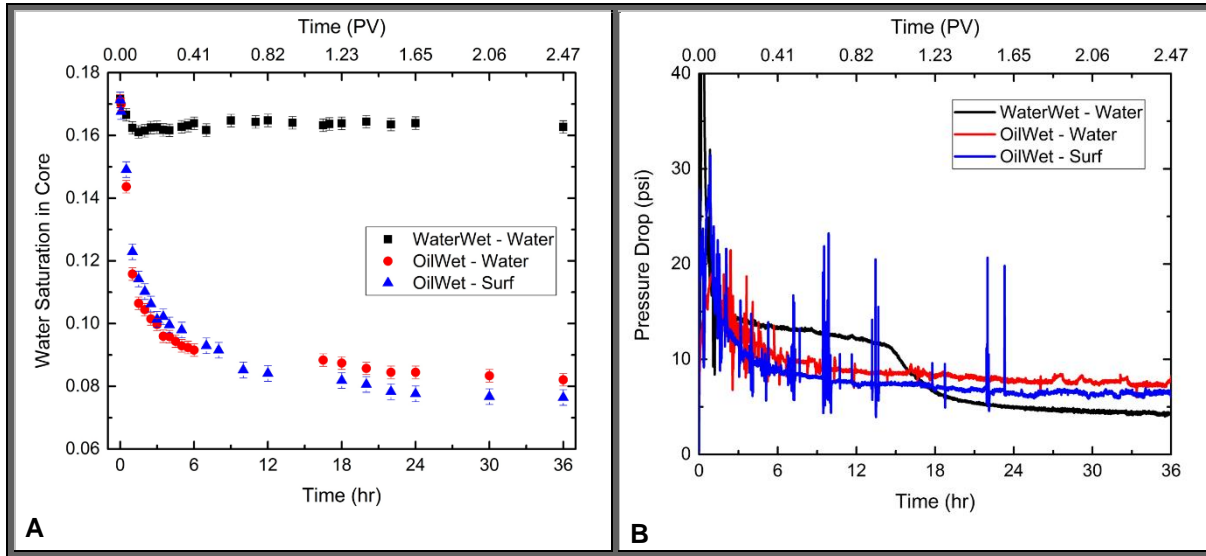


Figure 8.10: Comparison of changes of the total water saturation within the core (A) or the pressure drop across the core (B) during flowback under various conditions (Step-3, Corefloods #1, #3 and #5).

## (2) Flowback from oil-wet rock without IFT reduction (Coreflood #3)

Prior to Coreflood #3, as mentioned already, the core sample was altered from water-wet into oil-wet. After the same amount of DI water invaded the core sample, pentane started to flow back as conducted in Coreflood #1.

Figure 8.11 shows the change of water saturation profile with time (in PV or real time) during Step-3 for such an oil-wet system. As shown in this figure, water saturation decreased uniformly within the entire invaded region; the invasion front did not propagate



further into the originally uninvaded region ( $>110\text{mm}$  from the fracture face in this case). Both support this core sample had been successfully altered into oil-wet.

The red discrete data points in Figure 8.10A show the change of the total water saturation within the core after pentane started to flow back during Coreflood #3. It can be noticed that water was recovered out of the core sample continuously from the beginning, resulting in around 52% change in water saturation (17.1% to 8.2%).

The red curve in Figure 8.10B shows the change of the pressure drop across the core during this step. When the core sample became oil-wet, the pressure drop decreased monotonically towards the steady state. Although its pressure drop was lower comparing to the water-wet case at the early time (16.2hr or 1.11PV in this case), it ended at a level almost twice as high as the water-wet case, indicating a halved rock permeability to pentane.

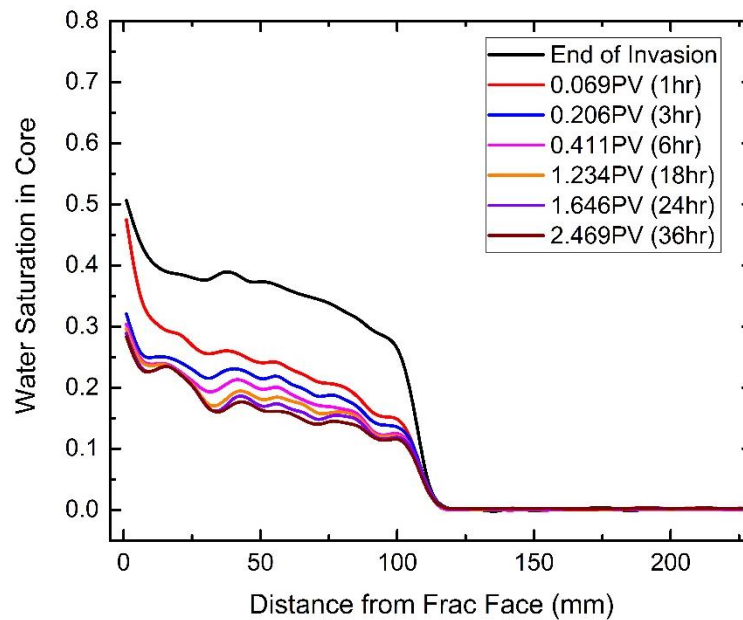


Figure 8.11: Change of water saturation profile during flowback after DI-water invasion into the core sample at the oil-wet state (Step-3, Coreflood #3).

### **(3) Flowback from oil-wet rock with IFT reduction (Coreflood #5)**

In this coreflood, 1wt% surfactant solution, instead of DI water, was used as the mimicked fracturing fluid. Then pentane started to flow back through the core sample as conducted in Coreflood #1 and Coreflood #3.

Figure 8.12 shows the change of water saturation profile with time (in PV or real time) during Step-3 of Coreflood #5. Although water saturation profile discontinued at around 25mm from the fracture face, water saturation decreased uniformly within the entire invaded region. Similar to Coreflood #3, the invasion front did not propagate further into the originally uninvaded region (>100mm from the fracture face in this case).

The blue discrete data points in Figure 8.10A show the change of the total water saturation within the core after pentane started to flow back during Coreflood #5. It can be noticed that water was recovered out of the core sample continuously from the beginning, resulting in around 56% change in water saturation (17.1% to 7.6%). Comparing to Coreflood #3, flowback water was further increased by 6.7% (15.575cc vs 16.625cc) owing to IFT reduction.

The blue curve in Figure 8.10B shows the change of the pressure drop across the core during this step. When surfactant was used, the pressure drop was slight reduced for the oil-wet condition. As the comparison in this figure, pressure drops in both oil-wet cases, with or without using surfactant, were lower than the water-wet case at the early time (16.2hr/1.11PV or 17.4hr/1.19PV); however, they both ended with higher pressure drops than the water-wet case, indicating lower rock permeabilities to pentane under oil-wet conditions.

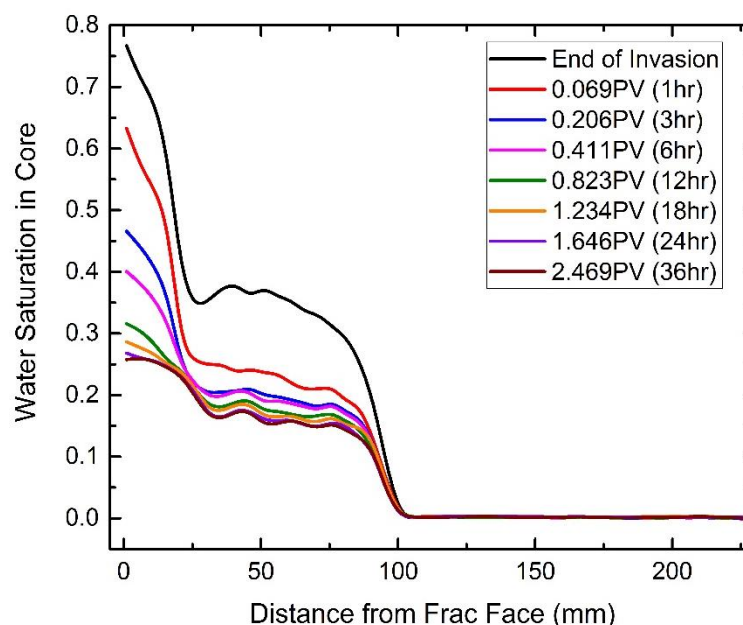


Figure 8.12: Change of water saturation profile during flowback after surfactant solution invasion into the core sample at the oil-wet state (Step-3, Coreflood #5).

### 8.5.3 Water block vs. flow rates under different wettability

In this section, results from Coreflood #2 and Coreflood #4 are shown to compare with the ones from Coreflood #1 and Coreflood #3 respectively. Among these four corefloods, the same amount of water invaded the same core sample, either water-wet or oil-wet; then pentane flowed back through the core at constant flow rates, either at 0.1cc/min or 0.2cc/min. Detailed information about each coreflood has been provided in Table 8.2. The target of this comparison was to explore the severity of water block during flowback and hydrocarbon production under different drawdowns in the water-wet or oil-wet system.

#### ***8.5.3.1 Flowback and hydrocarbon production (Step-3) under different drawdowns for water-wet rock (Coreflood #2 vs. Coreflood #1)***

Comparing to Coreflood #1, the same amount of DI water invaded the same water-wet core sample in Coreflood #2; then pentane started to flow back at half the flow rate (0.1cc/min). Therefore, both cases behaved identical in Step-2 and only results from Step-3 are shown below.

Figure 8.13 shows the change of water saturation profile with time (in PV or real time) during the flowback step of Coreflood #2. Similar to the results of Coreflood #1 (Figure 8.9), water saturation decreased with time within the invaded region (0-100mm from the fracture face in this case); meanwhile, the invasion front propagated further into the originally uninvaded region (>100mm from the fracture face in this case). However, in Coreflood #2, the retained water saturation at the fracture face decreased at an earlier time (before 12hr/0.411PV) of pentane flood. In short, the higher the production drawdown, the longer it will take to dissipate the trapped water near the fracture face in the water-wet system.

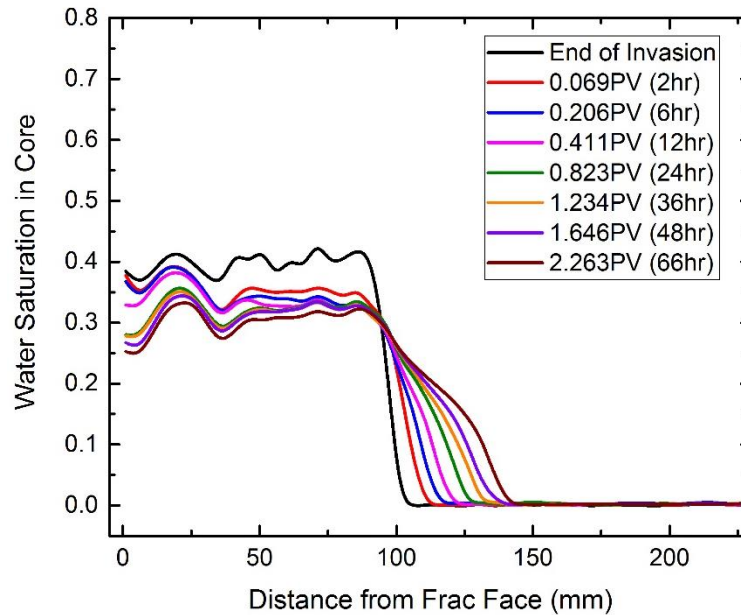


Figure 8.13: Change of water saturation profile during flowback (flow rate=0.1cc/min) after DI-water invasion into the core sample at the water-wet state (Step-3, Coreflood #2).

The red discrete data points in Figure 8.14A show the change of the total water saturation within the core after pentane started to flow back in Coreflood #2; it compares with the change in Coreflood #1, which is shown by the black discrete data points in the same figure. Water saturation in both cases changed from 17.1% to around 16.2% after 2.5PV of pentane flood, giving the same amount of flowback water out of the core sample.

The pressure drop across the core during this step in Coreflood #2 is shown by a red curve in Figure 8.14B. Comparing to the pressure drop in Coreflood #1 (black curve), it can be noticed that both curves have abrupt changes from one early plateau to another; however, when pentane flow rate was doubled from 0.1cc/min to 0.2cc/min, the time of this change was more than doubled: it increased from about 0.3PV to 1PV.

Two more cases in the oil-wet state are also shown in Figure 8.14B for comparison, and they will be discussed in the next section.

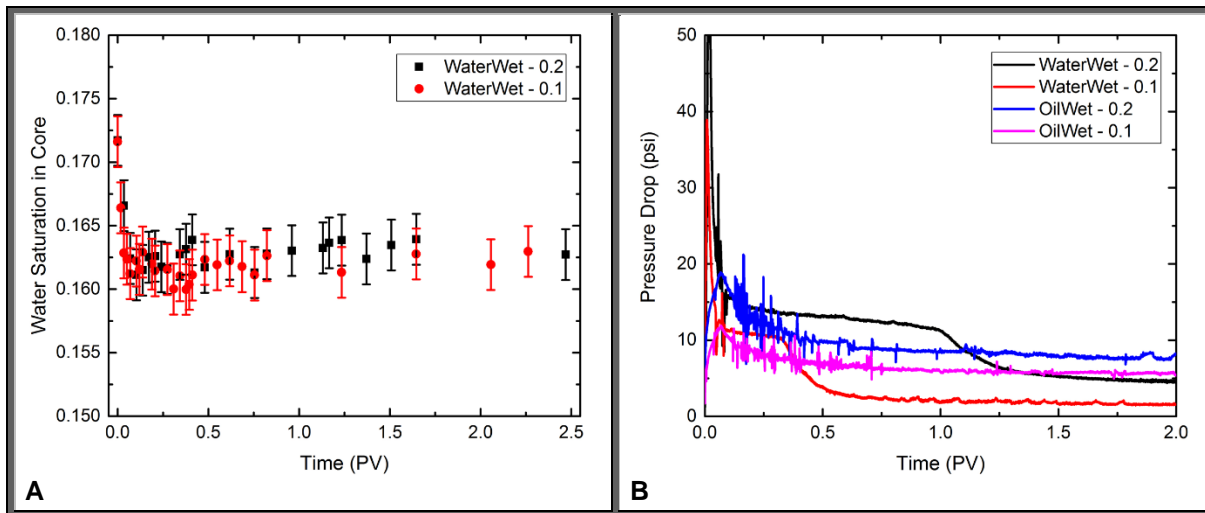


Figure 8.14: Comparison of changes of the total water saturation within the core (A) or the pressure drop across the core (B) during flowback under various conditions (Step-3, Corefloods #1-#4).

#### 8.5.3.2 Flowback and hydrocarbon production (Step-3) under different drawdowns for oil-wet rock (Coreflood #4 vs. Coreflood #3)

Similarly, after the core sample was altered into oil-wet, the lower flow rate of 0.1cc/min was also tested as in Coreflood #4; this was compared with the result in Coreflood #3 in order to explore the impact of drawdown on water block in the oil-wet system.

Pressure drops across the core in both cases are shown in Figure 8.14B for comparison: the blue curve represents the pressure drop during the flowback at 0.2cc/min, while the magenta curve represents the pressure drop during the flowback at 0.1cc/min. Both curves decreased uniformly with time and no discontinuity was observed as in water-wet cases. When flow rate was doubled from 0.1cc/min to 0.2cc/min, the pressure drop was less than doubled (from 5.67psi to 7.62psi); this indicates an improved rock

permeability to pentane, which is elaborated in the later section. For flowback at the same flow rate but different wettability, pressure drop curves intersected each other; the oil-wet state resulted in a lower pressure drop at the early time, but a higher one at the late time.

## **8.6 DISCUSSION**

### **8.6.1 Permeability regaining as a function of wettability and IFT**

After water invaded the core sample, pentane started to flow towards the opposite direction, resulting in the flowback of water as well as the regaining of rock permeability to hydrocarbon. Because of the high mobility ratio during this process, pentane breaks through the water invaded region very fast ( $<0.1$  PV in this study), both for water-wet and oil-wet states. Therefore, from the pressure drop curves shown in Figure 8.10B, the regained rock permeability to pentane can be estimated from single phase Darcy's Law, as shown in Figure 8.15.

#### ***8.6.1.1 Water block and permeability regaining in the water-wet state***

In the water-wet state, it has been found that the shape of water saturation profile, instead of the total water saturation in place, mainly impacts the permeability regaining during the early time of flowback; matrix-fracture interaction causes water trapping near the fracture face and results in water block (Liang et al., 2015a, 2016). However, this type of water block can be naturally cured with time once water saturation profile is redistributed through countercurrent imbibition. As the black curve shown in Figure 8.15, the regained relative permeability  $k_{ro}$  increased from 0.15 to 0.45 without a change of the total water saturation in the core sample (black discrete data points in Figure 8.10A).

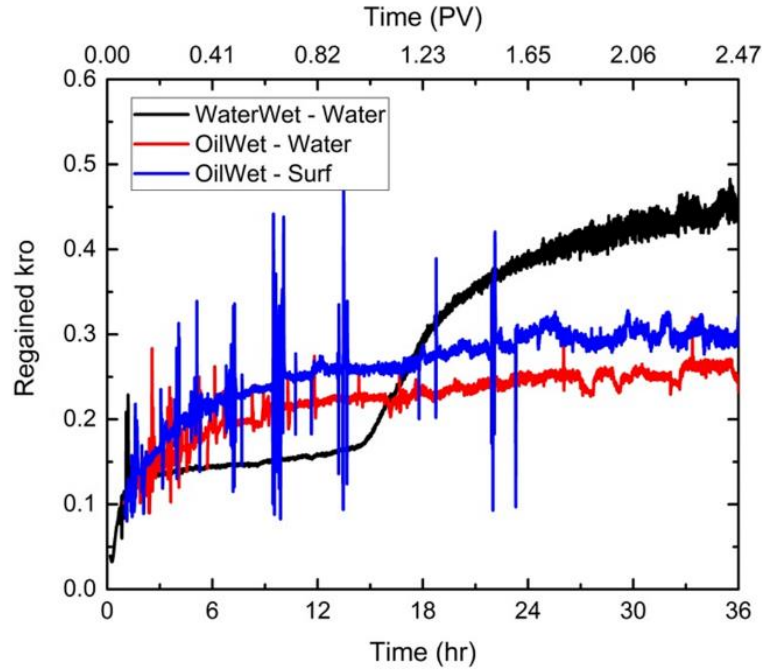


Figure 8.15: Comparison of changes of regained permeability to pentane under various conditions.

#### 8.6.1.2 Water block and permeability regaining in the oil-wet state

For the same porous media in the oil-wet state, the regained relative permeability  $k_{ro}$  increased monotonously to 0.26 after 2.5PV of pentane flood, as shown by the red curve in Figure 8.15. Although the flowback in this case was about 9 times higher than the water-wet case (15.175cc vs. 1.575cc, also see Figure 8.10A), its late time relative permeability was 42% less than the water-wet case (0.26 vs 0.45). For the oil-wet case, trapped water tends to locate in bigger pores; it forces oil to flow through smaller pores, resulting in a lower relative permeability to oil comparing to the water-wet case.

In addition, neither an abrupt change in  $k_{ro}$  nor an extra volume of trapped water near the fracture face was observed in the oil-wet case; the regained permeability was



increasing toward a plateau with the decrease of water saturation in the core. Since the type of water block caused by matrix-fracture interaction did not exist in the oil-wet case, its regained permeability was higher than the water-wet case at the early time (0.26 vs. 0.15 before 1.2PV). Considering that the length of this “early time” is scaled to  $\sqrt{k/\phi}$  for the same amount of invaded water (Liang et al., Submitted), the tighter the rock is, the longer the production benefits from the oil-wet state.

In short, flowback from the oil-wet case is much more than the water-wet case, however, its regained permeability can be either more or less than the water-wet case, depending on the stage of flowback. Therefore, the forms of water block vary in the oil-wet and water-wet systems, and the amount of flowback cannot be used for judging the quality of well stimulation.

#### ***8.6.1.3 Using surfactants for oil-wet reservoirs: reducing IFT or altering wettability?***

The blue curve in Figure 8.15 shows the permeability regaining when surfactants were used to reduce oil-water IFT for the oil-wet state. The regained relative permeability to oil was improved to 0.30 after 2.5PV, which was 15.4% higher than the DI water case. However, it was still smaller than the permeability regaining in the late time of the water-wet case. Surfactants mobilize the water trapped by capillarity so as to enhance the rock permeability; for tighter reservoirs that the production drawdown is even less, the enhancement from IFT reduction might be more significant. Nevertheless, this requires more in-depth studies.

When the oil-wet rock is completely altered into water-wet, regained permeability at the steady state will be enhanced but the amount of flowback water will be significantly reduced. However, before the steady state is achieved, permeability reduction due to

matrix-fracture interaction may take place, depending on the change of IFT (Liang et al., 2015b). Nevertheless, both technical and economic considerations need to be taken before using surfactants to alter the wettability; they include the extra loss of water and surfactants into the reservoir rock, the effectiveness of wettability alteration for rocks with complicated mineralogy, the degree of IFT reduction and the potential of forming unstable macroemulsions.

### 8.6.2 Permeability regaining as a function of drawdown in water-wet or oil-wet states

In a similar way, the regained rock permeability to pentane under different drawdowns can also be estimated from Figure 8.14B and single phase Darcy's Law. Since different flow rates change the calculation of flooded pore volumes, the comparisons with time in pore volumes and real time are both shown in Figure 8.16.

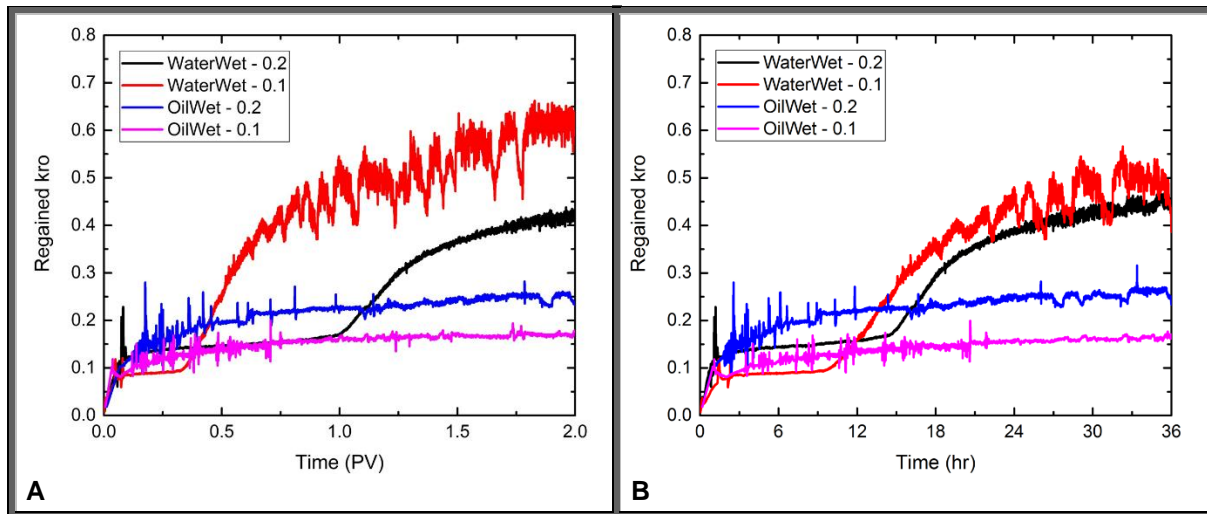


Figure 8.16: Comparison of changes of regained permeability to pentane with time (in pore volumes (A) or hours (B)) under various conditions.

In the water-wet state, higher flow rate (drawdown) resulted in higher permeability regaining during the early time plateau (when the water block due to matrix-fracture interaction was not cleaned up yet); however, it resulted in lower permeability regaining at the late time (black and red curves shown in Figure 16A). Since the mitigation of water block at the early time is driven by countercurrent imbibition, a higher drawdown in the opposition direction delays the imbibition process, and thus the permeability regaining. Once capillary force removes the trapped water at the fracture face, a similar steady state will be achieved regardless of the viscous force, and thus the regained permeability to oil. This can be seen more or less from their late time  $k_{ro}$  shown in Figure 16B.

In the oil-wet state, on the other hand, the relationship between drawdown and permeability regaining is more straightforward: the higher the drawdown, the higher the regained permeability during the entire period of the flood. This confirms that water block in the oil-wet state is mainly attributed to the bypassed water; to mobilize this water, it must either increase the production drawdown or decrease the oil-water IFT.

In short, production drawdown impacts the permeability regaining after hydraulic fracturing differently in water-wet or oil-wet reservoirs; higher drawdown does not always give rise to a smaller permeability reduction due to the invaded water.

## 8.7 CONCLUSIONS

A coreflood setup was designed in this work that can simulate fracturing fluid invasion, flowback and hydrocarbon production; pressure drop measurement and real-time CT scans were coupled to explore the mechanisms behind the formation and mitigation of water block in rock matrix. 1.5wt% cyclohexanepentanoic acid in n-pentane was proved to be able to alter a natively water-wet Indiana Limestone core sample into oil-wet; this core

sample was tested through an identical experimental procedure before and after this wettability alteration, which provided a straightforward comparison of water block in both wetting states. A microemulsion-forming surfactant was then tested in the core sample at the oil-wet state, also through the identical experimental procedure; this provided another straightforward comparison on rock permeability regaining from either one of these two approaches on the same porous media.

The key findings are summarized as follows.

1. Aging in cyclohexanepentanoic acid can alter natively water-wet Indiana Limestone core into oil-wet; this agent was strongly bonded on rock surface that high temperature above its boiling point does not destroy the bond.
2. Water block in the water-wet state is mainly caused by matrix-fracture interaction; however, it can be naturally cured over time through countercurrent imbibition.
3. Comparing to the water-wet state, water block in the oil-wet state is more serious and the late-time permeability is much lower (42% less in this case), although its flowback is much more (9 times more in this study).
4. When rock mineralogy and its distribution of wettability are not fully understood, the amount of flowback cannot be used for judging the degree of permeability recovery.
5. Using IFT reducing surfactants in the oil-wet state generates more flowback and higher permeability regaining; however, this regained permeability is still not as high as the water-wet case.

## Chapter 9: Exploration of the Relationship between Flowback and Permeability Enhancement<sup>7</sup>

The amount of flowback is sometimes used to forecast the quality of hydraulic fracturing job as well as the production enhancement in the field. However, as the previous chapter showed, more flowback can lead to either lower or higher production rate due to the uncertainty of rock mineralogy/wettability. This chapter presents a study to show the impact of another key parameter regarding the initial reservoir condition on the regaining of rock permeability to hydrocarbon during flowback. Generally speaking, even only from the viewpoint of multiphase flow in porous media, the amount of flowback cannot be used for judging the quality of overall well stimulation.

### 9.1 QUICK OVERVIEW OF THIS CHAPTER

Only a small fraction of fracturing fluid is recovered as flowback after hydraulic stimulation of low permeability formations. From the point of view of relative permeabilities, the minimization of fracturing fluid losses is desirable to maximize the flow of hydrocarbon. On the other hand, field observations indicate that wells where less fracturing fluid is recovered as flowback performed better in production, leading to an apparent contradiction. We present a physics-based model that can account for both observations. Our model is the result of an experimental investigation using a coreflood sequence that simulates fracturing fluid invasion, fluid flowback and hydrocarbon recovery in a hydrocarbon-rich, hydraulically-fractured reservoir. We elucidate the interplay

---

<sup>7</sup> This chapter is based on the following paper:

Longoria, R.A., **Liang, T.**, Nguyen, Q.P., DiCarlo, D.A., 2015. When Less Flowback Is More: A Mechanism of Permeability Damage and Its Implications on the Application of EOR Techniques. SPE-178583-MS. doi:10.2118/178583-MS

between capillary suction and viscous displacement of the fracturing fluid and the impact of water block on hydrocarbon permeability. This model reveals the inherent relationship between flowback and hydrocarbon production for different initial petrophysical properties.

## **9.2 INTRODUCTION**

A large volume of water-based fracturing fluid is pumped downhole during hydraulic fracturing operations, however, only a small fraction of it is usually recovered as flowback. Although unconventional reservoirs are characterized by low or ultra-low permeabilities, several recent studies have shown that imbibition of water-based fluids, while slow, can be significant (Bostrom et al., 2014; Dutta et al., 2014) and thus, at least part of the lost fracturing fluid is believed to invade the formation via spontaneous imbibition. Loss of fracturing fluids can affect the reservoir in several ways. For example, a mismatch in salinity or chemistry between the reservoir fluids or mineral composition and the fracturing fluid could lead to clay swelling or formation softening (Das et al., 2014), both believed to negatively affect the flow of hydrocarbons. Another potential mechanism of damage is from capillary trapping of water near the fracture face. Water trapping in tight formations has been studied in the past (Bennion et al., 1996) and permeability damage due to water block has been documented (Tannich, 1975; Abrams and Vinegar, 1985; Bennion et al., 2000).

From the point of view of relative permeabilities, minimization of fracturing fluid invasion is desirable for maximizing the flow of hydrocarbon. However, in some cases where large portions of the fracturing fluid are recovered as flowback, gas production appears hindered while in other cases production is not affected even though very little

fracturing fluid flows back (Shaoul et al., 2011). To make matters worse, long periods of shut-ins, e.g. up to several months in length, are commonly used in the field after hydraulic fracturing. This practice leads to even lower fluid recovery as flowback (Bertoncello et al., 2014) but appears to enhance the production of hydrocarbons. This apparent contradiction and lack of consistency can make it difficult for field operators to come up with well operation plans that optimize production.

Fluid recovery from the matrix during flowback is a competition between the capillary and viscous forces. Due to the small pore size characteristic of unconventional reservoirs, high capillary pressures are expected when both water and hydrocarbon are present, and thus, loss of fracturing fluid via spontaneous imbibition can be significant, especially during long periods of shut-in. Several studies suggest that such shut-ins can help regain permeability after fluid invasion by redistributing the imbibed fracturing fluid further into the reservoir (Le et al., 2012; Bertoncello et al., 2014; Bostrom et al., 2014; Dutta et al., 2014). How this practice relates to long-term fluid recovery as flowback has not been investigated, although the expectation in such cases is to have little to no produced water. On the other hand, several fluid additives aimed to enhance flowback and hydrocarbon permeability have been designed and tested in the laboratory (Zelenev and Ellena, 2009; Penny et al., 2012b; Rostami and Nasr-El-Din, 2014). In these studies, an increase in relative permeability to the hydrocarbon was always accompanied by an increase in fluid flowback, agreeing with expectation from the point of view of relative permeabilities but not necessarily with field observations.

In this work, we perform coreflood experiments using a three-step sequence that simulates fluid invasion, fluid flowback and hydrocarbon production in an initially hydrocarbon-rich formation. In particular, we explore the effect of different initial water saturations of the formation on fracturing fluid loss, recovery as flowback and permeability

damage. Our results show that the observations from the field could be explained purely by a competition between capillary-driven imbibition and viscous displacement, and that whether higher permeability correlates with higher flowback or not is dependent on the initial petrophysical properties of the sample, in particular the difference between the initial and the residual water saturation for a given rock.

### **9.3 MATERIALS AND METHODS**

#### **9.3.1 Rock type and core dimensions**

All experiments were done on Texas Cream Limestone. Cylindrical core samples of 1.5” in diameter and 9.5” in length were obtained from an outcrop block. This rock has a permeability of 5-10mD and a porosity of about 26%. In our experiments, one of the end faces of the core represents the fracture face of a hydraulically fractured reservoir. Before each experiment, the core was dried in an oven at 75°C overnight. The porosity was measured via NMR with a water-saturated 1” by 1” cylindrical core plug. The core samples for corefloods were assumed to have the same porosity as the core plug for the calculation of the pore volume.

#### **9.3.2 Choice of hydrocarbon**

N-pentane was still used as the model hydrocarbon for this study.

#### **9.3.3 Coreflood sequence and experimental setup**

Here we use a three-step coreflood sequence that simulates fluid invasion, flowback and hydrocarbon production from hydrocarbon-rich hydraulically-fractured reservoir.



Here, one of the core faces represents the fracture face of a hydraulically-fractured reservoir. The coreflood steps are as detailed below.

***Step-1 – Establishing a hydrocarbon-rich reservoir***

A dry and evacuated limestone core was fully saturated with pentane first. The absolute permeability of the core was measured during this step. The pentane flood was followed by injection of a predetermined amount of water from the face of the core opposite to that where pentane was injected. The amount of water injected in this step corresponded to the target initial water saturation. The system was then shut-off overnight; this aging allowed for redistribution of water towards a more uniform water saturation profile via spontaneous imbibition. This water represents the initial (connate) water saturation of the reservoir.

***Step-2 – Simulating fracturing fluid invasion***

Following Step-1, a slug of water equal to 20% of the core's pore volume was injected at 0.1ml/min (i.e., Darcy velocity  $u=1.51E-6$ m/s). Again, the slug of water was injected from the face opposite to that where pentane is injected. The slug of water injected in this step represents the fracturing fluid lost to the formation during the fracturing operation. The volume of injected fracturing fluid was kept constant across the experiments to elucidate the effect of different initial water saturations of the core.

***Step-3 – Simulating fracturing fluid flowback and hydrocarbon production***

After Step-2, the core was again flooded with pentane to displace some of the water in the core. The flow rate of pentane was set to 0.1cc/min (i.e., Darcy velocity  $u=1.51E-6$ m/s) during this step. The recovered water mass and pressure drop across the core were recorded during this step. The effective permeability to the hydrocarbon after the flowback

ended was calculated from Darcy's law, the known viscosity of pentane and the core's geometry.

Figure 9.1 shows an illustration of the three-step coreflood sequence (Figure 9.1A) and a schematic of the coreflood experimental setup (Figure 9.1B).

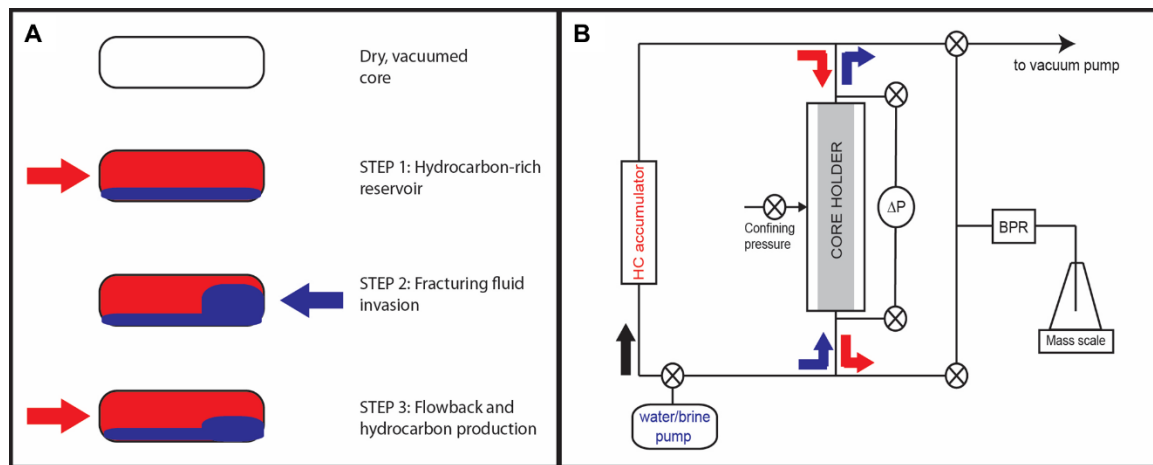


Figure 9.1: Schematic of coreflood sequence and setup. A) A three-step coreflood sequence that simulates fracturing fluid loss, fluid flowback and production from a hydraulically-fractured reservoir was developed. B) Hydrocarbon and water are injected through opposite faces of the core. The core face from which water is injected represents the fracture face of a hydraulically-fractured reservoir.

## 9.4 RESULTS AND DISCUSSION

The relationship between the amount of flowback (i.e., recovered injected water as the mimicked fracturing fluid) and regained rock permeability to hydrocarbon was studied via a three-step coreflood sequence that simulates fluid invasion, flowback and hydrocarbon production from hydrocarbon-rich hydraulically-fractured reservoir. We began this work by studying the relationship between initial water saturation and the

effective hydrocarbon permeability after fluid invasion and flowback. As described in the section of “materials and methods” (Section 9.3), a predetermined amount of water was introduced into a 100% hydrocarbon (i.e., n-pentane) saturated core. Four different initial water saturations values were used: 0%, 10%, 20% and 30%. After the aging process, a slug of water (20%PV) was injected to simulate a fixed amount of fracturing fluid lost to the formation immediately followed by a hydrocarbon flood to simulate flowback and hydrocarbon production. Figure 9.2 shows the effective hydrocarbon permeability after 1PV of hydrocarbon flowed through the core as a function of final average water saturation of the core sample (i.e. end of flowback). As expected, the permeability to hydrocarbon decreases with increasing water saturation of the core.

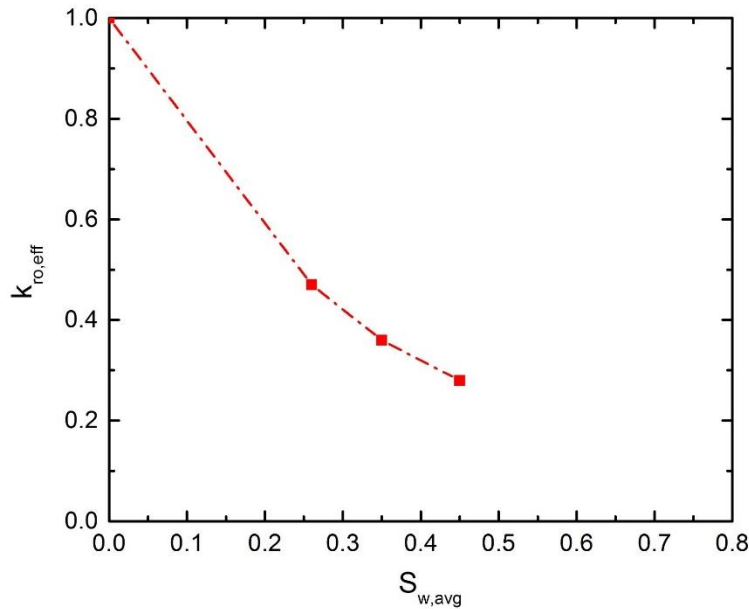


Figure 9.2: Effective relative permeability to hydrocarbon as a function of average water saturation of the core sample. The final water saturation is the result of the initial water saturation plus a slug of water injection (0.2PV) minus the total recovered water during flowback for 1PV.

On the other hand, the amount of recovered water as flowback can be quantified for each initial water saturation of the core. Figure 9.3 shows the percentage of flowback (relative to the injected slug volume) as a function of initial water saturation of the core. Here, the amount of flowback increased with increasing initial water saturation of the core. However, when the relationship between the regained rock permeability to hydrocarbon and the total flowback was plotted, it can be found that the permeability was decreasing with increasing fluid recovery rate as shown in Figure 9.4.

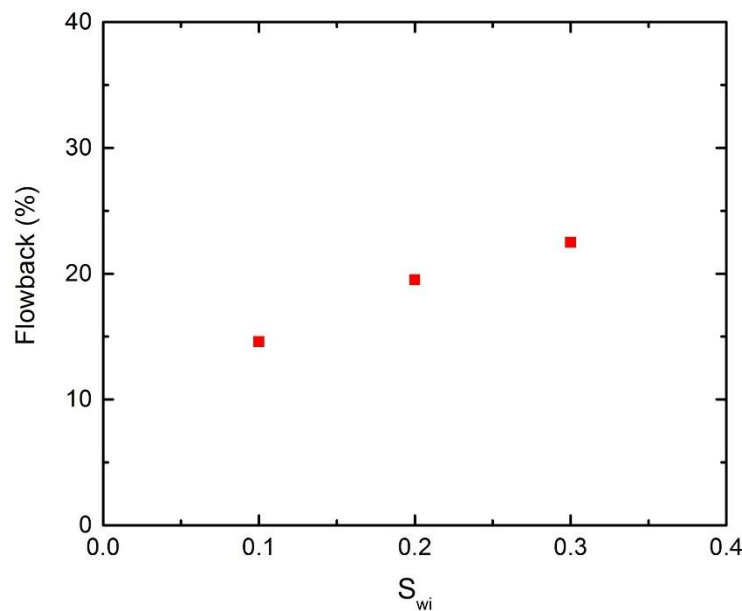


Figure 9.3: Flowback vs. initial water saturation ( $S_{wi}$ ). A 0.2PV water slug was injected into cores with different initial water saturations. The amount of fluid recovered as flowback increases with increasing initial water saturation of the core. The recovered flowback is reported as a percent of the injected water slug volume.

As mentioned in the Introduction, significant fluid losses via spontaneous imbibition can be expected from tight formations. Capillary pressures increase with decreasing water saturation, and thus, for a given water-wet rock, lower initial water

saturations would result in higher water imbibition rates. On the other hand, as long as the local water saturation is below the residual level, any imbibed water will not be recoverable during the flowback phase. It is this competition between capillary-driven imbibition and viscous drainage (during the flowback step) that gives rise to the observed relationships among flowback, regained rock permeability to hydrocarbon and initial water saturation of the rock sample.

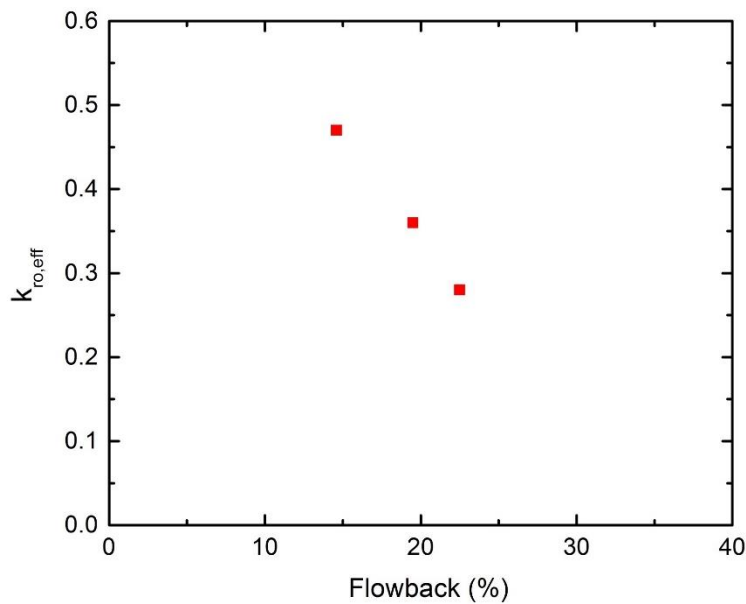


Figure 9.4: Effective hydrocarbon permeability vs. recovered flowback. A 0.2PV water slug was injected into cores with different initial water saturations. The hydrocarbon permeability was calculated after 1 PV of hydrocarbon flowed through the core and decreases with increasing fluid recovery during flowback. The recovered flowback is reported as a percentage of the original volume of water injected.

It is important to mention that although the calculation of rock permeability to hydrocarbon shown here was done after the flowback step had almost finished (i.e. no more water was detected as effluent), and thus the overall water saturation of the core sample

was not changing anymore. This calculation tells the effective relative permeability to hydrocarbon since the water saturation distribution in the core was not necessarily uniform at that moment. Indeed, several simulation studies have shown that the permeability to hydrocarbon continues to increase with production time due to the continuous imbibition of the fluid from the near fracture region into further in the reservoir (Le et al., 2012; Bertonecello et al., 2014).

Figure 9.5 shows the pressure drop across core as a function of time where a 20%PV water slug was injected into cores with different initial water saturations. Strikingly, the region with higher pressure drop (and thus lower rock permeability to hydrocarbon) extended longer in time with higher initial water saturations. Once again, although the major water block eventually dissipated in all three cases, higher initial water saturations resulted in lower imbibition rates (due to low capillary pressure gradients) and thus longer-lived periods of water-blocked production. For the same reason, while a well shut-in would result in higher rock permeability to hydrocarbon, the length of the required shut-in increases with increasing initial water saturation. This result also indicates that a lower regained permeability accompanied with a higher amount of flowback should be expected for reservoirs with smaller permeability where water redistribution is limited (see details in Section 4.4.4). Like initial water saturation, rock permeability and pore size distribution can also affect the imbibition process and thus impact the relationship between the amount of flowback and the hydrocarbon production rate; however, this is beyond the scope of this study.

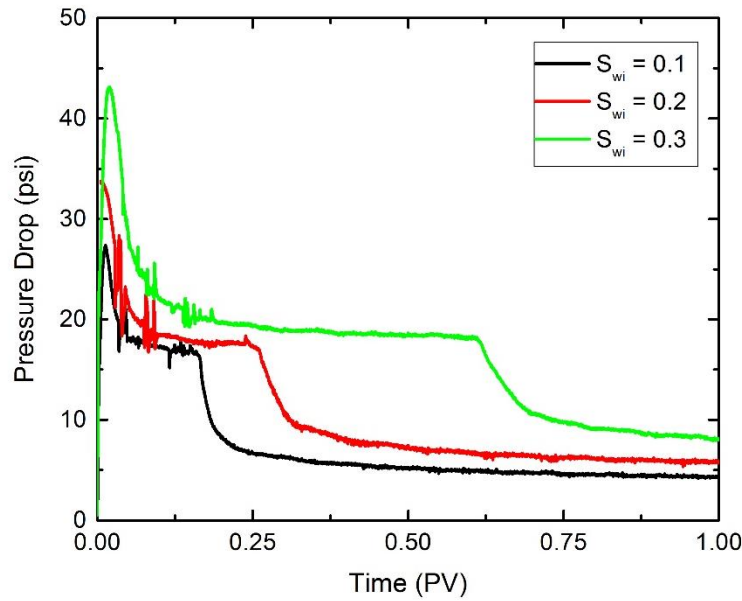


Figure 9.5: Pressure drop across core during flowback and production phase (Step-3) as a function of time (in pore volumes, PV) for different initial water saturations. A 0.2PV water slug was injected into cores with different initial water saturations. In all cases, the flowback phase began immediately after the slug-sized water injection.

## 9.5 CONCLUSIONS

The relationship among initial water saturation, rock permeability to hydrocarbon and flowback was studied experimentally via a three-step coreflood sequence in a low permeability rock. Our results show that capillary-driven dissipation via water imbibition can lead to low water recovery during flowback. Furthermore, with everything else being the same, the initial water saturation of the rock is the controlling parameter that determines how much water is recovered as flowback as well as the permeability damage due to water block near the fracture face. Due to the small pore sizes characteristic of unconventional rocks, their capillary pressure curves are expected to be very pronounced at low water saturation values. On the other hand, the driving force for capillary-driven imbibition is

proportional to the local gradient of capillary pressure, and thus, one could imagine significantly higher imbibition forces even for small reductions of initial water saturation. In field operations, this could translate to large variability in fluid flowback for different wells within a single field even when well logging/characterization techniques show similar initial conditions. In the long run, the ability to better predict production from unconventional reservoirs will likely necessitate the development of newer and more sensitive special core analysis, as well as reservoir characterization techniques.

It is important to note that while our work was performed on a low permeability carbonate rock, the physical model here described is believed to be directly applicable to any other rock type as long as a scaling of petrophysical parameters is properly performed. For example, different permeability and porosity values will change the length and time scales of the problem, e.g. the imbibition rates and depth of initial fluid invasion, however, they are not expected to change the governing physics of the problem. On the other hand, the wetting state of the formation (i.e., distribution of mixed wettabilities) can play a much more critical role since it determines the extent to which water-based fracturing fluid is spontaneously imbibed in rock matrix.

In summary, the amount of flowback is not linearly correlated with the enhancement of rock permeability to hydrocarbon, so it cannot be applied for judging the quality of well stimulation.



## **Chapter 10: Conclusions and Potential Future Work**

This chapter concludes the main findings of the completed work, and further gives some pertinent recommendations for the potential future work.

### **10.1 CONCLUSIONS OF THE COMPLETED WORK**

In this study, a three-step coreflood platform is developed to comprehensively understand water block from hydraulic fracturing in low permeability rocks under various reservoir/production conditions. This platform also provides a new avenue to compare the efficiency and effectiveness of various mitigation methods under different conditions, so that their governing mechanisms can be elucidated from the viewpoint of multiphase flow.

The key findings are summarized as follows.

1. For the water-wet portion of the rock matrix, matrix-fracture interaction can play a significant role on trapping the invaded fracturing fluid near the fracture face and thus reducing the rock permeability to hydrocarbon; its impact on permeability reduction increases when the ratio of pressure drawdown to capillary pressure decreases.
2. When water block forms, the shape of water saturation profile, instead of the total water saturation, within the water invaded region determines the degree of rock permeability reduction.
3. Water block due to matrix-fracture interaction can be naturally cured over time through spontaneous imbibition; however, the length of time increases when rock permeability decreases. After this type of water block is cleaned up, imbibition slows down when the residual water saturation is approached asymptotically. This water continues to hinder hydrocarbon production; to

further mitigate this second type of water block, capillary desaturation must be achieved.

4. Shut-in/soaking treatment allows spontaneous imbibition to happen and redistribute the invaded water before hydrocarbon production begins. On one hand, it can increase the initial hydrocarbon production rate, but not the ultimate production; on the other hand, it results in more water invaded into rock matrix that can potentially reduce the ultimate production.
5. When surfactant is used as the fracturing fluid additive, water block due to matrix-fracture interaction can be mitigated; as long as no thermodynamically unstable emulsion is formed, the lower the oil-water IFT, the less the impact of this water block. However, moderate IFT reduction slows down the spontaneous imbibition that helps clean up the trapped water near the fracture face, resulting in longer impact of this water block.
6. When ultralow IFT is achieved by surfactant, matrix-fracture interaction is eliminated and the first type of water block is cleaned up. Among different salinity conditions when different Winsor type microemulsions are formed, type-I condition gives the fastest recovery rate of the invaded water and results in the best enhancement on matrix permeability to hydrocarbon. According to the microfluidic model test, this is because surfactant tends to stay with the invaded water and keeps it being mobilized by hydrocarbon at a lower salinity condition (i.e., type-I condition).
7. For the oil-wet portion of the rock matrix, water block is mainly originated from the capillary-trapped water within the pores, and it has a more serious impact on rock permeability reduction comparing to that in water-wet condition. Using surfactant is very necessary on mitigating such water block; between two

typically surfactant approaches, achieving ultralow IFT seems to be a better option than altering wettability to water-wet for low permeability rocks.

8. Due to the uncertainty of key petrophysical properties of reservoir rock, e.g. mineralogy/wettability, pore size distribution, initial phase saturations, the amount of flowback cannot be used for judging the quality of well stimulation.

## **10.2 RECOMMENDATIONS FOR THE POTENTIAL FUTURE WORK**

To make the findings of this study more practical to people working in the field, the following future work should be considered.

1. Rocks with even lower permeability (i.e., in tens of nanoDarcies to tens of microDarcies), both water-wet and oil-wet, should be tested to further verify the proposed mechanisms on water block. Real shale samples are not suggested to be used unless (1) its initial petrophysical properties are fully characterized (e.g. initial phase saturations, mineralogy/wettability distribution, pore size distribution); (2) its initial state can be fully recovered after each experiment so that repeatable experiments can be conducted on the same rock sample to confirm the reproducibility of results.
2. This work studies water block in the completely water-wet or oil-wet rocks, and it shows their main blocking mechanisms are distinct. In the field, however, water block in mixed-wet rocks are the most common cases people deal with after hydraulic fracturing in unconventional tight reservoirs, like shales. Therefore, it is crucial to evaluate the formation and mitigation of water block in such rocks, as a function of the ratio of water-wet to oil-wet pores and their distribution or interconnection in the small-scale pore network.

3. It will be extremely valuable to create a numerical simulator that includes all proposed physics, and extends the knowledge to tighter rocks and larger scales. Although current commercial reservoir simulators can more or less approximate the impact of matrix-fracture interaction, a more stable simulator is needed that can handle the abrupt change in capillary pressure especially in low permeability rocks that have nanoscaled pores.
4. It will also be valuable to discover the correlation between the depth of water invasion and the length of water block due to matrix-fracture interaction. Together with the impact of water block as a function of rock permeability and wettability, this correlation can help people properly assess the time scale of water block and choose the most effective and efficient mitigation method.
5. The ultimate goal of this study is to establish a systematic criterion of choosing both effective and efficient mitigation methods to clean up water block for various reservoir conditions. Therefore, it is very necessary to conduct a statistical analysis on all reported field applications of different mitigation methods, and evaluate the performance of different methods in the corresponding reservoir/production conditions.

## Nomenclature

- $\theta$ : Contact angle, degree or rad
- $\mu$ : Viscosity of the displacing phase, Pa • s or cP
- $\sigma$ : Interfacial tension between two phases, mN/m
- $\varphi$ : Porosity, dimensionless
- 
- $A$ : Cross-sectional area of the porous media, m<sup>2</sup>
- $k$ : Permeability, m<sup>2</sup> or mD
- $k_r^0$ : End-point relative permeability, dimensionless
- $L$ : Length of the porous media, m or ft
- $n$ : Fluid exponent for Corey-type relative permeability functions, dimensionless
- $\Delta P$ : Pressure drop across the porous media, Pa or psi
- $P_c$ : Capillary pressure, Pa or psi
- $S$ : Saturation, dimensionless
- $S_r$ : Residual saturation in the porous media, dimensionless
- $u$ : Superficial velocity (i.e., Darcy velocity), m/s or ft/day

## Appendix A: Experimental Procedure of Three-Step Coreflood Sequence

### A.1 GENERAL SETUP PARAMETERS

*BPR pressure: ~500psi*

*Confining pressure: ~1500psi*

### A.2 EXPERIMENTAL SETUP

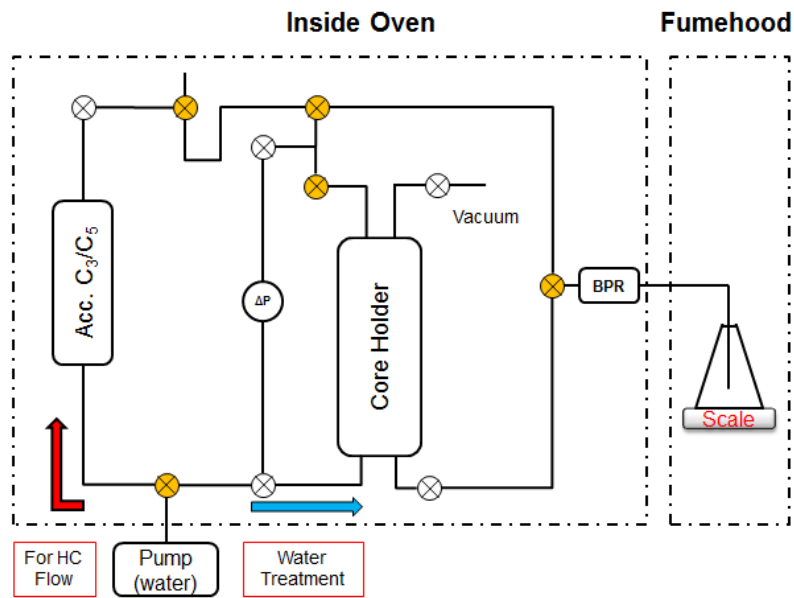


Figure A.1: Schematic of experimental setup when CT scanner is not used.



Figure A.2: Pump used in the coreflood experiments (Jasco PU-2080 HPLC pump).

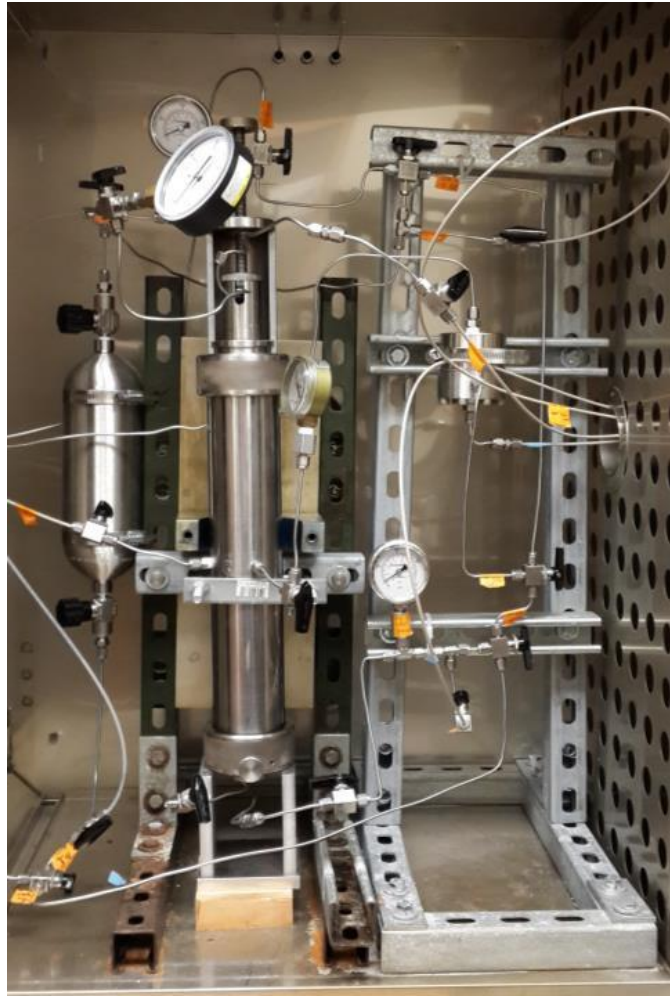


Figure A.3: Coreflood setup inside an oven when CT scanner is not used.





Figure A.4: Coreflood setup when CT scanner is used.

### **A.3 EXPERIMENTAL PROCEDURE (WITHOUT CT SCANS)**

#### **Step-0: Dry, mount and evacuate core sample**

1. Dry core at 80°C for at least 6 hours.
2. Load core into Hassler-type core holder.
3. Purge all lines in coreflood system with proper fluids.
4. Mount core holder into system and vacuum from first upstream valve (from core holder) to first downstream valve (from core holder) till vacuum reaches -27~-29inHg (at least 2 hours).

#### **Step-1: Simulate hydrocarbon-rich reservoir**

5. Connect lines from accumulator to coreholder slowly by opening every valve upstream except transducer valves.
6. Start filling core with hydrocarbon at a constant flow rate (3-10cc/min). Make sure to record pump starting time. The system is under-pressured from the vacuuming step. It takes about few minutes to pressurize. For safety, set a timer and monitor upstream pressure gauge after the timer goes off.
7. Once the pressure gauge starts going up, connect downstream lines to core holder. DO NOT OPEN TRANSDUCERS YET. Let pump run until effluent is collected in downstream beaker.
8. Stop pump and record time. Open transducer valves.
9. Begin file recording. Set pump at a proper flow rate and record the pressure drop once steady-state is achieved. Repeat at least 3 different flow rates to calculate absolute rock permeability.

10. Stop pump. Wait for the pressure drop across the core to become zero and then close hydrocarbon upstream valve.
11. Stop file recording.
12. Calculate pentane usage using flow rates and times.

**Step-2: Simulate fracturing fluid invasion**

13. Change liquid source of the pump to water or surfactant solution and switch lines for fluid invasion. Purge lines when necessary.
14. Set 60g of water on mass scale.
15. Rename a file and begin file recording. Measure evaporation rate of water by monitoring mass scale for at least 2 hours.
16. After 2 hours, start pump at 0.1cc/min (this flow rate can be adjusted depending on sample and/or experiment). The pump can be set to automatically turn on after a certain period of time using SHIFT-2 on pump keypad. Run fluid invasion for designed pore volumes (PVs). The time needs to be calculated based on core's pore volume and flow rate being used in Step-2.
17. Turn off pump once the designed fluid invasion is finished. The pump can be set to automatically turn off after a certain period of time using SHIFT-1 on pump keypad.
18. Record fluid evaporation rate for 2 hours after fluid invasion.
19. Stop file recording.

### **Step-3: Simulate fracturing fluid flowback during hydrocarbon production**

20. Change liquid source of the pump to DI water and switch lines for hydrocarbon injection. DO NOT CONNECT CORE HOLDER TO ACCUMULATOR YET!
21. Purge lines when necessary.
22. Set an appropriate flow rate on pump and rename a file.
23. Open valve connecting core holder to accumulator. As soon as the pressure reading goes up on the computer, begin data recording and turn pump on. Run hydrocarbon flood at least for 1PV. The time needs to be calculated based on core's pore volume and flow rate being used in Step-3.
24. Turn off pump after designed PVs of hydrocarbon flood. The pump can be set to automatically turn off after a certain period of time using SHIFT-1 on pump keypad.
25. Stop file recording.
26. Calculate total pentane usage based on flow rate and time.

### **Step-4: Remove core sample**

27. Wait for the pressure drop of coreflood system to become zero.
28. Close all valves. Make sure transducer's valves are all closed.
29. Release confining pressure.
30. Unscrew Swagelok fittings for core holder and move core holder to wooden support.
31. Disassemble core holder by removing bottom and top fittings.
32. Remove core sample from core holder.

## Appendix B: CT Scan Parameters and Saturation Calculation from CT Scan Results

### B.1 CT SCAN PARAMETERS

The in-situ saturation profile is acquired in real time by a Universal System HD-350 modified medical CT scanner. The *orbits* scan mode is used with the energy level of 130kv and 100mA. Once X-ray tube heat of the scanner is above 30%, the rock sample is scanned at 2mm intervals with 2s exposure time per slice, which gives 210μm resolution within the scanning plane.

### B.2 SATURATION CALCULATION FOR TWO-PHASE FLOW

The CT scanner reports the data as CT numbers on a voxel base, which measure the density of the material per voxel within each scanning plane. Before calculating saturation of any two-phase saturated rock sample, two single-phase scans (i.e., either in the dry or oil-saturated condition) must be obtained at the identical slice locations to calculate the porosity and rock CT number at each voxel of each slice.

$$\begin{cases} CT_{DC}^{voxel} = (1 - \phi^{voxel}) \cdot CT_{Rock}^{voxel} + \phi^{voxel} \cdot CT_{vac}^{bulk} \\ CT_{OC}^{voxel} = (1 - \phi^{voxel}) \cdot CT_{Rock}^{voxel} + \phi^{voxel} \cdot CT_{oil}^{bulk} \end{cases}$$

$$\Rightarrow \begin{cases} \phi^{voxel} = \frac{CT_{DC}^{voxel} - CT_{OC}^{voxel}}{CT_{vac}^{bulk} - CT_{oil}^{bulk}} \\ CT_{Rock}^{voxel} = \frac{CT_{DC}^{voxel} - \phi^{voxel} \cdot CT_{vac}^{bulk}}{(1 - \phi^{voxel})} \end{cases}$$

In the first set of equations shown above,  $CT_{DC}^{voxel}$  and  $CT_{OC}^{voxel}$  represent the measured CT numbers per voxel per slice from the scans on the dry core and the oil-saturated core;  $CT_{oil}^{bulk}$ ,  $CT_{vac}^{bulk}$  and  $CT_{DI}^{bulk}$  represent the CT numbers of bulk oil phase, vacuum and DI-water phase respectively. These fluid bulk CT numbers are measured in a

PEEK container (as shown in Figure B.1) at the same pressure as the corresponding coreflood. From the voxel values, the slice average of porosity (i.e.,  $\phi^{slice}$ ) and rock CT number (i.e.,  $CT_{Rock}^{slice}$ ) can be further determined.

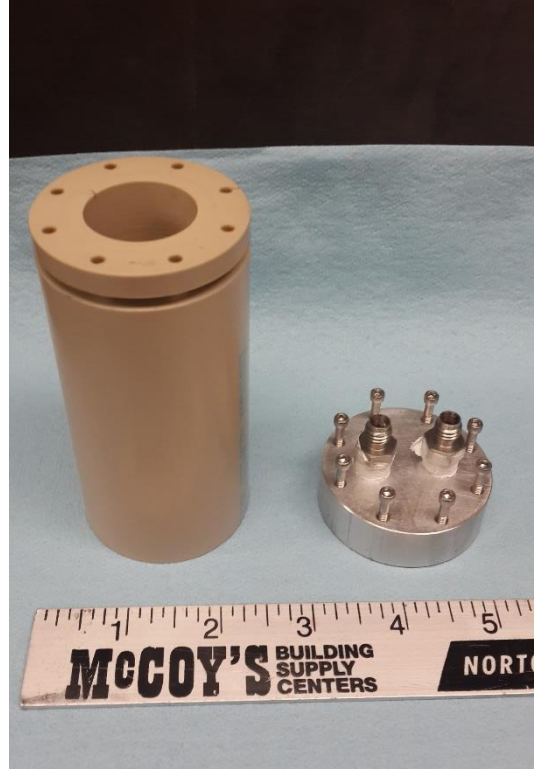


Figure B.1: PEEK container for measuring the fluid bulk CT number at the required pressure.

Using the calculated voxel values of porosity and rock CT number per slice, water saturation per voxel (i.e.,  $S_w^{slice}$ ) on that slice can be calculated from a CT scan on the two-phase saturated rock (i.e.,  $CT_{2C}^{voxel}$ ) through the following equations. From the voxel values of each slice, the slice average of water saturation (i.e.,  $S_w^{slice}$ ) can be further determined.

$$\begin{cases}
CT_{OC}^{voxel} = (1 - \phi^{voxel}) \cdot CT_{Rock}^{voxel} + \phi^{voxel} \cdot CT_{oil}^{bulk} \\
CT_{2C}^{voxel} = (1 - \phi^{voxel}) \cdot CT_{Rock}^{voxel} + \phi^{voxel} \cdot S_w^{voxel} \cdot CT_{DI}^{bulk} + \phi^{voxel} \cdot (1 - S_w^{voxel}) \cdot CT_{oil}^{bulk}
\end{cases}$$

$$\Rightarrow S_w^{voxel} = \frac{CT_{2C}^{voxel} - CT_{OC}^{voxel}}{\phi^{voxel} \cdot (CT_{DI}^{bulk} - CT_{oil}^{bulk})}$$

## Appendix C: Detailed Surfactant Formulations

### C.1 SURFACTANT SOLUTION USED IN CHAPTER 3

Formulation	Co-Surfactant 1	Co-Surfactant 2	Co-Solvent
1wt% AOT	0.8wt% Dihexyl Sodium Sulfosuccinate	0.2wt% Dioctyl Sodium Sulfosuccinate	/

### C.2 SURFACTANT SOLUTION USED IN CHAPTERS 6&7

Formulation	Co-Surfactant 1	Co-Surfactant 2	Co-Solvent
1wt% Surf	0.375wt% TDA-15PO-Sulfate	0.625wt% C <sub>15-18</sub> -IOS (ENORDET O332)	1.0wt% Isobutyl Alcohol

Notes: 1. TDA = Tridecyl Alcohol

2. PO = Propylene Oxide

3. IOS = Internal Olefin Sulfonate



## Bibliography

- Abrams, A., Vinegar, H.J., 1985. Impairment Mechanisms in Vicksburg Tight Gas Sands. SPE-13883-MS. doi:10.2118/13883-MS
- Agee, D.M., Wirajati, A.Y., Schafer, L., Grant, G., Garnier, A., Thouvenin, E., Wijanarko, A., 2010. Post-Fracturing Fluid Recovery Enhancement with Microemulsion. SPE-128098-MS. doi:10.2118/128098-MS
- Ahmadi, M., Sharma, M.M., Pope, G., Torres, D.E., McCulley, C.A., Linnemeyer, H., 2011. Chemical Treatment To Mitigate Condensate and Water Blocking in Gas Wells in Carbonate Reservoirs. SPE Prod. Oper. 26, 67–74. doi:10.2118/133591-PA
- Al-Anazi, H., Walker, J., Pope, G., Sharma, M., Hackney, D., 2005. A Successful Methanol Treatment in a Gas/condensate Reservoir: Field Application. SPE Prod. Facil. 20. doi:10.2118/80901-PA
- Almulhim, A., Alharthy, N., Tutuncu, A.N., Kazemi, H., 2014. Impact of Imbibition Mechanism on Flowback Behavior: A Numerical Study. SPE-171799-MS.
- Alramahi, B., Sundberg, M.I., 2012. Proppant Embedment And Conductivity of Hydraulic Fractures In Shales. Presented at the 46th U.S. Rock Mechanics/Geomechanics Symposium, ARMA-2012-291.
- Alvarez, J.O., Schechter, D.S., 2015. Wettability Alteration and Spontaneous Imbibition in Unconventional Liquid Reservoirs by Surfactant Additives. SPE-177057-MS. doi:10.2118/177057-MS
- Bazin, B., Peysson, Y., Lamy, F., Martin, F., Aubry, E., Chapuis, C., 2010. In-Situ Water-Blocking Measurements and Interpretation Related to Fracturing Operations in Tight Gas Reservoirs. SPE Prod. Oper. 25, 431–437. doi:10.2118/121812-PA
- Bazin, B., Peysson, Y., Lamy, F., Martin, F., Aubry, E., Chapuis, C., 2009. In Situ Water Blocking Measurements and Interpretation Related to Fracturing Operations in Tight Gas Reservoirs. SPE-121812-MS. doi:10.2118/121812-MS
- Bennion, B., Thomas, F., Bietz, R., Bennion, D., 1996. Remediation of Water And Hydrocarbon Phase Trapping Problems In Low Permeability Gas Reservoirs. PETSOC-96-80. doi:10.2118/96-80
- Bennion, D.B., Thomas, F.B., Bietz, R.F., Bennion, D.W., 1996. Water And Hydrocarbon Phase Trapping In Porous Media-Diagnosis, Prevention And Treatment. J. Can. Pet. Technol. 35. doi:10.2118/96-10-02
- Bennion, D.B., Thomas, F.B., Imer, D., Ma, T., 2000. Low Permeability Gas Reservoirs and Formation Damage -Tricks and Traps. SPE-59753-MS. doi:10.2118/59753-MS
- Bennion, D., Thomas, F., Imer, D., Ma, T., 2000. Low Permeability Gas Reservoirs and Formation Damage -Tricks and Traps SPE-59753-MS. doi:10.2118/59753-MS
- Bertoncello, A., Wallace, J., Blyton, C., Honarpour, M.M., Kabir, S., 2014. Imbibition and Water Blockage In Unconventional Reservoirs: Well-Management

- Implications During Flowback and Early Production. SPE Reserv. Eval. Eng. doi:10.2118/167698-PA
- Bostrom, N., Chertov, M., Pagels, M., Willberg, D., Chertova, A., Davis, M., Zagorski, W., 2014. The Time-Dependent Permeability Damage Caused by Fracture Fluid. SPE-168140-MS. doi:10.2118/168140-MS
- Bryndzia, L.T., 2012. Origin of High Salinities in Hydraulic Fracture Flow Back Fluids - An Example from the Haynesville Shale Gas Play, USA. Presented at the 3rd EAGE Shale Workshop - Shale Physics and Shale Chemistry. doi:10.3997/2214-4609.20143943
- Bui, K., Akkutlu, I.Y., Zelenev, A., Saboowala, H., Gillis, J.R., Silas, J.A., 2016. Insights Into Mobilization of Shale Oil by Use of Microemulsion. SPE J. 21, 613–620. doi:10.2118/178630-PA
- Caenn, R., Darley, H.C.H., Gray, G.R., 2011. Chapter 4 - Clay Mineralogy and the Colloid Chemistry of Drilling Fluids, in: Composition and Properties of Drilling and Completion Fluids (Sixth Edition). Gulf Professional Publishing, Boston, pp. 137–177.
- Chakraborty, N., Karpyn, Z.T., 2015. Gas Permeability Evolution with Soaking Time in Ultra Tight Shales. SPE-178740-STU. doi:10.2118/178740-STU
- Cheng, Y., 2012. Impact of Water Dynamics in Fractures on the Performance of Hydraulically Fractured Wells in Gas-Shale Reservoirs. J. Can. Pet. Technol. 51, 143–151. doi:10.2118/127863-PA
- Conn, C.A., Ma, K., Hirasaki, G.J., Biswal, S.L., 2014. Visualizing oil displacement with foam in a microfluidic device with permeability contrast. Lab Chip 14, 3968–3977. doi:10.1039/C4LC00620H
- Crafton, J.W., Noe, S., 2013. Factors Affecting Early Well Productivity in Six Shale Plays. SPE-166101-MS. doi:10.2118/166101-MS
- Curtis, M.E., Ambrose, R.J., Sondergeld, C.H., 2010. Structural Characterization of Gas Shales on the Micro- and Nano-Scales. SPE-137693-MS. doi:10.2118/137693-MS
- Curtis, M.E., Cardott, B.J., Sondergeld, C.H., Rai, C.S., 2012a. Development of organic porosity in the Woodford Shale with increasing thermal maturity. Int. J. Coal Geol., Shale Gas and Shale Oil Petrology and Petrophysics 103, 26–31. doi:10.1016/j.coal.2012.08.004
- Curtis, M.E., Sondergeld, C.H., Ambrose, R.J., Rai, C.S., 2012b. Microstructural investigation of gas shales in two and three dimensions using nanometer-scale resolution imaging. AAPG Bull. 96, 665–677. doi:10.1306/08151110188
- Das, P., Achalpurkar, M., Pal, O., 2014. Impact of Formation Softening and Rock Mechanical Properties on Selection of Shale Stimulation Fluid: Laboratory Evaluation. SPE-167787-MS. doi:10.2118/167787-MS
- Deen, T., Daal, J., Tucker, J., 2015. Maximizing Well Deliverability in the Eagle Ford Shale Through Flowback Operations. SPE-174831-MS. doi:10.2118/174831-MS

- Dehghanpour, H., Lan, Q., Saeed, Y., Fei, H., Qi, Z., 2013. Spontaneous Imbibition of Brine and Oil in Gas Shales: Effect of Water Adsorption and Resulting Microfractures. *Energy Fuels* 27, 3039–3049. doi:10.1021/ef4002814
- Dehghanpour, H., Zubair, H.A., Chhabra, A., Ullah, A., 2012. Liquid Intake of Organic Shales. *Energy Fuels* 26, 5750–5758. doi:10.1021/ef3009794
- DOE, 2009. Modern Shale Gas Development in the United States: A Primer. U.S. Department of Energy.
- Dutta, R., Lee, C.-H., Odumabo, S., Ye, P., Walker, S.C., Karpyn, Z.T., Ayala H., L.F., 2014. Experimental Investigation of Fracturing-Fluid Migration Caused by Spontaneous Imbibition in Fractured Low-Permeability Sands. *SPE Reserv. Eval. Eng.* 17, 74–81. doi:10.2118/154939-PA
- Economides, M.J., Hill, A.D., Ehlig-Economides, C., Zhu, D., 2012. *Petroleum Production Systems*, 2 edition. ed. Prentice Hall, Upper Saddle River, NJ.
- EIA, 2016a. EIA - Annual Energy Outlook 2016 [WWW Document]. URL <http://www.eia.gov/forecasts/aeo/> (accessed 10.14.16).
- EIA, 2016b. Hydraulic fracturing accounts for about half of current U.S. crude oil production - Today in Energy - U.S. Energy Information Administration (EIA) [WWW Document]. URL <http://www.eia.gov/todayinenergy/detail.php?id=25372> (accessed 10.13.16).
- EIA, 2016c. Hydraulically fractured wells provide two-thirds of U.S. natural gas production - Today in Energy - U.S. Energy Information Administration (EIA) [WWW Document]. URL <https://www.eia.gov/todayinenergy/detail.php?id=26112> (accessed 10.13.16).
- EIA, 2015. Technically Recoverable Shale Oil and Shale Gas Resources. U.S. Energy Information Administration.
- EIA, 2013. EIA/ARI World Shale Gas and Shale Oil Resource Assessment. U.S. Energy Information Administration.
- Engelder, T., Cathles, L.M., Bryndzia, L.T., 2014. The fate of residual treatment water in gas shale. *J. Unconv. Oil Gas Resour.* 7, 33–48. doi:10.1016/j.juogr.2014.03.002
- Fakcharoenphol, P., Kurtoglu, B., Kazemi, H., Charoenwongsa, S., Wu, Y.-S., 2014. The Effect of Osmotic Pressure on Improve Oil Recovery from Fractured Shale Formations. *SPE-168998-MS*. doi:10.2118/168998-MS
- Far, M.E., Buller, D., Quirein, J., Gu, M., Gokaraju, D., 2015. A new Integrated Data Analysis Algorithm and Workflow for Optimizing Horizontal Well Completion in Unconventional Reservoirs. Presented at the SPWLA 56th Annual Logging Symposium, SPWLA-2015-CCCC.
- Ferrill, D.A., McGinnis, R.N., Morris, A.P., Smart, K.J., Sickmann, Z.T., Bentz, M., Lehrmann, D., Evans, M.A., 2014. Control of mechanical stratigraphy on bed-restricted jointing and normal faulting: Eagle Ford Formation, south-central Texas. *AAPG Bull.* 98, 2477–2506. doi:10.1306/08191414053
- Fisher, M.K., Warpinski, N.R., 2012. Hydraulic-Fracture-Height Growth: Real Data. *SPE Prod. Oper.* 27, 8–19. doi:10.2118/145949-PA

- Gale, J.F.W., Laubach, S.E., Olson, J.E., Eichhubl, P., Fall, A., 2014. Natural fractures in shale: A review and new observations. *AAPG Bull.* 98, 2165–2216. doi:10.1306/08121413151
- Goddeeris, C., Cuppo, F., Reynaers, H., Bouwman, W.G., Van den Mooter, G., 2006. Light scattering measurements on microemulsions: Estimation of droplet sizes. *Int. J. Pharm.* 312, 187–195. doi:10.1016/j.ijpharm.2006.01.037
- Gupta, N., Rai, C.S., Sondergeld, C.H., 2013. Petrophysical Characterization of the Woodford Shale. *Petrophysics* 54, 368–382.
- Gupta, R., Mohanty, K.K., 2011. Wettability Alteration Mechanism for Oil Recovery from Fractured Carbonate Rocks. *Transp. Porous Media* 87, 635–652. doi:10.1007/s11242-010-9706-5
- He, K., Xu, L., 2015. Addressing Operator Concerns: Will Surfactant's Performance be Compromised Under Harsh Conditions? SPE-174361-MS. doi:10.2118/174361-MS
- He, K., Xu, L., Gao, Y., Yin, X., Neeves, K.B., 2015. Evaluation of surfactant performance in fracturing fluids for enhanced well productivity in unconventional reservoirs using Rock-on-a-Chip approach. *J. Pet. Sci. Eng.* 135, 531–541. doi:10.1016/j.petrol.2015.10.008
- Hirasaki, G., Miller, C.A., Puerto, M., 2011. Recent Advances in Surfactant EOR. *SPE J.* 16, 889–907. doi:10.2118/115386-PA
- Hoffman, R.L., 1975. A study of the advancing interface. I. Interface shape in liquid—gas systems. *J. Colloid Interface Sci.* 50, 228–241. doi:10.1016/0021-9797(75)90225-8
- Holditch, S.A., 1979. Factors Affecting Water Blocking and Gas Flow From Hydraulically Fractured Gas Wells. *J. Pet. Technol.* 31, 1515–1524. doi:10.2118/7561-PA
- Hou, M.J., Kim, M., Shah, D.O., 1988. A light scattering study on the droplet size and interdroplet interaction in microemulsions of AOT—oil—water system. *J. Colloid Interface Sci.* 123, 398–412. doi:10.1016/0021-9797(88)90261-5
- Howard, P., Mukhopadhyay, S., Moniaga, N., Schafer, L.A., Penny, G.S., Dismuke, K.I., 2010. Comparison of Flowback Aids: Understanding Their Capillary Pressure and Wetting Properties. *SPE Prod. Oper.* 25, 376–387. doi:10.2118/122307-PA
- Huang, D.D., Honarpour, M.M., 1998a. Capillary end effects in coreflood calculations. *J. Pet. Sci. Eng.* 19, 103–117. doi:10.1016/S0920-4105(97)00040-5
- Huang, D.D., Honarpour, M.M., 1998b. Capillary end effects in coreflood calculations. *J. Pet. Sci. Eng.* 19, 103–117. doi:10.1016/S0920-4105(97)00040-5
- Huh, C., 1979. Interfacial tensions and solubilizing ability of a microemulsion phase that coexists with oil and brine. *J. Colloid Interface Sci.* 71, 408–426. doi:10.1016/0021-9797(79)90249-2
- Jin, C.J., Sierra, L., Mayerhofer, M., 2013. A Production Optimization Approach to Completion and Fracture Spacing Optimization for Unconventional Shale Oil Exploitation. SPE-168813-MS, pp. 601–612. doi:10.1190/urtec2013-062

- Kamath, J., Laroche, C., 2003. Laboratory-Based Evaluation of Gas Well Deliverability Loss Caused by Water Blocking. SPE J. 8, 71–80. doi:10.2118/83659-PA
- Ke Xu, Tianbo Liang, Peixi Zhu, Jun Lu, Matthew Balhoff, Submitted. A 2.5 D Glass Micromodel for Investigation of Multiphase Flow in Porous Media.
- Kianinejad, A., Aminzadeh, B., Chen, X., DiCarlo, D.A., 2014. Three-Phase Relative Permeabilities as a Function of Flow History. SPE-169083-MS. doi:10.2118/169083-MS
- Kim, J., Zhang, H., Sun, H., Li, B., Carman, P., 2016. Choosing Surfactants for the Eagle Ford Shale Formation: Guidelines for Maximizing Flowback and Initial Oil Recovery. SPE-180227-MS. doi:10.2118/180227-MS
- King, G., 2015. Fracturing Flowback: Controls, Analysis & Benefits.
- King, G.E., 2012. Hydraulic Fracturing 101: What Every Representative, Environmentalist, Regulator, Reporter, Investor, University Researcher, Neighbor and Engineer Should Know About Estimating Frac Risk and Improving Frac Performance in Unconventional Gas and Oil Wells. SPE-152596-MS. doi:10.2118/152596-MS
- Kondash, A., Vengosh, A., 2015. Water Footprint of Hydraulic Fracturing. Environ. Sci. Technol. Lett. 2, 276–280. doi:10.1021/acs.estlett.5b00211
- Lake, L.W., Johns, R., Rossen, B., Pope, G., 2014. Fundamentals of Enhanced Oil Recovery. Society of Petroleum Engineers, Richardson, Texas.
- Landry, C.J., Eichhubl, P., Prodanović, M., Wilkins, S., 2016. Nanoscale grain boundary channels in fracture cement enhance flow in mudrocks. J. Geophys. Res. Solid Earth 121, 2016JB012810. doi:10.1002/2016JB012810
- Lan, Q., Ghanbari, E., Dehghanpour, H., Hawkes, R., 2014. Water Loss versus Soaking Time: Spontaneous Imbibition in Tight Rocks. SPE-167713-MS. doi:10.2118/167713-MS
- Lan, Q., Xu, M., Binazadeh, M., Dehghanpour, H., Wood, J.M., 2015. A comparative investigation of shale wettability: The significance of pore connectivity. J. Nat. Gas Sci. Eng. 27, Part 2, 1174–1188. doi:10.1016/j.jngse.2015.09.064
- Le, D., Hoang, H., Mahadevan, J., 2012. Gas Recovery From Tight Sands: Impact of Capillarity. SPE J. 17. doi:10.2118/119585-PA
- Lee, H.P., Olson, J.E., Holder, J., Gale, J.F.W., Myers, R.D., 2015. The interaction of propagating opening mode fractures with preexisting discontinuities in shale. J. Geophys. Res. Solid Earth 120, 2014JB011358. doi:10.1002/2014JB011358
- Lee, H.P., Olson, J.E., Schultz, R.A., 2016. The Interaction Analysis of Propagating Opening Mode Fractures with Veins Using Discrete Element Method. Presented at the 50th U.S. Rock Mechanics/Geomechanics Symposium, ARMA-2016-769.
- Levitt, D., Jackson, A., Heinson, C., Britton, L.N., Malik, T., Dwarakanath, V., Pope, G.A., 2009. Identification and Evaluation of High-Performance EOR Surfactants. SPE Reserv. Eval. Eng. 12, 243–253. doi:10.2118/100089-PA
- Liang, T., Achour, S.H., Longoria, R.A., DiCarlo, D.A., Nguyen, Q.P., 2016. Identifying and Evaluating Surfactant Additives to Reduce Water Blocks after Hydraulic

- Fracturing for Low Permeability Reservoirs. SPE-179601-MS.  
doi:10.2118/179601-MS
- Liang, T., Longoria, R.A., Lu, J., Nguyen, Q.P., DiCarlo, D.A., 2015a. Enhancing Hydrocarbon Permeability After Hydraulic Fracturing: Laboratory Evaluations of Shut-ins and Surfactant Additives. SPE-175101-MS. doi:10.2118/175101-MS
- Liang, T., Longoria, R.A., Lu, J., Nguyen, Q.P., DiCarlo, D.A., Huynh, U.T., 2015b. The Applicability of Surfactants on Enhancing the Productivity in Tight Formations. SPE-178584-MS. doi:10.2118/178584-MS
- Liang, T., Luo, X., Nguyen, Q., DiCarlo, D., Submitted. CT Measurements of Water Block in Low Permeability Rocks – Scaling and Clearing of Permeability Impairment.
- Longoria, R.A., Liang, T., Nguyen, Q.P., DiCarlo, D.A., 2015. When Less Flowback Is More: A Mechanism of Permeability Damage and its Implications on the Application of EOR Techniques. SPE-178583-MS. doi:10.2118/178583-MS
- Longoria, R., Liang, T., Huynh, U., Nguyen, Q., DiCarlo, D., Submitted. Water blocks in tight formations: The role of matrix-fracture interaction on permeability damage and its implications on the use of EOR-like techniques.
- Loucks, R.G., Reed, R.M., Ruppel, S.C., Hammes, U., 2012. Spectrum of pore types and networks in mudrocks and a descriptive classification for matrix-related mudrock pores. AAPG Bull. 96, 1071–1098. doi:10.1306/08171111061
- Loucks, R.G., Reed, R.M., Ruppel, S.C., Hammes, U., 2010. Preliminary Classification of Matrix Pores in Mudrocks.
- Loucks, R.G., Reed, R.M., Ruppel, S.C., Jarvie, D.M., 2009. Morphology, Genesis, and Distribution of Nanometer-Scale Pores in Siliceous Mudstones of the Mississippian Barnett Shale. J. Sediment. Res. 79, 848–861.  
doi:10.2110/jsr.2009.092
- Lu, J., Weerasooriya, U.P., Pope, G.A., 2014. Investigation of gravity-stable surfactant floods. Fuel 124, 76–84. doi:10.1016/j.fuel.2014.01.082
- Madsen, F.T., Müller-Vonmoos, M., 1989. The swelling behaviour of clays. Appl. Clay Sci. 4, 143–156. doi:10.1016/0169-1317(89)90005-7
- Mahadevan, J., Sharma, M.M., 2005. Factors Affecting Clean-up of Water-Blocks: A Laboratory Investigation. SPE J. 10, 238–246. doi:10.2118/84216-PA
- Mahadevan, J., Sharma, M.M., Yortsos, Y.C., 2007. Capillary Wicking in Gas Wells. SPE J. 12, 429–437. doi:10.2118/103229-PA
- Male, F., Marder, M.P., Browning, J., Ikonnikova, S., Patzek, T., 2016. Marcellus Wells' Ultimate Production Accurately Predicted from Initial Production. Society of Petroleum Engineers. doi:10.2118/180234-MS
- Mayerhofer, M., Stegent, N., Barth, J., Ryan, K., 2011. Integrating Fracture Diagnostics and Engineering Data in the Marcellus Shale. SPE-145463-MS.  
doi:10.2118/145463-MS
- McFann, G.J., Johnston, K.P., 1993. Phase behavior of nonionic surfactant/oil/water systems containing light alkanes. Langmuir 9, 2942–2948.  
doi:10.1021/la00035a035

- Milliken, K.L., Rudnicki, M., Awwiller, D.N., Zhang, T., 2013. Organic matter-hosted pore system, Marcellus Formation (Devonian), Pennsylvania. AAPG Bull. 97, 177–200. doi:10.1306/07231212048
- Milner, M., McLin, R., Petriello, J., 2010. Imaging Texture and Porosity in Mudstones and Shales: Comparison of Secondary and Ion-Milled Backscatter SEM Methods. SPE-138975-MS. doi:10.2118/138975-MS
- Mirzaei-Paiaman, A., Moghadasi, J., Masihi, M., 2010. Formation Damage Through Aqueous Phase Trapping in Gas Reservoirs. SPE-129637-MS. doi:10.2118/129637-MS
- Moos, D., Lacazette, A., Vassilellis, G.D., Cade, R., Franquet, J.A., Bourtembourg, E., Daniel, G., 2011. Predicting Shale Reservoir Response to Stimulation: the Mallory 145 Multi-Well Project. SPE-145849-MS. doi:10.2118/145849-MS
- Morales, D., Gutiérrez, J.M., García-Celma, M.J., Solans, Y.C., 2003. A Study of the Relation between Bicontinuous Microemulsions and Oil/Water Nano-emulsion Formation. *Langmuir* 19, 7196–7200. doi:10.1021/la0300737
- Morrill, J., Miskimins, J., 2012. Optimization of Hydraulic Fracture Spacing in Unconventional Shales. SPE-152595-MS. doi:10.2118/152595-MS
- Morsy, S., Sheng, J.J., 2015. Surfactant Preflood to Improve Waterflooding Performance in Bakken Shale Formation. *J. Pet. Sci. Res.*
- Nelson, P.H., 2009. Pore-throat sizes in sandstones, tight sandstones, and shales. AAPG Bull. 93, 329–340. doi:10.1306/10240808059
- Neog, A., Schechter, D.S., 2016. Investigation of Surfactant Induced Wettability Alteration in Wolfcamp Shale for Hydraulic Fracturing and EOR Applications. SPE-179600-MS. doi:10.2118/179600-MS
- Noe, S., Crafton, J., 2013. Impact of Delays and Shut-Ins on Well Productivity. SPE-165705-MS. doi:10.2118/165705-MS
- Odumabo, S.M., Karpyn, Z.T., Ayala H., L.F., 2014. Investigation of gas flow hindrance due to fracturing fluid leakoff in low permeability sandstones. *J. Nat. Gas Sci. Eng.* 17, 1–12. doi:10.1016/j.jngse.2013.12.002
- Odusina, E.O., Sondergeld, C.H., Rai, C.S., 2011. NMR Study of Shale Wettability. SPE-147371-MS. doi:10.2118/147371-MS
- Okouma, V., Guillot, F., Sarfare, M., San, V., Ilk, D., Blasingame, T.A., 2011. Estimated Ultimate Recovery (EUR) as a Function of Production Practices in the Haynesville Shale. SPE-147623-MS. doi:10.2118/147623-MS
- Pagels, M., Willberg, D.M., Edelman, E., Zagorski, W., Frantz, J., 2013. Quantifying Fracturing Fluid Damage on Reservoir Rock to Optimize Production. Society of Exploration Geophysicists, American Association of Petroleum Geologists, Society of Petroleum Engineers, pp. 1766–1774. doi:10.1190/urtec2013-180
- Paktinat, J., Pinkhouse, J.A., Stoner, W.P., Williams, C., Carder, G.A., Penny, G.S., 2005. Case Histories: Post-Frac Fluid Recovery Improvements of Appalachian Basin Gas Reservoirs. SPE-97365-MS. doi:10.2118/97365-MS

- Palmer, I.D., Moschovidis, Z.A., Schaefer, A., Mcketta, S., 2014. Case Histories From Fayetteville Shale: SRV Sizes, Fracture Networks, Spacing, Aperture Widths, and Implications for Proppant. SPE-169015-MS. doi:10.2118/169015-MS
- Palmer, I., Moschovidis, Z., Schafer, A., Mcketta, S., 2014. Case Histories From Fayetteville Shale: SRV Sizes, Fracture Networks, Spacing, Aperture Widths, and Implications for Proppant SPE-169015-MS. doi:10.2118/169015-MS
- Parekh, B., Sharma, M.M., 2004. Cleanup of Water Blocks in Depleted Low-Permeability Reservoirs. SPE-89837-MS. doi:10.2118/89837-MS
- Patzek, T., Male, F., Marder, M., 2014. A simple model of gas production from hydrofractured horizontal wells in shales. AAPG Bull. 98, 2507–2529. doi:10.1306/03241412125
- Patzek, T.W., Male, F., Marder, M., 2013. Gas production in the Barnett Shale obeys a simple scaling theory. Proc. Natl. Acad. Sci. 110, 19731–19736. doi:10.1073/pnas.1313380110
- Penny, G., Pursley, J., 2007. Field Studies of Drilling and Completion Fluids to Minimize Damage and Enhance Gas Production in Unconventional Reservoirs. SPE-107844-MS. doi:10.2118/107844-MS
- Penny, G.S., Zelenev, A., Lett, N., Paktinat, J., O’Neil, B.J., 2012a. Nano Surfactant System Improves Post Frac Oil and Gas Recovery in Hydrocarbon Rich Gas Reservoirs. Society of Petroleum Engineers. doi:10.2118/154308-MS
- Penny, G.S., Zelenev, A.S., Long, W., Lett, N.L., Crafton, J.W., 2012b. Laboratory and Field Evaluation of Proppants and Surfactants used in Fracturing of Hydrocarbon Rich Gas Reservoirs. Society of Petroleum Engineers. doi:10.2118/159692-MS
- Penny, G., Zelenev, A., Lett, N., Paktinat, J., O’Neil, B., 2012. Nano Surfactant System Improves Post Frac Oil and Gas Recovery in Hydrocarbon Rich Gas Reservoirs SPE-154308-MS. doi:10.2118/154308-MS
- Pope, G.A., 1980. The Application of Fractional Flow Theory to Enhanced Oil Recovery. Soc. Pet. Eng. J. 20, 191–205. doi:10.2118/7660-PA
- Pope, G.A., Wu, W., Narayanaswamy, G., Delshad, M., Sharma, M.M., Wang, P., 2000. Modeling Relative Permeability Effects in Gas-Condensate Reservoirs With a New Trapping Model. SPE Reserv. Eval. Eng. 3, 171–178. doi:10.2118/62497-PA
- Rapoport, L.A., Leas, W.J., 1953. Properties of Linear Waterfloods. J. Pet. Technol. 5, 139–148. doi:10.2118/213-G
- Roof, J.G., 1970. Snap-Off of Oil Droplets in Water-Wet Pores. Soc. Pet. Eng. J. 10, 85–90. doi:10.2118/2504-PA
- Rostami, A., Nasr-El-Din, H.A., 2014. Microemulsion vs. Surfactant Assisted Gas Recovery in Low Permeability Formations with Water Blockage. SPE West. North Am. Rocky Mt. Jt. Meet. 17-18 April Denver Colo.
- Shaoul, J.R., Zelm, V., F, L., de Pater, C.J., 2011. Damage Mechanisms in Unconventional-Gas-Well Stimulation--A New Look at an Old Problem. SPE Prod. Oper. 26, 388–400. doi:10.2118/142479-PA



- Sharma, M., Agrawal, S., 2013. Impact of Liquid Loading in Hydraulic Fractures on Well Productivity. SPE-163837-MS. doi:10.2118/163837-MS
- Sharma, M.M., Manchanda, R., 2015. The Role of Induced Un-propped (IU) Fractures in Unconventional Oil and Gas Wells. SPE-174946-MS. doi:10.2118/174946-MS
- Shuler, P.J., Lu, Z., Ma, Q., Tang, Y., 2016. Surfactant Huff-n-Puff Application Potentials for Unconventional Reservoirs. SPE-179667-MS. doi:10.2118/179667-MS
- Simpson, M.D., Patterson, R., Wu, K., 2016. Study of Stress Shadow Effects in Eagle Ford Shale: Insight from Field Data Analysis. Presented at the 50th U.S. Rock Mechanics/Geomechanics Symposium, ARMA-16-190.
- Sun, Y., Bai, B., Wei, M., 2015. Microfracture and Surfactant Impact on Linear Cocurrent Brine Imbibition in Gas-Saturated Shale. *Energy Fuels* 29, 1438–1446. doi:10.1021/ef5025559
- Tannich, J.D., 1975. Liquid Removal From Hydraulically Fractured Gas Wells. *J. Pet. Technol.* 27, 1309–1317. doi:10.2118/5113-PA
- Tannich, J.D., 1975. Liquid Removal From Hydraulically Fractured Gas Wells. *J. Pet. Technol.* 27, 1,309–1,317. doi:10.2118/5113-PA
- Taylor, R.S., Fyten, G., Romanson, R., McIntosh, G., Litun, R., Munn, D., Bennion, B., Piwowar, M., Hoch, O., 2010. Montney Fracturing-Fluid Considerations. *J. Can. Pet. Technol.* 49, 28–36. doi:10.2118/143113-PA
- Tran, T., Sinurat, P.D., Wattenbarger, B.A., 2011. Production Characteristics of the Bakken Shale Oil. SPE-145684-MS. doi:10.2118/145684-MS
- Wang, D., Butler, R., Zhang, J., Seright, R., 2012. Wettability Survey in Bakken Shale With Surfactant-Formulation Imbibition. *SPE Reserv. Eval. Eng.* 15, 695–705. doi:10.2118/153853-PA
- Wang, J., Liu, H., Yu, W., Cao, F., Sepehrnoori, K., 2016. Necessity of porosity correction before simulation and re-understanding of the effects of gas adsorption on production in shale gas reservoirs. *J. Pet. Sci. Eng.* 139, 162–170. doi:10.1016/j.petrol.2015.12.022
- Wang, L., Mutch, K.J., Eastoe, J., Heenan, R.K., Dong, J., 2008. Nanoemulsions Prepared by a Two-Step Low-Energy Process. *Langmuir* 24, 6092–6099. doi:10.1021/la800624z
- Warpinski, N.R., 1996. Hydraulic Fracture Diagnostics. *J. Pet. Technol.* 48, 907–910. doi:10.2118/36361-JPT
- Wasylishen, R., Fulton, S., 2012. Reuse of Flowback and Produced Water for Hydraulic Fracturing in Tight Oil. *Pet. Technol. Alliance Can.*
- Wilson, K., 2015. Analysis of Drawdown Sensitivity in Shale Reservoirs Using Coupled-Geomechanics Models. SPE-175029-MS. doi:10.2118/175029-MS
- Winsor, P.A., 1948. Hydrotrophy, solubilisation and related emulsification processes. *Trans. Faraday Soc.* 44, 376–398. doi:10.1039/TF9484400376
- Wu, K., Olson, J.E., 2016. Numerical Investigation of Complex Hydraulic-Fracture Development in Naturally Fractured Reservoirs. *SPE Prod. Oper.* doi:10.2118/173326-PA

- Wu, Y., Shuler, P.J., Blanco, M., Tang, Y., Goddard, W.A., 2008. An Experimental Study of Wetting Behavior and Surfactant EOR in Carbonates With Model Compounds. SPE J. 13, 26–34. doi:10.2118/99612-PA
- Xu, L., Fu, Q., 2012. Ensuring Better Well Stimulation in Unconventional Oil and Gas Formations by Optimizing Surfactant Additives. SPE-154242-MS. doi:10.2118/154242-MS
- Yaich, E., Williams, S., Bowser, A., Goddard, P., Souza, O.C.D. de, Foster, R.A., 2015. A Case Study: The Impact of Soaking on Well Performance in the Marcellus. SPE-178614-MS. doi:10.2118/178614-MS
- Yang, H.T., Britton, C., Liyanage, P.J., Solairaj, S., Kim, D.H., Nguyen, Q.P., Weerasooriya, U., Pope, G.A., 2010. Low-Cost, High-Performance Chemicals for Enhanced Oil Recovery. SPE-129978-MS. doi:10.2118/129978-MS
- Yan, Q., Lemanski, C., Karpyn, Z.T., Ayala, L.F., 2015. Experimental investigation of shale gas production impairment due to fracturing fluid migration during shut-in time. J. Nat. Gas Sci. Eng. 24, 99–105. doi:10.1016/j.jngse.2015.03.017
- Yu, W., Sepehrnoori, K., 2014a. Simulation of gas desorption and geomechanics effects for unconventional gas reservoirs. Fuel 116, 455–464. doi:10.1016/j.fuel.2013.08.032
- Yu, W., Sepehrnoori, K., 2014b. Optimization of Well Spacing for Bakken Tight Oil Reservoirs. Presented at the Unconventional Resources Technology Conference, SPE-1922108-MS. doi:10.15530/urtec-2014-1922108
- Zelenev, A., Ellena, L., 2009. Microemulsion Technology for Improved Fluid Recovery and Enhanced Core Permeability to Gas. SPE-122109-MS. doi:10.2118/122109-MS
- Zelenev, A., Zhou, H., Ellena, L., Penny, G., 2010. Microemulsion-Assisted Fluid Recovery and Improved Permeability to Gas in Shale Formations SPE-127922-MS. doi:10.2118/127922-MS
- Zhang, J., Zhu, D., Hill, A.D., 2015. Water-Induced Fracture Conductivity Damage in Shale Formations. SPE-173346-MS. doi:10.2118/173346-MS
- Zhang, X., Morrow, N.R., Ma, S., 1996. Experimental Verification of a Modified Scaling Group for Spontaneous Imbibition. SPE Reserv. Eng. 11, 280–285. doi:10.2118/30762-PA
- Zhou, Z., Abass, H., Li, X., Bearinger, D., Frank, W., 2016. Mechanisms of imbibition during hydraulic fracturing in shale formations. J. Pet. Sci. Eng. 141, 125–132. doi:10.1016/j.petrol.2016.01.021
- Zuo, L., Yu, W., Wu, K., 2016. A fractional decline curve analysis model for shale gas reservoirs. Int. J. Coal Geol. 163, 140–148. doi:10.1016/j.coal.2016.07.006